Developments in constitutive modelling of sand with applications to numerical analysis of offshore wind turbine foundations



Dimitrios Konstantinidis
Linacre College
University of Oxford

A thesis submitted for the degree of
Doctor of Philosophy
Trinity 2025

Abstract

Developments in constitutive modelling of sand with applications to numerical analysis of offshore wind turbine foundations

Dimitrios Konstantinidis

Linacre College, University of Oxford

A thesis submitted for the degree of *Doctor of Philosophy*

Trinity 2025

Offshore wind plays a central role in the global energy transition, with monopiles being the most widely adopted foundation type for offshore wind turbines (OWTs). While significant progress has been made in modelling monotonic behaviour and predicting ultimate capacity, simulating long-term cyclic response remains a major challenge. OWTs are subjected to millions of loading cycles over their lifetime, and design methods must account for the resulting permanent deformation and evolving soil stiffness and strength. This requires advanced constitutive models within finite element analyses (FEA), yet intrinsic (step-by-step) approaches remain underutilised due to their complexity and computational cost.

This thesis develops and applies a new intrinsic constitutive model for the cyclic response of sand under high-cycle loading relevant to OWTs. A critical evaluation of three existing models and a newly developed parallel Iwan model identified the Ta-Ger framework as the most suitable basis for further development. A high-cycle variant, Ta-Ger HC, incorporating a nonlinear anisotropic hyperelastic law, was formulated to capture cyclic strain accumulation across a wide range of densities and stress levels using a single calibration. Ta-Ger HC, along with a simpler variant named Ta-Ger B that instead incorporates a hypoelastic law, were extended to account for sands containing non-plastic and low-plasticity fines through the framework of equivalent granular state theory.

Ta-Ger B was implemented in PLAXIS 3D as a user-defined soil model and validated through FEA of selected PISA Dunkirk monopile field tests. Results demonstrate the model's ability to reproduce key behavioural trends, including monopile rotation accumulation, consistent with field observations and experimental trends. The simulations also offer insight into local soil mechanisms in the vicinity of the monopile. By clarifying implementation procedures and calibration steps, this work supports the effective application of all Ta-Ger variants in modelling OWT monopile foundations in sand under cyclic loading.

Acknowledgements

First and foremost, I would like to express my deepest gratitude to my supervisors, Prof. Chris Martin and Prof. Harvey Burd. I have been extremely privileged to work under their guidance throughout my DPhil. From the very beginning, I remember learning from Chris the importance of critical thinking at every stage of research and developing a strong numerical understanding of soil behaviour, while from Harvey I greatly benefited from his guidance in approaching coding with an engineer's mindset, treating every problem as solvable, and in producing clear and precise academic writing. Their trust, invaluable advice, and constant support have been fundamental to the successful completion of this research.

This research would not have been possible without the financial support of Fugro, and I am especially grateful to James Faroppa and Nigel Kee for their trust and backing. I also thank the staff and community at Linacre College, particularly our Principal, Nick Brown, the Academic Office, and Karen, the Accommodation Manager, for their assistance and for making it possible for me to stay in the beautiful Ursula Hicks House on Banbury Road.

I thank my best friend since our Anatolia College days, Giannis, for supporting me through every difficulty. I am especially grateful to my dear friend Miad for our engaging discussions, from soccer and cuisine to sand behaviour. I also thank Andrew, Daniel, Zheng-You, Rory, and Onur for their friendship, and Rachel, Gerry, and Abhinanda for their camaraderie. I am grateful to the Oxford Civil Engineering Group and WAMESS CDT for an inspiring environment, and to Alison and Clive for always being there to help us all.

I am also grateful to Profs. Nikos Gerolymos and Yiannis Dafalias at NTUA, Prof. Benjamin Cerfontaine at Southampton, and Prof. Guy Houlsby at Oxford for their valuable insights and discussions. I am thankful as well to all those who have believed in me along the way: my early teachers at Anatolia College; my professors at DUTH, especially Profs. Nikos Klimis, Nikos Zevgolis, and Ioannis Markou; and at Imperial College, Profs. David Taborda, Lidija Zdravković, David Potts, James Lawrence, and Jamie Standing.

Finally, I am deeply grateful to my family: my parents, Agapi and Sotiris, for their encouragement and unconditional support throughout my life; my brother Ionas, an electrical and computer engineer whom I deeply admire; my grandmother, architect Eugenia Gkinali Flampouriari, and her husband, Prof. Nikos Stefanidis. Their love and support are the foundation of all I have achieved.

Contents

Nomenclature viii
Introduction 1
1.1 Background 1
1.1.1 Offshore wind in the clean energy transition 1
1.1.2 Foundations of offshore wind turbines (OWTs) 2
1.1.3 Loading conditions and design requirements of OWT monopile foundations 2
1.1.4 OWT monopile foundation design under monotonic loading 5
1.1.5 Cyclic loading and available modelling strategies 5
1.1.5.1 Definition of cyclic loading 5
1.1.5.2 Overview of constitutive modelling approaches 6
1.1.6 OWT monopile foundation design under cyclic loading 9
1.2 Problem definition and scope of the project 10
1.2.1 Motivation 10
1.2.2 Objectives 11
1.3 Outline of the thesis 12
Literature Review 14
2.1 Key properties of offshore sand 14
2.1.1 Granular medium 14
2.1.2 Drainage conditions 15
2.2 Cyclic loading of sands and principal phenomena 15
2.2.1 Drained conditions 15
2.2.1.1 Cyclic strain accumulation patterns 15
2.2.1.2 Factors governing drained cyclic behaviour 18
2.2.2 Undrained conditions 20
2.2.2.1 Deformation modes 20
2.2.2.2 Factors governing undrained cyclic behaviour 22
2.3 Intrinsic constitutive modelling approaches for sand 24
2.3.1 Multi-surface plasticity 24
2.3.1.1 Series multi-surface plasticity models 24
2.3.1.2 Parallel Iwan multi-surface plasticity models 27
2.3.2 Bounding surface plasticity 28
2.3.2.1 SANISAND family and derived models 29
2.3.3 Other intrinsic constitutive modelling approaches 30
2.3.3.1 Elastoplastic original concepts 30
2.3.3.2 Hypoplasticity 31
2.3.3.3 Hyperplasticity 32
2.3.3.4 Ta-Ger novel plasticity framework 32

2.3.4 Performance of intrinsic models at element level 34
2.3.4.1 Comparative review of SANISAND variants, Hypoplastic and ISA models .. 34
2.3.4.2 Performance of multi-surface plasticity models 36
2.3.4.3 High-cycle performance of SANISAND-MS 38
2.3.5 Constitutive modelling of sand with non-plastic (or low-plasticity) fines 40
2.3.5.1 Equivalent granular state theory (EGST) 40
2.3.5.2 Overview of modelling strategies 42
2.4 Intrinsic step-by-step 3D-FEA/FDA of OWT foundations in sand 43
2.4.1 SANISAND-MS in OWT foundation BVP applications 43
2.4.2 Ta-Ger in OWT foundation BVP applications 48
2.4.3 Multi-surface models in OWT foundation BVP applications 50
2.5 Choice of suitable plasticity frameworks for further evaluation 51
Evaluation of four constitutive models for monotonic and cyclic loading of sands 53
3.1 Introduction 53
3.2 Brief description of the models 54
3.2.1 SANISAND DM04 model 55
3.2.2 Ta-Ger B model 57
3.2.3 Prevost model 60
3.2.4 PIMSS (Parallel Iwan Multi-Surface Sand) model 61
3.2.4.1 Motivation for the development of PIMSS 61
3.2.4.2 Micro-model formulation 62
3.2.4.3 Series versus parallel multi-surface plasticity approach 63
3.2.4.4 Multi-surface extension and numerical implementation 64
3.3 Comparative evaluation via element tests 66
3.3.1 Parameter calibration 67
3.3.1.1 SANISAND DM04 model parameters 67
3.3.1.2 Ta-Ger B model parameters 68
3.3.1.3 Prevost model parameters 69
3.3.1.4 PIMSS model parameters 71
3.3.2 Monotonic triaxial tests 73
3.3.2.1 Drained conditions 73
3.3.2.2 Undrained conditions 76
3.3.3 Undrained cyclic triaxial tests 78
3.3.4 Final verdict 83
3.3.4.1 Comparative insights on constitutive frameworks 83
3.3.4.2 Preferred constitutive approach 84
3.3.4.3 Considerations in the constitutive approach selection 86
Ta-Ger HC: A cyclic plasticity model for sands 88
4.1 Envisioning a high-cycle Ta-Ger model 88

4.2 Original formulation of Ta-Ger 89
4.2.1 Constitutive equations in multiaxial stress space 89
4.2.1.1 Elastic region 90
4.2.1.2 Bounding-surface-dependent plastic matrix 90
4.2.1.3 Flow rule 94
4.2.1.4 Lode angle dependency 95
4.2.1.5 Critical-state dependency 96
4.2.1.6 Hardening exponent equation 98
4.2.1.7 Load reversal criterion 99
4.2.2 Summary of parameters 99
4.2.3 Single-element simulations and numerical implementation recommendations 101
4.2.3.1 Summary of the stress integration schemes 101
4.2.3.2 Convergence analysis for monotonic loading 102
4.2.3.3 Guidelines for accurate simulation of softening behaviour 107
4.3 Key features of the proposed high-cycle formulation 108
4.3.1 Hyperelasticity 109
4.3.1.1 Motivation for inclusion of a hyperelastic law in Ta-Ger HC 109
4.3.1.2 Equations of the nonlinear anisotropic hyperelastic law 110
4.3.1.3 Purely elastic single-element simulations 113
4.3.1.4 Hyperelastic upgrade of Ta-Ger model 117
4.3.2 Bounding and phase transformation stress ratio equations 125
4.3.2.1 Monotonic critical state compliance 125
4.3.2.2 Identified numerical-instability issue in Ta-Ger A 128
4.3.2.3 High-cycle performance assessment 129
4.3.3 Hardening exponent equation 134
4.3.4 Significance of the stress integration scheme for high-cycle simulations 136
4.3.4.1 Elastic nonlinearity accumulation 136
4.3.4.2 Evaluation of two explicit integration schemes for high-cycle loading 138
4.3.5 Summary of parameters 140
4.3.6 Model performance 143
4.3.6.1 Cyclic tests on Hostun sand 143
4.3.6.2 Cyclic tests on quartz sand No.3 146
4.3.7 Conclusions 149
Adaptations of the Ta-Ger sand model to account for fines content 152
5.1 Targeting a unified critical state plasticity model for sand with fines 152
5.2 Model adaptation methodology 153
5.2.1 Equivalent granular void ratio $\boldsymbol{e}*$ and state parameter $\boldsymbol{\psi}*$ 153
5.2.2 Constitutive equations in multiaxial stress space 155
5.3 Single-element simulations 159

5.3.1 Simulation strategy and material database selection 159
5.3.2 Sydney sand with Majura silt 160
5.3.2.1 Parameter calibration 160
5.3.2.2 Drained monotonic triaxial tests 163
5.3.2.3 Undrained monotonic triaxial tests 164
5.3.2.4 Effectiveness of EGST 167
5.3.3 Karlsruhe fine sand with low-plasticity kaolinite 168
5.3.3.1 Parameter calibration 168
5.3.3.2 Drained monotonic triaxial tests 171
5.3.3.3 Undrained monotonic triaxial tests 173
5.3.3.4 Drained high-cycle triaxial tests 175
5.3.3.5 Effectiveness of EGST for predicting high-cycle strain accumulation 176
5.3.4 Conclusions 177
Application of the Ta-Ger model to 3D-FE simulations of monopile foundation 180
6.1 Introduction 180
6.2 Numerical implementation of Ta-Ger B in commercial 3D-FE software 182
6.2.1 Implementation of a User-Defined Soil Model (UDSM) in PLAXIS 3D 182
6.2.2 Benchmarking the implementation via triaxial test simulations in PLAXIS 3D 183
6.2.3 Implementation considerations for the robust application of Ta-Ger B to BVPs 184
6.3 3D-FE modelling of PISA monopile field tests at Dunkirk 186
6.3.1 Overview of simulation programme 186
6.3.2 Ground conditions for Dunkirk simulations 187
6.3.3 3D-FE model set-up for Dunkirk simulations 190
6.3.4 Calibration of Ta-Ger B parameters for Dunkirk sand 194
6.3.5 Monotonic monopile behaviour (DM4) 197
6.3.5.1 Comparison to field data and other studies 197
6.3.5.2 Mesh sensitivity 200
6.3.6 Essential terminology for assessing cyclic monopile response 202
6.3.7 Cyclic monopile behaviour (DM2) 204
6.3.7.1 Configuration I: parameter fitting to field data 204
6.3.7.2 Configuration II: load history effects on monopile cyclic response 207
6.3.7.3 Configuration III: Pisanò et al. (2024) calibration and installation effects 209
6.3.8 Simplified configuration: qualitative assessment of Ta-Ger B 213
6.3.8.1 Scope and rationale 213
6.3.8.2 Ground conditions, 3D-FE model setup, and Ta-Ger B parameters 214
6.3.8.3 Assessment against LeBlanc et al. (2010) empirical power law 216
6.3.8.4 Insights from key soil element responses around the monopile 220
6.3.9 Conclusions 224
Conclusions 226

7.1 Introduction 226
7.2 Key contributions 227
7.3 Implications for design 232
7.4 Research limitations and future work 233
7.4.1 PIMSS research pathway 233
7.4.2 Ta-Ger research pathway 234
7.4.2.1 Clean sands 234
7.4.2.2 Sands with fines 236
7.4.2.3 Improving the Ta-Ger UDSM implementation 237
References 238

Nomenclature

Basic assumptions: The soil mechanics sign convention is adopted, with compressive stresses and strains taken as positive and tensile as negative. All stress quantities are expressed in effective terms, consistent with standard constitutive modelling practice, and the prime notation is omitted unless otherwise stated. Tensors are represented using bold symbols, while scalars are denoted by regular letters.

Variables: upper-case letters	
Symbol	Meaning
A	Fabric anisotropy variable
A	Constant controlling the evolution of n (Ta-Ger HC model)
A_{d}	Dilatancy model variable (SANISAND DM04)
A_0	Dilatancy model parameter (SANISAND DM04)
$\mathbf{A}$	Differential of $\overline{r_0}$ with respect to $\bar{\boldsymbol{\varepsilon}}$ (hyperelasticity law)
B	Constant controlling the evolution of n (Ta-Ger HC model)
C	Complementary energy
$\mathbb{C}$	Second differential of $\overline{r_0}$ with respect to $\bar{\boldsymbol{\varepsilon}}$ (hyperelasticity law)
C_{u}	Uniformity coefficient
D	Outer pile diameter
$\mathbb{D}$	Stiffness matrix (hyperelasticity law)
D_{10}	Diameter in particle-size distribution curve corresponding to 10% and finer
D_{50}	Diameter in particle-size distribution curve corresponding to 50% and finer
D_{r}	Relative density
D_{r0}	Initial value of D_{r}
D_{r}^{*}	Equivalent granular relative density
$D_{\mathrm{r0}}^{\mathrm{m}}$	Model-scale D_{r0} from experimental test data (LeBlanc et al., 2010)
$D_{\mathrm{r0}}^{\mathrm{p}}$	Prototype-scale D_{r0} derived as the equivalent of the model-scale density for comparison purposes (LeBlanc et al., 2010)
D_{r0}^{*}	Equivalent granular initial relative density
$D_{ep_{micro}}^{i}$	Elastoplastic matrix of the *i*th micro-model
E	Strain energy
E	Young's modulus
E_X	Relative error (quantitative convergence criterion)
$\mathbf{E}^{\mathrm{e}}$	Elastic matrix
$\mathbf{E}^{\mathrm{ep}}$	Elastoplastic matrix
F	Bounding/limit surface (bounding surface plasticity)
G	Elastic shear modulus
G_0	Dimensionless small-strain shear modulus parameter
G_{hh}	Shear modulus in the horizontal plane (hyperelasticity law)
G_{max}	Small-strain shear modulus
G_{vh}	Shear modulus in the vertical plane (hyperelasticity law)
G^{i}	Elastic shear modulus of the *i*th micro-model
${G_0}^{i}$	Maximum (small-strain) elastic shear modulus of the *i*th micro-model
H	Horizontal load applied to monopile

Variables: upper-case letters	
Symbol	Meaning
H	Plastic modulus (SANISAND DM04)
$\mathbf{H}$	Plastic matrix (Ta-Ger model)
$\boldsymbol{H}$	Non-linear tensorial function (hypoplasticity)
H_{av}	Average horizontal cyclic load amplitude applied to the monopile
H_{cy}	Cyclic horizontal load variation applied to the monopile
H_{max}	Maximum horizontal load applied to monopile
H_{min}	Minimum horizontal load applied to monopile
H_{ref}	Reference horizontal load applied to monopile
$\mathrm{H}^{i'}$	Plastic modulus associated with the active surface (Prevost model)
$\mathbf{I}$	Identity matrix
I_P	Plasticity index
I_{r}	Bolton's relative dilatancy index
I_{r0}	Initial value of I_{r}
J_2	Second deviatoric stress invariant
J_3	Third deviatoric stress invariant
K	Elastic bulk modulus
K_0	Earth pressure coefficient
K^i	Elastic bulk modulus of the *i*th micro-model
L	Loading (or yield) surface (Ta-Ger model)
L	Plastic multiplier
L	Pile embedment length
$L^{(n)}$	Plastic multiplier of each subcomponent (series multi-surface plasticity)
M	Moment applied to monopile
M	Failure stress ratio
M_{cs}	Critical state stress ratio
M_{max}	Maximum moment applied to monopile
M_{min}	Minimum moment applied to monopile
M_{ref}	Reference moment applied to monopile
M_{pt}	Phase transformation stress ratio (Ta-Ger model)
M_{pt0}	Initial value of M_{pt} (Ta-Ger A model)
M_{s}	Bounding (ultimate strength) stress ratio (Ta-Ger model)
M_{sp}	Potentially maximum value of M_{s} (Ta-Ger A model)
M_{speak}	Maximum value of M_{s} (Ta-Ger A model)
M_{s0}	Initial value of M_{s} (Ta-Ger A model)
$M_{\mathrm{s,c}}$	Bounding (ultimate strength) stress ratio in compression (Ta-Ger model)
$M_{\mathrm{s,e}}$	Bounding (ultimate strength) stress ratio in extension (Ta-Ger model)
$M_{\mathrm{s,ss}}$	Bounding (ultimate strength) stress ratio in simple shear (Ta-Ger model)
$M_{\mathrm{s},\theta}$	Bounding (ultimate strength) stress ratio dependent on the Lode angle θ (Ta-Ger model)
M^i	Aperture of the *i*th conical yield surface (Prevost, PIMSS)
N	Number of loading cycles
N	Switch parameter (hyperelasticity law)
NYS	Number of yield surfaces (Prevost model)
P_{r}	Reference pressure (hyperelasticity law)
$\boldsymbol{P}^i$	Direction of plastic deformation of the *i*th micro-model (Superscript *i* is specific to PIMSS. For the Prevost model, no superscript is used)
$(\boldsymbol{P}^i)'$	Deviatoric component of the direction of plastic deformation of the *i*th micro-model (Superscript *i* is specific to PIMSS. For the Prevost model, no superscript is used)

Variables: upper-case letters	
Symbol	Meaning
$(P^i)''$	Volumetric component of the direction of plastic deformation of the *i*th micro-model (Superscript *i* is specific to PIMSS. For the Prevost model, no superscript is used)
Q	First constant determining I_r
$\boldsymbol{Q}^i$	Unit normal to the yield surface of the *i*th micro-model (Superscript *i* is specific to PIMSS. For the Prevost model, no superscript is used)
$(\boldsymbol{Q}^i)'$	Deviatoric component of the unit normal to the yield surface of the *i*th micro-model (Superscript *i* is specific to PIMSS. For the Prevost model, no superscript is used)
R	Second constant determining I_r
R_d	Dilatancy variable capturing densification effects (Ta-Ger model)
S_r	Degree of saturation
T_b	Empirical function for ratcheting response
T_c	Empirical function for ratcheting response
U_R	Accumulated pile head deflection at ground surface (relative to first cycle in load set)
U_x	Pile head deflection at ground surface
$U^i_{j,max}$	Pile head deflection at the peak force in the i-th load-cycle for loading sequence j
$U^0_{j,max}$	Reference deflection value for obtaining U_R, typically taken as the maximum deflection from the initial monotonic load (0th cycle)
$\Delta\boldsymbol{\sigma}^i_{micro}$	Incremental micro-stress tensor of the *i*th micro-model
$\Delta\eta$	Cyclic stress ratio amplitude
$\Delta\theta$	Accumulated pile rotation from the end of pre-cycling (θ_0) to N cycles (θ_N)
$\boldsymbol{\Phi}_\mathrm{f}$	Gradient of yield surface (Ta-Ger model)
$\boldsymbol{\Phi}_\mathrm{g}$	Gradient of plastic potential surface (Ta-Ger model)

Variables: lower-case letters	
Symbol	Meaning
a	Back-stress ratio (SANISAND DM04)
$\mathbf{a}$, a_ij	Anisotropy tensor (hyperelasticity law)
$\boldsymbol{\alpha}^i$	Kinematic deviatoric stress tensor defining the centre of each surface (Prevost model)
b	Fraction of fine particles contributing to force transmission within the soil skeleton
b_0	Pressure- and void-ratio-dependent stiffness parameter (SANISAND DM04)
c	Parameter controlling the rate of evolution of M_s and M_pt towards M_cs (Ta-Ger model)
c_h	Plastic modulus model parameter (SANISAND DM04)
c_z	Parameter controlling the evolution of the fabric-dilatancy quantity (SANISAND DM04)
d	Dilatancy (Ta-Ger model)
d_{50}	Diameter in particle-size distribution curve corresponding to 50% and finer (fines)
$\mathrm{d}\boldsymbol{\varepsilon}$	Incremental strain tensor
$\mathrm{d}\boldsymbol{\varepsilon}^\mathrm{e}$	Incremental elastic strain tensor
$\mathrm{d}\boldsymbol{\varepsilon}^\mathrm{p}$	Incremental plastic strain tensor
$\mathrm{d}\boldsymbol{\varepsilon}^{\mathrm{p}(n)}$	Incremental plastic strain subcomponent tensor (series multi-surface plasticity)
$\mathrm{d}\varepsilon_p$	Volumetric strain increment
$\mathrm{d}\varepsilon_p^\mathrm{e}$	Elastic volumetric strain increment
$\mathrm{d}\varepsilon_p^\mathrm{p}$	Plastic volumetric strain increment
$\mathrm{d}\varepsilon_q$	Deviatoric strain increment
$\mathrm{d}\varepsilon_q^\mathrm{e}$	Elastic deviatoric strain increment
$\mathrm{d}\varepsilon_q^\mathrm{p}$	Plastic deviatoric strain increment
$\mathrm{d}W$	First-order work (Ta-Ger model)

Variables: lower-case letters	
Symbol	Meaning
e	Void ratio
e^*	Equivalent granular void ratio
e_0	CSL model parameter
e_c	Void ratio at critical state
e_c^*	Equivalent granular void ratio at critical state
e_in^*	Equivalent granular initial void ratio
e_in	Initial void ratio
e_T	Terminal void ratio
e_max	Maximum void ratio
$e_\mathrm{max,HS}$	Maximum void ratio of the host sand
e_min	Minimum void ratio
$e_\mathrm{min,HS}$	Maximum void ratio of the host sand
f	Yield surface
f_0	First natural frequency of the turbine-foundation-soil system
f_{1p}	Rotor motion frequency
f_{3p}	Blade-passing frequency
f_c	Fines content
f_{thre}	Threshold fines content
f^i	Individual yield surfaces of series or parallel multi-surface plasticity models
g	Plastic potential function
$\mathrm{g}^{(n)}$	Plastic potential function of each subcomponent (series multi-surface plasticity)
g	Dimensionless shear modulus coefficient (hyperelasticity law)
h	Hardening variable (SANISAND DM04)
h	Lateral load eccentricity above ground surface
h_0	Plastic modulus model parameter (SANISAND DM04)
k	Dimensionless bulk modulus coefficient (hyperelasticity law)
k_n	Interface normal stiffness
k_s	Interface shear stiffness
m	Size of yield surface (SANISAND DM04)
m	Dimensionless parameter determining the rate of variation of G and K with p
n	Exponent in power-law relationship for stiffness (hyperelasticity law)
n	Hardening exponent parameter (Ta-Ger model)
$\boldsymbol{n}$	Normalised stress ratio tensor
n_0	Initial value of hardening exponent parameter n (Ta-Ger model)
n_b	Bounding surface model parameter (Ta-Ger model)
n_d	Dilatancy model parameter (Ta-Ger model)
n_f	Final value of hardening exponent parameter n (Ta-Ger model)
n_p	Stress ratio denoting distance of $\boldsymbol{r}_\mathrm{p}$ from hydrostatic axis (Ta-Ger model)
n_peak	Peak value of hardening exponent parameter n (Ta-Ger model)
p	Mean effective stress
p_at	Atmospheric pressure
p_in	Initial mean effective stress
p_p	Mean effective stress at last load reversal (Ta-Ger model)
p^ave	Average mean effective stress
p^i	Mean effective stress of the *i*th micro-model
p^min	Minimum mean effective stress
q	Deviatoric stress ratio
q^ampl	Cyclic deviatoric stress amplitude

Variables: lower-case letters	
Symbol	Meaning
q^{ave}	Average deviatoric stress
$q^{\max}$	Maximum deviatoric stress
$q^{\min}$	Minimum deviatoric stress
$\overline{r_0}$	Strain function used in definition of nonlinearity (hyperelasticity law)
$\boldsymbol{r}$	Second-order deviatoric stress ratio tensor
$\boldsymbol{r}_{\mathbf{p}}$	Second-order deviatoric stress ratio tensor at last load reversal (Ta-Ger model)
s	Loading direction for SANISAND DM04 triaxial space formulation
$\boldsymbol{s}$	Second-order deviatoric stress tensor
$\boldsymbol{s}_{\mathbf{p}}$	Second-order deviatoric stress tensor at last load reversal (Ta-Ger model)
$\boldsymbol{s}^i$	Second-order deviatoric stress tensor of the *i*th micro-model
t	Pile wall thickness
u	Pore water pressure
w^i	Weight corresponding to the *i*th micro-model (parallel Iwan arrangement)
x	Response variable (quantitative convergence criterion)
y	Anisotropy coefficient (hyperelasticity law)
z	Fabric-dilatancy quantity (SANISAND DM04)
$z_{\max}$	Maximum allowable z value (SANISAND DM04)
α	Ratcheting power-law exponent
α	Dilatancy-related constant controlling the rate of change of R_{d} (Ta-Ger model)
β	Constant controlling the evolution of n (Ta-Ger model)
γ	Constant controlling the evolution of n (Ta-Ger model)
γ	Unit weight
γ_w	Water unit weight
δ	Distance between stress point on yield surface and its projection on bounding surface
$\boldsymbol{\delta}$	Second-order identity matrix
$\delta\boldsymbol{\varepsilon}$	Incremental strain tensor
$\delta\boldsymbol{\sigma}$	Incremental stress tensor
$\delta\boldsymbol{\sigma}^i_{micro}$	Incremental micro-stress tensor of the *i*th micro-model
ε	Total strain (scalar)
$\boldsymbol{\varepsilon}$	Strain tensor
ε_{a}	Axial strain
ε_{z}	Axial strain
$\varepsilon^{\mathrm{acc}}$	Accumulated total strain (magnitude)
$\varepsilon_{\mathrm{a}}^{\mathrm{acc}}$	Accumulated axial strain
$\varepsilon^{\mathrm{ampl}}$	Resilient portion of strain during cyclic loading
ε_q	Deviatoric strain
$\varepsilon_q^{\mathrm{acc}}$	Accumulated deviatoric strain
ε_{v}	Volumetric strain
$\varepsilon_{\mathrm{v}}^{\mathrm{acc}}$	Accumulated volumetric strain
$\varepsilon_{\mathrm{v}}^{\mathrm{inst}}$	Enforced installation volumetric strain
$\overline{\boldsymbol{\varepsilon}}$	Equivalent symmetric strain tensor for introducing anisotropy (hyperelasticity law)
$\dot{\boldsymbol{\varepsilon}}$	Strain rate tensor
$\varsigma^{\mathrm{ampl}}$	Stress amplitude ratio
ζ	SANISAND-MS model cyclic parameter
ζ	Hardening variable (Ta-Ger model)
ζ	Dilatancy state parameter
ζ^*	Equivalent dilatancy state parameter
ζ_{b}	Cyclic load amplitude characterisation
ζ_{c}	Cyclic load asymmetry characterisation

Variables: lower-case letters	
Symbol	Meaning
η	Deviatoric stress ratio in triaxial space
η_{in}	Stress ratio at the start of loading (SANISAND DM04)
η^{ave}	Average deviatoric stress ratio in triaxial space
η^i	Deviatoric stress ratio of the *i*th micro-model (Superscript *i* is specific to PIMSS. For the Prevost model, no superscript is used)
$\bar{\eta}^i$	Parameter defining phase transformation stress ratio for the *i*th micro-model (Superscript *i* is specific to PIMSS. For the Prevost model, no superscript is used)
θ	Lode angle
θ	Pile rotation
θ_0	Pile rotation at the end of the pre-cycling monotonic phase
θ_G	Pile rotation at ground surface
θ_N	Pile rotation accumulated after N cycles
θ_s	Reference pile rotation defined by LeBlanc et al. (2010)
λ	CSL model parameter
μ_0	Cyclic parameter in the SANISAND-MS model
$\boldsymbol{\mu}^i$	Translation direction tensor of the *i*th surface in deviatoric space (Prevost model)
v	Poisson's ratio
v_{int}	Interface Poisson's ratio
ξ	CSL model parameter
$\boldsymbol{\sigma}$	Stress tensor
$\boldsymbol{\sigma}^i_{micro}$	Micro-stress tensor of the *i*th micro-model (parallel Iwan arrangement)
$\boldsymbol{\sigma}_{\mathbf{p}}$	Effective stress tensor at last load reversal (Ta-Ger model)
σ_{n}	Interface normal stress
σ_{r}	Radial stress
φ	Friction angle
φ_{cs}	Critical state friction angle
φ_{max}	Peak friction angle
χ	Particle size ratio
χ	Parameter accounting for Lode angle effects (Ta-Ger model)
ψ	State parameter
ψ	Pile rotation
$\bar{\psi}_{\text{acc}}$	Accumulated pile head rotation at the ground surface (relative to first cycle in load set)
ψ_{in}	Initial state parameter
ψ^*	Equivalent granular state parameter
ψ^i	State parameter of the *i*th micro-model (Superscript *i* is specific to PIMSS. For the Prevost model, no superscript is used)
ψ^*_{in}	Equivalent granular initial state parameter
ψ^i_{max}	Rigid rotation of the pile in the *i*-th load-cycle
ω	Direction of strain accumulation

Abbreviations	
Abbreviation	Meaning
1D	One dimensional
2D	Two dimensional
3D	Three dimensional
ACST	Anisotropical critical state theory
API	American Petroleum Institute
B-SDM	Bounding surface stiffness degradation method
BVP	Boundary value problem
cDSS	Cyclic direct simple shear test
CS	Critical state
CSL	Critical state line
CSSM	Critical state soil mechanics
CST	Critical state theory
EG-CSL	Equivalent granular critical state line
EGST	Equivalent granular state theory
FD	Finite difference
FDA	Finite difference analysis
FE	Finite element
FEA	Finite element analysis
FLS	Fatigue Limit State
GW	Gigawatt
HARM	Harmonic Response Analysis Model
HCA	High Cycle Accumulation model
ISA	Intergranular Strain Anisotropic model
LS	Load set
MW	Megawatt
MWh	Megawatt-hour
OWF	Offshore wind farm
OWT	Offshore wind turbine
PDMY01	Pressure dependent multi-yield 01 (or 02) model
PIMS	Parallel Iwan Multi-Surface model
PIMSS	Parallel Iwan Multi-Surface Sand model
PISA	Pile Soil Analyses
PTL	Phase-transformation line
RK1 (or FE)	First-order accurate single-step forward Euler
RKF23	Third-order accurate Runge-Kutta-Fehlberg substepping scheme
SANISAND	Simple Anisotropic Sand model
SDM	Stiffness degradation method
SLS	Serviceability Limit State
SOLCYP	French National Sollicitations Cycliques sur Pieux (French acronym)
STOL	Integration error tolerance
Ta-Ger	Tasiopoulou Gerolymos model
ULS	Ultimate Limit State
USD	United States Dollar
VELACS	Verification of Liquefaction Analyses by Centrifuge Studies

Chapter 1
Introduction

1.1 Background

1.1.1 Offshore wind in the clean energy transition

Offshore wind plays a crucial role in combating global warming by accelerating the shift from fossil fuels to renewable energy. Many countries are rapidly expanding their offshore wind capacity or have ambitious development plans. The UK's British Energy Security Strategy (April 2022) targets 50 GW of offshore wind capacity by 2030, with 45 GW expected from bottom-fixed structures (United Kingdom government, 2022). Even Greece, where offshore wind is yet to be developed, passed its first offshore wind law (4964/2022) in July 2022, setting a 2 GW target by 2030, focusing on floating farms due to deep waters (HEREMA, 2022). Currently, the European Union's cumulative offshore wind capacity stands at 19.4 GW, meeting 2% of its electricity demand, while the UK has 14.8 GW, supplying 17% of its demand (Wind Europe, 2024). To achieve climate neutrality by 2050, the European Commission estimates offshore wind capacity must expand to 300 GW, requiring approximately €800 billion in investment (European Commission, 2020). Despite offshore wind's advantages over onshore, construction and maintenance costs remain high.

A recent National Renewable Energy Laboratory (NREL) analysis (Stehly et al., 2024) estimates the levelized cost of energy (LCOE) at 42USD/MWh for land-based wind in the US, compared to 117USD/MWh for fixed-bottom offshore wind in the North Atlantic and 181USD/MWh for floating offshore wind off the Pacific Coast.

1.1.2 Foundations of offshore wind turbines (OWTs)

An offshore wind turbine (OWT) comprises a foundation system, tower, nacelle, rotor, and blades. Figure 1.1 illustrates different bottom-fixed foundation types. Foundation systems, including installation, contribute 20-30% of the total capital costs of OWTs, with monopiles being the dominant foundation type in Europe (Byrne *et al.*, 2019). Modern monopiles are large-diameter (8-10 m) open-ended steel tubes, typically ranging from 30 to 50 m in embedded length and are installed by driving into the seabed. Their dimensions are expected to increase further for the next generation of OWTs in deeper waters (Byrne, 2020), as larger turbines are being developed to maximize energy production while new offshore sites in deeper waters are being explored. Optimizing monopile design could lead to significant cost savings and enhance the feasibility of offshore wind expansion.

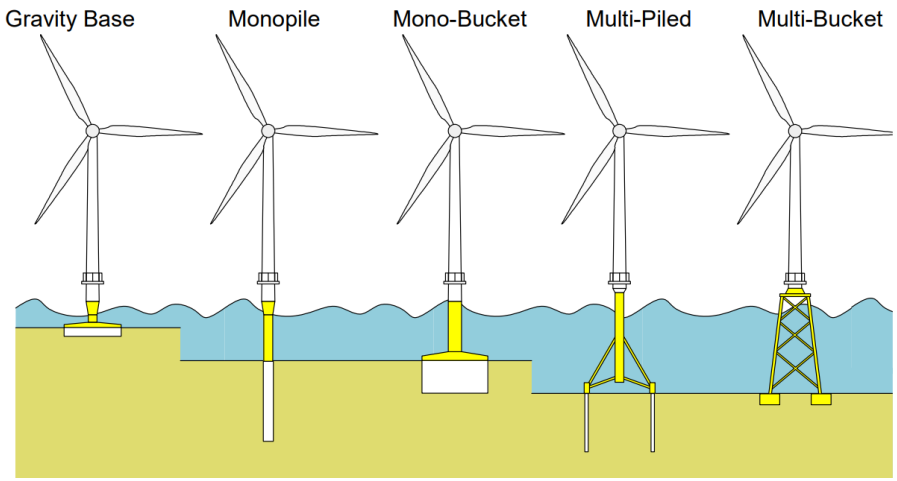

Figure 1.1: Types of fixed-bottom foundations of OWTs (Byrne, 2011).

1.1.3 Loading conditions and design requirements of OWT monopile foundations

OWTs are subjected to multiple loads, including self-weight, aerodynamic forces on the blades and tower, hydrodynamic loads from waves and currents, accidental impacts, and

operational loads from rotating components. Unlike offshore oil and gas structures, where vertical loads govern design, OWT monopile design is primarily governed by horizontal cyclic loads induced by wind, waves, and rotor motions, with frequencies ranging from 0.001 to 10Hz (Arany *et al.*, 2017). Among these, wave-induced loads typically dominate the cyclic component, occurring at frequencies around 0.1Hz. These environmental and operational loads combine to impose temporally and spatially varying horizontal (H) and moment (M) loading at the monopile foundation, as shown in Figure 1.2. The combined loading is cyclic, multi-directional and pseudo-random with continuously varying amplitude (irregular), frequency, and eccentricity (M/H). This complexity is further illustrated in Figure 1.3, which presents measured mudline moments in a single direction over a 30-second period during idling conditions (Page *et al.*, 2019).

For monopile foundations, design must ensure structural integrity across operational and extreme conditions (Kallehave *et al.*, 2015) by adhering to the limit state design philosophy, with the following key requirements (Bhattacharya, 2019):

- The first natural frequency of the turbine-foundation-soil system (f_0) must fall within the 'soft-stiff' range, i.e., $f_{1p} < f_0 < f_{3p}$, where f_{1p} and f_{3p} correspond to rotor motion and blade-passing frequencies, respectively (Figure 1.4).
- Sufficient fatigue resistance to long-term operational loads (Fatigue Limit State, FLS).
- Sufficient strength to withstand extreme loads without failure (Ultimate Limit State, ULS), ensuring a maximum mudline rotation of 2° and a maximum mudline displacement of $0.1D$ (Byrne *et al.*, 2017). Cyclic degradation effects on lateral resistance must also be considered in ULS design to account for strength and stiffness reduction under repeated loading (DNV GL, 2016).
- Compliance with serviceability requirements (Serviceability Limit State, SLS) is achieved by limiting deformations under environmental and operational loads, with a

focus on permanent accumulated rotation at the mudline. A permanent mudline rotation limit of 0.25° is typically applied separately to account for initial installation misalignment and cyclic loading-induced soil deformations, respectively (Peralta *et al.*, 2017; Wang and Larsen, 2019), although this value is often project-specific and governed by turbine manufacturer requirements (DNV GL, 2016).

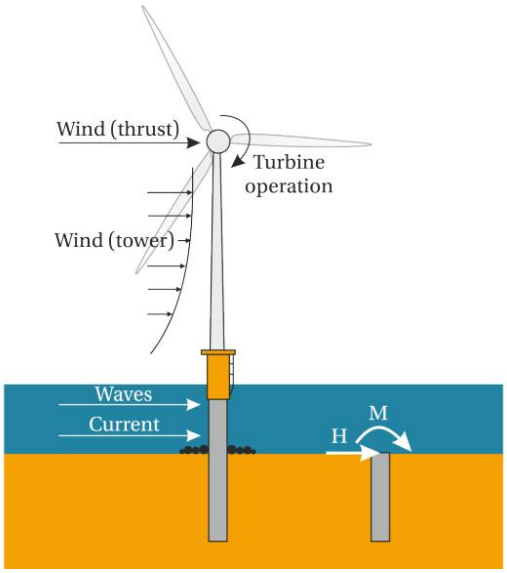

Figure 1.2: Illustration of lateral loading components on an OWT monopile foundation (Richards, 2019).

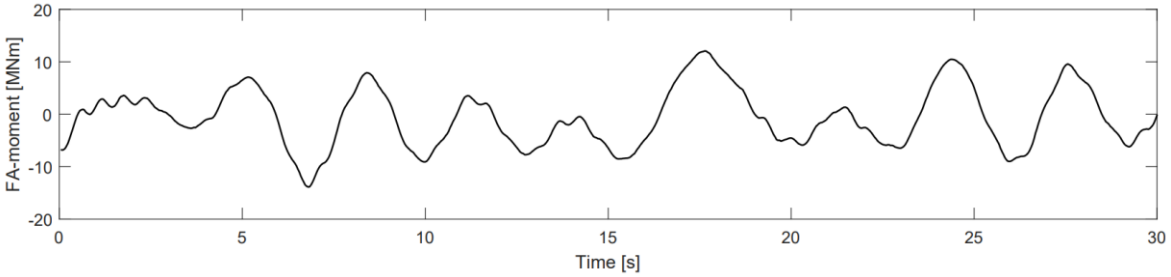

Figure 1.3: Example of 30-second moment loading time series for an OWT monopile at the mudline in the North Sea under idling conditions, derived from strain measurements. The loading shown is in the fore-aft (FA) direction, which, in this case, aligns with the wind direction (Page *et al.*, 2019).

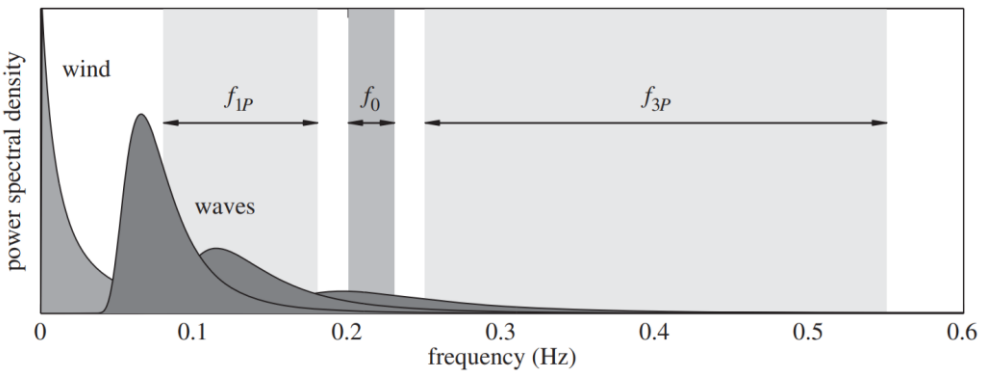

Figure 1.4: Wave and wind loading frequencies overlaid with the first natural frequency of the OWT-soil system (f_0), the rotor frequency (f_{1p}) and the blade-passing frequency (f_{3p}) (Kallehave *et al.*, 2015).

1.1.4 OWT monopile foundation design under monotonic loading

Until recently, the design of OWT monopile foundations was based on guidelines originally proposed for the oil and gas industry, employing a simplified one-dimensional (1D) analysis design approach known as the 'p-y' method based on the Winkler assumption (API, 2011; DNV GL, 2016). However, the monopiles used for OWT are less slender (stiffer and shorter in length) compared to the piles utilized for oil and gas platforms and hence they behave quite differently. Using these methods for the design of OWT monopiles can lead to unreliable design (Gavin and Doherty, 2012). The PISA project (Byrne *et al.*, 2019) developed a new design framework for laterally loaded monopiles, using 3D finite element analysis (3D-FEA) to derive soil reactions, which were then used to calibrate depth-dependent conic functions in a 1D Winkler-type model (Burd et al., 2020; Byrne et al., 2020a). While conventional p-y methods account only for lateral soil reactions along the embedded length of the pile, the PISA design model additionally includes vertical shear tractions along the pile (modelled as distributed moments in 1D), as well as the horizontal force and base moment at the pile base, offering a more realistic representation of soil-structure interaction and enabling reliable and efficient ULS design across varying ground conditions. As such, the PISA framework has established a new benchmark for the monotonic design of OWT monopile foundations in practice.

1.1.5 Cyclic loading and available modelling strategies

1.1.5.1 Definition of cyclic loading

Before reviewing current design practices for OWT monopile foundations under cyclic loading, it is important to clarify that the terminology around cyclic loading modelling used in this thesis follows the definitions of Houlsby et al. (2020). 'Cyclic loading' is a term commonly used in industry to describe a range of complex loading scenarios, as explained in section 1.1.3. However, in laboratory settings, it typically refers to repeated loading cycles

with constant frequency and uniform amplitude, and existing design methods often rely on data from these tests. To bridge the gap between irregular offshore loading and the simplified cyclic loading used in laboratory tests, a process known as 'rainflow counting' is often applied. This technique breaks down complex, variable-amplitude loading sequences into simpler cycles, effectively translating the pseudo-random loading experienced offshore into a form similar to the data obtained from laboratory tests. This process is widely used in existing cyclic constitutive modelling approaches and hence design methods.

1.1.5.2 Overview of constitutive modelling approaches

The dynamic loads acting on the monopile throughout an OWT's operational life often exceed 10^7 loading cycles, influencing stiffness, damping, accumulated displacement, and post-cyclic monotonic response to ULS loading (Houlsby *et al.*, 2020). The ability to numerically predict these long-term effects is crucial for OWT foundation design. The constitutive modelling approaches addressing this challenge to varying degrees fall into two major groups: the 'intrinsic' and the 'extrinsic' (Houlsby *et al.*, 2020), also termed 'implicit' and 'explicit' respectively (Niemunis et al., 2005). These approaches serve as numerical tools for prediction within broader design methodologies but are not complete design methods. The key characteristics of each approach include:

- Intrinsic approach (step-by-step): Simulates soil response analytically by integrating stress-strain increments over the full loading history, enabling the model to handle any loading sequence without requiring rainflow counting.
- Extrinsic approach: Calculates the response to a few initial cycles, using advanced FEA. The effects of many subsequent cycles, such as accumulated displacements or excess pore pressures, are then added using simplified laws. Rainflow counting is used to break down pseudo-random multi-amplitude loading into regular cycles grouped in bins and processed seperately to account for their effects.

Extrinsic models vary, but two key types for OWT foundation design are ‘skip-cycle strain-accumulation’ models and the ‘stiffness degradation method’ (SDM) (Achmus et al., 2009; Gao et al., 2023). Both model the first few cycles using an intrinsic constitutive model, with skip-cycle models typically modelling the first one or two cycles and SDM only the first cycle. In skip-cycle models, such as the High Cycle Accumulation (HCA) model proposed by Niemunis et al. (2005), strain accumulation in subsequent cycles is predicted using a calibrated strain accumulation law accounting for factors such as cyclic stress amplitude, average stress ratio, and number of cycles at each point within the finite element (FE) mesh. In SDM, strain accumulation in subsequent cycles is modeled by scaling the plastic modulus and dilatancy relationship through a stiffness degradation phase, also governed by a calibrated strain accumulation law. Figure 1.5 illustrates the differences in loading histories for OWT monopile foundations across intrinsic and extrinsic modelling approaches.

Choosing a suitable modelling approach is challenging, as each offers advantages and limitations. Early extrinsic models focused on individual aspects of cyclic strain accumulation, such as volumetric strain, deviatoric strain, or total strain magnitude or direction (Lentz and Baladi, 1981; Sawicki and Swidzinski, 1989; Sweere, 1990). Recent advancements have enabled models that capture the cyclic evolution of the entire strain tensor, including both magnitude and direction (Bouckovaklas et al., 1985; Suiker and de Borst, 2003; Niemunis et al., 2005; François et al., 2009). However, the applicability of extrinsic models can be limited, particularly when derived from laboratory tests, as they rely solely on observed trends rather than analytically modelling the soil response, making them highly dependent on experimental conditions (Liu, 2020). Their low computational cost has led to their widespread use in 3D-FE simulations for offshore foundations under long-term loading conditions (Niemunis et al., 2005; Achmus et al., 2009; Wichtmann et al., 2010; Pasten et al., 2014; Jostad et al., 2015; Chong and Pasten, 2017; Staubach and Wichtmann,

2020; Page et al., 2021; Gao et al., 2023; Tantivangphaisal et al., 2025). While extrinsic models offer practical advantages, only intrinsic models can fully capture the cyclic soil response if computational constraints were not a limitation. Extrinsic models extrapolate results over many cycles but cannot entirely replace intrinsic constitutive models. Unlike intrinsic models, which integrate stress-strain responses across the entire system while enforcing boundary conditions, extrinsic skip-cycle models determine strain accumulation locally at individual integration points. This localized approach can introduce inaccuracies in large-scale applications, as it may fail to comply with boundary conditions, causing divergence from global equilibrium in FE simulations (Gao et al., 2023).

Even the extrinsic SDM (Achmus et al., 2009) and its enhanced version, 'bounding surface stiffness degradation method' (B-SDM) (Gao et al., 2023), developed to address limitations of SDM and extrinsic skip-cycle models, still face simplifications. B-SDM integrates bounding surface plasticity, to improve its ability to capture the first regular cycle. However, it remains reliant on empirical calibration, cannot capture softening behaviour, and is limited to drained conditions. Despite incorporating bounding surface concepts, it requires different parameter calibrations for the same sand under varying densities, complicating its application. B-SDM is designed to predict displacements under long-term loading, limiting its versatility. Its validation is limited to a small number of cycles at the single-element and finite-single-element levels, and it cannot simulate, realistic storm loading, as it only models discrete cyclic amplitude packets.

Intrinsic constitutive models often involve complex formulations and calibration procedures with numerous parameters that lack physical meaning. This complexity can result in high computational demands (Whyte et al., 2020; Liu et al., 2022a). Additionally, intrinsic models may suffer from numerical errors accumulating over many load cycles (Niemunis et al., 2005; Pasten et al., 2014).

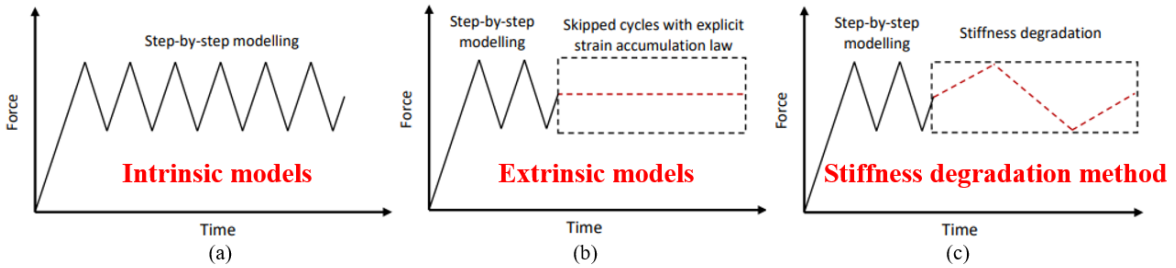

Figure 1.5: Idealised loading histories for OWT monopile foundations for: (a) intrinsic step-by-step models; (b) extrinsic skip-cycle strain-accumulation models; (c) (extrinsic) stiffness degradation method (SDM) (modified after Gao et al. (2023)).

1.1.6 OWT monopile foundation design under cyclic loading

Various methods have been proposed, employing either intrinsic or extrinsic models applied at different scales, including full 3D-FEA, intermediate approaches such as p-y curves, or simplified micro-scale models, all aiming to capture key elements of cyclic behaviour necessary to ensure foundation reliability. However, these methods often do not provide complete guidance for cyclic design, focusing instead on predicting how specific phenomena (e.g., ratcheting, hysteretic response, stiffness changes) affect the monopile's behaviour. Methods that rely on intrinsic models are classified as intrinsic methods, while those using extrinsic models are classified as extrinsic methods. In addition, cyclic effects are often addressed by applying empirical degradation factors to soil reaction curves (API, 2011), a design-focused approach commonly referred to as the factoring method. Some methods do not fit neatly into a single category, as they combine elements from all three approaches.

However, no widely accepted framework currently exists for cyclic loading in design practice, in contrast to the well-established PISA methodology for static loading. Nevertheless, several noteworthy methods have been proposed. The SOLCYP factoring method extends the API method by locally degrading p-y curves or incorporating full-scale and centrifuge test data into macro-models (Puech and Garnier, 2017). The NGI (Norwegian Geotechnical Institute) method scales cyclic response based on element tests, such as cyclic simple shear or triaxial tests, to predict ratcheting (Andersen, 2015; Zhang *et al.*, 2016), combining features from both factoring and extrinsic methods. The Hyperplastic Accelerated

Ratcheting Model (HARM) applies a hyperplastic macro-element model to capture the monopile's 1D cyclic response (Houlsby *et al.*, 2017). Although intrinsic in nature, HARM incorporates advantages of both intrinsic and extrinsic methods (Houlsby *et al.*, 2020). A more recent approach integrates an accumulation procedure with 3D-FEA results and the extrinsic HCA constitutive model that accounts for strain accumulation, sand density, and load characteristics to predict monopile rotation for SLS assessment (Page *et al.*, 2021).

1.2 Problem definition and scope of the project

1.2.1 Motivation

Design methods for OWT monopile foundations under monotonic loading are well established. However, methods for predicting monopile performance under cyclic loading remain significantly less well developed and subject to inherent limitations. As larger OWTs are installed in deeper waters, the need for reliable cyclic design methods to meet SLS and FLS criteria becomes increasingly critical. Designers need tools to predict the behaviour of monopiles when subjected to repeated loads, particularly to capture two key effects:

- The accumulation of lateral displacements under biased long-term cyclic loading.
- The changes in strength and stiffness of the surrounding soil due to cyclic loading.

While the primary focus is on long-term cyclic response, these effects can result from both high-amplitude storm events spanning only a few cycles ('low-cycle' loading) and low-amplitude loading acting over thousands of cycles ('high-cycle' loading). Constitutive models are central to such predictive tools and should ideally represent both regimes of cyclic behaviour. Although various models have been developed for this purpose, significant uncertainties remain regarding their calibration, numerical implementation, and predictive accuracy. Intrinsic models, in particular, offer a rigorous approach to simulating cyclic soil behaviour, but they are often complex to calibrate and difficult to implement robustly in FE

codes, frequently encountering convergence issues. As a result, their adoption remains limited, with industry continuing to rely on simplified default models available in commercial FE software (Grammatikopoulou *et al.*, 2017; Kaltekis *et al.*, 2023).

Despite these challenges, intrinsic step-by-step 3D-FEA provides valuable insights into the geomechanical processes governing OWT behaviour, supporting the development of more reliable foundation design methods tailored for cyclic loading (Cuéllar *et al.*, 2014). This approach can also capture pile-soil interactions even in conditions not directly observed through field monitoring or experimental testing (Truong *et al.*, 2018). The central challenge lies in the absence of suitable intrinsic constitutive models that can accurately and efficiently simulate soil behaviour under cyclic loading when incorporated into 3D-FEA. Research is therefore needed to assess and further develop intrinsic constitutive models that support advanced cyclic design methods suited to offshore industry applications.

1.2.2 Objectives

This project, a joint effort between Fugro and the University of Oxford, aims to improve the numerical modelling of cyclic loading effects on OWT monopile foundations in sand, addressing key challenges relevant to both research and industry. To achieve this, a range of modelling approaches was first identified through a comprehensive review of intrinsic constitutive models for sand subjected to cyclic loading. This was followed by a systematic evaluation involving the numerical implementation of selected models, representative of key theoretical constitutive frameworks. These models were assessed for their predictive capabilities, strengths, and limitations at element level. One model was subsequently selected as the most appropriate for meeting the project's objectives. These are to:

- Adapt the selected intrinsic sand constitutive model to capture high-cycle loading and associated long-term effects, while maintaining precision in short-term behaviour.

- Validate the adapted model through monotonic and high-cycle element-level simulations against laboratory data, ensuring it captures sand behaviour across varying densities and stress levels using a single parameter set.
- Extend the model to reproduce the effects of fines content without recalibration.
- Implement the model efficiently in commercial FE software to enable its practical use in intrinsic step-by-step 3D-FEA of OWT monopile foundations.
- Evaluate the model in full-scale 3D-FEA BVPs through simulation of the PISA Dunkirk monopile field tests under monotonic and cyclic loading.
- Benchmark the model's predictions against empirical trends from experimental studies relevant to OWT monopile design.
- Investigate key soil element responses around the monopile and the evolution of associated state parameters under cyclic loading, demonstrating how local soil behaviour informs global foundation performance.

1.3 Outline of the thesis

The methodological approach to addressing the problem outlined in section 1.2 is presented across seven chapters, excluding this one. A summary of each chapter follows:

- In the literature review (chapter 2), the cyclic behaviour of sand is examined through laboratory observations, with key influencing factors identified. Constitutive model families are reviewed, with emphasis on limitations under cyclic loading. A critical review of 3D implementations in FE and FD codes supports the selection of plasticity frameworks suitable for OWT foundation BVPs. Existing approaches for modelling sand with non-plastic fines are also reviewed to support a practical, design-ready model.
- In chapter 3, four constitutive models are evaluated under monotonic and cyclic loading. The comparison includes two multi-surface plasticity models, one based on the series

approach (Prevost model) and a newly developed parallel Iwan model (PIMSS), as well as the widely adopted SANISAND DM04 and the more recent state-dependent Ta-Ger model. This analysis highlights the strengths and limitations of each framework, informing the selection of the most suitable model for the project's objectives.

- In chapter 4, the development of Ta-Ger HC, a new high-cycle variant of the Ta-Ger constitutive model family, is presented. The formulation incorporates a nonlinear anisotropic hyperelastic law, along with other refinements, to capture long-term cyclic response while maintaining accuracy in short-term predictions. Its performance under high-cycle loading is validated against experimental data from the literature, covering up to 10000 loading cycles. The proposed modifications address key limitations of existing models, making Ta-Ger HC a promising tool for element-level simulations and BVPs.
- In chapter 5, Ta-Ger HC and its simpler variant Ta-Ger B, employing a hypoelastic rather than a hyperelastic formulation, are adapted to account for fines content using the equivalent granular state theory (EGST) framework. This extension enables realistic predictions of sand behaviour under monotonic and high-cycle loading without recalibration across fines contents, enhancing model robustness and providing a reference for adapting other constitutive models.
- In chapter 6, the implementation of Ta-Ger B in PLAXIS 3D is detailed and validated through 3D-FEA of PISA Dunkirk monopile field tests under monotonic and cyclic loading. Results reproduce key field behaviours, and soil-monopile interaction mechanisms are analysed through comparisons with small-scale experimental trends. The chapter demonstrates the model's practical applicability and provides guidance on its implementation and calibration, with broader relevance to other Ta-Ger variants.
- In chapter 7, key conclusions from the preceding chapters are summarized, along with recommendations for future research.

Chapter 2
Literature Review

2.1 Key properties of offshore sand

2.1.1 Granular medium

Sand consists of solid particles and voids. In offshore environments, the voids are typically saturated with water, making the response of sand highly dependent on drainage conditions. Sand particles vary in chemical composition, size, shape, roundness, roughness, and brittleness, and may exhibit bonding (Soga and Mitchell, 2005), while natural sands can also contain silt, clay, or gravel.

The spatial arrangement and orientation of these particles, termed fabric, depend on the deposition method as well as current and past stress states. Although sand can be modelled as a continuous material using continuum mechanics, its granular nature induces anisotropy that evolves over time due to fabric, deposition, and stress history. Its behaviour is highly complex, exhibiting non-linearity, history dependence, and sensitivity to strain localization, particle rearrangement, and stress paths. Understanding these characteristics is crucial for accurately modelling offshore foundations.

2.1.2 Drainage conditions

Saturated sand can exhibit three primary drainage conditions: drained, where water circulates freely without excess pore pressures; undrained, where water cannot circulate, resulting in pore pressure changes; and partially drained, where water movement is too slow to fully prevent pore pressure changes. A fourth condition may occur during seismic events when a sand layer lies beneath a low-permeability layer, causing upward water flow and increased pore pressure in the upper sand (Adamidis and Madabhushi, 2018). For offshore wind turbine (OWT) foundations, loading conditions can range from drained to undrained, including partially drained scenarios (Li et al., 2019). Accurate modelling of OWT foundations under cyclic loading must account for all these drainage conditions.

2.2 Cyclic loading of sands and principal phenomena

The cyclic response of sands is governed by complex micromechanical processes that produce highly non-linear hydro-mechanical behaviour at the macro scale, leading to phenomena such as irreversible deformation, hysteresis, and pore pressure build-up (di Prisco and Wood, 2012). This section explores the experimental aspects of cyclic sand behaviour relevant to offshore (wind) geotechnical engineering, focusing on key response patterns observed under both drained and undrained conditions. Subsequently, the influence of primary governing factors is analysed for each drainage condition.

2.2.1 Drained conditions

2.2.1.1 Cyclic strain accumulation patterns

In offshore engineering, long-lasting cyclic loading events termed ‘high-cycle’ are those expected to act on the soils and the foundations of the wind turbines, whose design must ensure full functionality during the whole operational life, up to 10^8-10^9 loading cycles (N) with alternating sequences of small-amplitude vibrations and severe storm loading (Liu *et al.*, 2019). Sand cyclic behaviour is affected by ‘ratcheting’, denoting the gradual

accumulation of plastic strains under many cycles, contrasted to the occurrence of 'shakedown' which does not accumulate strains (Liu *et al.*, 2019). In laboratory experiments, sand samples subjected to cyclic shear loading under drained conditions demonstrate a progressive accumulation of deviatoric strain (Lekarp and Dawson, 1998). Figure 2.1 illustrates potential responses of elastoplastic materials under cyclic loading (Collins and Boulbibane, 2000). When the applied load remains below the elastic limit, the material behaves elastically and returns to its original state. If the load exceeds the elastic limit, three distinct long-term patterns may emerge:

- Elastic shakedown: After an initial phase of plastic deformation, the material behaves elastically in subsequent cycles without further plastic straining.
- Plastic shakedown: Plastic strains accumulate during early cycles but stabilize into a cyclic loop, with no additional net plastic strain in subsequent cycles.
- Ratcheting: Plastic strains continue to accumulate during each cycle, with the rate of accumulation decreasing but not vanishing.

Figure 2.2 highlights the key phenomena that must be captured when simulating OWT foundations under drained cyclic loading. Over numerous cycles, permanent displacements accumulate as the initial hysteretic loop does not close. Yet, with repeated load reversals, the rate of strain accumulation progressively diminishes as the number of cycles increases (Bouckovalas et al., 1984; Wichtmann, 2005). The load-unload AB loop gradually drifts, and its characteristics may evolve. The secant stiffness has been observed to increase, while the loop area decreases, indicating reduced energy dissipation, commonly referred to as the 'damping ratio' (Houlsby *et al.*, 2020).

In terms of volumetric straining, the response of sand to cyclic loading is often characterised by the attainment of a stable density or void ratio, known as the terminal density (or terminal

void ratio) (Narsilio and Santamarina, 2008; Park and Santamarina, 2020). This state is achieved when the accumulated net volumetric strain increment over a complete stress cycle becomes zero. Depending on material properties, load settings, and boundary conditions, sand may either contract or dilate to reach this state (Narsilio and Santamarina, 2008; Park and Santamarina, 2020). Under monotonic shearing, the terminal density corresponds to the critical state (CS), where the material deforms without further volume change, while in cyclic loading, it represents the upper limit of volumetric changes under specific conditions (Liu, 2020). This state can develop alongside shear deformation patterns as ratcheting or shakedown. Figure 2.3 illustrates the behaviour of drained sand under triaxial cyclic loading, highlighting these patterns and defining key symbols used in subsequent discussions.

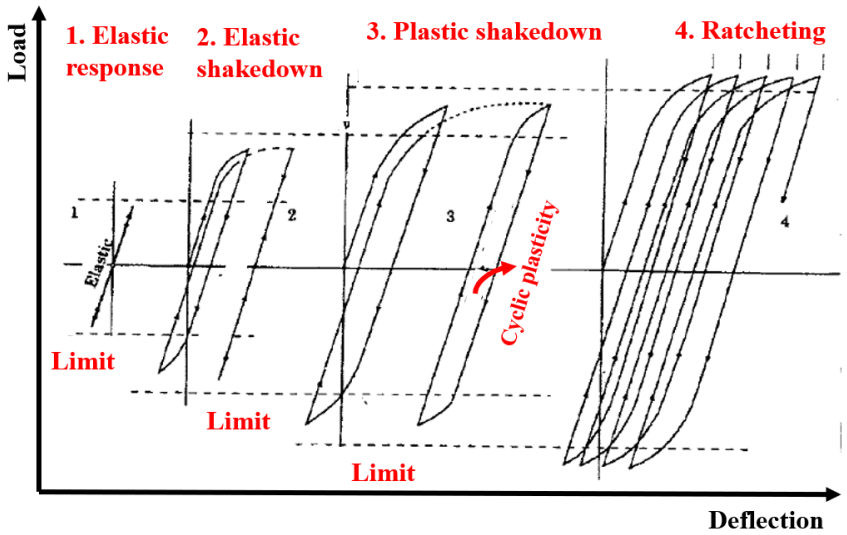

Figure 2.1: Elastoplastic structure responses to cyclic loading (modified after Collins and Boulbibane (2000)).

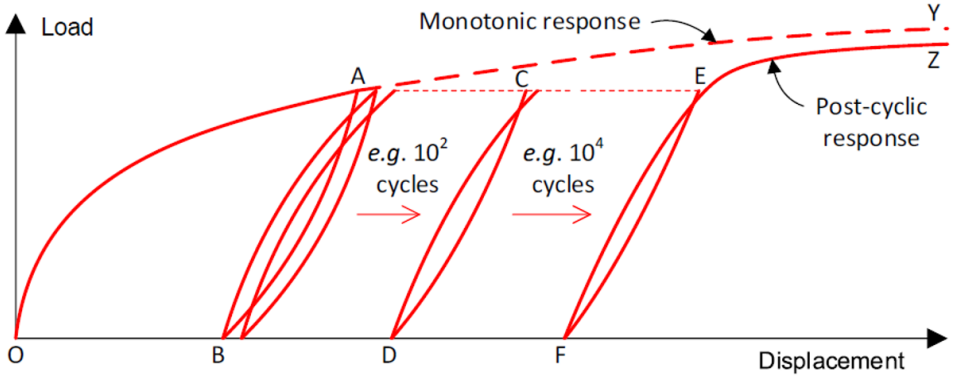

Figure 2.2: Phenomena expected to take place offshore under cyclic loading (Houlsby *et al.*, 2020).

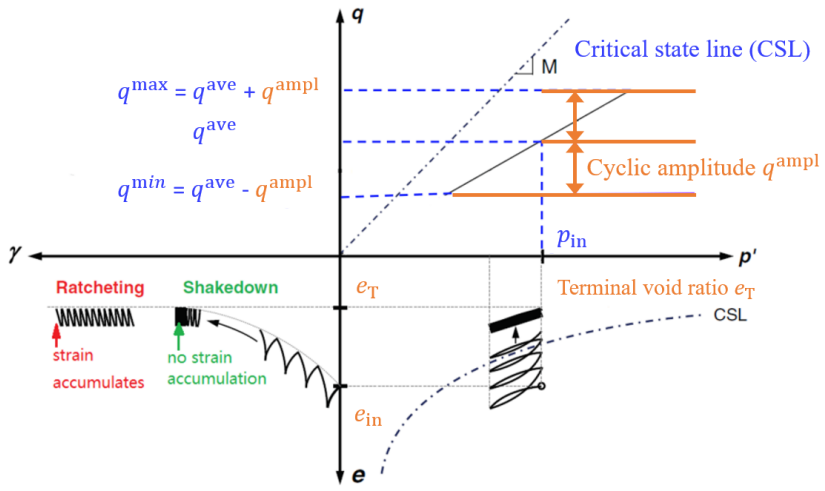

Figure 2.3: Sand behaviour under drained triaxial cyclic loading, illustrating key loading and stress variables as defined in this chapter (modified after Park and Santamarina (2020) and Liu (2020)).

2.2.1.2 Factors governing drained cyclic behaviour

Since ratcheting and the resulting strain accumulation in the surrounding soil cause monopile tilting, which is a key serviceability consideration in OWT foundation design, it is crucial to examine how geotechnical and loading factors affect strain accumulation. A notable study examining these factors is the one conducted by Wichtmann (2005) on quartz sand No. 3. The tests of interest, one-way asymmetric drained high-cycle triaxial tests consisted of three phases: (i) isotropic consolidation under an initial mean effective stress (p_{in}); (ii) shearing along a constant-p path up to the average deviatoric stress ratio ($\eta^{ave} = q^{ave}/p^{ave}$), where q^{ave} is the average deviatoric stress and p^{ave} is the average mean effective stress, which remains equal to p_{in}; and (iii) cyclic loading with amplitudes $q = q^{ave} \pm q^{ampl}$ applied under a consistent radial stress $\sigma_r = p_{in}$.

During drained cyclic loading, strain gradually accumulates in the sand sample. The direction of strain accumulation is quantified as the ratio $\omega = \varepsilon_v^{acc}/\varepsilon_q^{acc}$, representing the relationship between accumulated volumetric strain (ε_v^{acc}) and deviatoric strain (ε_q^{acc}). Findings of Wichtmann (2005) from the aforementioned tests indicate that ω is primarily governed by the average deviatoric stress ratio (η^{ave}) (Figure 2.4). In contrast, mean effective stress, p, and initial void ratio, e_{in}, were found to have minimal influence on the

strain direction, consistent with earlier findings by Chang and Whitman (1988). Chang and Whitman (1988) also demonstrated that in drained cyclic tests, the number of cycles has no significant effect on strain direction up to $N = 10^3$ cycles, whereas Wichtmann (2005) observed a slight increase in ω when the number of cycles reaches $N = 10^5$. Furthermore, Wichtmann (2005) found that variations in loading frequency, cyclic deviatoric stress amplitude, q^{ampl}, and static pre-loading had negligible or unclear effects on ω.

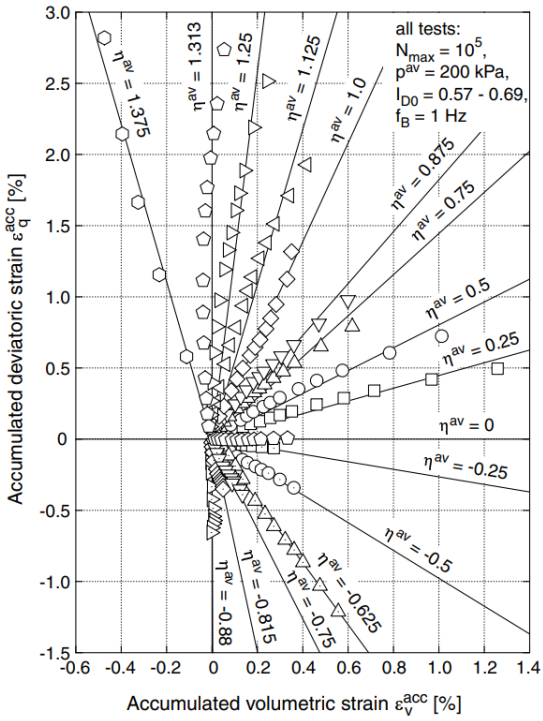

Figure 2.4: Strain paths ($\varepsilon_v^{acc} - \varepsilon_q^{acc}$) from drained high-cycle triaxial tests on quartz sand No.3 at $p^{ave} = 200$ kPa, illustrating the influence of different average deviatoric stress ratios ($-0.88 \leq \eta^{ave} \leq 1.47$) on accumulated strain behaviour (Wichtmann, 2005).

The magnitude of the accumulated strain is defined as $\varepsilon^{acc} = \sqrt{(\varepsilon_v^{acc})^2/3 + 1.5(\varepsilon_q^{acc})^2}$. Under drained cyclic loading, accumulated strain progresses with the number of cycles, N, at a decreasing rate and is notably influenced by the loading characteristics and the properties of the sand. Specifically, the magnitude of accumulated strain increases with greater cyclic deviatoric stress amplitudes, q^{ampl}, (Figure 2.5a) and greater average stress ratios, η^{ave}, (Figure 2.5b), assuming all other conditions remain unchanged. Furthermore, samples with higher initial relative density D_{r0} (lower void ratio, e_{in}) exhibit a reduced strain accumulation

rate per loading cycle and a lower overall accumulated strain for a given number of cycles, N (Figure 2.5c). The impact of the average mean effective stress, p^{ave}, on the magnitude of accumulated strain remains inconclusive. Wichtmann (2005) demonstrated that the effect of p^{ave} is marginal for fewer than 10^4 cycles, as accumulated strains tend to lie within a limited range (Figure 2.6a). For higher cycle numbers, increased mean effective stress leads to reduced strain accumulation. Later tests conducted by Wichtmann and Triantafyllidis (2017) on a different sand (Cuxhaven fine sand) revealed a clearer pattern, indicating that strain accumulation increases with higher mean effective stress (Figure 2.6b).

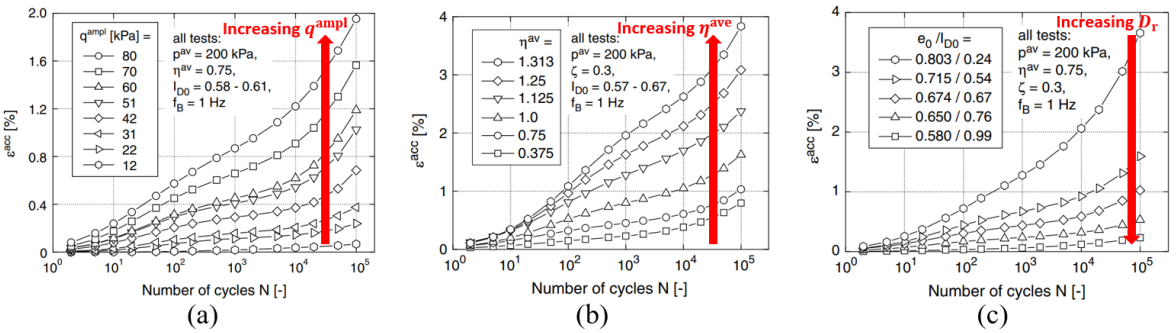

Figure 2.5: Insights from drained high-cycle triaxial tests on quartz sand with subangular grains (quartz sand No. 3) at $p^{ave} = 200$ kPa illustrating the influence of (a) cyclic deviatoric stress amplitude, q^{ampl}; (b) average deviatoric stress ratio, η^{ave}; (c) relative density D_r, on the magnitude accumulated strain.

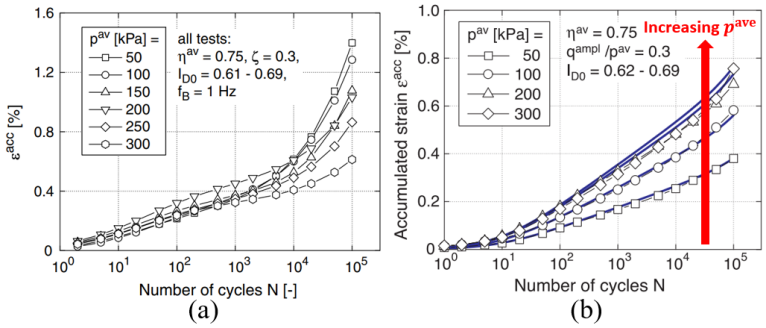

Figure 2.6: Insights from drained high-cycle triaxial tests on (a) quartz sand No. 3 (Wichtmann, 2005); (b) Cuxhaven fine sand (Wichtmann and Triantafyllidis, 2017), illustrating the influence of average mean effective stress, p^{ave}, on the magnitude accumulated strain.

2.2.2 Undrained conditions

2.2.2.1 Deformation modes

Before exploring undrained sand behaviour, it is essential to introduce the 'phase transformation line' (PTL), which defines the transition between contractive and dilative

responses (Ishihara et al., 1975). Unlike drained conditions, where volume changes occur freely, undrained conditions prevent any volume change, and contractive or dilative tendencies manifest as changes in pore pressure, leading to a corresponding decrease or increase in mean effective stress. The PTL represents a specific locus in the stress space that governs this behaviour (Figure 2.7). Below the PTL, sands exhibit a tendency to contract, resulting in positive excess pore pressures under shear loading. Stress states above the PTL produce a dilative tendency, expressed as negative excess pore pressures.

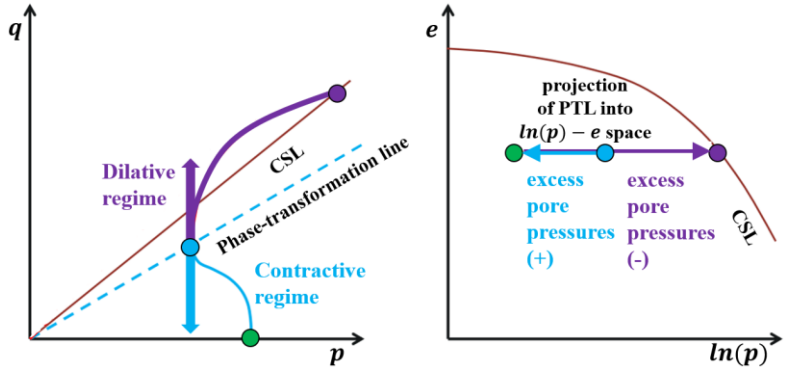

Figure 2.7: Representation of the PTL in $p - q$ and its projection into ln $(p) - e$ space.

Under undrained cyclic loading, sands experience pore pressure buildup (Andersen, 2009), stiffness degradation, and deviatoric strain accumulation (Dobry *et al.*, 1985). Their behaviour is governed by soil properties and loading factors, resulting in distinct deformation modes (Elgamal *et al.*, 2003; Ziotopoulou and Boulanger, 2013). Using the same symbols as for drained loading (Figure 2.3), this section categorizes key deformation modes observed during single-amplitude undrained cyclic loading of sand (Liu, 2020):

- Cyclic liquefaction (Figure 2.8a, b): Occurs in loose sands when pore pressure nearly equals the initial mean effective stress, causing a sudden loss of shear strength and rapid, uncontrollable deformation. Initially, strain accumulation is minimal, but deformation accelerates sharply as effective stress nears zero (Figure 2.8b).
- Cyclic mobility (Figure 2.8c, d): Observed in medium-dense to dense saturated sands under two-way loading conditions, where stress alternates between positive and negative

deviatoric stress states (Figure 2.8c) (Vaid and Chern, 1985). The effective stress path exhibits a 'butterfly-shaped' pattern due to alternating contractive and dilative tendencies, with pore pressures fluctuations depending on the stress state relative to the PTL. As mean effective stress nears zero, deviatoric strain develops without collapse (Iai et al., 1992). Deviatoric strain amplitude increases with each cycle, eventually causing failure due to uncontrollable deformation (Figure 2.8d).

- Strain accumulation in the presence of the static preshear (Figure 2.8e, f): Occurs under one-way undrained cyclic loading, where static preshear prevents changes in the sign of deviatoric stress. Unlike cyclic mobility, the stress path forms 'lens-shaped' loops, with pore pressure build-up stabilizing over time (Liu, 2020). Deviatoric strain accumulates steadily in one direction with each cycle, eventually resulting in failure (Liu, 2020).

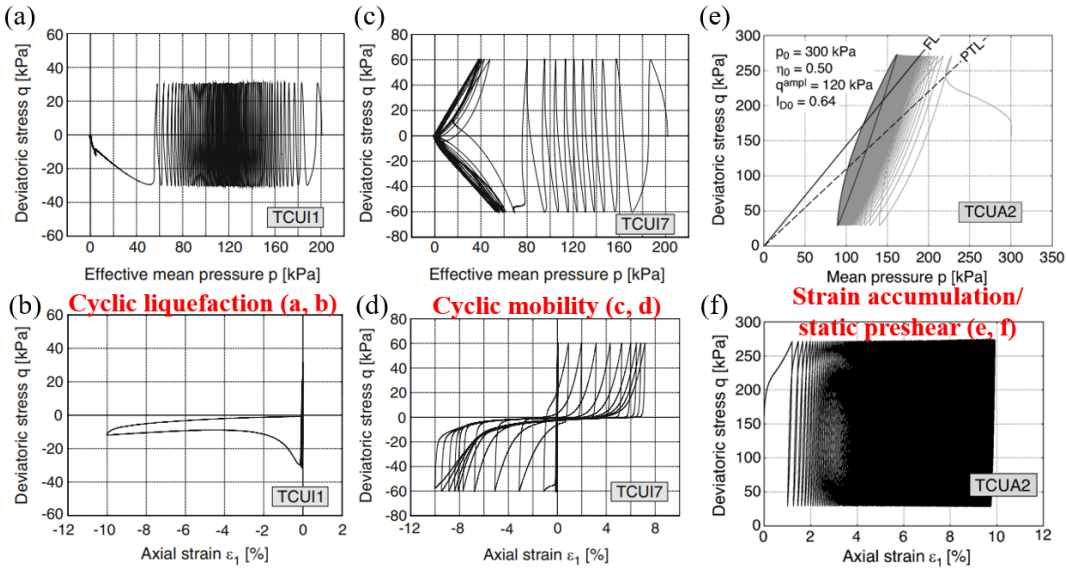

Figure 2.8: Results of triaxial tests on Karlsruhe sand (modified after Wichtmann and Triantafyllidis (2016)) illustrating the key deformation modes observed during single-amplitude undrained cyclic loading of sand: (a, b) cyclic liquefaction ($D_{r0} = 27\%$, $q^{ampl} = 30$ kPa, $p_{in} = 200$ kPa); (c, d) cyclic mobility ($D_{r0} = 67\%$, $q^{ampl} = 60$ kPa, $p_{in} = 200$ kPa); (e, f) strain accumulation in the presence of static preshear ($D_{r0} = 64\%$, $q^{ampl} = 120$ kPa, $p_{in} = 300$ kPa, 1 drained pre-cycle prior to undrained shearing).

2.2.2.2 Factors governing undrained cyclic behaviour

Undrained cyclic behaviour of sand, including deformation mode and strain accumulation, is governed by the properties of sand, and loading characteristics. Key factors influencing

this response include the initial void ratio (e_{in}), mean effective stress (p_{in}), initial stress ratio ($q^{\mathrm{ave}}/p_{\mathrm{in}}$), cyclic deviatoric stress amplitude (q^{ampl}), and the type of cyclic loading. Specifically, the effect of three out of the four general cyclic loading patterns, as defined by Gourvenec and Randolph (2011), is examined: (i) one-way (no zero-stress crossing), (ii) symmetric two-way (q^{ampl} applied around $q^{\mathrm{ave}} = 0$), and (iii) non-symmetric two-way loading (q^{ampl} applied around $q^{\mathrm{ave}} \neq 0$). The effects of one-way loading (anisotropically consolidated sample) versus symmetric two-way loading (isotropically consolidated sample) are discussed in section 2.2.2.1. One-way loading (Figure 2.8e, f) leads to strain accumulation and lens-shaped stress path loops, whereas symmetric two-way loading (Figure 2.8c, d) results in cyclic mobility and butterfly-shaped stress paths, with strain accumulation typically higher on the compression side than on the extension side (Wichtmann and Triantafyllidis, 2016b). In non-symmetric loading (anisotropically consolidated sample), a positive q^{ave} causes higher strain accumulation on the compression side, while a negative q^{ave} leads to greater strain accumulation on the extension side. Additionally, Wichtmann and Triantafyllidis (2016) demonstrated that, for samples with the same e_{in}, higher q^{ampl} leads to failure after fewer cycles under two-way loading. Furthermore, under one-way loading, an increase in q^{ampl} results in greater axial strain accumulation and higher pore pressure levels.

The influence of initial void ratio (e_{in}) on cyclic resistance, the soil's ability to resist failure under repeated loading, is evident, as Wichtmann and Triantafyllidis (2016) found that looser samples fail more quickly than denser ones. However, the role of initial mean effective stress (p_{in}) in liquefaction resistance remains debated, with some studies indicating an increase in resistance at higher mean effective stresses (Youd *et al.*, 2001), while others suggest minimal influence when stress ratio and density are maintained constant (Wichtmann and Triantafyllidis, 2016b). Similarly, static preshear enhances undrained

cyclic resistance in medium-dense and dense sands (initial state below the critical state line (CSL)), but has a more complex effect on loose sands (initial state above the CSL), which exhibit a non-linear response (Yang and Sze, 2011).

2.3 Intrinsic constitutive modelling approaches for sand

This section reviews the main families of constitutive models for clean sand, with emphasis on those capable of simulating cyclic loading. Their performance is briefly assessed based on published studies, highlighting key strengths and limitations. Finally, modelling approaches proposed to capture the behaviour of sand with non-plastic fines are reviewed.

2.3.1 Multi-surface plasticity

Multi-surface plasticity was first introduced by Iwan (1966, 1967) and Mroz (1967, 1969) as a framework for modelling material behaviour under cyclic loading. Iwan proposed two distinct one-dimensional (1D) models: the 'parallel-series' ('parallel Iwan') and 'series-parallel' ('series Mroz-Iwan') models, later extending the latter into a three-dimensional (3D) formulation. This 3D extension closely aligns with the approaches developed by Mroz (1967) and was further refined by Prevost (1977, 1978) . The original parallel-series model proposed by Iwan is physically motivated and assumes that a 'hysteretic system may be thought of as consisting of a large number of ideal elastoplastic elements having different yield levels' (Iwan, 1966). As will be shown in the following sections, these concepts have led to the development of several 3D continuum models based on both the parallel and series frameworks. In this thesis, the term 'series' refers to the 3D extension of the 'series-parallel' model, while 'parallel' (or parallel Iwan) denotes the 'parallel-series' model.

2.3.1.1 Series multi-surface plasticity models

The series multi-surface plasticity theory assumes that the total strain increment is decomposed into elastic and plastic components with the latter being the sum of multiple

plastic sub-mechanisms (Mroz, 1967). Each plastic strain sub-component $\mathrm{d}\boldsymbol{\varepsilon}^{\mathrm{p}(n)}$ is associated with an individual yield surface ($\mathrm{f}^1, \mathrm{f}^2, \ldots, \mathrm{f}^n$) controlling distinct yield strengths and plastic moduli, with the yield surfaces being completely independent and hence, no coupling among the different plastic sub-mechanisms occurs. The main differences of the simple elastoplastic and the series multi-surface theories are summarised in Table 2.1.

Table 2.1: Basic assumptions of classic and series multi-surface elastoplasticity theories (Mroz, 1967; Houlsby and Puzrin, 2006).

Elastoplasticity	**Series multi-surface elastoplasticity**
$\mathrm{d}\boldsymbol{\varepsilon} = \mathrm{d}\boldsymbol{\varepsilon}^{\mathrm{e}} + \mathrm{d}\boldsymbol{\varepsilon}^{\mathrm{p}}$	$\mathrm{d}\boldsymbol{\varepsilon} = \mathrm{d}\boldsymbol{\varepsilon}^{\mathrm{e}} + \sum_{n=1}^{N} \mathrm{d}\boldsymbol{\varepsilon}^{\mathrm{p}(n)}$
$\mathrm{d}\boldsymbol{\varepsilon}^{\mathrm{p}} = < L > \frac{\partial \mathrm{g}}{\partial \boldsymbol{\sigma}}$	$\mathrm{d}\boldsymbol{\varepsilon}^{\mathrm{p}(n)} = < L^{(n)} > \frac{\partial \mathrm{g}^{(n)}}{\partial \boldsymbol{\sigma}}$
where $< L >$ is the plastic multiplier, a non-negative scalar quantity defining the amplitude of the plastic strain increment	

Figure 2.9 illustrates a loading-unloading scenario, demonstrating how series multi-surface plasticity models stress-strain behaviour through a sequence of straight segments, each corresponding to a specific yield surface and slope. In this example, the model consists of four nested surfaces. When the stress path remains within the first surface, the material exhibits elastic behaviour, and the yield surfaces remain fixed. Once the stress path reaches the first surface, plastic behaviour is activated, leading to a change in the stress-strain slope. Kinematic hardening causes the activated yield surface and the stress point to move together until they engage the next surface. During unloading, the response becomes elastic again as the stress point re-enters the first surface. Early formulations of multi-surface models enforced nested yield surfaces with only tangential contact and no intersection. However, this restriction is not essential, and allowing the surfaces to intersect can simplify the model by removing the need for complex translation rules (Houlsby and Puzrin, 2006). The advantages and disadvantages of series multi-surface plasticity are summarised in Table 2.2.

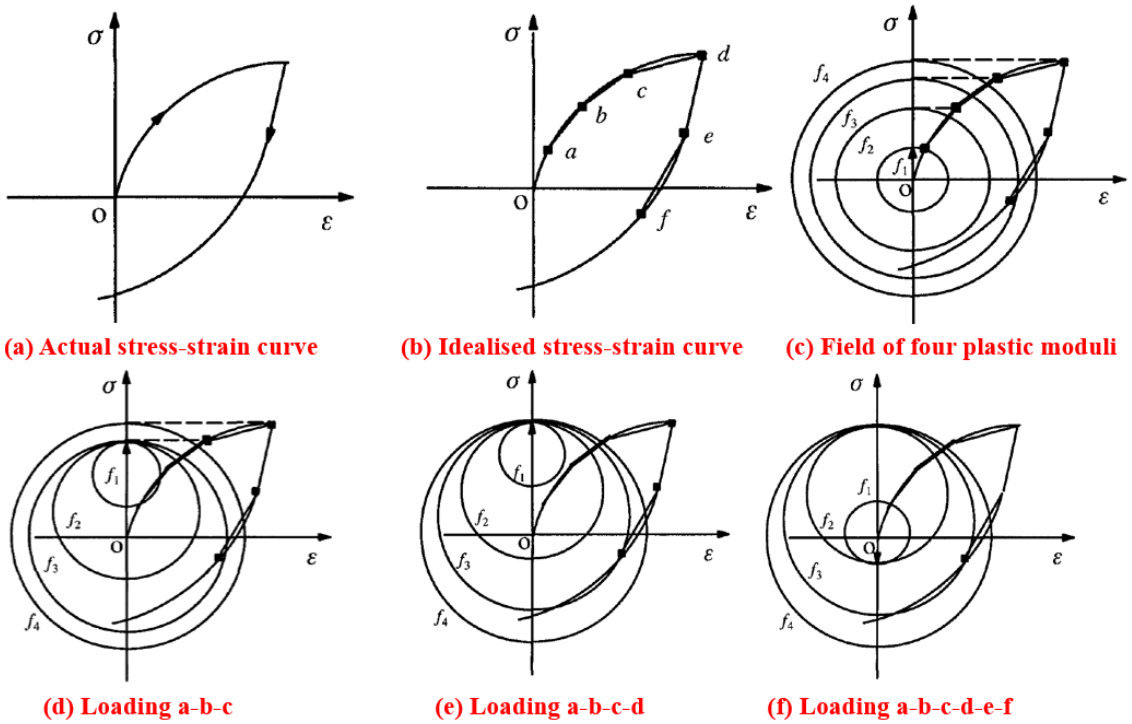

Figure 2.9: Stress-strain response with multi-surface plasticity (modified after Yu (2006)).

Multi-surface models have been developed to simulate the behaviour of sand under cyclic loading, with the Prevost model (Prevost, 1985) being a key example. Initially established as PDMY01 by Parra (1996), this model is known for its versatility in capturing non-linear hysteretic responses, shear-induced anisotropy, and dilatancy effects. Originally designed to study seismically induced liquefaction, it has been successfully applied in earthquake engineering to investigate liquefaction propagation in soil deposits and earth dams (Zerfa and Loret, 2003). The model was later advanced by Elgamal et al. (2003) and Yang et al. (2003), evolving into PDMY02, which was further extended to incorporate the Lode angle effect (Yang and Elgamal, 2008). More recently, the Prevost model has been utilized to examine the cyclic behaviour of suction caissons in OWT foundations in very dense sands (Cerfontaine, 2014). A notable modification of the PDMY02 model was introduced by Elbadawy et al. (2024), addressing a significant limitation by integrating critical state theory (CST). This enhancement allows for the estimation of model parameters through correlations with soil relative density, enabling a single set of parameters to predict the behaviour of sands across varying densities.

Table 2.2: Advantages and disadvantages of series multi-surface plasticity theory.

Advantages	Disadvantages
Accurately simulates monotonic loading (Houlsby and Puzrin, 2006)	Each yield surface requires assigned properties and plastic laws
Captures the Bauschinger effect, where plastic deformation increases yield strength in one direction but decreases it in the opposite	Enforcing non-intersecting yield surfaces requires complex mapping and translation rules (Houlsby and Puzrin, 2006)*
Reproduces hysteretic loops during loading-unloading cycles, following Masing's rule (Masing, 1926)	If isotropic hardening is assumed, the complexity of mapping rules further increases (Houlsby and Puzrin, 2006)*
Flexible in adapting to experimental data (Prevost, 1982; Houlsby and Puzrin, 2006)	**Applies only to non-intersecting nested surfaces, which is not always required*
Simpler than other cyclic loading models, such as bounding surface plasticity (e.g., bounding surface plasticity) (Houlsby and Puzrin, 2006)	Using multiple surfaces increases computational cost, requiring a trade-off between accuracy and efficiency

2.3.1.2 Parallel Iwan multi-surface plasticity models

The aforementioned multi-surface plasticity models utilize kinematic yield surfaces arranged in series. Although effective in capturing hysteretic response, series models are often complex to implement (Whyte, 2020). A simpler yet accurate alternative is the parallel multi-surface approach (Iwan, 1966). This is based on a 1D model consisting of several spring-slider elements with different yield strengths and elastic stiffnesses, arranged in parallel. This model assumes strain equivalence across all spring-slider elements, so for an increment of strain the corresponding stress is calculated as a weighted sum of the individual stresses in the elements. Driven by the original 1D concept, over the years the parallel Iwan approach has been adopted as the basis for the development of continuum plasticity models for metals (Chiang and Beck, 1994), clays (Grimstad et al., 2014; Whyte, 2020; Whyte et al., 2020) and sands (Lee et al., 2009; Dawson, 2013; Dawson et al., 2013; Dawson and Roth, 2018; Numanoglu, 2019; Numanoglu et al., 2023).

When this approach is incorporated to develop a constitutive model, a number of individual micro-models are arranged in parallel and therefore are subjected to the same strain history

(Whyte, 2020; Whyte *et al.*, 2020). The resulting macro-stress tensor ($\boldsymbol{\sigma}$) is calculated as the weighted sum of the individual micro-stress tensors ($\boldsymbol{\sigma}^i_{micro}$) as:

$$\boldsymbol{\sigma} = \sum_{i=1}^{n} w^i \boldsymbol{\sigma}^i_{micro} \tag{2.1}$$

where n is the total number of micro-models and w_i is the weight corresponding to each micro-stress. The sum of the weights must be equal to unity ($\sum_{i=1}^{n} w^i = 1$). This approach can produce a Masing-type non-linear response, without the need for translating surfaces (Whyte, 2020) and hence kinematic hardening and mapping rules are not needed. Another advantage of this concept is that each micro-model is numerically implemented as a single-surface plasticity model, which eases the implementation of the final macro-model (Grimstad et al., 2014; Whyte, 2020).

2.3.2 Bounding surface plasticity

Bounding surface plasticity, independently introduced by Krieg (1975) and Dafalias and Popov (1975), is often referred to as 'two-surface plasticity' due to its use of two distinct surfaces in stress space. The inner loading/yield surface ($\mathrm{f} = 0$) encloses the domain of pure elasticity, whereas the outer bounding/limit surface ($\mathrm{F} = 0$) separates the admissible from non-admissible states. One of the most important assumptions of this theory is that the hardening of the material depends on the distance between the stress point lying on the yield surface and its projection/image on the bounding surface, shown as δ in Figure 2.10. The projection follows a mapping rule, with several options available in the literature. When the stress state is far from the bounding surface, the material exhibits a stiff response, whereas as it approaches the bounding surface, the stiffness gradually decreases, allowing for a smooth transition (Yu, 2006). Initially developed for metals, bounding surface plasticity has since been widely applied to soils. Its mathematical foundation is explained in Dafalias (1986). The main advantages of bounding surface plasticity are presented in Table 2.3.

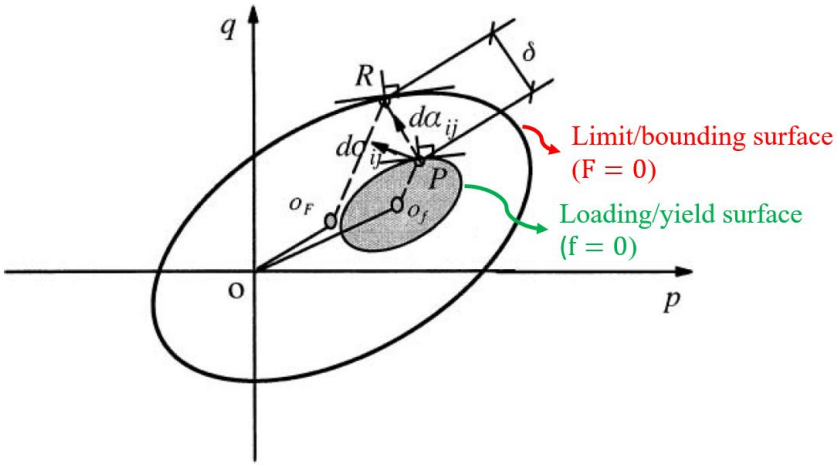

Figure 2.10: Bounding surface plasticity theory (modified after Yu (2006)).

Table 2.3: Advantages and disadvantages of bounding surface theory.

Advantages	Disadvantages
Requires only the definition of the distance-dependent hardening modulus (Houlsby and Puzrin, 2006)	Predicts exaggerated ratcheting in small unload-reload loops as reloading plasticity occurs producing plastic strains, especially in prolonged cyclic shear loading or biased cyclic loading (Houlsby and Puzrin, 2006; Liu, 2020)
Accurately simulates hysteresis for large unload-reload loops (Houlsby and Puzrin, 2006)	Some mapping rules in bounding surface models are complex and computationally demanding (E-Kan and Taiebat, 2014)
Extensively used for sand's cyclic behaviour, with abundant literature available	Many models fitted to laboratory tests require numerous parameters and extensive calibration
**The term 'explicit' refers to stress integration schemes (time integration methods) and not to high-cycle (extrinsic or explicit) loading strategies*	'Overshooting' occurs in BVPs, especially with explicit integration schemes, leading to unrealistically stiff behaviour in small unload-reload cycles (E-Kan and Taiebat, 2014)*

2.3.2.1 SANISAND family and derived models

Bounding surface plasticity for sands was significantly enhanced by incorporating the state parameter concept (Been and Jefferies, 1985) into a kinematic hardening model, forming the foundation for many subsequent models (Manzari and Dafalias, 1997). This initiated the 'SANISAND' (Simple Anisotropic Sand) family of models (Taiebat and Dafalias, 2008), which integrates principles from critical state soil mechanics (CSSM). The original formulation was adapted to address the abrupt reduction in shear stiffness caused by dilative plastic volume changes under undrained cyclic loading. Papadimitriou et al. (2001) tackled this issue through a fabric-related scalar index affecting the plastic modulus, while Dafalias

and Manzari (2004) introduced the 'DM04' model, employing a fabric-dilatancy tensor to represent directional fabric evolution during dilation. The tensorial variable in DM04 provides a macroscopic measure of directional dependence in dilatancy response and should not be confused with micromechanical fabric tensors, which describe particle-scale grain arrangements and contact orientations. Further advancements included the addition of a cap-like yield surface by Taiebat and Dafalias (2008) to enable plastic straining under constant deviatoric stress ratios. Recently, Petalas et al. (2020) proposed an improved formulation based on anisotropic critical state theory (ACST) (Li and Dafalias, 2012), enhancing fabric evolution by incorporating principal stress axis rotation (Petalas et al., 2019). A notable advancement in capturing fabric-related processes is the concept of a memory surface, originally introduced by Corti et al. (2016) in the context of another bounding surface model, which led to the development of SANISAND-MS (Liu *et al.*, 2019, 2020). Unlike earlier SANISAND models that relied on scalar or tensors to represent fabric effects, the memory surface offers a phenomenological approach, serving as a third locus in stress space. Building on this, the SANISAND-MSf model incorporates a refined memory surface and a semifluidised state formulation, enhancing its ability to simulate both pre- and post-liquefaction stages under undrained cyclic loading (Yang et al., 2022). Other bounding surface models, linked or independent of the SANISAND family, have been proposed (Wang et al., 1990; Gajo and Muir Wood, 1999; Loukidis and Salgado, 2009; Taborda et al., 2014; Cheng and Detournay, 2021).

2.3.3 Other intrinsic constitutive modelling approaches

2.3.3.1 Elastoplastic original concepts

A key constitutive model for sand is Norsand, developed based on CSSM to simulate sand behaviour (Jefferies, 1993). It was later extended to account for principal stress rotation under constant effective stress invariants by incorporating yield surface softening (Jefferies

et al., 2015). Other notable models include those proposed by Mroz and Pietruszczak (1983), Pastor et al. (1985), and Pestana and Whittle (1999), with the latter introducing a unified framework for both sands and clays. However, these models and their extensions are seldom used for cyclic loading applications due to inherent limitations in their formulations, such as Norsand's sole reliance on isotropic hardening and the absence of kinematic hardening mechanisms.

2.3.3.2 Hypoplasticity

An alternative to elastoplasticity is hypoplasticity, a concept rooted in the work of Truesdell (1955). Unlike elastoplasticity, it does not rely on conventional strain decomposition into elastic and plastic parts or a yield surface. Instead, it employs rate-type equations to directly estimate stress increments (Kolymbas, 2000):

$$\delta\boldsymbol{\sigma} = \boldsymbol{H}(\boldsymbol{\sigma}, \delta\boldsymbol{\varepsilon}) \tag{2.2}$$

where $\boldsymbol{H}$ is a non-linear tensorial function dependent on the stress state $\boldsymbol{\sigma}$ and strain increment $\delta\boldsymbol{\varepsilon}$. As a result, hypoplasticity establishes a non-linear relationship that can be easily calibrated to laboratory tests. However, since $\boldsymbol{H}$ depends solely on the current stress state and not on the loading path, with no memory incorporated into its formulation, it can produce unrealistic ratcheting under small unload-reload cycles (Houlsby, 1981). This issue was addressed with the introduction of the concept of 'intergranular strain' (Niemunis and Herle, 1997), establishing an elastic domain defined by a strain amplitude, similar to a yield surface. A significant advancement is the Intergranular Strain Anisotropic (ISA) model by Fuentes and Triantafyllidis (2015a; 2015b), designed for cyclic loading. The ISA model incorporates intergranular strains as a 'yield surface in the intergranular strain space' and combines hypoplasticity with bounding surface plasticity, improving its predictive accuracy by accounting for inherent fabric effects.

2.3.3.3 Hyperplasticity

Elastoplastic models are typically developed based on laboratory experiments, with their elasticity, yield functions, and plastic potential derived independently from experimental data. While many provide accurate predictions of laboratory element and foundation-load tests when used in FE calculations, they often lack consideration of thermodynamic laws during development (Whyte, 2020). In contrast, hyperplastic models inherently satisfy thermodynamic principles by deriving their behaviour from two scalar potential functions: the energy and dissipation functions (Houlsby and Puzrin, 2006). This makes hyperplastic models systematic and physically consistent. Hyperplasticity traces its origins to the work of Ziegler (1976), with its first applications to soil mechanics introduced by Houlsby (1981). While hyperplastic constitutive models for sand remain relatively scarce, a recent model, 'HySand', building on the early work of Houlsby and Mortara (2004) and proposed by Simonin (2023) and Simonin et al. (2023), demonstrates promising potential for simulating short-term cyclic sand behaviour and may lead to the development of derivatives with broader applications.

2.3.3.4 Ta-Ger novel plasticity framework

Another notable modelling framework is the one accommodating the state-dependent sand model, Ta-Ger, (Tasiopoulou and Gerolymos, 2016a) which employs principles from CSSM to simulate sand behaviour. Its underlying framework combines perfect elastoplasticity with smooth hysteresis by employing a hardening law inspired by the Bouc-Wen model. The Bouc-Wen model, first introduced by Bouc (1967) and extended by Wen (1976), is widely used due to its versatility and simplicity. Governed by a single nonlinear differential equation, it can efficiently simulate hysteretic phenomena in fields such as magnetism, electricity, material behaviour, and elastoplasticy of solids (Charalampakis and Koumousis, 2010). Departing from classical plasticity, the Ta-Ger approach defines the plastic modulus

as a scaling factor for the plastic component of the incremental stiffness matrix, $\mathbf{E}^{\mathrm{ep}}$, rather than as an additive term in the denominator (Tasiopoulou and Gerolymos, 2016a):

$$\mathbf{E}^{\mathrm{ep}} = \mathbf{E}^{\mathrm{e}}\left[\mathbf{I} - \frac{\boldsymbol{\Phi}_{\mathrm{g}}\boldsymbol{\Phi}_{\mathrm{f}}{}^{\mathrm{T}}\mathbf{E}^{\mathrm{e}}\mathbf{H}}{\boldsymbol{\Phi}_{\mathrm{f}}{}^{\mathrm{T}}\mathbf{E}^{\mathrm{e}}\boldsymbol{\Phi}_{\mathrm{g}}}\right] \tag{2.3}$$

where $\mathbf{E}^{\mathrm{e}}$ is the elastic stiffness matrix, $\boldsymbol{\Phi}_{\mathrm{f}}$ and $\boldsymbol{\Phi}_{\mathrm{g}}$ are the gradients of the yield surface and plastic potential surface, and $\mathbf{H}$ is the matrix playing the role of the plastic modulus. $\mathbf{H}$ is defined as $\mathbf{H} = \zeta^{n}\mathbf{I}$, where ζ is responsible for the hardening/softening through a mapping rule and n is a hardening parameter. The framework aligns with bounding surface theory (Dafalias and Popov, 1975), where material hardening depends on the distance between the current stress point and its projection/image on a bounding (failure or ultimate-strength) surface. This concept is illustrated by considering a material that follows a cone-type failure criterion in triaxial space, such as Drucker Prager (Tasiopoulou and Gerolymos, 2016a):

$$\mathrm{f} = 0 \;\Leftrightarrow q - Mp = 0 \tag{2.4}$$

where q is the deviatoric stress, p is the mean effective stress, and M signifies the failure stress ratio. The determination of ζ stems directly from the equation of the designated failure surface by assuming it is equal to 1, instead of 0 as shown in (2.4):

$$\zeta = \frac{(q/p)}{M} \tag{2.5}$$

Fundamentally, ζ ranges between 0 and 1, while stress ratio q/p varies between 0 and M (Tasiopoulou and Gerolymos, 2016a). Clearly, when ζ is equal to 0, $\mathbf{H} = 0$ and $\mathbf{E}^{\mathrm{ep}} = \mathbf{E}^{\mathrm{e}}$, implying that elasticity is degenarated to a line. This means the material response remains entirely elastic under specific loading conditions, such as isotropic loading. Thus, a model within this framework is best described as a bounding surface model with a vanished, yet nonzero elastic region, as the yield surface reduces to a line under triaxial conditions.

Notably, each stress state corresponds to a unique value of ζ, resulting in an agreeing loading surface, proportional to the assigned failure surface by ζ:

$$q - \zeta Mp = 0 \tag{2.6}$$

Some advantages associated with defining **H** as a scaling quantity include: (i) it facilitates a smooth transition from the elastic to a perfectly plastic response by controlling pre-failure nonlinearity and quantifying the coupling between the elastic and plastic components that make up the total strain increment (Tasiopoulou and Gerolymos, 2016a); (ii) it streamlines numerical implementation, ensuring accurate predictions without explicitly checking the yield criterion at every integration step, significantly reducing the computational cost of the analyses; and (iii) it offers versatility if employed alongside stiffness degradation models, such as those proposed by Achmus et al. (2009) or Gao et al. (2023) for the long-term response of OWT foundations, where the plastic part of the incremental stiffness matrix needs to be scaled to capture strain accumulation after a number of cycles.

2.3.4 Performance of intrinsic models at element level

The continuous development of new constitutive models for sand highlights that none have yet achieved adequate accuracy in simulating cyclic loading, even at the element level, let alone for practical applications in BVPs. This section summarizes key conclusions from original model proposals and comparative studies, focusing on models deemed most suitable for further development, at least at the element level.

2.3.4.1 Comparative review of SANISAND variants, Hypoplastic and ISA models

A recent study (Wichtmann et al., 2019) evaluated the performance of three sophisticated models: the DM04 SANISAND version (Dafalias and Manzari, 2004), a hypoplastic model with intergranular strain (Niemunis and Herle, 1997) and ISA model (Fuentes and Triantafyllidis, 2015a; 2015b), which integrates hypoplasticity with bounding surface

plasticity. The models were tested using laboratory experiments conducted on Karlsruhe fine sand (Wichtmann and Triantafyllidis, 2016a; 2016b) to assess their predictive capabilities. The study by Wichtmann revealed that, despite their complexity and extensive parameter sets, none of the models could optimally predict all monotonic drained and cyclic undrained tests using a single set of parameters. Even for monotonic loading, parameter adjustments were required across different test conditions. In undrained cyclic, stress-controlled liquefaction tests, none of the models accurately reproduced the observed pore pressure build-up. Both the hypoplastic model and SANISAND exhibited unrealistic ratcheting in their stress-strain responses. Furthermore, all three models provided inaccurate predictions of strain accumulation and stress paths in undrained one-way cyclic stress-controlled tests. Under strain-controlled conditions, SANISAND and ISA struggled to capture small-strain behaviour, while none of the models effectively simulated the response of dense sands under large-strain loading.

A similar study by Duque et al. (2022) evaluated these three constitutive models, together with the upgraded version of DM04, SANISAND-MSf (Yang et al., 2022), incorporating a memory surface and semifluidised state. Experimental data from Toyoura (Ishihara, 1996) and Karlsruhe fine sands (Wichtmann and Triantafyllidis, 2016a; 2016b) were used. Key limitations include stress overshooting after reverse loading, one-way ratcheting in cyclic strain accumulation, difficulties in simulating liquefaction strength curves, and inaccuracies in strain-controlled shearing, particularly in reaching the liquefaction state (stress attractor $p = q = 0$) due to stress path and stress-strain loop lockup. Additional challenges involve excessive plastic and artificial strain accumulation on small $p - q$ closed loops, where an almost elastic response is expected based on experimental findings, attributed to the hypoelastic component employed by the models.

2.3.4.2 Performance of multi-surface plasticity models

The work of Cerfontaine (2014) highlights the performance of the series multi-surface Prevost model (Prevost, 1985) in simulating cyclic loading. Calibrated using triaxial tests on Nevada sand from the VELACS program (Arulmoli *et al.*, 1992), the model successfully captured key trends in cyclic sand behaviour, including pore pressure build-up and effective stress path translation toward initial liquefaction (Figure 2.11a). It also predicted a positive axial deformation consistent with laboratory observations (Figure 2.11b). However, discrepancies arose, notably an overestimation of negative deformation in extension, not reflected in experimental data (Figure 2.11c). Since it does not integrate principles from CSSM, the Prevost model requires separate calibration for each sand density and, like DM04, SANISAND-MSf, hypoplastic, and ISA models, it also struggles to provide a unified parameter set for different loading conditions (monotonic, cyclic, drained, and undrained).

An interesting application of the parallel Iwan multi-surface plasticity concept is demonstrated in the work of Lee et al. (2009) on seismic site response analysis. The model, combining elastic-perfectly plastic and isotropic hardening micro-models in parallel, was validated using cyclic tests of three consecutive loading of 30 cycles performed with a Stokoe type fixed-free torsional shear device on Toyoura dry sand. As shown in Figure 2.12, the numerical simulations closely matched experimental results, particularly for the first cycle, and effectively captured cyclic hardening, a critical feature for reducing design conservatism in OWT monopile foundations.

Another constitutive model based on the parallel Iwan concept is the ‘I-soil’ model (Numanoglu *et al.*, 2023), designed to simulate seismic settlements in dense sand (Numanoglu, 2019). The model incorporates Drucker-Prager micro-models arranged in parallel, non-Masing unloading/reloading rules, and a simplified formulation for shear-induced volumetric response. It was evaluated at the element level using constant volume

cyclic direct simple shear (cDSS) tests. As shown in Figure 2.13, I-soil successfully replicated the initial hysteretic response and excess pore pressure generation observed in Salt Fork River sand tests, with only minor deviations during later cycles. Its accurate prediction of stress paths and pore pressure demonstrates its reliability for cyclic loading simulations.

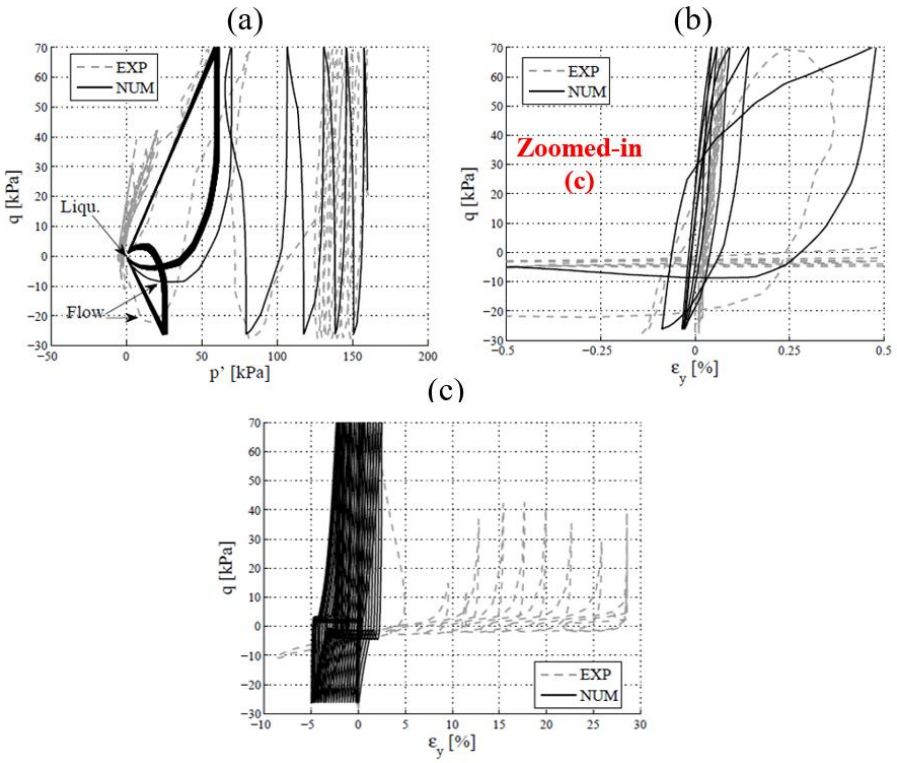

Figure 2.11: Simulation of undrained cyclic triaxial test ($D_{r0} = 40\%$, $p_{in} = 160$ kPa, $q^{ampl} = 48.4$ kPa): (a) Flow deformation and liquefaction in $p - q$ space; (b) Axial deformation-deviatoric stress for the 5 first cycles (zoom of c); (c) Axial deformation-deviatoric stress for the 15 first cycles (EXP: experimental data, NUM: numerical simulation) (modified after Cerfontaine (2014)).

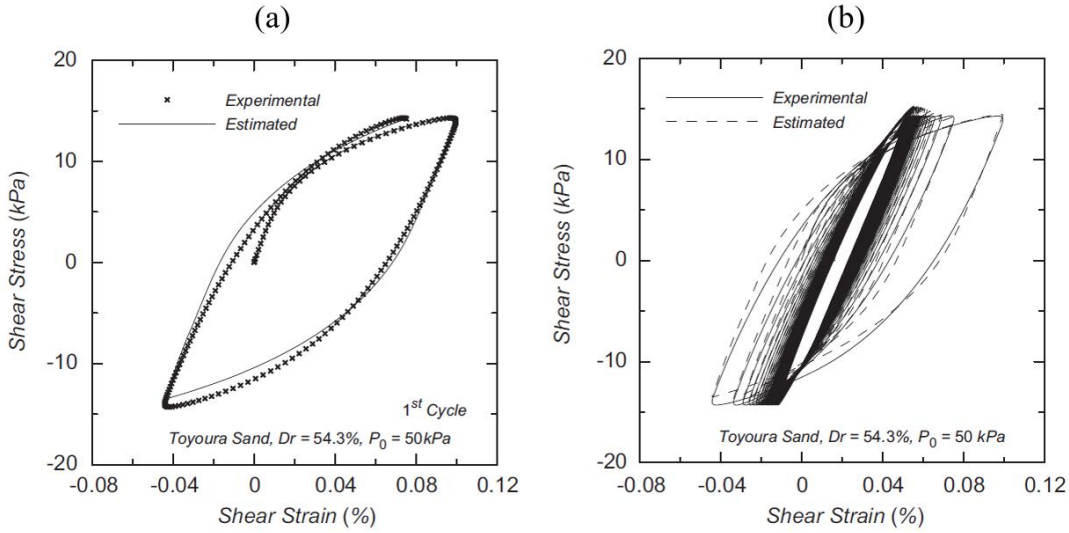

Figure 2.12: Symmetric-limit cyclic shear tests of Toyoura dry sand ($D_{r0} = 54.3\%$, $p_{in} = 50$ kPa): (a) first loading cycle; (b) response after 30 cycles (modified after Lee et al. (2009)).

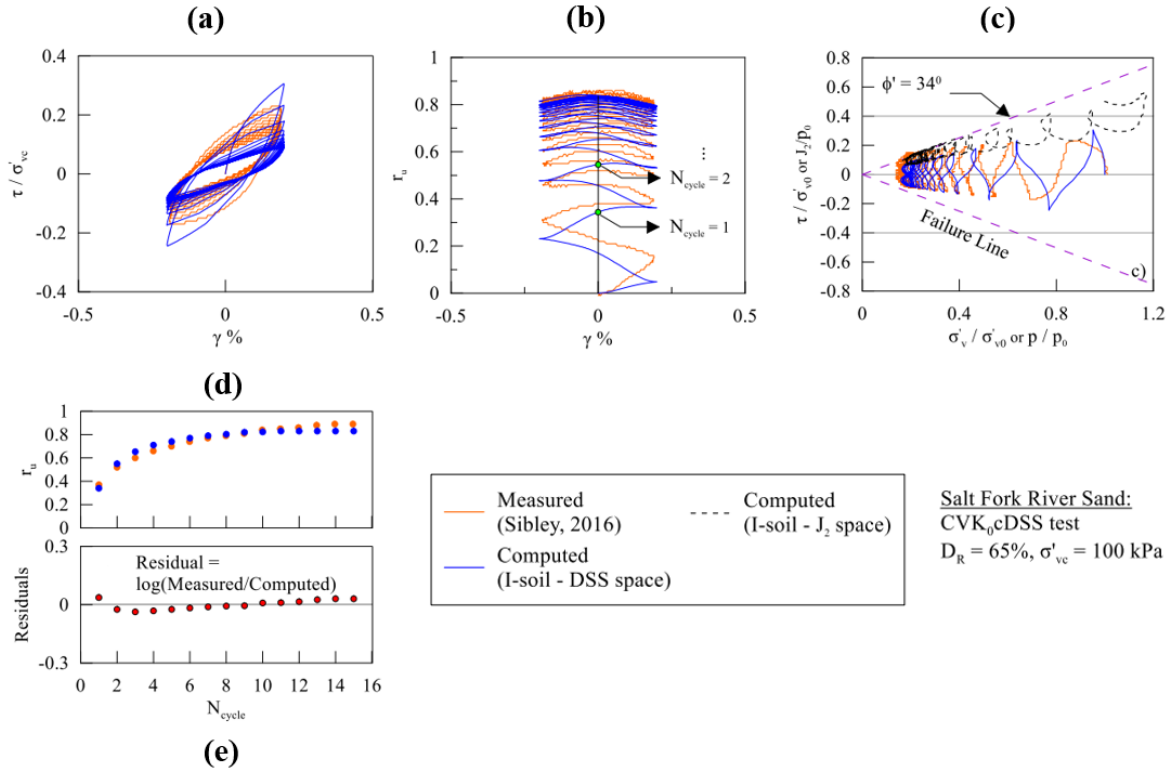

Figure 2.13: Constant volume, K_0-consolidated, cyclic direct simple shear tests (K_0-cDSS) on Salt Fork river sand ($D_{r0} = 65\%$) with 100 kPa effective vertical stress after consolidation, followed by a constant volume shearing: (a) stress-strain response; (b) excess porewater pressure versus shear strain; (c) stress path; (d) normalized excess porewater pressure versus number of cycles; (e) residuals estimated from measured and computed results (modified after Numanoglu et al. (2023)).

2.3.4.3 High-cycle performance of SANISAND-MS

Research on constitutive modelling of sand under cyclic loading has primarily focused on undrained, short-term loading, with limited studies addressing intrinsic high-cycle behaviour and the associated ratcheting effects critical to OWT foundations. Very few examples in literature stand out so far with SANISAND-MS being the most notable (Liu *et al.*, 2019). Chen et al. (2024) further refined SANISAND-MS by modifying the memory surface evolution and plastic modulus to enhance drained cyclic predictions and mitigate numerical issues. A robust stress integration strategy was also developed to improve computational efficiency over extended cycles. However, the model introduces numerous parameters with limited physical meaning, complicating calibration. Its mathematical complexity also poses challenges for numerical implementation, even at the element level, raising concerns about its practicality for large-scale BVP applications.

Some indicative SANISAND-MS simulations of the drained high-cycle tests by Wichtmann (2005) (section 2.2.1.2) are shown in Figure 2.14 and Figure 2.15, assessing the model's ability to capture cyclic strain accumulation. Figure 2.14 shows the effect of the initial void ratio (e_{in}) with SANISAND-MS replicating the trend of higher strain accumulation in looser sands, though slightly overpredicting at higher void ratios. Figure 2.15 examines the average stress ratio (η^{ave}), where the model generally aligns with experiments but overestimates strain accumulation at higher stress ratios ($\eta^{\mathrm{ave}} > 1$). Additionally, numerical issues may arise when η^{ave} significantly increases, particularly when approaching or exceeding the critical state stress ratio (M_{cs}), leading to potential simulation instability (Chen et al., 2024). Despite some limitations in high-stress conditions and numerical stability issues, SANISAND-MS appears quite effective in simulating the high-cycle response of sands.

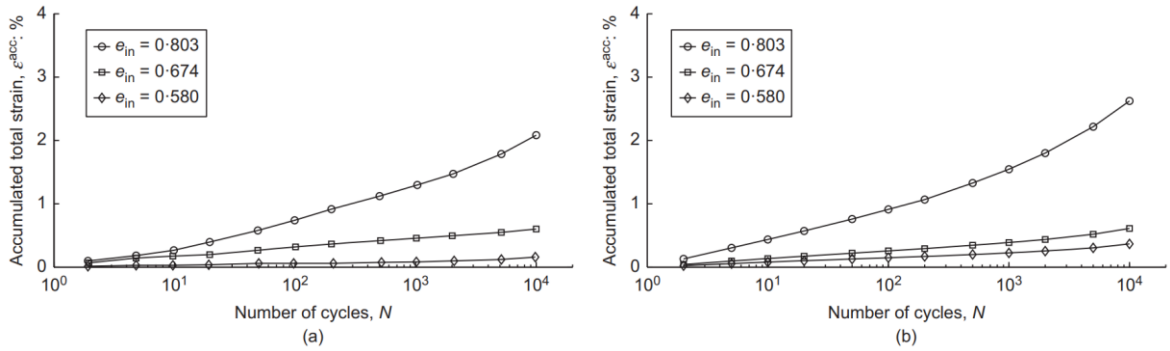

Figure 2.14: Influence of the initial void ratio, e_{in}, on cyclic strain accumulation for quartz sand No. 3 with test/simulation settings as $p_{\mathrm{in}} = 200$ kPa, $\eta^{\mathrm{ave}} = 0.75$, $q^{\mathrm{ampl}} = 60$ kPa: (a) experimental data (Wichtmann, 2005); (b) SANISAND-MS (Liu *et al.*, 2019).

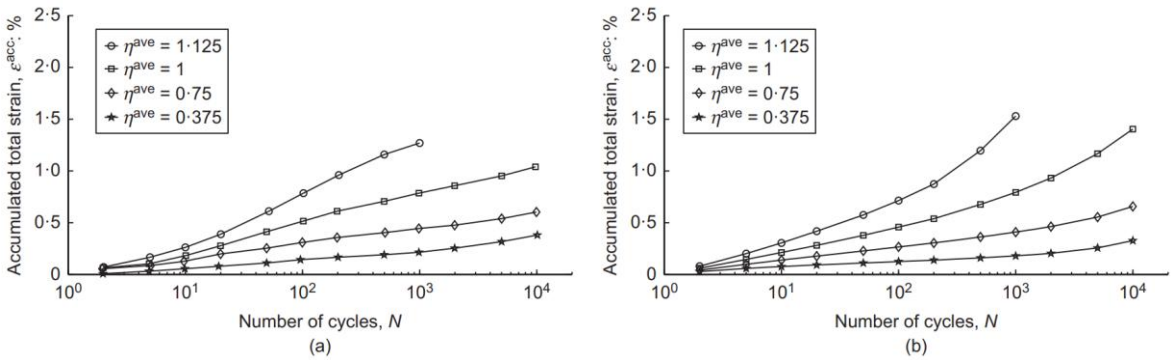

Figure 2.15: Influence of the average stress ratio, η^{ave}, on cyclic strain accumulation for quartz sand No. 3 with test/simulation settings as $p_{\mathrm{in}} = 200$ kPa, $e_{\mathrm{in}} = 0.684$, $q^{\mathrm{ampl}} = 60$ kPa: (a) experimental data (Wichtmann, 2005); (b) SANISAND-MS (Liu *et al.*, 2019).

2.3.5 Constitutive modelling of sand with non-plastic (or low-plasticity) fines

Over the past decades, significant progress has been made in constitutive modelling for clean sand. A key milestone has been the integration of CST (Roscoe *et al.*, 1958) with the state parameter framework (Been and Jefferies, 1985) in the core development of sand models. Models following this approach (Li and Dafalias, 2000) aim to provide unified predictions for both dense and loose sand by incorporating the effects of void ratio and stress level using a single set of material parameters. However, many natural sand deposits contain varying amounts of fines within the sand matrix, creating the need for models that can accurately predict the behaviour of sand with different fines contents, f_c. In practice, this implies that a model also should be capable of simulating the behaviour of sand with varying f_c without requiring adjustments to the model parameters for each specific case.

2.3.5.1 Equivalent granular state theory (EGST)

Traditionally, void ratio e has been as a key state variable in the CSSM framework, representing the structure of sand through its force skeleton, which is the network of interparticle contact forces transmitting stresses and providing stability to the granular assembly. However, when fine particles are added, the force skeleton remains largely unchanged while e changes significantly. To address this, the concept of an equivalent granular void ratio e^* was introduced, incorporating a participation factor b to account for the active role of fines (Thevanayagam and Martin, 2002):

$$e^* = \frac{e + (1-b)f_c}{1 + (1-b)f_c} \tag{2.7}$$

Here, b represents the fraction of fine particles actively contributing to force transmission within the soil skeleton. This concept is applicable to ‘fines-in-sand’ mixtures, where coarse particles dominate the sand matrix, up to a threshold fines content f_{thre}. Beyond this, the mixture transitions from a ‘fines-in-sand’ to a ‘sand-in-fines’ classification, as described by

Thevanayagam and Martin (2002). This threshold value can be determined either from empirical relationships (Rahman and Lo, 2008) or experimentally. In this study, the value of b is determined using a semi-empirical equation proposed by Rahman and Lo (2008):

$$b = \left[1 - \exp\left(-0.3\frac{1}{1-\chi^{-0.25}}\frac{f_c}{f_{thre}}\right)\right]\left(\frac{1}{\chi}\frac{f_c}{f_{thre}}\right)^{1/\chi} \tag{2.8}$$

where χ is the particle size ratio, defined as D_{10}/d_{50} (with D_{10} being the effective size of the host sand and d_{50} the median size of the fines). According to the state parameter framework (Been and Jefferies, 1985), mechanical behaviour of clean sands is governed by the combined effects of void ratio and mean effective normal stress. Been and Jefferies introduced the state parameter $\psi = e - e_c$, where e_c is the void ratio on the CSL corresponding to the current mean effective stress p. When plotting CS data points (p, e) of sand with non-plastic or low-plasticity fines in $\ln(p) - e$ space (Figure 2.16a), the trend exhibits significant spread and strong dependence on fines content. However, within the EGST framework (Rahman, 2021), using the equivalent granular void ratio e^* instead, the CS data points (p, e^*) collapse onto a single trend curve in $\ln(p) - e^*$ space (Figure 2.16b) for fines content up to f_{thre} (Rahman and Lo, 2007). This allows for the definition of an equivalent granular state parameter ψ^* as $\psi^* = e^* - e_c^*$, where $e_c^* = e_c$ since the equivalent granular CSL (EG-CSL) coincides with the clean sand CSL when $f_c = 0$.

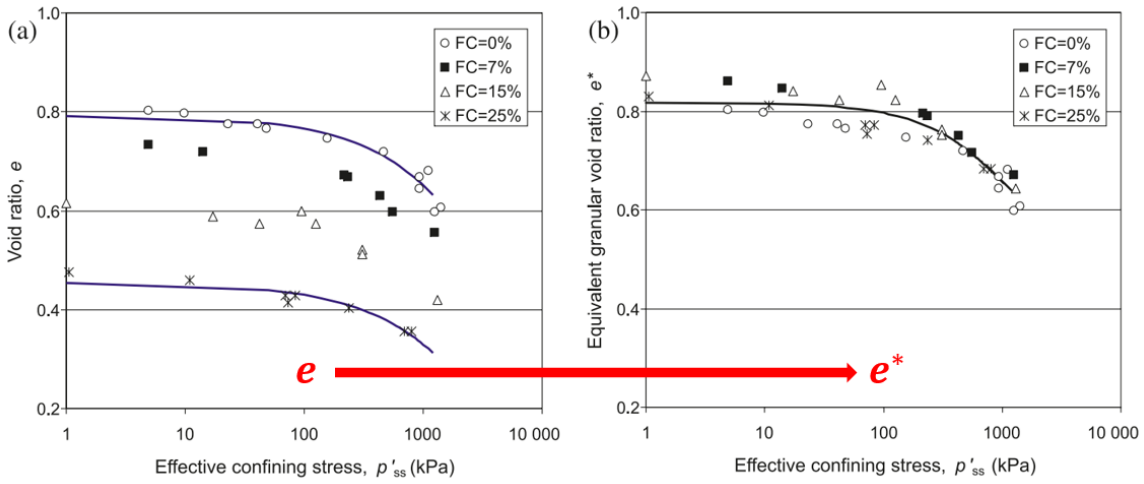

Figure 2.16: EG-CSL for foundry sand with non-plastic fines: (a) source data after Thevanayagam and Martin (2002)); (b) obtained by substituting e^* for e (modified after Rahman et al. (2008)).

2.3.5.2 Overview of modelling strategies

EGST can be seamlessly integrated into a clean sand state-dependent model by replacing e and ψ with their equivalent granular counterparts e^* and ψ^*, enabling a unified approach to simulate sand with non-plastic or low-plasticity fines across various densities, stress levels, and fines content using a single parameter set (Rahman et al., 2014). A more recent approach combines EGST with ACST, incorporating both fines content and evolving fabric anisotropy (Rahman and Dafalias, 2022). ACST extends CST by introducing a fabric anisotropy variable (FAV), A and a dilatancy state paremeter (DSP), ζ in place of the state parameter ψ (Li and Dafalias, 2012). EGST is then incorporated by substituting ζ^* for ζ. Lashkari (2014) proposed an alternative approach to adapting a clean sand model for non-plastic fines and fabric anisotropy, differing slightly from the combined EGST-ACST framework. While also substituting e and ψ with e^* and ψ^* respectively, Lashkari modified additional model components, unlike Rahman et al. (2014) who applied a direct substitution of these key state variables. Moreover, instead of ACST, Lashkari assumed a fixed inherent fabric tensor to account for fabric anisotropy.

A distinct approach was proposed by Wei and Yang (2019) who built upon an existing CS-based constitutive model (Li and Dafalias, 2000) to develop a formulation in triaxial space

that captures the behaviour of sand with varying non-plastic fines content. Their model employs a unified set of parameters for the elastic and hardening components across all f_c but requires separate CSL and dilatancy parameters for each f_c to achieve optimal accuracy. To extend its applicability to cyclic loading, an additional term was later introduced in the elastic shear modulus expression (Wei et al., 2020).

2.4 Intrinsic step-by-step 3D-FEA/FDA of OWT foundations in sand

Despite the extensive development of sand constitutive models with promising validation at the element level, only few newly proposed models have been successfully implemented to simulate the cyclic behaviour of OWT foundations in sand using 3D-FEA or finite difference analyses (FDA). This section emphasizes studies in which authors developed and implemented models rather than relying on default software models, demonstrating the feasibility of the developed models for numerical implementation and practical application.

2.4.1 SANISAND-MS in OWT foundation BVP applications

A notable example is the series of studies by Liu and colleagues, which effectively utilize the SANISAND-MS model (Liu *et al.*, 2019). Initially, Liu et al. (2022a) explored the application of SANISAND-MS in 3D-FEA to capture cyclic ratcheting in dry sand, focusing on the link between local soil response and global monopile behaviour, particularly tilt accumulation. The study investigated short loading histories, limited to 100 cycles, and involved a semi-quantitative comparison with experimental data. The simulation programme in this study examined the effects of cyclic load amplitude and asymmetry, controlled using the dimensionless factors ζ_b and ζ_c as defined by LeBlanc et al. (2010):

$$\zeta_b = \frac{H_{\max}}{H_{\mathrm{ref}}} = \frac{M_{\max}}{M_{\mathrm{ref}}}\,;\ \zeta_c = \frac{H_{\min}}{H_{\mathrm{ref}}} = \frac{M_{\min}}{M_{\mathrm{ref}}} \tag{2.9}$$

where $H_{\max}$ ($M_{\max}$) and $H_{\min}$ ($M_{\min}$) represent the maximum and minimum lateral loads (or moments at the mudline), respectively, and H_{ref} (M_{ref}) corresponds to the load inducing

a ground-level deflection of $0.1D$. Figure 2.17 presents typical cyclic responses at the pile head from 3D-FE simulations using the SANISAND-MS model for initial relative densities (D_{r0}) of 30% and 70%, demonstrating that the displacement caused by the first monotonic loading is relatively insensitive to density variations. As shown in Figure 2.17a and Figure 2.17b cyclic loading leads to progressive displacement accumulation, though at a diminishing rate over time, resembling the ratcheting behaviour observed in cyclic sand tests (Niemunis et al., 2005; Liu et al., 2019). Moreover Figure 2.17c, which illustrates the pile tilting response in terms of accumulated displacement and rotation over the number of cycles, aligns with experimental findings that highlight the significant influence of relative density on the accumulation of permanent pile rotation (LeBlanc et al., 2010). Further validation of SANISAND-MS was provided through normalised pile rotation ($\Delta\theta/\theta_s$) trends, where $\Delta\theta = \theta_N - \theta_0$ is the difference between the rotation accumulated after N cycles (θ_N) and the rotation at the end of the pre-cycling monotonic phase (θ_0) (Figure 2.18a). Within the adopted numerical modelling framework, it was assumed that $\theta_s = \theta_0$. Comparisons of SANISAND-MS 3D-FE simulations (Figure 2.18c) against small-scale experimental data (Figure 2.18b) from LeBlanc et al. (2010), illustrate that larger cyclic load amplitude ratios (ζ_b) result in increased pile rotation accumulation, with the numerical results closely following experimental trends. As shown in Figure 2.18c, this behaviour follows the empirical power-law relationship proposed by LeBlanc et al. (2010):

$$\frac{\Delta\theta}{\theta_s} = T_b(\zeta_b) \cdot T_c(\zeta_c) \cdot \mathrm{N}^{\alpha} \tag{2.10}$$

where $T_b(\zeta_b)$ and $T_c(\zeta_c)$ are dimensionless functions capturing the influence of the cyclic load amplitude and asymmetry, respectively, and α is a parameter originally taken as 0.31 in LeBlanc et al. (2010).

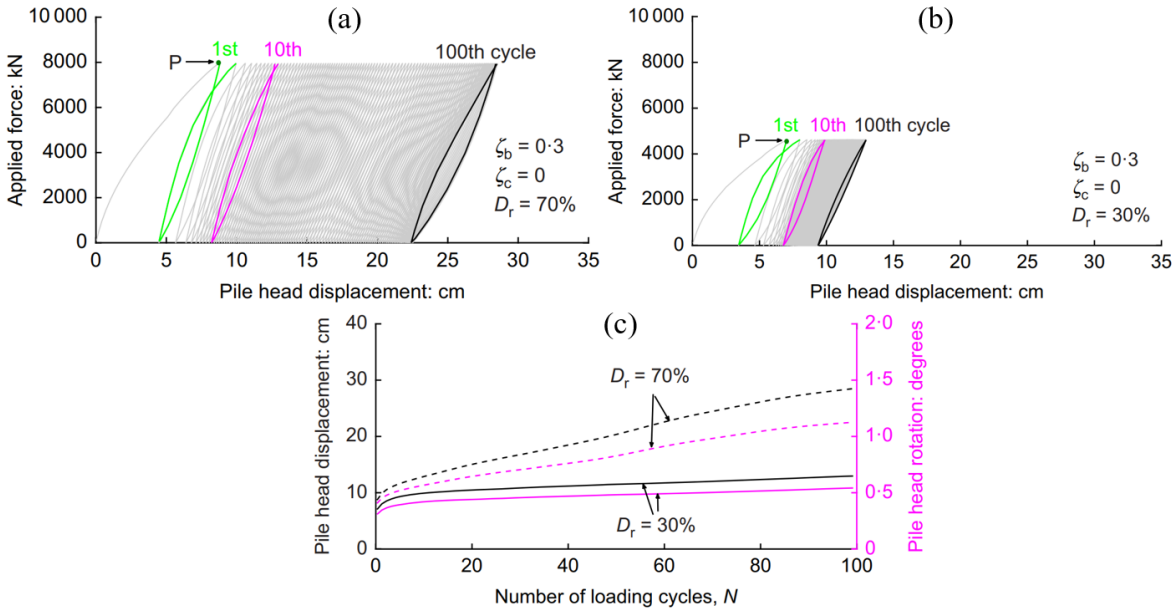

Figure 2.17: Cyclic pile head response from 3D-FE simulations using the SANISAND-MS model: (a) lateral force-pile head displacement for $D_{r0} = 70\%$; (b) lateral force-pile head displacement for $D_{r0} = 30\%$; (c) accumulated pile head displacement and rotation as a function of the number of loading cycles (modified after Liu et al. (2022a)).

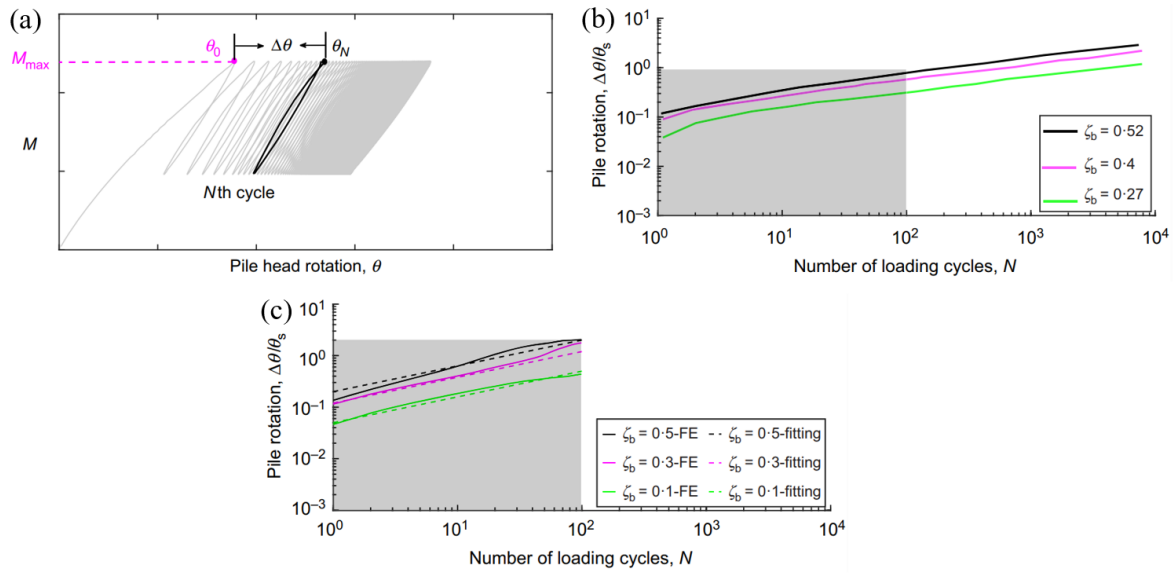

Figure 2.18: (a) Definition of pile rotation values; (b) experimental data from LeBlanc et al. (2010) for a model-scale initial relative density $D_{r0}^{m} = 38\%$ and a corresponding prototype-scale $D_{r0}^{p} = 75\%$; (c) SANISAND-MS 3D-FEM simulations for $D_{r0} = 70\%$; (modified after Liu et al. (2022a)).

A subsequent study (Liu et al., 2022b) expanded the initial findings on dry sand by examining the applicability of Miner's rule at the element level through drained high-cycle tests using SANISAND-MS, aiming to establish a connection between the soil's elemental response and the global monopile behaviour. According to Miner's rule: (i) irreversible plastic strains accumulate only when the current cyclic load amplitude exceeds all previously

applied amplitudes, and (ii) the sequence of load packages in a variable-amplitude loading history has only a minor influence on the final accumulated plastic strain. 3D-FEA under drained conditions partially supported these assumptions, particularly regarding pile head displacements of a large-diameter OWT monopile. Specifically, Figure 2.19a demonstrates that as the cyclic amplitude increases with each successive load package, the lateral displacement of the pile head accumulates progressively. Figure 2.19b further supports this trend, showing displacement accumulation consistent with Miner's assumptions and predicting the same overall accumulated displacement as Figure 2.19a. However, Figure 2.19c indicates that applying a lower amplitude package after a higher one still leads to displacement accumulation, albeit at a significantly reduced rate. This deviates from principle (ii), which states that once the soil has been subjected to a higher cyclic amplitude, no further accumulation should occur under subsequent lower-amplitude cycles.

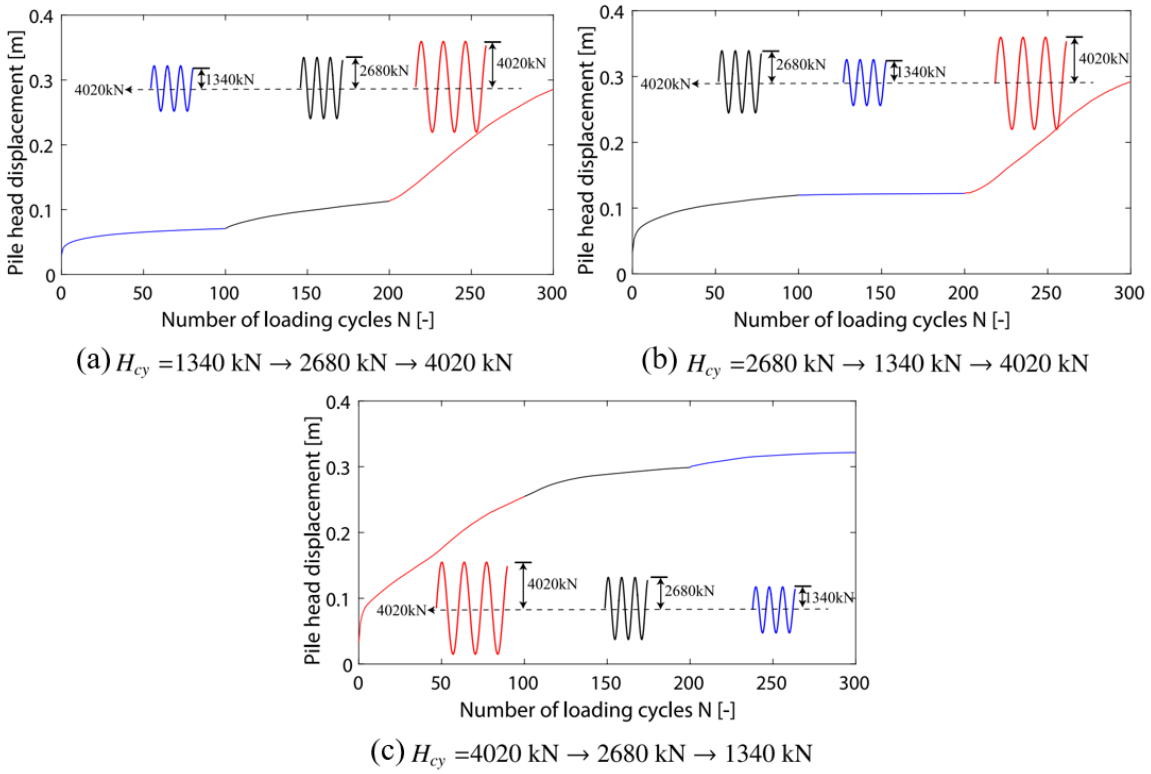

Figure 2.19: Effect of cyclic loading sequence on monopile tilt evolution, showing pile head lateral displacement versus loading cycles from 3D-FE simulations using SANISAND-MS. Displacement accumulation is examined in sand with $D_{r0} = 70\%$ under a constant average load level $H_{av} = 4020$kN where $H_{max}/H_{min} = H_{av} \pm H_{cy}$ (modified after Liu, et al. (2022b)).

A later study (Liu and Kaynia, 2022), employing a modified version of SANISAND-MS known as 'SANISAND-MSu', specifically designed for undrained conditions in 3D-FEA, examined the effects of pore water pressure on the lateral response of monopiles under monotonic and cyclic loading in undrained sand. The results revealed significant cycle-by-cycle displacement accumulation compared to drained conditions, highlighting the influence of pile geometry on displacement trends and the critical role of drainage conditions and excess pore pressure in optimizing monopile design.

One of the most recent studies (Pisanò *et al.*, 2024) utilizing SANISAND-MS involved a 3D-FE investigation of monopile response under multi-amplitude cyclic loading, with numerical simulations compared to pile load test data (Beuckelaers, 2017) from the PISA field campaign in Dunkirk (Byrne et al., 2020b). The study highlighted the role of accounting for pile installation effects in predicting short-term monopile tilt and emphasized the influence of microstructural soil mechanisms, such as ratcheting and fabric damage, on cyclic response. Additionally, it underscored the need for further research into the calibration of soil parameters for advanced constitutive models. Figure 2.20 presents the 3D-FE SANISAND-MS simulation of pile DM2 at Dunkirk compared to field data, illustrating monopile deflection accumulation at the ground surface. The vertical axis represents U_{R}, the accumulated pile head deflection per cycle, measured relative to the maximum deflection from the initial monotonic load (0th cycle) (LeBlanc et al., 2010), with $U_{\mathrm{R}} = U^{i}_{j,max} - U^{i}_{0,max}$ where i denotes the cycle number and j the load set (LS). Figure 2.20a shows simulation results for a wished-in-place monopile, while Figure 2.20b demonstrates improved agreement with field data when considering installation effects. Figure 2.20c further refines the match through recalibration of the cyclic parameter ζ.

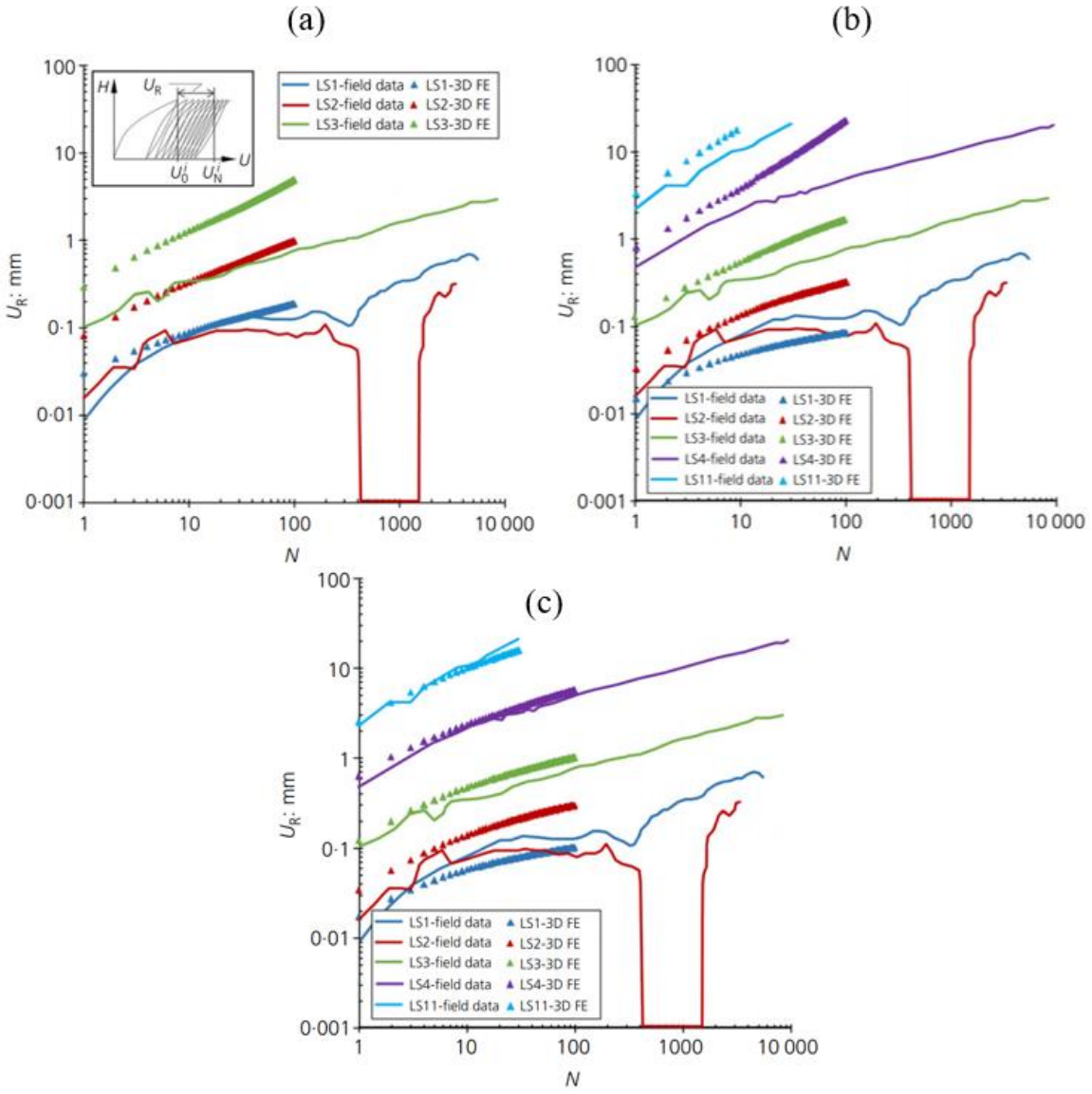

Figure 2.20: 3D-FE SANISAND-MS simulation of PISA's cyclic test at Dunkirk on pile DM2, showing-ground surface monopile deflection accumulation, comparing: (a) wished-in-place monopile; (b) installation effects (ζ=10^{-4}); (c) installation effects with inhibited memory surface shrinkage (ζ=10^{3}) (Pisanò *et al.*, 2024).

The same model was applied to other foundation types such as the evaluation of suction bucket performance in sand under vertical cyclic loading (Roy *et al.*, 2024).

2.4.2 Ta-Ger in OWT foundation BVP applications

Another notable model in the literature for its successful application in simulating the cyclic behaviour of OWT foundations in sand is the 'Ta-Ger' model (Tasiopoulou and Gerolymos, 2016a; 2016b), which has been exclusively implemented using 3D-FDA, as no successful 3D-FE implementation has been reported to date. One example is its implementation in the finite difference (FD) software FLAC3D, validated through numerical simulations of

centrifuge experiments investigating liquefaction-induced settlements of shallow foundations on loose and dense sand layers (Tasiopoulou *et al.*, 2019).

Another notable application is a study on drainage effects using a slightly upgraded Ta-Ger model (Tasiopoulou *et al.*, 2021), validated through high-amplitude cyclic centrifuge tests in dry sand under drained conditions. The same 3D-FD model was then employed to assess the impact of drainage conditions on the long-term cyclic lateral response of bucket foundations across varying soil permeabilities in saturated conditions.

Particularly relevant to this project, as it focuses on monopile foundations, was the application of the Ta-Ger model in FLAC3D to simulate selected PISA field tests (Byrne et al., 2020b) on monopiles installed in Dunkirk sand under monotonic (DM4) and cyclic (DM2) lateral loading (Tasiopoulou *et al.*, 2020). Unlike Pisanò et al. (2024), this study modelled only a single loading amplitude (80 kN lateral force, 800 kNm moment) over 230 cycles. Prior loading sequences were not explicitly simulated but were accounted for by tuning the hardening exponent based on accumulated shear strain increments, calibrated to match field data. Figure 2.21 compares numerical and field results, showing good agreement in moment-rotation loops and cyclic rotation accumulation, successfully capturing key drained cyclic mechanisms. While this validation serves as one example of the model's predictive capabilities, further assessments across a wider range of loading amplitudes and sequences are required to establish its robustness.

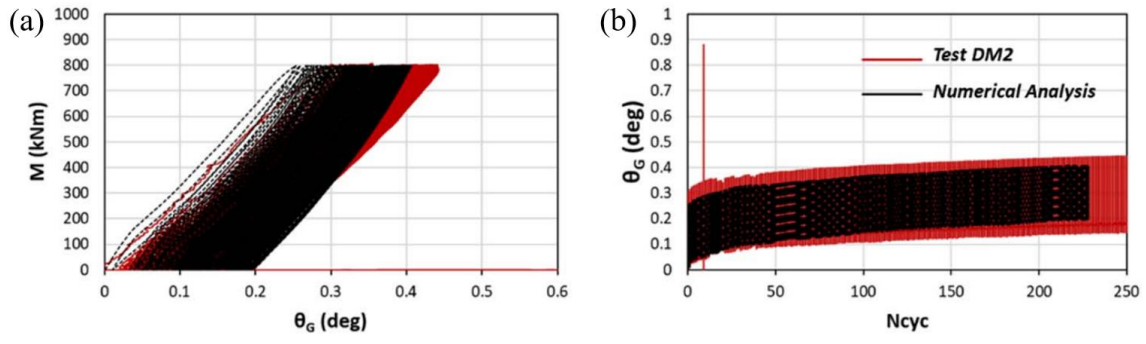

Figure 2.21: 3D-FD Ta-Ger simulation of PISA's cyclic test at Dunkirk on pile DM2 (LS4): (a) applied moment M-rotation θ_G; (b) rotation θ_G-loading cycles N (modified after Tasiopoulou et al. (2020)).

Lastly, a promising study (Chaloulos *et al.*, 2024) conducted 3D coupled cyclic time history analyses of a monopile foundation supporting a 12 MW OWT, founded in dense sand and subjected to a 600-s load history during the peak phase of a 35-h design storm. Using the Ta-Ger model implemented in FLAC3D and validated against centrifuge tests, the analyses effectively captured key soil-foundation interaction mechanisms and emphasized the critical role of drainage conditions in determining monopile performance. The numerical model was validated against centrifuge test D2-L10-02 (Takahashi *et al.*, 2022), which involved applying 20 cycles of harmonic horizontal displacement to a 2.0 m diameter, 10 m embedded monopile in dense Toyoura sand ($D_{r0} = 80\%$). Figure 2.22 presents this validation, showing good agreement in monopile response under cyclic loading. This agreement supported the application of the model for examining drainage effects and other key design considerations.

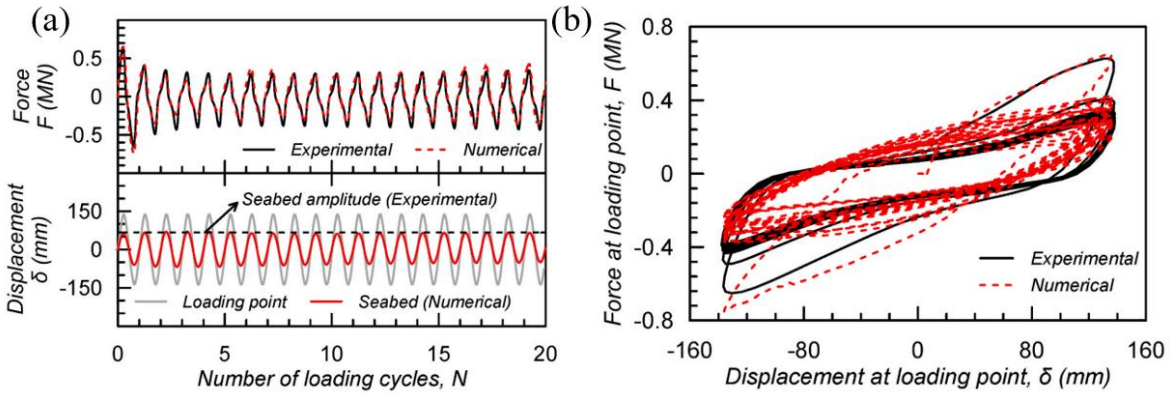

Figure 2.22: Validation of 3D-FD Ta-Ger simulation against centrifuge test data (Takahashi *et al.*, 2022), for a monopile in dense Toyoura sand ($D_{r0} = 80\%$), showing response under cyclic loading: (a) force history at loading point (top) and applied and corresponding seabed displacement (bottom); (b) force-displacement at loading point (modified after Chaloulos et al. (2024)).

2.4.3 Multi-surface models in OWT foundation BVP applications

Examples of 3D simulations of OWT foundations in sand using multi-surface constitutive models are rare, with Cerfontaine (2014) being a notable exception, successfully applying a series multi-surface model in FE software to simulate the cyclic behaviour of an OWT suction caisson foundation in dense sand. Since no application of parallel multi-surface models for OWT foundations in sand is available, their potential is instead demonstrated by the successful implementation of the 'Parallel Iwan Multi-Surface' (PIMS) model for clay.

Whyte et al. (2020) applied PIMS in 3D-FEA simulations of OWT monopile foundations, capturing key degradation mechanisms of stiffness and strength under monotonic and cyclic loading in undrained clay. Figure 2.23 presents the predicted monopile lateral response under cyclic loading, showing progressive rotation accumulation and system stiffening, aligning well with experimental trends.

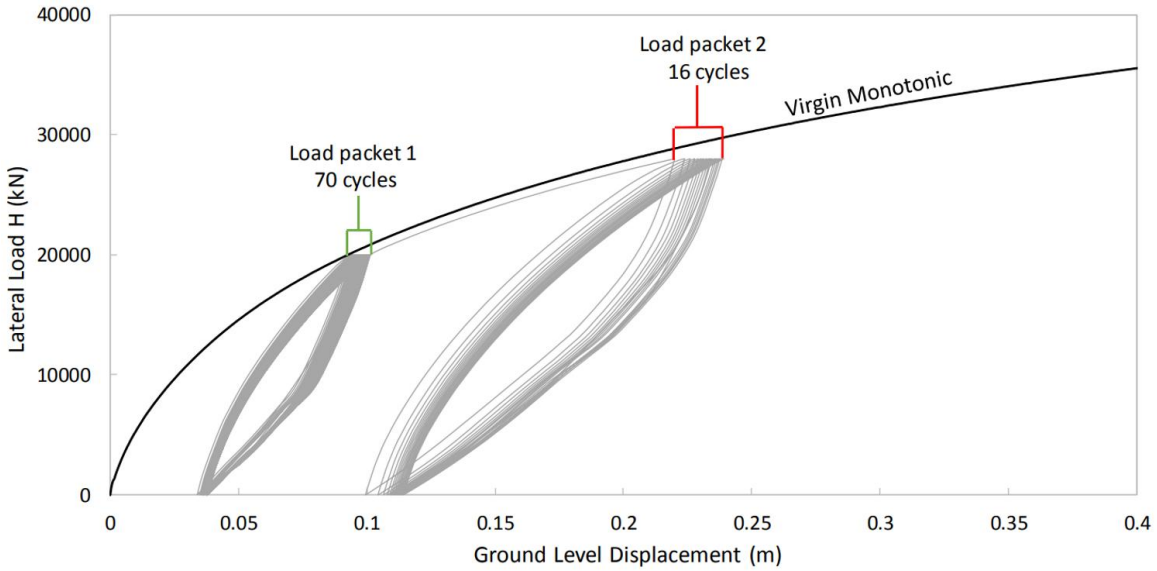

Figure 2.23: 3D-FE PIMS model simulation of monopile response under cyclic loading in clay, showing cyclic load-displacement response at ground level (modified after Whyte et al. (2020)).

2.5 Choice of suitable plasticity frameworks for further evaluation

The selection of a suitable plasticity framework requires balancing several considerations. For a framework to be suitable, models formulated within it should be capable of capturing both low-cycle and high-cycle cyclic soil behaviour, remain computationally efficient, and allow robust implementation in 3D-FEA of complex BVPs such as monopile-sand interaction. Other desirable attributes include consistent performance across a range of densities, stress states, and drainage conditions; a moderate number of parameters calibrated using standard laboratory tests; physical interpretability of constitutive components; and flexibility to incorporate more realistic seabed environments, including sands with fines.

The literature review indicated that no single framework, and by extension no individual model, fully satisfies all these requirements. Some demonstrate strengths in particular

aspects, while others address different limitations. At this stage, beyond reviewing, it was necessary to identify the most promising candidates for implementation and further assessment. Of the criteria listed above, the decisive one for selection beyond predictive capabilities was prior demonstration in the literature of successful application to 3D numerical analyses of monopile foundations.

Among the main classes of frameworks, three stand out as particularly relevant: (i) bounding surface plasticity, represented by the widely adopted and state-dependent SANISAND family; (ii) multi-surface plasticity, in both series and parallel forms; and (iii) the state-dependent Ta-Ger framework, which departs from classical plasticity in favour of a simpler formulation. The Ta-Ger framework offers two notable advantages: a relatively simple plasticity scheme that facilitates efficient implementation, and conceptual alignment with bounding surface plasticity, enabling cross-framework insights. At the same time, the literature highlights clear opportunities for extension, particularly in drained high-cycle loading predictions and offshore monopile modelling, where applications remain limited.

These frameworks were therefore selected for further study, with their performance examined in chapter 3 against the criteria outlined above and additional considerations, ultimately informing the choice of the most appropriate constitutive platform for subsequent adaptation and implementation in large-scale 3D-FEA of OWT monopile foundations.

Chapter 3

Evaluation of four constitutive models for monotonic and cyclic loading of sands

3.1 Introduction

The influence of cyclic loading on OWT foundations has been discussed in earlier chapters, emphasizing the need for advanced constitutive models capable of capturing the complex response of sands under repeated loading. While many models perform well under monotonic conditions, their reliability diminishes when applied to cyclic loading scenarios (Wichtmann et al., 2019). Moreover, these models often require extensive calibration procedures and involve highly complex formulations, which can limit their practicality for routine engineering applications. Despite their theoretical robustness, they frequently prove insufficient for accurately representing all loading conditions using a single set of parameters. With the aim of investigating these challenges and identifying a suitable constitutive modelling framework for sands under cyclic loading, this chapter presents a comparative evaluation of four sand constitutive models: (i) SANISAND DM04 model (Dafalias and Manzari, 2004), (ii) a variant of the state-dependent sand model ‘Ta-Ger’ (Tasiopoulou and Gerolymos, 2016a; 2016b) denoted here as ‘Ta-Ger B’, (iii) the original

Prevost sand model (Prevost, 1985), and (iv) the new practical effective stress model PIMSS (Parallel Iwan Multi-Surface Sand). The chapter briefly introduces the three existing models and subsequently presents the theoretical formulation and numerical implementation of PIMSS. Selected monotonic and cyclic tests were simulated using all four models, and their predictive capabilities are examined.

The models are not selected to provide an exhaustive comparison or to identify the most advanced formulation available in the literature. Instead, they are chosen to represent distinct theoretical approaches in sand plasticity identified as particularly relevant through the literature review. In doing so, the chapter compares the following constitutive modelling frameworks: bounding surface plasticity, multi-surface plasticity (both the series and parallel approaches), and the plasticity framework underpinning the Ta-Ger model. The comparison therefore focuses on evaluating the relative strengths and limitations of these approaches under monotonic and cyclic loading, ensuring that the conclusions drawn are general and transferable. Based on this comparative analysis, the most suitable constitutive framework is identified as the preferred platform for further development and 3D-FE implementation.

3.2 Brief description of the models

For brevity, only a concise description of the SANISAND DM04 (Dafalias and Manzari, 2004), Ta-Ger B (Tasiopoulou and Gerolymos, 2016a) and Prevost (Prevost, 1985) models is provided, with further details available in the original references. A detailed description of PIMSS is included in this chapter, as it is a newly developed model. All four models (SANISAND DM04, Ta-Ger B, Prevost and PIMSS) were implemented in MATLAB using a simple forward Euler stress integration scheme. Ta-Ger B, Prevost and PIMSS models were formulated in multiaxial stress space, while SANISAND DM04 was implemented in triaxial space following the framework of Li and Dafalias (2000).

3.2.1 SANISAND DM04 model

The SANISAND DM04 model (Dafalias and Manzari, 2004) is formulated within the framework of bounding surface plasticity and incorporates principles from critical state soil mechanics (CSSM). It features four conical surfaces defined in deviatoric stress space: a small yield surface governed by kinematic hardening and centred at the back-stress ratio, and three concentric surfaces anchored at the origin, the bounding surface, critical state surface, and dilatancy (or phase transformation) surface. The plastic modulus and dilatancy behaviour are governed by the relative positions between the current back-stress ratio and its images on the bounding and phase transformation surfaces, respectively. To ensure CSSM compatibility, these two surfaces evolve with the state parameter ψ. The model also introduces a fabric-dilatancy quantity z (a tensor in multi-axial stress space, but a scalar under triaxial conditions) to capture the fabric evolution during cyclic loading. This internal variable enhances the model's ability to capture cyclic mobility effects, particularly the reduction of effective stress and stiffness during undrained cyclic shear (Duque *et al.*, 2022).

Although newer SANISAND variants exist, such as SANISAND-MS (Liu *et al.*, 2019), the DM04 formulation was selected as a representative benchmark due to its widespread use, availability of calibrated parameters for the experimental database considered, and numerical robustness. The inclusion of more recent variants incorporating memory surfaces would introduce additional internal variables, calibration requirements, and implementation complexity, thereby extending the scope of the comparison beyond the objectives of this chapter. Consistent with the aim of comparing representative constitutive frameworks rather than benchmarking all available SANISAND variants, the DM04 model therefore provides a suitable and well-established reference formulation within the SANISAND family and the broader context of bounding surface plasticity.

The triaxial constitutive equations of SANISAND DM04 are listed in Table 3.1.

Table 3.1: Triaxial constitutive equations of the SANISAND DM04 model (Dafalias and Manzari, 2004).

SANISAND DM04 triaxial equations
Critical state line: $$e_{\mathrm{c}} = e_0 - \lambda(p/p_{\mathrm{at}})^{\xi} \quad (3.1)$$ where e_{c} is the is the critical state void ratio at mean pressure p, e_0 is the void ratio at $p = 0$, λ and ξ are constants, and p_{at} is atmospheric pressure.
Elastic deviatoric strain increment: $$\mathrm{d}\varepsilon_q^{\mathrm{e}} = \frac{\mathrm{d}q}{3G} \quad (3.2)$$ where G is the shear modulus and $\mathrm{d}q$ is the deviatoric stress increment in triaxial space. $$G = G_0 p_{\mathrm{at}}[(2.97 - e)^2/(1 + e)](p/p_{\mathrm{at}})^{1/2} \quad (3.3)$$ where G_0 is a small-strain modulus constant and e is the current void ratio.
Elastic volumetric strain increment: $$\mathrm{d}\varepsilon_p^{\mathrm{e}} = \mathrm{d}p/K \quad (3.4)$$ where K is the bulk modulus and $\mathrm{d}p$ is the mean effective stress increment. $$K = 2G(1 + v)/3(1 - 2v) \quad (3.5)$$ where v is Poisson's ratio.
Yield surface: $$\mathrm{f} = |\eta - \alpha| - \mathrm{m} = 0 \quad (3.6)$$ where $\eta = q/p$, α is the back-stress ratio signifying the position of the yield surface in $p - q$ space, and m controls the yield surface size.
Plastic deviatoric strain increment: $$\mathrm{d}\varepsilon_q^{\mathrm{p}} = \mathrm{d}\eta/H \quad (3.7)$$ where H is the plastic modulus that governs deviatoric plastic flow. $$H = h(M_{\mathrm{s}} - \eta) \quad (3.8)$$ where h is a hardening variable and M_{s} the bounding stress ratio. $$M_{\mathrm{s}} = M_{\mathrm{cs}} e^{-n_{\mathrm{b}}\psi} \quad (3.9)$$ where M_{cs} is the critical state stress ratio, n_{d} is a positive material constant, and $\psi = e - e_{\mathrm{c}}$ is the state parameter. $$h = b_0/|\eta - \eta_{\mathrm{in}}| \quad (3.10)$$ where η_{in} is the stress ratio at the start of loading, and b_0 is a pressure- and void-ratio-dependent stiffness parameter. $$b_0 = G_0 h_0 (1 - c_{\mathrm{h}} e)(p/p_{at})^{-1/2} \quad (3.11)$$ where h_0 and c_{h} are material constants.
Plastic volumetric strain increment: $$\mathrm{d}\varepsilon_p^{\mathrm{p}} = d\left|\mathrm{d}\varepsilon_q^{\mathrm{p}}\right| \quad (3.12)$$ where d is the dilatancy ratio, defined as: $$d = A_{\mathrm{d}}\left(M^{\mathrm{d}} - \eta\right) \quad (3.13)$$ where A_{d} is a function of the state, and M_{pt} is the dilatancy stress ratio defined as: $$M_{\mathrm{pt}} = M_{\mathrm{cs}} e^{n_{\mathrm{d}}\psi} \quad (3.14)$$ where n_{d} is a positive material constant. $$A_{\mathrm{d}} = A_0(1 + \langle sz \rangle) \quad (3.15)$$ where A_0 is a dilatancy parameter, $s = \pm 1$ indicates loading direction, and z is the fabric-dilatancy quantity.
Fabric-dilatancy quantity update (z: tensor in general, scalar in triaxial): (3.16)

SANISAND DM04 triaxial equations
$$\mathrm{d}z = -c_z\langle -\mathrm{d}\varepsilon_p^{\mathrm{p}}\rangle(sz_{max} + z)$$ where c_z controls the evolution rate of z, and z_{max} is the maximum allowable z value.
Back-stress ratio update: $$\mathrm{d}\alpha = \mathrm{d}\eta \quad (3.17)$$ where α evolves with the stress ratio η to model kinematic hardening.
It is noted that the bounding and phase transformation stress ratios M_{s} and M_{pt} are denoted as M_b and M_d in the original publication, with M_d referred to as dilatancy stress ratio. The present notation follows the Ta-Ger nomenclature for consistency, as the quantities are equivalent.

3.2.2 Ta-Ger B model

The Ta-Ger model is formulated within a framework that merges perfect elastoplasticity with smooth hysteresis, achieved through a hardening law inspired by the Bouc-Wen approach. Unlike traditional plasticity formulations, it introduces a plastic modulus that directly scales the plastic component of the incremental stiffness matrix, rather than being added as a term in the denominator (Tasiopoulou and Gerolymos, 2016a):

$$\mathbf{E}^{\mathrm{ep}} = \mathbf{E}^{\mathrm{e}}\left[\mathbf{I} - \frac{\boldsymbol{\Phi}_{\mathrm{g}}\boldsymbol{\Phi}_{\mathrm{f}}{}^{\mathrm{T}}\mathbf{E}^{\mathrm{e}}\mathbf{H}}{\boldsymbol{\Phi}_{\mathrm{f}}{}^{\mathrm{T}}\mathbf{E}^{\mathrm{e}}\boldsymbol{\Phi}_{\mathrm{g}}}\right] \quad (3.18)$$

Here, $\mathbf{E}^{\mathrm{e}}$ denotes the elastic stiffness matrix, while $\boldsymbol{\Phi}_{\mathrm{f}}$ and $\boldsymbol{\Phi}_{\mathrm{g}}$ represent the gradients of the yield surface and plastic potential, respectively. The matrix $\mathbf{H}$, which governs the plastic modulus, is defined as $\mathbf{H} = \zeta^n\mathbf{I}$, where ζ controls the hardening/softening through a mapping rule, and n is a hardening parameter. Equation (3.18) is identical to equation (2.3) introduced in chapter 2 and is recalled here for completeness.

Although formulated within a different theoretical framework, the Ta-Ger model closely follows many of the core principles established in the SANISAND family, particularly SANISAND DM04 (Dafalias and Manzari, 2004). Both models are stress-ratio controlled, defining key surfaces and plasticity conditions relative to stress ratio measures in the π-plane for multi-axial formulations or in the $p - q$ plane for triaxial formulations. Furthermore,

both models are compatible with the CSSM framework, employing bounding and dilatancy surfaces to regulate hardening/softening and volumetric response, respectively.

Ta-Ger B (Tasiopoulou and Gerolymos, 2016a) is a variant of the original Ta-Ger model, differing only in the equations used for the phase transformation stress ratio, M_{pt}, and the bounding surface stress ratio, M_{s}, and thus in the associated state parameters. In the original formulation, Tasiopoulou and Gerolymos (2016a) introduced a novel set of evolution equations for M_{s} and M_{pt}, using the cumulative incremental deviatoric strain, $\Sigma \mathrm{d}\varepsilon_{\mathrm{q}}$, and the relative dilatancy index, I_{r} (Bolton, 1986) as state parameters. However, they also demonstrated the adaptability of the model by showing it can accommodate alternative equations for M_{s} and M_{pt}, such as those based on the classical state parameter ψ (Been and Jefferies, 1985), as used in SANISAND DM04 (Dafalias and Manzari, 2004). This modified version is referred to as Ta-Ger B. Table 3.2 presents the multi-axial equations necessary for the explicit numerical implementation of the Ta-Ger B model and the assembly of the elastoplastic stiffness matrix in equation (3.18). The present description is intended to provide a high-level overview of the Ta-Ger B formulation for completeness and to maintain the standalone nature of this chapter. The full set of governing equations, using consistent notation, is presented in chapter 4, which is adopted as the main reference for the Ta-Ger model used throughout this thesis.

Table 3.2: Multi-axial constitutive equations of the Ta-Ger B model (Tasiopoulou and Gerolymos, 2016a).

Ta-Ger B multi-axial equations
Elasticity matrix: $$\mathbf{E}^{e} = \begin{bmatrix} E_1 & E_2 & E_2 & 0 & 0 & 0 \\ E_2 & E_1 & E_2 & 0 & 0 & 0 \\ E_2 & E_2 & E_1 & 0 & 0 & 0 \\ 0 & 0 & 0 & 2G & 0 & 0 \\ 0 & 0 & 0 & 0 & 2G & 0 \\ 0 & 0 & 0 & 0 & 0 & 2G \end{bmatrix} \quad (3.19)$$
with: $$E_1 = K + 4G/3,\ E_2 = K - 2G/3 \quad (3.20)$$
where K is the bulk modulus and G is the shear modulus.

Ta-Ger B multi-axial equations

$$G = G_0 p_{at}[(2.97 - e)^2/(1 + e)](p/p_{at})^{1/2} \quad (3.21)$$

where G_0 is a small-strain modulus constant and e is the current void ratio.

$$K = 2G(1 + v)/3(1 - 2v) \quad (3.22)$$

where v is Poisson's ratio.

Yield function:

$$\mathrm{f} = \left[(\boldsymbol{s} - \boldsymbol{r}_{\mathrm{p}} p) : (\boldsymbol{s} - \boldsymbol{r}_{\mathrm{p}} p)\right]^{1/2} \quad (3.23)$$

where $\boldsymbol{s}$ is the deviatoric stress tensor, p is the mean effective stress, and $\boldsymbol{r}_{\mathrm{p}}$, acts as the back-stress ratio in conventional bounding surface models and is defined as:

$$\boldsymbol{r}_{\mathrm{p}} = \boldsymbol{s}_{\mathrm{p}}/p_{\mathrm{p}} \quad (3.24)$$

where $\boldsymbol{s}_{\mathrm{p}}$ and p_{p} are the deviatoric stress tensor and mean effective stress, respectively, at the pivot points corresponding to loading reversals. The function f in equation (3.23) is not enforced as an active yield condition and is introduced solely for the evaluation of the gradient $\boldsymbol{\Phi}_{\mathrm{f}}$ used in the elastoplastic matrix.

Gradient of yield surface:

$$\boldsymbol{\Phi}_{\mathrm{f}} = \boldsymbol{n} - \frac{1}{3}\boldsymbol{n} : \boldsymbol{r} \quad (3.25)$$

where $\boldsymbol{r} = \boldsymbol{s}/p$ and $\boldsymbol{n}$ is the normalised stress ratio tensor, defined as:

$$\boldsymbol{n} = \frac{\boldsymbol{s} - \boldsymbol{r}_{\mathrm{p}} p}{\left[(\boldsymbol{s} - \boldsymbol{r}_{\mathrm{p}} p) : (\boldsymbol{s} - \boldsymbol{r}_{\mathrm{p}} p)\right]^{1/2}} \quad (3.26)$$

Flow rule:

$$\boldsymbol{\Phi}_{\mathrm{g}} = \boldsymbol{n} + \boldsymbol{n}^{\boldsymbol{2}} d \quad (3.27)$$

where d is the dilatancy ratio, defined as:

$$d = R_{\mathrm{d}}\left(\sqrt{\frac{2}{3}} M_{\mathrm{pt}} \chi - \frac{\boldsymbol{s}}{p} : \boldsymbol{n}\right) \quad (3.28)$$

where R_{d} is an internal variable controlling the amount of densification induced during drained loading and is estimated as:

$$R_{\mathrm{d}} = e^{-\alpha(D_{\mathrm{r}} - D_{\mathrm{r0}})} \quad (3.29)$$

where α is a constant, D_{r} is the current relative density, and D_{r0} is the initial relative density.

χ is an internal variable incorporating Lode angle (θ) effects, M_{pt} is the phase transformation stress ratio evolving as a function of the state parameter ψ according to:

$$M_{\mathrm{pt}} = M_{\mathrm{cs}} e^{n_{\mathrm{d}} \psi} \quad (3.30)$$

Hardening matrix:

$$\mathbf{H} = \zeta^n \mathbf{I} \quad (3.31)$$

where ζ controls the hardening/softening through a mapping rule:

$$\zeta = \frac{\left[(\boldsymbol{r} - \boldsymbol{r}_{\mathrm{p}}) : (\boldsymbol{r} - \boldsymbol{r}_{\mathrm{p}})\right]^{1/2}}{\sqrt{\frac{2}{3}} M_{\mathrm{s}} \chi - n_{\mathrm{p}}} \quad (3.32)$$

M_{s} is the bounding surface stress ratio evolving as a function of the state parameter ψ according to:

$$M_{\mathrm{s}} = M_{\mathrm{cs}} e^{-n_{\mathrm{b}} \psi} \quad (3.33)$$

n_{p} is a scalar quantity representing the distance of the pivot stress ratio $\boldsymbol{r}_{\mathrm{p}}$ from the hydrostatic axis, defined as:

Ta-Ger B multi-axial equations
$$n_{\mathrm{p}} = \boldsymbol{n}{:}\,\boldsymbol{r}_{\mathrm{p}} \quad (3.34)$$
The hardening parameter n regulates the degree of coupling between the elastic and plastic components of the total strain increment. For monotonic loading, a constant value of n is typically adopted. For cyclic loading, n evolves according to:
$$n = n_{\mathrm{f}} + \left[n_{\mathrm{peak}} + \left(n_0 - n_{\mathrm{peak}}\right)e^{-\beta\Sigma \mathrm{d}\varepsilon_{\mathrm{q}}} - n_{\mathrm{f}}\right]e^{-\gamma\left(1-\mathrm{sign}\left(\Sigma\left\lvert \mathrm{d}\varepsilon_{\mathrm{p}}\right\rvert\right)\right)\Sigma \mathrm{d}\varepsilon_{\mathrm{q}}} \quad (3.35)$$
where n_0, n_{peak}, n_{f}, β and γ are input parameters, and $\Sigma \mathrm{d}\varepsilon_{\mathrm{q}}$ is the cumulative incremental deviatoric strain.
Load reversal criterion:
$$\mathrm{d}W = \left(\boldsymbol{r} - \boldsymbol{r}_{\mathrm{p}}\right){:}\,\dot{\boldsymbol{\varepsilon}} \quad (3.36)$$
where $\mathrm{d}W$ is the incremental first-order work, and $\dot{\boldsymbol{\varepsilon}}$ is the strain rate tensor. If $\mathrm{d}W$ changes sign, a load reversal is detected, and $\boldsymbol{r}_{\mathrm{p}}$ is updated using the current $\boldsymbol{r}$.

3.2.3 Prevost model

The Prevost model employs a family of nested, homothetic surfaces that are conical in principal stress space. These surfaces evolve through a purely deviatoric kinematic hardening rule, which governs their translation in stress space, and discretizes the plastic modulus to represent hardening. The innermost surface acts as the yield surface, while the outer surfaces, referred to as hardening surfaces, serve only to modulate the plastic modulus. The size of the elastic domain remains fixed, while plastic deformation is governed by the position and activation of the hardening surfaces. The current implementation differs from the original model (Prevost, 1985) only in that the volumetric flow is scaled by a scalar parameter, ψ, as described by Cerfontaine (2014). Table 3.3 summarizes the multi-axial constitutive equations of the Prevost model.

Table 3.3: Multi-axial constitutive equations of the Prevost model (Prevost, 1985).

Prevost multi-axial equations
Yield functions:
$$\mathrm{f}^i = \left(\boldsymbol{s} - p \cdot \boldsymbol{\alpha}^i\right){:}\left(\boldsymbol{s} - p \cdot \boldsymbol{\alpha}^i\right) - \frac{2}{3}\left(p \cdot M^i\right)^2 = 0 \quad (3.37)$$
where $\boldsymbol{s}$ and p are the deviatoric stress tensor and the mean effective stress, respectively. $\boldsymbol{\alpha}^i$ is the kinematic deviatoric stress tensor defining the centre of the ith surface in deviatoric space, and M^i is a parameter that controls the aperture of each surface.
Plastic flow rule:
$$\boldsymbol{P} = \boldsymbol{P}' + P'' \cdot \boldsymbol{\delta} \quad (3.38)$$

Prevost multi-axial equations

where $\boldsymbol{P'}$ is the deviatoric component of the plastic strain rate direction $\boldsymbol{P}$, and $P'' \cdot \boldsymbol{\delta}$ is the volumetric, non-associative component.

$$\boldsymbol{P'} = \boldsymbol{Q'} = \frac{2 \cdot (\boldsymbol{s} - p \cdot \boldsymbol{\alpha}^i)}{\left\| \frac{\partial f}{\partial \boldsymbol{\sigma}} \right\|} \tag{3.39}$$

where $\boldsymbol{Q'}$ is the deviatoric part of the second-order tensor $\boldsymbol{Q}$, which is the unit normal to the *i*th surface.

$$(P)'' = \frac{\psi}{3} \cdot \frac{\bar{\eta}^2 - \eta^2}{\bar{\eta}^2 + \eta^2} \text{ and } \eta = \frac{(3/2 \cdot \boldsymbol{s}:\boldsymbol{s})^{1/2}}{p} \tag{3.40}$$

where ψ is a parameter scaling the volumetric component of the plastic strain rate, and $\bar{\eta}$ is the stress ratio at which phase transformation occurs.

Hardening rule:

$$\mathrm{p}' \cdot \dot{\boldsymbol{\alpha}}^{\mathrm{i}} = \frac{\mathrm{H}^{i'}}{\mathbf{Q}' : \boldsymbol{\mu}^i} \cdot \langle \mathrm{L} \rangle \cdot \boldsymbol{\mu}^i \tag{3.41}$$

where $\mathrm{H}^{i'}$ is the plastic modulus associated with the active surface, L is the plastic multiplier (expressed using Macaulay brackets), and $\boldsymbol{\mu}^i$ is a tensor defining the direction of translation of the *i*th surface in the deviatoric space. An option for $\boldsymbol{\mu}^i$ is the Mroz translation rule, defined as:

$$\boldsymbol{\mu}^i = \frac{\mathrm{M}^{\mathrm{i+1}}}{\mathrm{M}^{\mathrm{i}}} \cdot \left(\boldsymbol{s} - p' \cdot \boldsymbol{\alpha}^i\right) - \left(\boldsymbol{s} - p' \cdot \boldsymbol{\alpha}^{i+1}\right) \tag{3.42}$$

where M^{i} and $\mathrm{M}^{\mathrm{i+1}}$ are the aperture parameters of the active and the adjacent outer surfaces, respectively. For $i = NYS$ (where NYS denotes the total number of yield surfaces and thus corresponds to the outermost surface) it is assumed that $\boldsymbol{\mu}^{NYS} = \mathbf{Q}'$.

Stiffness evolution:

$$X(p) = X_0 \cdot \left(\frac{p}{p_{ref}}\right)^m \text{ where } X = \{K, G, \mathrm{H}^{i'}\} \tag{3.43}$$

where X_0 is the reference value of the modulus at reference pressure p_{ref}, and m is a material exponent usually taken as 0.5. K and G denote the bulk and shear moduli respectively, and are linked throught the relation $K = 2G(1+\nu)/3(1-2\nu)$ by introducing a constant Poisson's ratio ν.

3.2.4 PIMSS (Parallel Iwan Multi-Surface Sand) model

3.2.4.1 Motivation for the development of PIMSS

The PIMSS model belongs to the broader class of multi-surface plasticity and is formulated based on the parallel Iwan approach. It was developed for practical design applications, with a focus on modelling the short-term cyclic response of OWT monopile foundations in sand. Its development was motivated by two main considerations: (i) the successful application of the parallel Iwan method to simulate monopile behaviour in clays under monotonic and cyclic lateral loading (Whyte *et al.*, 2020); and (ii) the strong predictive performance of the

Prevost model (Cerfontaine, 2014), prompting interest in a parallel variant that omits kinematic hardening.

3.2.4.2 Micro-model formulation

PIMSS is a parallel arrangement of several stationary micro-models, each incorporating the same yield surface, plastic potential, and elasticity as in the Prevost model implementation by Cerfontaine (2014). The yield surface equation of the *i*th micro-model is:

$$\mathrm{f}^i = \boldsymbol{s}^i : \boldsymbol{s}^i - \frac{2}{3}\left(p^i \cdot M^i\right)^2 = 0 \tag{3.44}$$

Here, $\boldsymbol{s}^i$ and p^i are the deviatoric stress tensor and the mean effective stress of the *i*th micro-model, respectively, and M^i defines the aperture of its yield surface. The incremental plastic strain direction $\boldsymbol{P}^i$ of each micro-model is split into a deviatoric component, which is associative, and a volumetric component, which is non-associative, as:

$$\boldsymbol{P}^i = (\boldsymbol{P}^i)' + (P^i)'' \cdot \boldsymbol{\delta} \tag{3.45}$$

$$\left(\boldsymbol{P}^i\right)' = \left(\boldsymbol{Q}^i\right)' = \frac{2 \cdot \boldsymbol{s}^i}{\left\|\frac{\partial f^i}{\partial \boldsymbol{\sigma}^i}\right\|} \tag{3.46}$$

$$(P^i)'' = \frac{\psi^i}{3} \cdot \frac{(\bar{\eta}^i)^2 - (\eta^i)^2}{(\bar{\eta}^i)^2 + (\eta^i)^2} \text{ and } \eta^i = \frac{(3/2 \cdot \boldsymbol{s}^i : \boldsymbol{s}^i)^{1/2}}{p^i} \tag{3.47}$$

where $(\boldsymbol{P}^i)'$ is the deviatoric component of the plastic strain rate direction, and $(P^i)'' \cdot \boldsymbol{\delta}$ its volumetric counterpart. $(\boldsymbol{Q}^i)'$ denotes the deviatoric part of the second-order tensor $\boldsymbol{Q}^i$, which defines the unit outer normal to the yield surface. The parameter ψ^i scales the volumetric component of the plastic strain rate, while $\bar{\eta}^i$ defines the stress ratio at which phase transformation occurs. The elastic stiffness of each micro-model varies with mean effective stress as:

$$G^i(p^i) = {G_0}^i \cdot \left(\frac{p^i}{p_{ref}}\right)^m \tag{3.48}$$

Here G^i is the shear stiffness, p_{ref} is a reference pressure, ${G_0}^i$ is the small-strain shear modulus at p_{ref} and m is typically taken as 0.5 for cohesionless soils (Prevost, 1985). K^i is obtained from $K = 2G(1+\nu)/3(1-2\nu)$ by introducing a constant Poisson's ratio ν.

3.2.4.3 Series versus parallel multi-surface plasticity approach

Before detailing the numerical implementation of PIMSS, it is important to clarify the distinction between the Prevost model and PIMSS, as both share the multi-surface plasticity framework but differ fundamentally in structure. Multi-surface plasticity was first conceived by Iwan (1966, 1967) and Mroz (1967, 1969), with Iwan proposing two distinct 1D models: the 'parallel-series' ('parallel Iwan') and 'series-parallel' ('series Mroz-Iwan') models, the latter of which was later extended into a 3D formulation. In this study the term 'series' refers to the 'series-parallel' configuration and specifically its 3D continuum extension, whereas 'parallel' is used to refer to 'parallel-series' respectively.

The Prevost model adopts a series formulation, where hardening is captured through the sequential activation and translation of nested yield surfaces aligned with the current stress point. The plastic modulus evolves accordingly, discretized by the activated surfaces. In contrast, PIMSS is a parallel formulation, comprising multiple stationary micro-models, each subjected to the same strain increment. Each micro-model responds independently, producing distinct stress contributions, with the overall macro-response obtained by averaging the weighted outputs. Thus, while a series model involves one model with many evolving surfaces, a parallel model is an assembly of individual micro-models with coexisting stress states. This key difference is illustrated in Figure 3.1, which compares a series configuration of three nested Drucker-Prager surfaces with a parallel configuration of three independent Drucker-Prager micro-models.

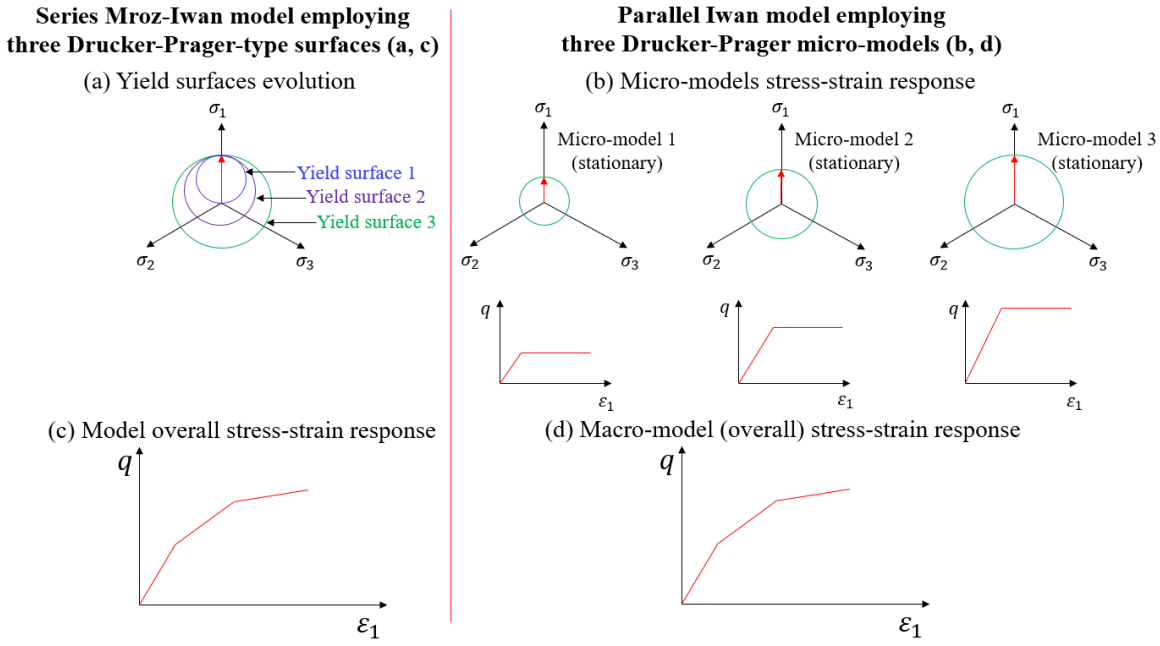

Figure 3.1: Triaxial compression stress path schematic comparing multi-surface plasticity configurations: (a, c) a series Mroz-Iwan model with three nested Drucker-Prager-type surfaces; (b, d) a parallel Iwan model composed of three stationary Drucker-Prager micro-models (modified from Whyte (2020)).

3.2.4.4 Multi-surface extension and numerical implementation

Since PIMSS is based on the parallel Iwan approach, the macro-stress tensor $\boldsymbol{\sigma}$ is computed as a weighted sum of the individual micro-stress tensors $\boldsymbol{\sigma}^i_{micro}$. For a given infinitesimal strain increment tensor $\delta\boldsymbol{\varepsilon}$, the corresponding macro-stress increment $\delta\boldsymbol{\sigma}$ is evaluated as:

$$\delta\boldsymbol{\sigma} = \sum_{i=1}^{n} w^i \cdot \delta\boldsymbol{\sigma}^i_{micro} \tag{3.49}$$

where n is the total number of micro-models and w^i is the weight corresponding to each, with the constraint $\sum_{i=1}^{n} w^i = 1$. The micro-stress increment is calculated as $\delta\boldsymbol{\sigma}^i_{micro} = D^i_{ep_{micro}}\delta\boldsymbol{\varepsilon}$, where $D^i_{ep_{micro}}$ is the elastoplastic stiffness matrix of the ith micro-model. A key advantage of this approach is that each micro-model is implemented as a single-surface plasticity model, simplifying the construction of the macro-model. This enables multi-surface formulations to be built around existing single-surface implementations with minimal additional coding, using a parallel Iwan 'wrapper' routine. The algorithm adopted in PIMSS, which organises micro-models incorporating the constitutive components

described in section 3.2.4.2, builds on the approach originally presented by Whyte (2020). The core steps of the algorithm are outlined below:

1. Enter the macro-model subroutine with the initial macro-stress state tensor $\boldsymbol{\sigma}_{initial}$, the total applied strain increment tensor $\Delta\boldsymbol{\varepsilon}$, the macro-state-variables array '*state_var*' (including the stress state $\boldsymbol{\sigma}^{i}_{micro,initial}$ of each micro model), and the input parameter array '*params*'. Initialize the micro-model counter: $i = 0$.
2. Repeat steps 3 to 7 for n micro-models (as initially specified), then exit the loop with updated macro-stress tensor ($\boldsymbol{\sigma}_{new}$).
3. Increment the counter $i = i + 1$.
4. Extract the material parameters and weight w^i corresponding to the ith micro-model from the '*params*' array and store them in a micro-model-specific array '*params_i*'. Retrieve the current micro-stress tensor ($\boldsymbol{\sigma}^{i}_{micro,initial}$) from the '*state_var*' array.
5. Call the micro-model subroutine with $\boldsymbol{\sigma}^{i}_{micro,initial}$, $\delta\boldsymbol{\varepsilon}$, and '*params_i*'. Exit with the micro-stress increment $\Delta\boldsymbol{\sigma}^{i}_{micro}$.
6. Update the micro-stress tensor using $\boldsymbol{\sigma}^{i}_{micro,new} = \boldsymbol{\sigma}^{i}_{micro,initial} + \Delta\boldsymbol{\sigma}^{i}_{micro}$, and store the updated value back in '*state_var*' array.
7. Update the macro-stress tensor using $\boldsymbol{\sigma}_{new} = \boldsymbol{\sigma}_{initial} + w^i\Delta\boldsymbol{\sigma}^{i}_{micro}$.

Figure 3.2 presents a parallel Iwan model composed of four perfectly elastoplastic Drucker-Prager micro-models under strain-controlled cyclic triaxial loading. Figure 3.2a illustrates the macro-model response, while Figure 3.2b shows the individual responses of the micro-models. Due to variations in strength parameters and assigned weights, the stress states of the micro-models from one another and from the macro-response, and may lie outside other micro-models' yield surfaces. Nonetheless, each micro-model independently satisfies its consistency condition, maintaining stress on its yield surface during plastic loading (Whyte

et al., 2020). This example highlights how a parallel assembly of simple elastoplastic micro-models, implemented via the present wrapper, can reproduce nonlinear hysteresis consistent with Masing-type behaviour without invoking any kinematic hardening rules.

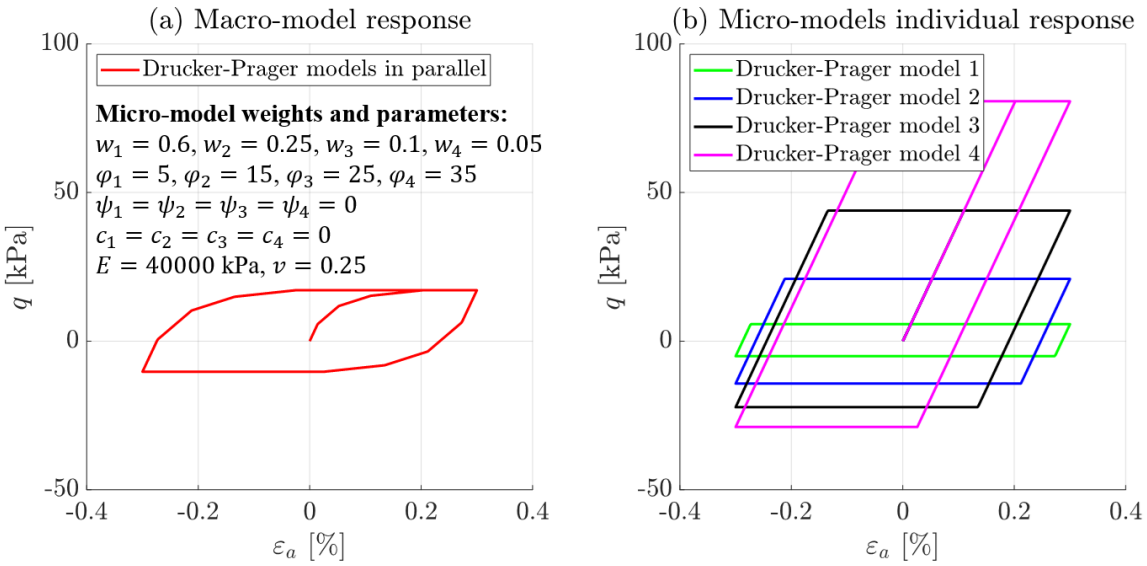

Figure 3.2: Example results from a two-way strain-controlled cyclic triaxial test showing: (a) the overall stress-strain behaviour of a parallel Iwan-type model composed of four Drucker-Prager micro-models, and (b) the individual contributions of each micro-model.

3.3 Comparative evaluation via element tests

To evaluate the performance of all four models, this study uses experimental data from laboratory tests conducted on Karlsruhe fine sand (Wichtmann and Triantafyllidis, 2016a; 2016b). Though not tailored to OWT foundations, this dataset is one of the few widely used for model development and validation in constitutive modelling. The comparison of PIMSS and Ta-Ger B (Tasiopoulou and Gerolymos, 2016a) with the original Prevost model (Prevost, 1985) and SANISAND DM04 (Dafalias and Manzari, 2004) serves multiple purposes: (i) to assess the effect of omitting kinematic hardening by comparing the parallel PIMSS model to the series-based Prevost model, both sharing the same constitutive ingredients; (ii) to benchmark all models against SANISAND DM04, a widely used CSSM-compatible model; and (iii) to guide the selection of the most suitable constitutive framework for further development and implementation in commercial 3D-FE software.

3.3.1 Parameter calibration

The experimental data employed for model assessment comprise monotonic drained, monotonic undrained, and cyclic undrained triaxial tests on Karlsruhe fine sand (Wichtmann and Triantafyllidis, 2016a; 2016b). These tests cover three relative density ranges: loose ($D_{\mathrm{r0}} = 15\% - 29\%$), medium-dense ($D_{\mathrm{r0}} = 57\% - 68\%$), and dense ($D_{\mathrm{r0}} = 85\% - 98\%$). As critical state-based models, SANISAND DM04 and Ta-Ger B utilise a single set of parameters across all densities and initial mean effective stresses. In contrast, the Prevost model and PIMSS require separate calibration for each density range, though their pressure-dependent formulations capture the influence of varying initial stress conditions.

In the following subsections, the calibration procedure and adopted parameter sets for each constitutive model are described. Where applicable, it is stated which experimental tests were used for parameter calibration and which simulations constitute independent model predictions. This distinction is maintained consistently to allow a transparent assessment of model performance.

3.3.1.1 SANISAND DM04 model parameters

The parameters adopted for SANISAND DM04 are listed in Table 3.4. This model has been previously calibrated for Karlsruhe fine sand in several studies (Wichtmann, 2016; Wichtmann et al., 2019; Duque et al., 2022), which report consistent values for the critical state, yield surface, and dilatancy parameters. Variations are observed in the elasticity, plastic modulus, and fabric-dilatancy parameters, depending on the specific test data targeted for calibration. In this study, parameters from Wichtmann (2016) were adopted, except for Poisson's ratio, which follows the lower value used by Wichtmann et al. (2019) and Duque et al. (2022), as a higher value was found to overestimate the dilative tendency of the samples under undrained loading. As noted in the cited works, certain parameters must be tailored to

the loading conditions. Thus, following Wichtmann (2016), different values were used for monotonic and cyclic simulations, with cyclic values shown in parentheses in Table 3.4.

The cyclic parameter values adopted here were derived in Wichtmann (2016) to reproduce the strain amplitudes, pore water pressure accumulation, and stress path evolution observed during a specific undrained cyclic triaxial test with an initial relative density of $D_{r0} = 94\%$ and an initial mean effective stress $p_{\mathrm{in}} = 200$ kPa. This test is also considered in the present study (see Figure 3.12). In the context of this chapter, the remaining cyclic simulations performed using these parameters are therefore treated as independent model predictions.

The monotonic parameter values were identified using monotonic drained triaxial tests reported within the same experimental programme. As the specific drained tests used for parameter identification are not explicitly distinguished in the literature, the adopted monotonic parameters are applied with due caution and their performance is interpreted accordingly. Monotonic undrained simulations presented herein are treated as independent model predictions, as these tests are not reported to have been used for calibration in Wichtmann (2016), whose parameter set is adopted in this study.

Table 3.4: SANISAND DM04 parameters for Karlsruhe fine sand (Wichtmann, 2016; Wichtmann, et al., 2019).

Critical state					**Yield surface**	**Elasticity**		**Plastic modulus**			**Dilatancy**		**Fabric-dilatancy**	
e_0 **[-]**	λ [-]	ξ [-]	M_{cs} [-]	M_e [-]	**m** [-]	G_0 [-]	ν [-]	h_0 [-]	c_h [-]	n_b [-]	A_0 [-]	n_d [-]	z_{max} [-]	c_z [-]
1.103	0.122	0.205	1.34	0.938	0.05	100 (130)	0.05	4.0 (20)	0.95 (0.70)	1.2	0.9	2.0	1.0 (20)	100 (5000)

3.3.1.2 Ta-Ger B model parameters

The parameters used for Ta-Ger B simulations are listed in Table 3.5. The calibration process is straightforward due to the model's structural similarities with SANISAND formulations, such as SANISAND DM04 (Dafalias and Manzari, 2004). Since Ta-Ger B adopts the same elastic formulation, critical state line (CSL), bounding surface, and phase transformation

equations, the corresponding parameters were taken directly from those adopted for SANISAND DM04. As with SANISAND DM04, the shear modulus used for monotonic simulations required slight adjustment to better reproduce the initial stiffness and strain amplitudes observed in undrained cyclic triaxial tests. For consistency, this adjustment was based on the same reference test used for SANISAND DM04 (see Figure 3.12), The modified cyclic value is shown in parentheses.

The only Ta-Ger B specific parameters, namely the dilatancy constant a and the hardening exponent n (assumed constant across all simulations), were estimated to achieve good agreement with experiments. Parameter a was calibrated against volumetric responses from drained triaxial tests on medium-dense sand ($D_{r0} = 57\% - 68\%$) (see Figure 3.4), while n was selected to provide a balanced fit across these tests and the corresponding undrained responses within a similar density range ($D_{r0} = 57\% - 68\%$) (see Figure 3.7). All remaining simulations presented are therefore treated as independent model predictions.

Table 3.5: Ta-Ger B parameters for Karlsruhe fine sand.

Critical state				**Elasticity**			**Bounding surface**	**Dilatancy**		**Hardening exponent**
e_0 **[-]**	λ [-]	ξ [-]	M_{cs} [-]	G_0 [-]	ν [-]	m [-]	n_b [-]	a [-]	n_d [-]	n [-]
1.103	0.122	0.205	1.34	100 (130)	0.05	0.5	1.2	0.3	2.0	0.15

3.3.1.3 Prevost model parameters

The calibrated parameters for the Prevost model are listed in Table 3.6-Table 3.8, following the methodology proposed by Prevost (1985). The surface-specific parameters M, H' and α were calibrated using drained triaxial compression tests at an initial mean effective pressure of 100 kPa for each density range, with the corresponding test results shown in Figure 3.3, Figure 3.4, and Figure 3.5. Experimental stress-strain curves were approximated by linear segments, each representing a constant plastic modulus H', with the number of segments

matching the number of yield surfaces. Once H' values were set, the upper and lower bounds of each surface in terms of the stress ratio $\eta = {}^{q}/_{p}$ were identified to compute M and α. The upper bounds, η_c, were assumed to correspond to transition points between segments on the compression curve. Due to lack of drained extension data, lower bounds η_e were assumed as $\eta_e = 0.60 \cdot \eta_c$, using a fictitious extension curve. The elastic shear modulus G_0 was estimated as the secant stiffness from the initial, nearly elastic, portion of the $\varepsilon_a - q$ curve of the same drained triaxial tests, given the lack of bender element or local strain data.

Ideally, accurate volumetric predictions would require the parameter $\bar{\eta}$ to be defined at the onset of dilation. In practice, however, $\bar{\eta}$ was adjusted by trial and error to fit drained and undrained responses under both monotonic and cyclic loading. A similar trial-and-error approach was adopted for the calibration of the parameter ψ. For the medium-dense density range ($D_{\mathrm{r0}} = 57\% - 68\%$), the present study utilised a relatively broader experimental basis, including monotonic drained triaxial tests at five different initial mean effective stress levels (see Figure 3.4), monotonic undrained tests at four different p_{in} levels (see Figure 3.7), and cyclic undrained tests at two different p_{in} levels (see Figure 3.10 and Figure 3.11). The adopted values of $\bar{\eta}$ and ψ therefore reflect an averaged representation of the model response across these loading conditions, with particular emphasis on achieving optimal behaviour at $p_{\mathrm{in}} = 100$ kPa, which is common to all three loading conditions.

For the loose ($D_{\mathrm{r0}} = 15\% - 29\%$) and dense ($D_{\mathrm{r0}} = 85\% - 98\%$) density ranges, the availability of undrained monotonic and cyclic test data is more limited. Consequently, for these density ranges and loading conditions, the separation between calibration and prediction is less sharply defined. This is not the case for monotonic drained conditions, where, apart from the drained triaxial compression tests at initial mean effective pressures of 100 and 200 kPa used directly for calibration at each density range, the remaining

monotonic drained simulations may be regarded as independent evaluations of model performance. While this aspect should be borne in mind when interpreting the predictive capability of the Prevost model, response-based calibration is intrinsic to non-critical-state-based plasticity formulations, which are inherently fitted to experimental responses.

Table 3.6: Prevost parameters for Karlsruhe fine sand with a relative density D_{r0} in the range of 15 to 29%.

Surface	**1**	**2**	**3**	**4**	**5**	**6**	**7**	**8**	**Global**	
M **[-]**	0.033	0.266	0.324	0.396	0.569	0.723	0.94	1.026	G_0 **[MPa]**	K_0 **[MPa]**
H' **[MPa]**	30	28	18	10	2	1.1	0.3	0.2	20	13.3
α **[-]**	0.006	0.047	0.057	0.07	0.101	0.128	0.166	0.181		
Surface	**9**	**10**	**11**	**12**	**13**	**14**	**15**		**Global**	
M **[-]**	1.075	1.103	1.121	1.136	1.146	1.153	1.158		$\bar{\eta}$ **[-]**	ψ **[-]**
H' **[MPa]**	0.1	0.09	0.08	0.05	0.03	0.01	0.001		1.2	0.4
α **[-]**	0.19	0.195	0.198	0.20	0.202	0.203	0.204			

Table 3.7: Prevost parameters for Karlsruhe fine sand with a relative density D_{r0} in the range of 57 to 68%.

Surface	**1**	**2**	**3**	**4**	**5**	**6**	**7**	**8**	**Global**	
M **[-]**	0.074	0.178	0.546	0.744	0.838	0.906	1.018	1.114	G_0 **[MPa]**	K_0 **[MPa]**
H' **[MPa]**	70	22	15	8	3	2	0.9	0.6	30	20
α **[-]**	0.019	0.045	0.137	0.186	0.209	0.227	0.255	0.278		
Surface	**9**	**10**	**11**	**12**	**13**	**14**	**15**		**Global**	
M **[-]**	1.165	1.201	1.222	1.236	1.244	1.249	1.25		$\bar{\eta}$ **[-]**	ψ **[-]**
H' **[MPa]**	0.3	0.25	0.2	0.1	0.05	0.01	0.001		1.19	0.8
α **[-]**	0.291	0.3	0.305	0.309	0.311	0.312	0.312			

Table 3.8: Prevost parameters for Karlsruhe fine sand with a relative density D_{r0} in the range of 85 to 95%.

Surface	**1**	**2**	**3**	**4**	**5**	**6**	**7**	**8**	**Global**	
M **[-]**	0.113	0.487	0.721	0.886	1.001	1.084	1.147	1.197	G_0 **[MPa]**	K_0 **[MPa]**
H' **[MPa]**	200	25	15	8	5	4	3	1.5	45	30
α **[-]**	0.02	0.086	0.127	0.156	0.177	0.191	0.203	0.211		
Surface	**9**	**10**	**11**	**12**	**13**	**14**	**15**		**Global**	
M **[-]**	1.302	1.381	1.425	1.451	1.462	1.468	1.468		$\bar{\eta}$ **[-]**	ψ **[-]**
H' **[MPa]**	0.7	0.5	0.2	0.1	0.1	0.05	0.001		1	0.6
α **[-]**	0.23	0.244	0.251	0.256	0.258	0.259	0.259			

3.3.1.4 PIMSS model parameters

The calibrated parameters for PIMSS are shown in Table 3.9-Table 3.11. Due to the inherent flexibility of the parallel Iwan framework, a model based on this approach can be calibrated to fit a backbone curve in a variety of ways. Two common strategies are: (i) distributing strength and stiffness among micro-models with equal weightings (Kaklamanos, Dorfmann

and Baise, 2015), or (ii) keeping stiffness constant across all micro-models while varying the weights and strength parameters (Whyte *et al.*, 2020). This study adopts the first strategy.

For all density ranges, the strength and stiffness parameters were distributed among micro-models to match the experimental backbone curves from drained triaxial tests at an initial mean effective pressure of 100 kPa. These are the same tests used for the calibration of the monotonic parameters of the Prevost model (see section 3.3.1.4). While conceptually similar to the Prevost calibration procedure, the PIMSS calibration is more elaborate due to the need to coordinate the response across multiple micro-models.

Regarding the volumetric response parameters $\bar{\eta}^i$ and ψ^i, micro-models were divided into two groups across all three density ranges. Micro-models 1-6 were assigned values that promote a purely contractive response, while micro-models 7-15 were calibrated to exhibit a milder initial contraction followed by a more pronounced dilative behaviour. This combination yielded the desired monotonic behaviour, with the assigned values calibrated to provide an average fit to the responses observed in monotonic undrained and drained triaxial tests. As shown in Table 3.9-Table 3.11, $\bar{\eta}^i$ and ψ^i were further adjusted for certain cyclic simulations. The modified values are indicated in parentheses for $\bar{\eta}^i$ in all tables, and for ψ^i in Table 3.10 only.

Due to the density-dependent nature of the PIMSS formulation, and because the parameters $\bar{\eta}^i$ and ψ^i were obtained through response-based fitting using the same limited set of undrained monotonic and cyclic tests employed for the Prevost model, the distinction between calibration and prediction is likewise not strictly delineated for PIMSS. Consequently, some parameters reflect an averaged representation of the experimental response rather than a strict point-wise prediction. This aspect should therefore be borne in mind when interpreting the PIMSS model response.

Table 3.9: PIMSS parameters for Karlsruhe fine sand with a relative density D_{r0} in the range of 15 to 29%.

Surface	**1**	**2**	**3**	**4**	**5**	**6**	**7**	**8**	**Micro-models 1-6**	
$\boldsymbol{w^i}$ **[-]**	0.062	0.067	0.067	0.067	0.067	0.067	0.067	0.067	$\boldsymbol{\bar{\eta}^i}$ **[-]**	$\boldsymbol{\psi^i}$ **[-]**
$\boldsymbol{M^i}$ **[-]**	0.108	0.196	0.293	0.414	0.647	0.75	0.818	1.04	$1.5M^i$	0.9
$\boldsymbol{G_0{}^i}$ **[MPa]**	25	23.33	21.67	20	18.33	16.67	15	13.31	$(3M^i)$	
Surface	**9**	**10**	**11**	**12**	**13**	**14**	**15**		**Micro-models 7-15**	
$\boldsymbol{w^i}$ **[-]**	0.067	0.067	0.067	0.067	0.067	0.067	0.067		$\boldsymbol{\bar{\eta}^i}$ **[-]**	$\boldsymbol{\psi^i}$ **[-]**
$\boldsymbol{M^i}$ **[-]**	1.235	1.4	1.65	1.8	1.9	2	2.15		$0.65M^i$	0.9
$\boldsymbol{G_0{}^i}$ **[MPa]**	11.67	10	8.33	6.67	5	3.33	1.67		$(2M^i)$	

Table 3.10: PIMSS parameters for Karlsruhe fine sand with a relative density D_{r0} in the range of 57 to 68%.

Surface	**1**	**2**	**3**	**4**	**5**	**6**	**7**	**8**	**Micro-models 1-6**	
$\boldsymbol{w^i}$ **[-]**	0.062	0.067	0.067	0.067	0.067	0.067	0.067	0.067	$\boldsymbol{\bar{\eta}^i}$ **[-]**	$\boldsymbol{\psi^i}$ **[-]**
$\boldsymbol{M^i}$ **[-]**	0.124	0.211	0.4	0.64	0.838	1.0	1.2	1.4	$2M^i$	1.7
$\boldsymbol{G_0{}^i}$ **[MPa]**	37	34	33	32	30	28	25	20	$(2.5M^i)$	(0.9)
Surface	**9**	**10**	**11**	**12**	**13**	**14**	**15**		**Micro-models 7-15**	
$\boldsymbol{w^i}$ **[-]**	0.067	0.067	0.067	0.067	0.067	0.067	0.067		$\boldsymbol{\bar{\eta}^i}$ **[-]**	$\boldsymbol{\psi^i}$ **[-]**
$\boldsymbol{M^i}$ **[-]**	1.5	1.6	1.8	2.0	2.05	2.15	2.3		$0.5M^i$	1.1
$\boldsymbol{G_0{}^i}$ **[MPa]**	19	17	15	13	10	7	5		$(1.3M^i)$	(0.9)

Table 3.11: PIMSS parameters for Karlsruhe fine sand with a relative density D_{r0} in the range of 85 to 95%.

Surface	**1**	**2**	**3**	**4**	**5**	**6**	**7**	**8**	**Micro-models 1-6**	
$\boldsymbol{w^i}$ **[-]**	0.062	0.067	0.067	0.067	0.067	0.067	0.067	0.067	$\boldsymbol{\bar{\eta}^i}$ **[-]**	$\boldsymbol{\psi^i}$ **[-]**
$\boldsymbol{M^i}$ **[-]**	0.21	0.37	0.55	0.75	1.07	1.2	1.3	1.55	$1.5M^i$	1.0
$\boldsymbol{G_0{}^i}$ **[MPa]**	50	46.67	43.33	40	36.67	33.33	30	26.67	$(3M^i)$	
Surface	**9**	**10**	**11**	**12**	**13**	**14**	**15**		**Micro-models 7-15**	
$\boldsymbol{w^i}$ **[-]**	0.067	0.067	0.067	0.067	0.067	0.067	0.067		$\boldsymbol{\bar{\eta}^i}$ **[-]**	$\boldsymbol{\psi^i}$ **[-]**
$\boldsymbol{M^i}$ **[-]**	1.75	1.875	2	2.1	2.15	2.25	2.35		$0.35M^i$	1.0
$\boldsymbol{G_0{}^i}$ **[MPa]**	23.33	20	18	15	12	8	6		$(1.05M^i)$	

3.3.2 Monotonic triaxial tests

3.3.2.1 Drained conditions

Figure 3.3-Figure 3.5 show simulations of monotonic drained triaxial compression tests on Karlsruhe fine sand across three relative density ranges under varying initial stresses (mean effective stresses, p_{in}, of 50, 100, 200, 300 and 400 kPa). Figure 3.3 corresponds to loose samples ($15\% \leq D_{r0} \leq 25\%$), Figure 3.4 to medium-dense ($57\% \leq D_{r0} \leq 68\%$), and Figure 3.5 to dense ($85\% \leq D_{r0} \leq 95\%$).

In terms of stress-strain response, all models capture the general trend of increasing shear strength with confining pressure. Pre-peak stiffness is reasonably reproduced, especially at

lower p_{in} ($50 - 200$ kPa), though slightly underestimated at higher p_{in} ($300 - 400$ kPa). At these higher p_{in}, Ta-Ger B and SANISAND DM04 also slightly underestimate peak strength, particularly in medium-dense (Figure 3.4) and dense (Figure 3.5) samples. The Prevost and PIMSS models more closely match the peak but lack a strain-softening mechanism essential for reproducing post-peak behaviour in denser sands. As a result, they must be calibrated either to match peak strength, overestimating at large strains, or to capture residual strength, underestimating the peak. This trade-off reduces their predictive flexibility, producing conservative outcomes in the former case and unconservative outcomes in the latter. Because these biases are inherently strain-dependent, calibration for design applications requires careful consideration of the strain range relevant to the problem.

In terms of volumetric behaviour, SANISAND DM04 and Ta-Ger B generally outperform the multi-surface models, which tend to overpredict contraction or dilation depending on initial relative density. For loose samples (Figure 3.3), PIMSS significantly overestimates contraction. In medium-dense (Figure 3.4) and dense (Figure 3.5) samples, where contraction is followed by marked dilation, only Ta-Ger B and SANISAND DM04 accurately capture this trend. Although the Prevost and PIMSS models reproduce a reasonable contractive-dilative transition, they fail to suppress dilation at large strains and therefore cannot capture the progression toward a terminal void ratio and corresponding density, reflecting their incompatibility with the principles of CSSM.

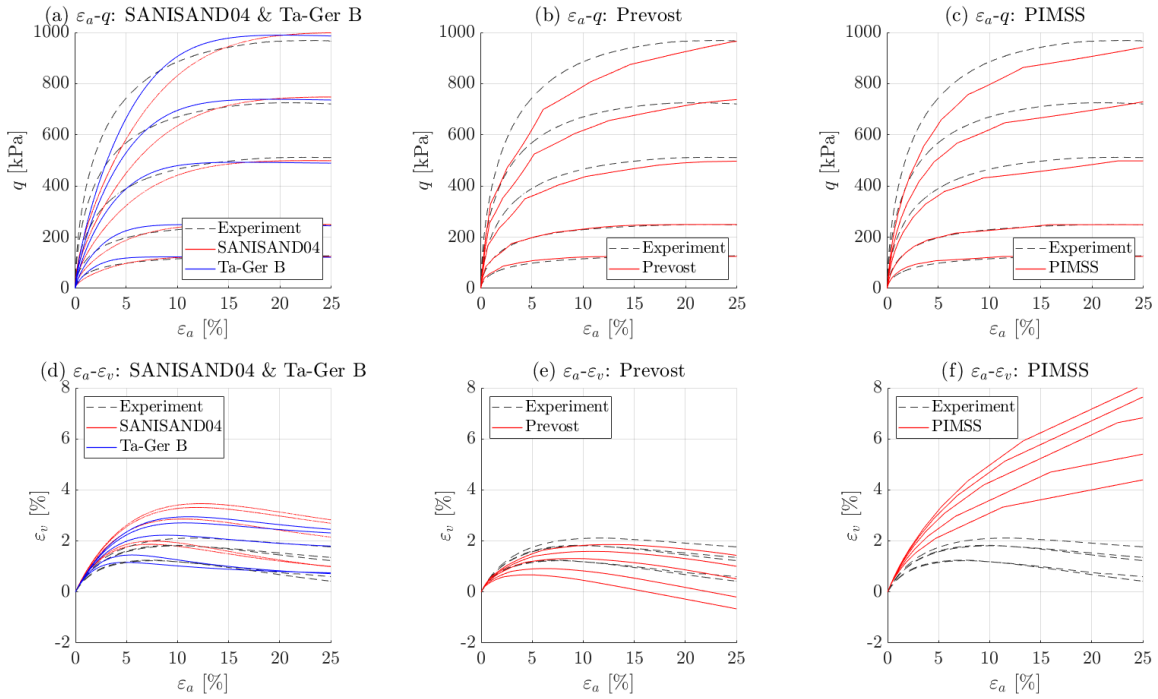

Figure 3.3: Simulations of drained monotonic triaxial tests on loose samples ($15\% \leq D_{r0} \leq 25\%$) with different initial stresses (mean effective stresses, p_{in}, of 50, 100, 200, 300 and 400 kPa): a,d) Prevost, b,e) PIMSS, c,f) SANISAND04 and Ta-Ger B.

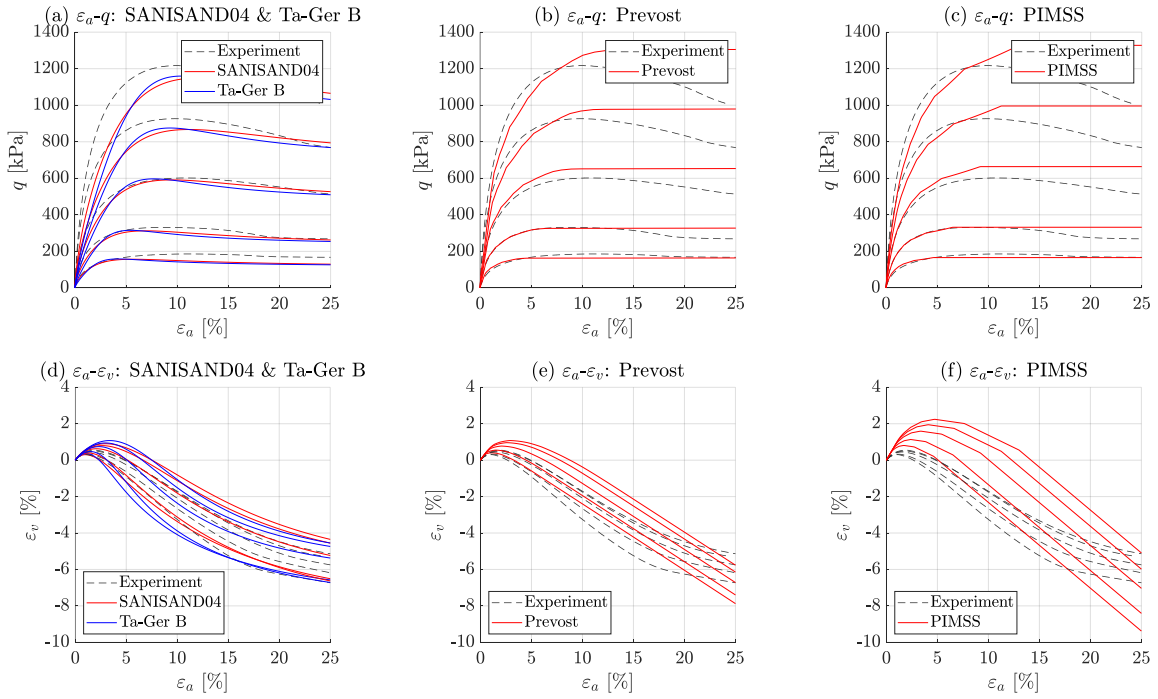

Figure 3.4: Simulations of drained monotonic triaxial tests on medium-dense samples ($57\% \leq D_{r0} \leq 68\%$) with different initial stresses (mean effective stresses, p_{in}, of 50, 100, 200, 300 and 400 kPa): a,d) Prevost, b,e) PIMSS, c,f) SANISAND04 and Ta-Ger B.

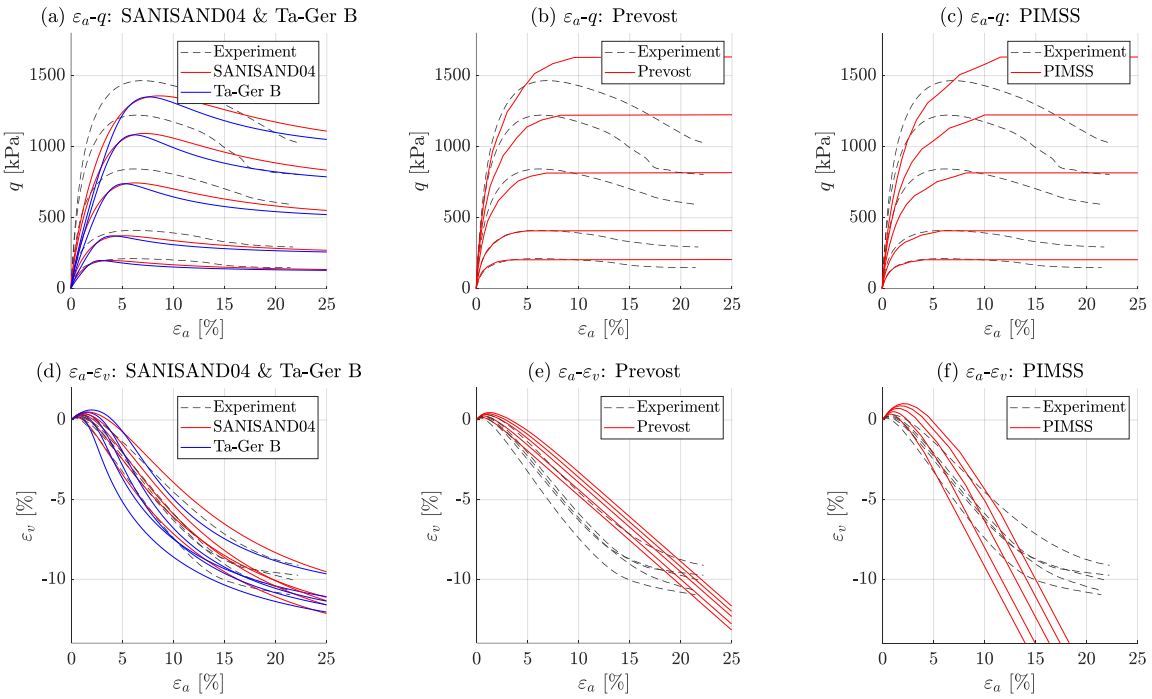

Figure 3.5: Simulations of drained monotonic triaxial tests on dense samples ($85\% \leq D_{r0} \leq 95\%$) with different initial stresses (mean effective stresses, p_{in}, of 50, 100, 200, 300 and 400 kPa): a,d) Prevost, b,e) PIMSS, c,f) SANISAND04 and Ta-Ger B.

3.3.2.2 Undrained conditions

Figure 3.6-Figure 3.8 show simulations of monotonic undrained triaxial compression tests on Karlsruhe fine sand at three relative density ranges. Figure 3.6 presents results for a loose sample ($D_{r0} = 29\%$) tested at an initial mean effective stress, p_{in}, of 200 kPa, Figure 3.7 for medium-dense samples ($57\% \leq D_{r0} \leq 68\%$) tested under varying initial stresses (mean effective stresses, p_{in}, of 100, 200, 300 and 400 kPa), and Figure 3.8 for a dense sand sample ($D_{r0} = 87\%$), tested at an initial mean effective stress, p_{in}, of 200 kPa.

Overall, all four models reproduce the stress-strain behaviour reasonably well and broadly align with experimental trends, capturing the general characteristics of the response with reasonable quantitative accuracy and qualitative agreement. Most discrepancies between the predictions and the experiments are attributable to differences in the gradients of the stress-strain curves, and consequently in the corresponding stiffness. While none achieves a perfect match, all provide satisfactory results across the full range of densities and initial mean effective stresses.

Regarding stress paths, all models capture the overall trends across all density levels. The main discrepancies lie in the predicted tendencies of the sand to contract or dilate, reflected in the development of positive or negative excess pore pressures, respectively. The Prevost and PIMSS models generally underpredict contraction and overpredict dilation, especially in the loose sample. PIMSS also consistently overestimates the slopes of the $p - q$ curves across all densities, while the Prevost model shows similar overestimation in the medium-dense and dense cases, though to a lesser extent. In contrast, SANISAND DM04 and Ta-Ger B closely match both the shape and curvature of the experimental paths, demonstrating superior ability to capture phase transformation.

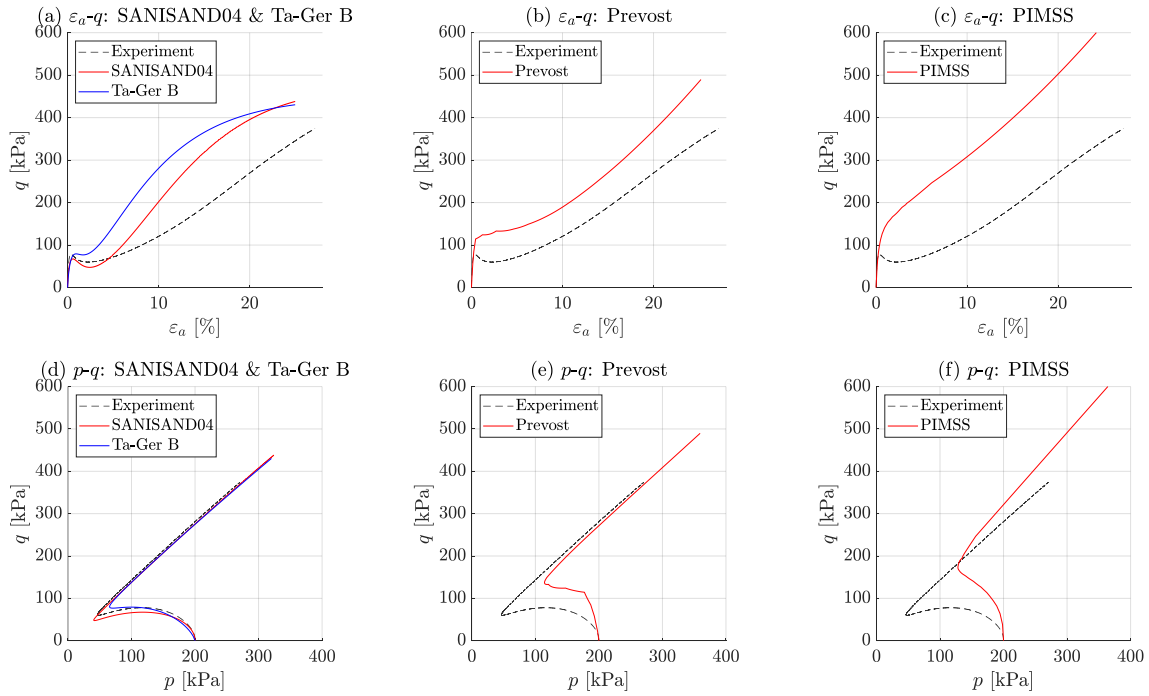

Figure 3.6: Simulations of undrained monotonic triaxial test on loose sample ($D_{r0} = 29\%$) with initial mean effective stress, p_{in}, of 200 kPa: a,d) Prevost, b,e) PIMSS, c,f) SANISAND04 and Ta-Ger B.

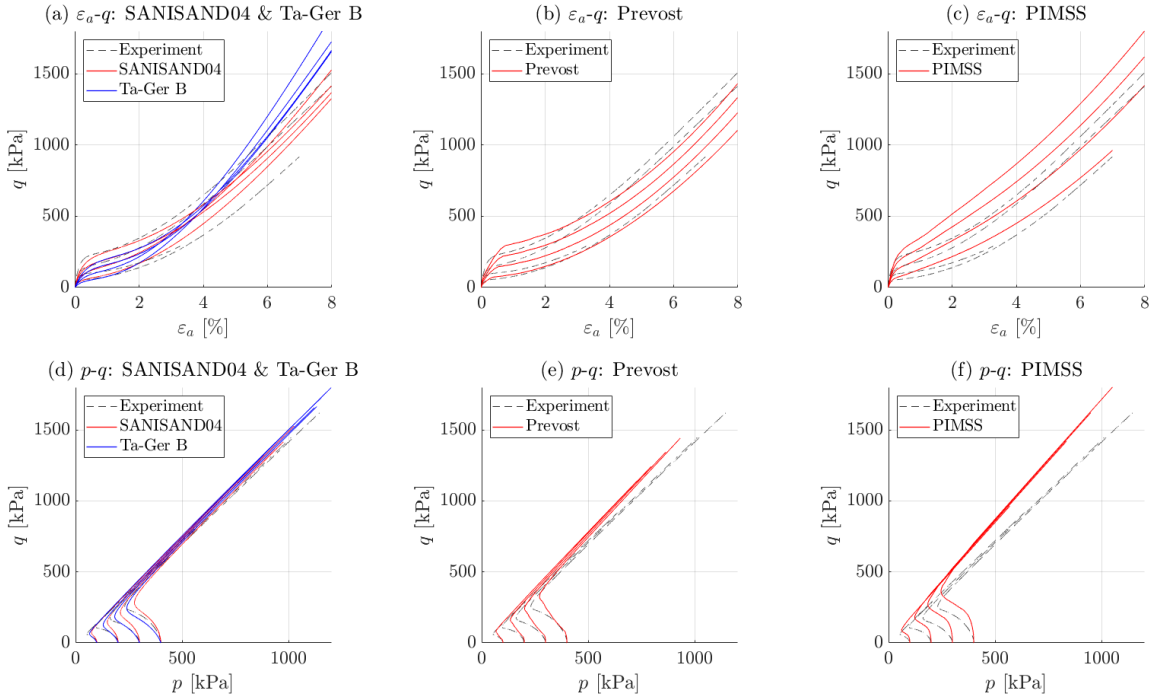

Figure 3.7: Simulations of undrained monotonic triaxial tests on medium-dense samples ($60\% \leq D_{r0} \leq 64\%$) with different initial stresses (mean effective stresses, p_{in}, of 100, 200, 300 and 400 kPa): a,d) Prevost, b,e) PIMSS, c,f) SANISAND04 and Ta-Ger B.

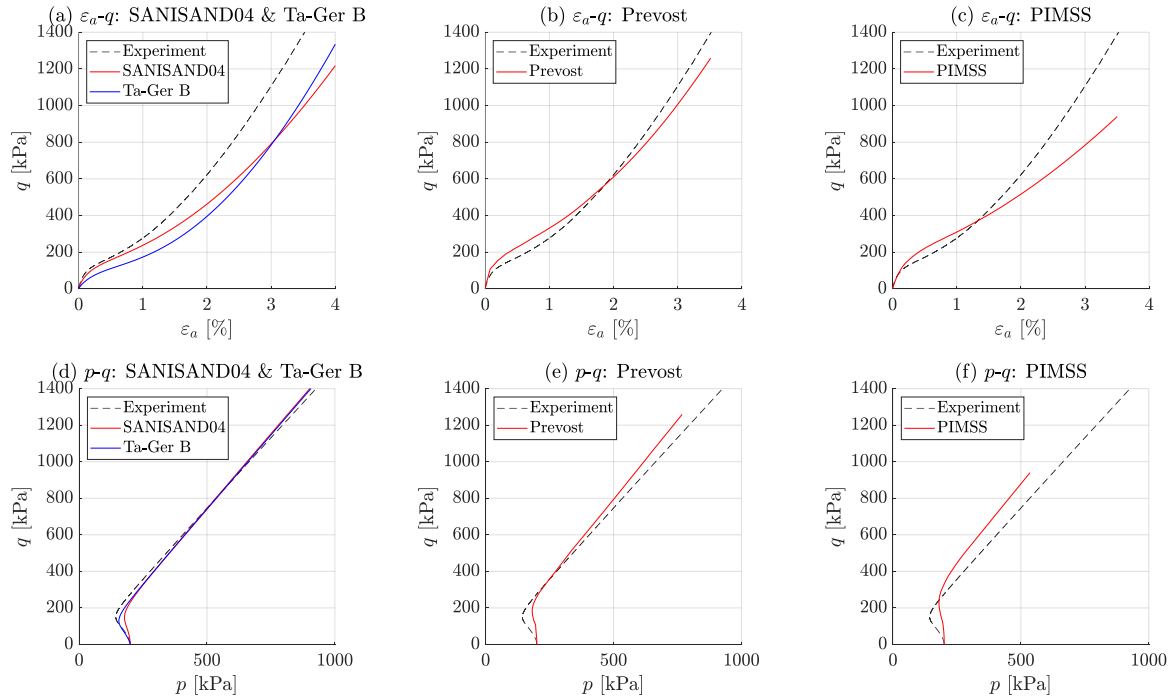

Figure 3.8: Simulations of undrained monotonic triaxial test on dense sample ($D_{r0} = 87\%$) with initial mean effective stress, p_{in}, of 200 kPa: a,d) Prevost, b,e) PIMSS, c,f) SANISAND04 and Ta-Ger B.

3.3.3 Undrained cyclic triaxial tests

Figure 3.9-Figure 3.12 present simulations of strain-controlled cyclic undrained triaxial tests on Karlsruhe fine sand at three relative density ranges, all conducted under large cyclic strain

amplitudes. Each test was performed with a constant axial strain amplitude ($\varepsilon_1^{ampl.}$). Figure 3.9 presents a loose sample ($D_{r0} = 29\%$) tested at an initial mean effective stress, p_{in}, of 200 kPa. Figure 3.10 and Figure 3.11 correspond to medium-dense samples ($D_{r0} = 64\%$ and $D_{r0} = 63\%$) tested at p_{in} of 100 kPa and 200 kPa, respectively. Figure 3.12 shows a dense sample ($D_{r0} = 94\%$) tested at p_{in} of 200 kPa.

To evaluate the ability of the models to capture the cyclic behaviour observed in the tests, a set of key performance criteria is adopted. These are: (i) the extent of cyclic stiffness degradation, observed as a progressive decrease in the slope of the stress-strain curves and hence flattening of the loops with increasing cycles; (ii) the progressive reduction of deviatoric stress amplitude ($q^{ampl.}$) with increasing cycles; (iii) the ability to reach the liquefaction state in $p - q$ space ($p = q = 0$), which as noted by Duque et al. (2022) acts as an attractor of the stress path due to pore pressure build-up; (iv) the number of cycles required to reach this state; and (v) the representation of the contractive-dilative transition, typically most pronounced near the origin and especially in medium-dense and dense samples, where it manifests as butterfly-shaped stress paths.

Figure 3.9-Figure 3.12 (subplots a-c) show the evolution of stress-strain loops during cyclic loading, allowing assessment of criteria (i) and (ii). Ta-Ger B and the Prevost model most consistently capture stiffness degradation and the reduction in $q^{ampl.}$ across all densities, as indicated by the progressive flattening of the stress-strain loops over successive cycles. However, both models retain significant residual stiffness in the dense sample, with deviatoric stress amplitudes remaining above experimental levels (Figure 3.12a, b). Ta-Ger B also underperforms in one medium-dense case (Figure 3.10a). PIMSS does not capture the degradation trend, maintaining steep stress-strain loops and elevated deviatoric stress amplitudes across all densities (subplots c of Figure 3.9-Figure 3.12). SANISAND DM04

performs poorest, consistently overpredicting $q^{ampl.}$ with only limited reduction across cycles. This shortcoming is evident for all densities resulting in notable discrepancies with the experiments despite the model having been calibrated specifically for the dense case.

The excessive hardening predicted by SANISAND DM04 during the first quarter cycle, particularly evident in Figure 3.9 and Figure 3.10, is primarily governed by parameters controlling the elastic-plastic transition during initial loading. In strain-controlled cyclic tests, the initial loading phase is effectively quasi-monotonic, and the response during this stage is highly sensitive to the elastic stiffness and plastic modulus parameters, notably G_0 and h_0. Variations in these parameters strongly affect the slope of the stress-strain response during the first cycle, whereas their influence diminishes in subsequent cycles. A reduction of the plastic modulus parameter h_0 would be expected to soften the initial elastic-plastic transition and reduce the excessive hardening observed during the first quarter cycle. Consequently, the overprediction of $q^{ampl.}$ observed in the first cycle should be interpreted as a calibration-transfer effect. While a dedicated recalibration could improve first-cycle agreement, it would not necessarily enhance predictions of cyclic degradation or stress path evolution and therefore does not affect the overall comparative conclusions of this study.

Figure 3.9-Figure 3.12 (subplots d-f) show the evolution stress paths in $p - q$ space, used to assess criteria (iii) to (v). Among the four models, only PIMSS fails to reach liquefaction ($p = q = 0$) (criterion iii), as its stress loops stagnate at a minimum mean effective stress and remain locked-up. The other three models successfully predict liquefaction, but their estimates differ from the experiments in terms of the number of cycles required (criterion iv). For the loose (Figure 3.9d-f) and the medium-dense samples (Figure 3.10d-f and Figure 3.11d-f), predictions are generally closer to the experimental results, with Prevost being the most accurate overall. For the dense sample (Figure 3.12d-f), all three models predict liquefaction prematurely, underestimating the number of cycles needed. Criterion (v)

addresses the contractive-dilative transition, reflected in changes in pore pressure and corresponding shifts in mean effective stress. Prevost captures this behaviour well during early loading but underestimates dilation near the origin, often failing to reproduce the full butterfly-shaped stress paths (Figure 3.10b-Figure 3.12b). Ta-Ger B tends to exaggerate dilation, particularly in the loose and medium-dense cases (Figure 3.9, Figure 3.10). SANISAND DM04 consistently overpredicts dilation across all densities, producing butterfly-shaped paths even in loose sand, which is inconsistent with experimental trends.

Such deviations between simulations and cyclic test results are well documented for other constitutive frameworks (Wichtmann et al., 2019; Duque et al., 2022). Even when partially addressed, improvements often require additional parameters and mechanisms tailored to specific behaviours. While all models evaluated have limitations, Ta-Ger B demonstrates the most robust overall performance, capturing stiffness degradation and realistic stress path evolution across varying relative densities using a single set of parameters.

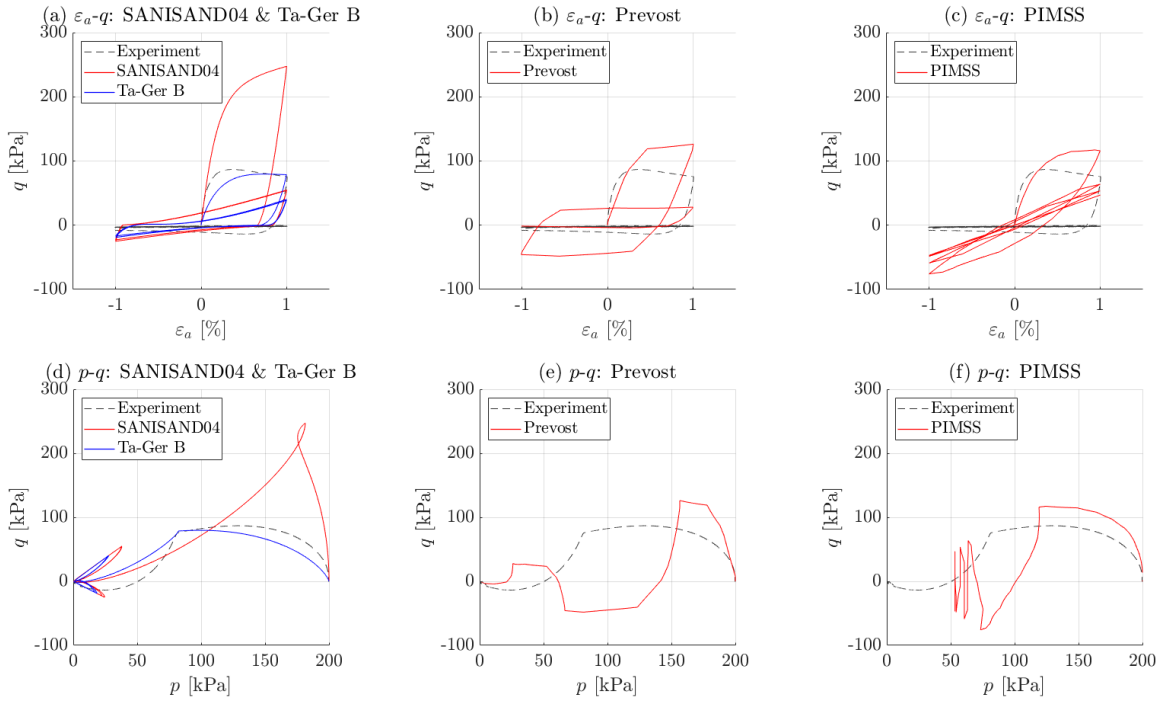

Figure 3.9: Simulations of an undrained cyclic triaxial test on loose sample ($D_{r0} = 29\%$) with isotropic consolidation (initial mean effective stress, p_{in}, of 200 kPa) large-amplitude strain cycles ($\varepsilon_1^{ampl.} = 1 \cdot 10^{-2}$): a,d) Prevost, b,e) PIMSS, c,f) SANISAND04 and Ta-Ger B.

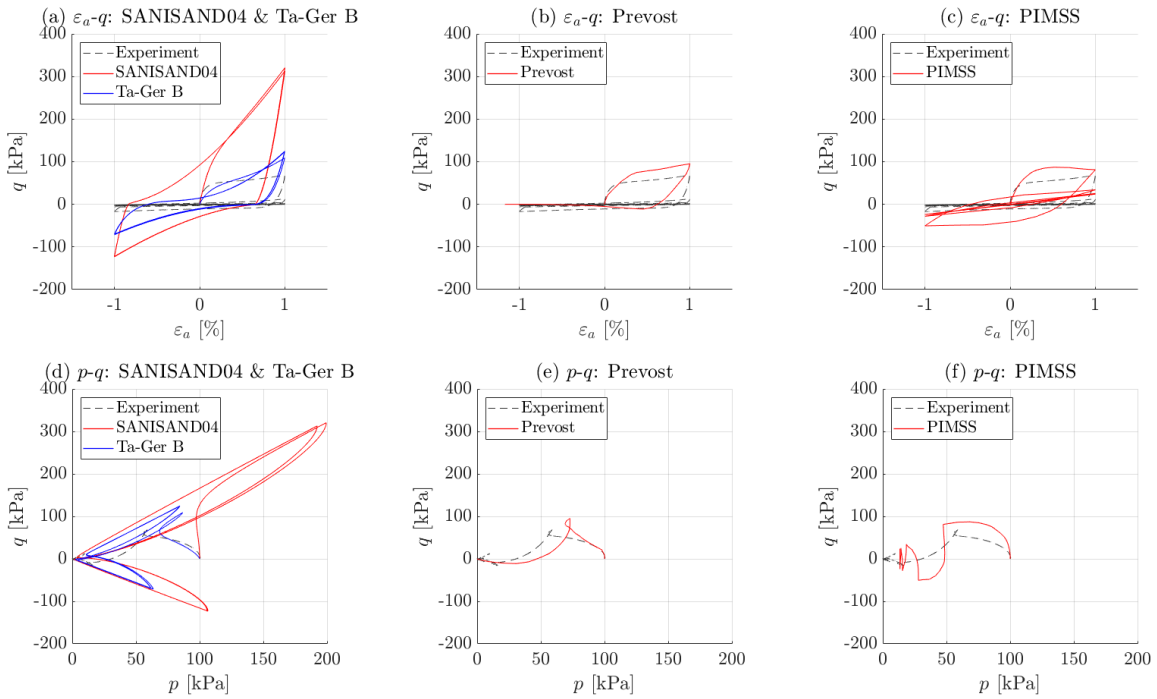

Figure 3.10: Simulations of an undrained cyclic triaxial test on medium-dense sample ($D_{r0} = 64\%$) with isotropic consolidation (initial mean effective stress, p_{in}, of 100 kPa) large-amplitude strain cycles ($\varepsilon_1^{ampl.} = 1 \cdot 10^{-2}$): a,d) Prevost, b,e) PIMSS, c,f) SANISAND04 and Ta-Ger B.

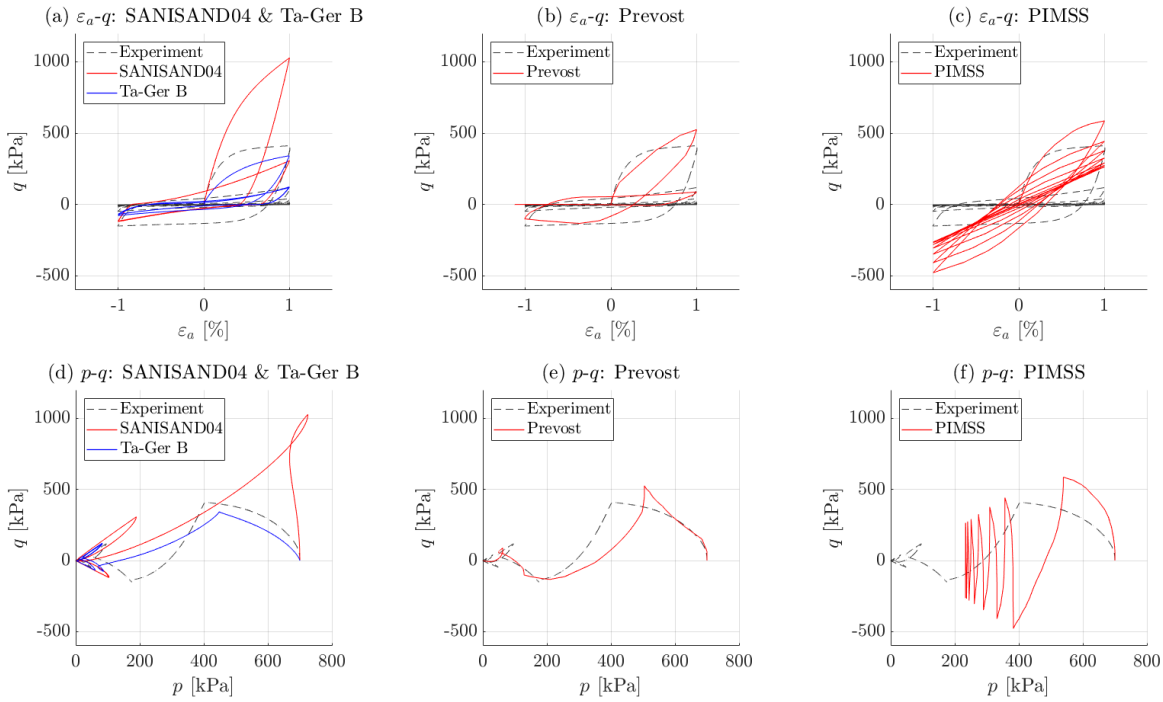

Figure 3.11: Simulations of an undrained cyclic triaxial test on medium-dense sample ($D_{r0} = 63\%$) with isotropic consolidation (initial mean effective stress, p_{in}, of 200 kPa) large-amplitude strain cycles ($\varepsilon_1^{ampl.} = 5 \cdot 10^{-3}$): a,d) Prevost, b,e) PIMSS, c,f) SANISAND04 and Ta-Ger B.

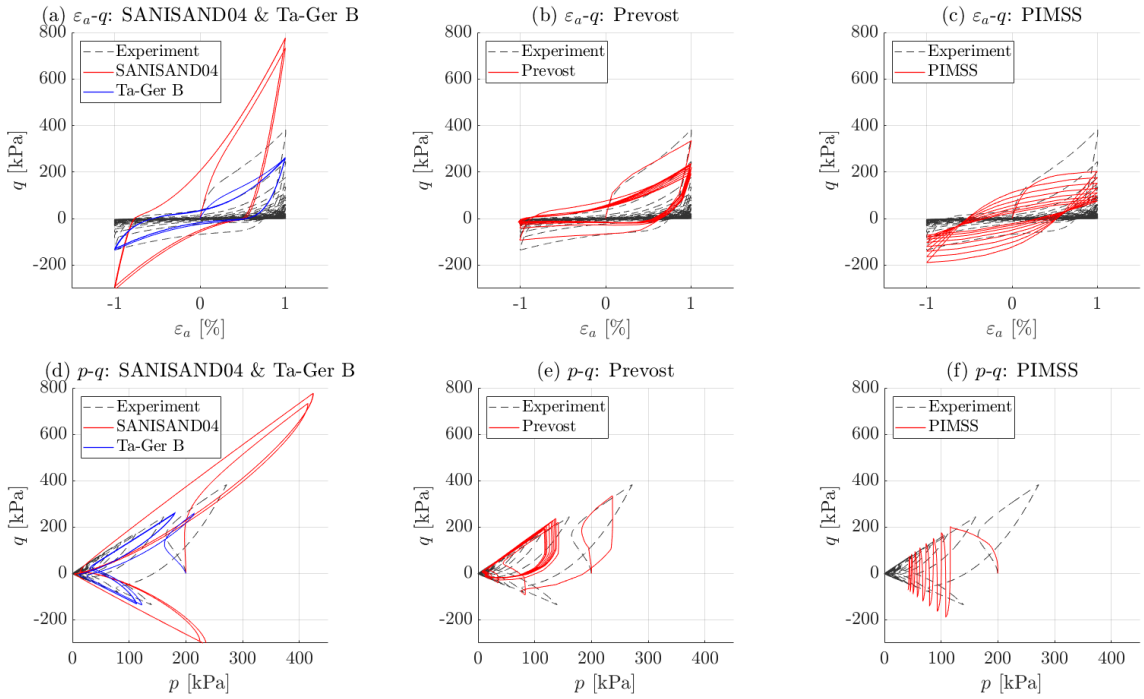

Figure 3.12: Simulations of an undrained cyclic triaxial test on medium-dense sample ($D_{r0} = 94\%$) with isotropic consolidation (initial mean effective stress, p_{in}, of 200 kPa) large-amplitude strain cycles ($\varepsilon_1^{ampl.} = 1 \cdot 10^{-2}$): a,d) Prevost, b,e) PIMSS, c,f) SANISAND04 and Ta-Ger B.

3.3.4 Final verdict

3.3.4.1 Comparative insights on constitutive frameworks

Comparing the predictive capabilities of PIMSS and the Prevost model under monotonic loading, both drained and undrained, reveals only minor differences, supporting the view that the absence of kinematic hardening in PIMSS does not significantly impair its performance in such conditions. However, under cyclic loading, the lack of kinematic hardening in PIMSS becomes more evident. While the Prevost model offers smoother stiffness degradation and more realistic stress paths, PIMSS is affected by shear locking, leading to less accurate cyclic behaviour. This stems from the averaging nature of the parallel formulation, where suboptimal responses from individual micro-models influence the overall behaviour. Nevertheless, when compared to more established models such as SANISAND DM04, PIMSS demonstrates reasonably satisfactory performance, particularly considering its simplicity and practical design intent. Due to the model's modular structure

and ease of modification, such limitations can potentially be mitigated through targeted adjustments or future enhancements.

A strong resemblance is observed between the responses of Ta-Ger B and SANISAND DM04, reflecting structural similarities between the two frameworks, particularly in their elastic formulations and, more critically, in the equations defining the bounding and phase transformation stress ratios. The most significant difference lies in their respective definitions of the plastic modulus. The results of this comparative assessment suggest that the novel plastic modulus adopted in Ta-Ger B, when coupled with the other constitutive components, provides improved overall performance. This performance could be further enhanced by incorporating additional features such as the fabric-dilatancy tensor from SANISAND DM04, given the modularity and adaptability of the Ta-Ger framework. Furthermore, Ta-Ger offers practical advantages in numerical implementation, enabling explicit stress updates without evaluating the stress state relative to the yield surface. This eliminates the need for return mapping procedures or root-finding algorithms, such as bisection, which would otherwise increase computational cost, particularly in large-scale 3D-FE simulations involving numerous cyclic load applications.

3.3.4.2 Preferred constitutive approach

The selection of a suitable constitutive model for this project should be guided by several key criteria: (i) strong predictive capability for critical aspects of sand behaviour under both monotonic and cyclic loading; (ii) consistent performance across a wide range of relative densities and confining pressures, ideally using a single parameter set; (iii) a relatively small number of parameters; (iv) flexibility for future extensions to account for more realistic seabed environments, including the presence of fines, without requiring recalibration for varying fines content; (v) numerical robustness of the formulation; (vi) ease of numerical implementation; (vii) straightforward calibration using conventional laboratory test data;

(viii) physical transparency and interpretability of both the model structure and its parameters; (ix) low computational cost to ensure feasibility in large-scale 3D-FE analyses; and (x) reliable predictive performance without the need for reparameterization for different loading scenarios. Table 3.12 provides a qualitative assessment of how each model performs against the above criteria, serving as the basis for the final selection.

Among the models evaluated, the Ta-Ger framework best satisfies the majority of these requirements, making it the most suitable candidate for further development and implementation in commercial 3D-FE software. Criteria (i), (ii), (iii), (vii), and (x) are self-explanatory and evident from the simulation results and analysis presented throughout this chapter. Regarding criterion (iv), it should be noted that both Ta-Ger B and SANISAND DM04 are compatible with the CSSM framework, which facilitates the inclusion of fines content through straightforward adjustments to the void ratio (Rahman et al., 2014). In contrast, the multi-surface models, being incompatible with CSSM, would require full recalibration for each fines content percentage. As for criteria (v) and (vi), numerical robustness and ease of implementation, Ta-Ger B clearly stands out. Unlike the Prevost model, which relies on kinematic hardening and the management of multiple evolving surfaces (introducing risks such as surface crossing or the need for corrective measures), the Ta-Ger formulation avoids these issues. It also eliminates the need for yield function checks, return mapping, or bisection/root-finding algorithms, significantly simplifying implementation. Criterion (viii), which concerns physical transparency and interpretability, is well addressed in Ta-Ger due to its CSSM compatibility, making the model components more intuitive and conceptually linked to well-established concepts. Finally, criterion (ix) regarding computational efficiency is closely linked to (v) and (vi): the reduced number of equations and absence of complex corrective procedures translates into lower computational cost, especially in large-scale 3D-FE simulations.

Table 3.12: Qualitative ranking of the models based on their numerical implementation and simulation performance in the present study.

Selection criteria	SANISAND DM04	Ta-Ger B	Prevost	PIMSS
Predictive capability (monotonic loading)	++++	++++	+++	+++
Predictive capability (cyclic loading)	+++	++++	++++	+++
Unified performance across densities and pressures	+++++	+++++	++	++
Small number of parameters	+++	++++	++	++
Extensibility for fines content inclusion (in a unified manner)	+++++	+++++	+	+
Numerical robustness of formulation	++++	+++++	++	++++
Ease of implementation	+++	+++++	+	+++++
Ease of calibration	++++	++++	+++	++
Physical transparency and interpretability	++++	++++	+++	+++
Computational efficiency	+++	+++++	++	++*
Consistency; no need for recalibration across loading scenarios	++	++++	++	++

*While PIMSS shows moderate computational efficiency in this work (without parallel computing), its parallel Iwan structure is well-suited for parallelization, offering significant speed-up potential in large-scale 3D-FE applications.

3.3.4.3 Considerations in the constitutive approach selection

While the criteria-informed selection of the most suitable constitutive approach for this project is presented in section 3.3.4.3, the present subsection provides the methodological context underpinning that selection. It synthesises insights from the comparative model assessment and the preceding literature review in chapter 2, and clarifies how the available experimental evidence is interpreted when evaluating constitutive performance in light of the project motivation and objectives defined in 1.2.1 and 1.2.2 respectively.

Although the primary application of the selected constitutive framework in this project concerns cyclic drained conditions at the foundation scale, the element-level comparison of the four constitutive models was based on cyclic undrained triaxial tests. For the Karlsruhe sand dataset considered, no drained cyclic test data are available, whereas undrained strain-controlled cyclic triaxial tests provide a comprehensive and consistent experimental basis across relative densities, making them well suited for comparative evaluation. In addition, the undrained cyclic response directly reflects a model's ability to capture key internal

mechanisms governing cyclic sand behaviour, including stiffness and strength evolution and the transition between contractive and dilative response. Strain-controlled simulations are also numerically robust and closely aligned with the implementation strategies adopted for the models examined. In particular, the current implementation of PIMSS is restricted to strain-controlled loading due to the assumption of strain equivalence across micro-models, and extension to stress-controlled conditions would require additional development to ensure numerical stability and robustness, which is beyond the scope of the present study. Confidence in the selection of a suitable modelling approach for subsequent drained monopile-scale simulations is therefore gained not through direct equivalence of drainage conditions, but through validation of the constitutive mechanisms governing cyclic response at the element level, together with the broader selection criteria discussed in section 3.3.4.3.

Within this context, the relevance of a critical-state-based constitutive framework can be assessed. Although cyclic loading of offshore wind turbine monopiles (OWT) is typically associated with relatively small-strain amplitudes and may not necessarily imply attainment of the critical state, formulations grounded in critical-state concepts provide a unified and physically consistent description of sand behaviour across a wide range of densities, stress levels, and loading paths, while maintaining a largely consistent parameter set. Through the use of the state parameter ψ, key mechanisms governing cyclic response, particularly the transition from contractive to dilative behaviour, are represented in a robust and interpretable manner. While the primary focus of this project is long-term small-strain amplitude cyclic loading, the constitutive framework must also remain valid for short-term loading episodes involving higher strain levels without requiring reparameterization. Furthermore, since monopile failure is commonly defined in terms of large ground-level displacements, the formulation must consistently capture both small-strain cyclic response and large-strain behaviour within a single constitutive framework.

Chapter 4

Ta-Ger HC: A cyclic plasticity model for sands

4.1 Envisioning a high-cycle Ta-Ger model

As explained in the introductory chapters, despite extensive efforts in the geotechnical community (Pisanò and Gavin, 2017), uncertainties persist in various aspects of the operational analysis of monopiles (Byrne *et al.*, 2017). According to Arany et al. (2017), some of these uncertainties are related to the cyclic/dynamic performance of a monopile, with the main ones concerning (Liu et al., 2022a): (i) lateral stiffness of monopiles and its variation during storms, (ii) dynamic damping resulting from the interaction between the foundation and the surrounding soil (Versteijlen *et al.*, 2011), and (iii) long-term alterations in the stiffness and capacity throughout the entire operational lifespan (Leblanc, et al., 2010). During recent decades, many sophisticated constitutive models have been proposed and used with success for tackling uncertainties (i) and (ii). However, since interest in the long-term response of monopile foundations (uncertainty (iii)) has only been renewed recently (Liu *et al.*, 2019; Liu, 2020), there has not been a widely accepted modelling approach to resolve this issue. The primary numerical approaches for addressing strain accumulation can be categorized into extrinsic and intrinsic methods (Houlsby *et al.*, 2020) with an additional

extrinsic subcategory known as the stiffness degradation method (Achmus et al., 2009; Gao and Zhao, 2015). Each of these approaches has its own advantages and limitations, which must be carefully considered, understood, and, if necessary, mitigated before utilization. This chapter presents a new intrinsic cyclic plasticity model suitable for simulating the long-term cyclic behaviour of sand by realistically capturing the occurrence of ratcheting via its phenomenological constitutive formulation. The new plasticity model overcomes practicality hurdles that could arise when utilizing the intrinsic memory-enhanced bounding-surface plasticity model (Liu *et al.*, 2019), which, while successful, introduces complexities and increases computational expense by incorporating an additional surface (Li and Liu, 2020). The new model, named 'Ta-Ger HC', is built upon the state-dependent sand model 'Ta-Ger' (Tasiopoulou and Gerolymos, 2016a; 2016b).

4.2 Original formulation of Ta-Ger

Before introducing modifications, this section presents the original constitutive equations of the Ta-Ger model, formulated in multiaxial stress space. These equations were first presented by Tasiopoulou and Gerolymos (2016a; 2016b), and are not original contributions of this study. However, some expressions presented here differ slightly from those in the original publications and are marked with an asterisk (*). These revisions result from careful analytical derivation and numerical implementation, during which minor inconsistencies or typographical errors were identified. In addition, guidance is provided on the numerical implementation of the original Ta-Ger formulation, highlighting potential challenges and undocumented assumptions that may hinder independent reproduction. These considerations are included to enhance clarity and support reliable future implementation.

4.2.1 Constitutive equations in multiaxial stress space

As explained in section 2.3.3.4, the framework upon which Ta-Ger is built merges perfect elastoplasticity with smooth hysteresis through a hardening law inspired by the Bouc-Wen

approach. Departing from classical plasticity, it introduces a plastic modulus that directly scales the plastic component of the incremental stiffness matrix, rather than appearing as an additive term in the denominator (Tasiopoulou and Gerolymos, 2016a):

$$\mathbf{E}^{\mathrm{ep}} = \mathbf{E}^{\mathrm{e}}\left[\mathbf{I} - \frac{\boldsymbol{\Phi}_{\mathrm{g}}\boldsymbol{\Phi}_{\mathrm{f}}{}^{\mathrm{T}}\mathbf{E}^{\mathrm{e}}\mathbf{H}}{\boldsymbol{\Phi}_{\mathrm{f}}{}^{\mathrm{T}}\mathbf{E}^{\mathrm{e}}\boldsymbol{\Phi}_{\mathrm{g}}}\right] \tag{4.1}$$

Equation (4.1) is identical in form to equations (2.3) and (3.18) and is restated here as part of the complete multiaxial formulation adopted in this thesis. Here, $\mathbf{E}^{\mathrm{e}}$ is the elastic stiffness matrix, while $\boldsymbol{\Phi}_{\mathrm{f}}$ and $\boldsymbol{\Phi}_{\mathrm{g}}$ correspond to the gradients of the yield surface and plastic potential, respectively. The plastic modulus is governed by the matrix $\mathbf{H}$, defined as $\mathbf{H} = \zeta^{n}\mathbf{I}$, where ζ regulates the hardening or softening via a mapping rule, and n is a hardening parameter. The formulation of the original multiaxial Ta-Ger model within this general plasticity framework requires the specification of constitutive ingredients that populate the elastoplastic matrix in equation (4.1):

4.2.1.1 Elastic region

The elastic matrix $\mathbf{E}^{\mathrm{e}}$ of equation (4.1) consists of terms that are expressed as functions of non-linear tangent shear (G) and bulk (K) moduli as specified by Li and Dafalias (2000):

$$G = G_0 p_{\mathrm{at}} \frac{(2.97 - e)^2}{1 + e}\left(\frac{p}{p_{\mathrm{at}}}\right)^{m} \tag{4.2}$$

where G_0 and m are dimensionless parameters, p_{at} is the atmospheric pressure, and e is the current void ratio. The bulk modulus K is obtained from $K = 2G(1+v)/3(1-2v)$ assuming a constant Poisson's ratio, v.

4.2.1.2 Bounding-surface-dependent plastic matrix

Ta-Ger model features an open-end, cone-type bounding surface that depends on the current and last loading reversal stress states:

$$\mathrm{f} = \left[(\boldsymbol{s} - \boldsymbol{r}_{\mathrm{p}} p) : (\boldsymbol{s} - \boldsymbol{r}_{\mathrm{p}} p)\right]^{1/2} - \left(\sqrt{\frac{2}{3}} M_{\mathrm{s}} \chi - n_{\mathrm{p}}\right) p = 0 \tag{4.3}$$

where $\boldsymbol{s}$ is the deviatoric stress tensor, M_{s} is the bounding stress ratio controlling the ultimate strength, and χ is an internal model parameter that incorporates Lode angle, θ, effects. The stress ratio tensor, $\boldsymbol{r}_{\mathrm{p}}$, plays the role of the 'back-stress' ratio in conventional bounding surface models. It is calculated as:

$$\boldsymbol{r}_{\mathrm{p}} = \frac{\boldsymbol{s}_{\mathrm{p}}}{p_{\mathrm{p}}} = \frac{\boldsymbol{\sigma}_{\mathrm{p}} - p_{\mathrm{p}} \mathbf{I}}{p_{\mathrm{p}}} \tag{4.4}$$

where $\boldsymbol{\sigma}_{\mathrm{p}}$ and p_{p} are the effective stress tensor and the mean effective stress at the most recent pivot point. Tasiopoulou and Gerolymos (2016a) define pivot points as the points where a loading reversal occurs, which is detected by the change in sign of the incremental first-order work ($\mathrm{d}W$). The term n_{p} is a stress ratio and hence a scalar quantity representing the distance of the pivot stress ratio, $\boldsymbol{r}_{\mathrm{p}}$, from the hydrostatic axis:

$$n_{\mathrm{p}} = \boldsymbol{n} : \boldsymbol{r}_{\mathrm{p}} \tag{4.5}$$

with $\boldsymbol{n}$ being a normalised stress tensor with $\mathrm{tr}(\boldsymbol{n}) = 0$ and $\mathrm{tr}(\boldsymbol{n}^2) = 1$:

$$\boldsymbol{n} = \frac{\boldsymbol{s} - \boldsymbol{r}_{\mathrm{p}} p}{\left[(\boldsymbol{s} - \boldsymbol{r}_{\mathrm{p}} p) : (\boldsymbol{s} - \boldsymbol{r}_{\mathrm{p}} p)\right]^{1/2}} \tag{4.6}$$

Under monotonic loading, the bounding surface f, defined in equation (4.3), reduces to a Lode angle-dependent Drucker-Prager form that coincides with the target failure surface, as the pivot stress ratio tensor, $\boldsymbol{r}_{\mathrm{p}}$ remains zero throughout the loading process:

$$\mathrm{F} = [\boldsymbol{s} : \boldsymbol{s}]^{1/2} - \sqrt{\frac{2}{3}} M_{\mathrm{s}} \chi p = 0 \tag{4.7}$$

To govern material hardening based on the relative position between the current stress state and its image on the bounding surface, the Ta-Ger framework introduces hardening variable ζ, defined in analogy to the triaxial case (section 2.3.3.4):

$$\zeta = \frac{\left[(\boldsymbol{r}-\boldsymbol{r}_{\mathrm{p}}):(\boldsymbol{r}-\boldsymbol{r}_{\mathrm{p}})\right]^{1/2}}{\sqrt{\frac{2}{3}}M_{\mathrm{s}}\chi - n_{\mathrm{p}}} \tag{4.8}$$

in which $\boldsymbol{r} = \boldsymbol{s}/p$ is the current deviatoric stress ratio tensor. When a loading reversal occurs, $\boldsymbol{r} = \boldsymbol{r}_{\mathrm{p}}$ and consequently $\zeta = 0$, momentarily triggering elastic unloading. Since the elastic region is a line in triaxial space, pure elastic behaviour occurs only at the initial step of stress paths with a nonzero varying $\boldsymbol{r}$, when numerically integrated. The definition of ζ allows for the specification of a loading surface that accommodates the current stress state:

$$\mathrm{L} = \left[(\boldsymbol{s}-\boldsymbol{r}_{\mathrm{p}}p):(\boldsymbol{s}-\boldsymbol{r}_{\mathrm{p}}p)\right]^{1/2} - \zeta\left(\sqrt{\frac{2}{3}}M_{\mathrm{s}}\chi - n_{\mathrm{p}}\right)p = 0 \tag{4.9}$$

The yield surface of the model is obtained by setting $\zeta = 0$, and its gradient is derived by differentiating equation (4.9) with respect to stress, evaluated at $\zeta = 0$:

$$\boldsymbol{\Phi}_{\mathrm{f}} = \boldsymbol{n} - \frac{1}{3}\boldsymbol{n}:\boldsymbol{r} \tag{4.10}$$

Figure 4.1 and Figure 4.2 clarify the above concepts by illustrating the evolution of the bounding surface (equation (4.3), $\mathrm{f} = 0$), loading surface (equation (4.9), $\mathrm{L} = 0$) and target failure surface (equation (4.7), $\mathrm{F} = 0$) in the π-plane during a cyclic simple shear constant-p test. The stress path follows a straight line at $\theta = 30°$, with star symbols marking the current stress states and circles indicating the corresponding image points. At the onset of loading (point A), the loading surface collapses to a line ($\zeta = 0$) that passes through stress point A on the hydrostatic axis. As loading proceeds, plasticity develops and ζ increases, causing the loading surface to expand. Upon the first reversal (point C^{+}), the first-order work

changes sign, the pivot stress ratio $\boldsymbol{r}_{\mathrm{p}}$ is updated to reflect the state at C^{-}, and ζ resets to zero. Momentarily, the loading surface collapses again to a line. Although the bounding surface is generally convex, it adapts to perfectly match the target failure surface at the point opposite the current stress state, known as the image point. As shown in Figure 4.2, this point corresponds to the intersection between the projection of the current tensor $\boldsymbol{r} - \boldsymbol{r}_{\mathrm{p}}$ and the bounding surface ($\mathrm{f} = 0$). This mechanism reflects the model's ability to continuously adapt the bounding surface to the target failure surface along any given stress path. The latter mathematically represents the locus of image points derived from the bounding surface. The uniqueness of this framework lies in the fact that the mapping rule is inherently embedded in the definition of the hardening variable ζ, and thus in the plastic matrix $\mathbf{H} = \zeta^{n}\mathbf{I}$.

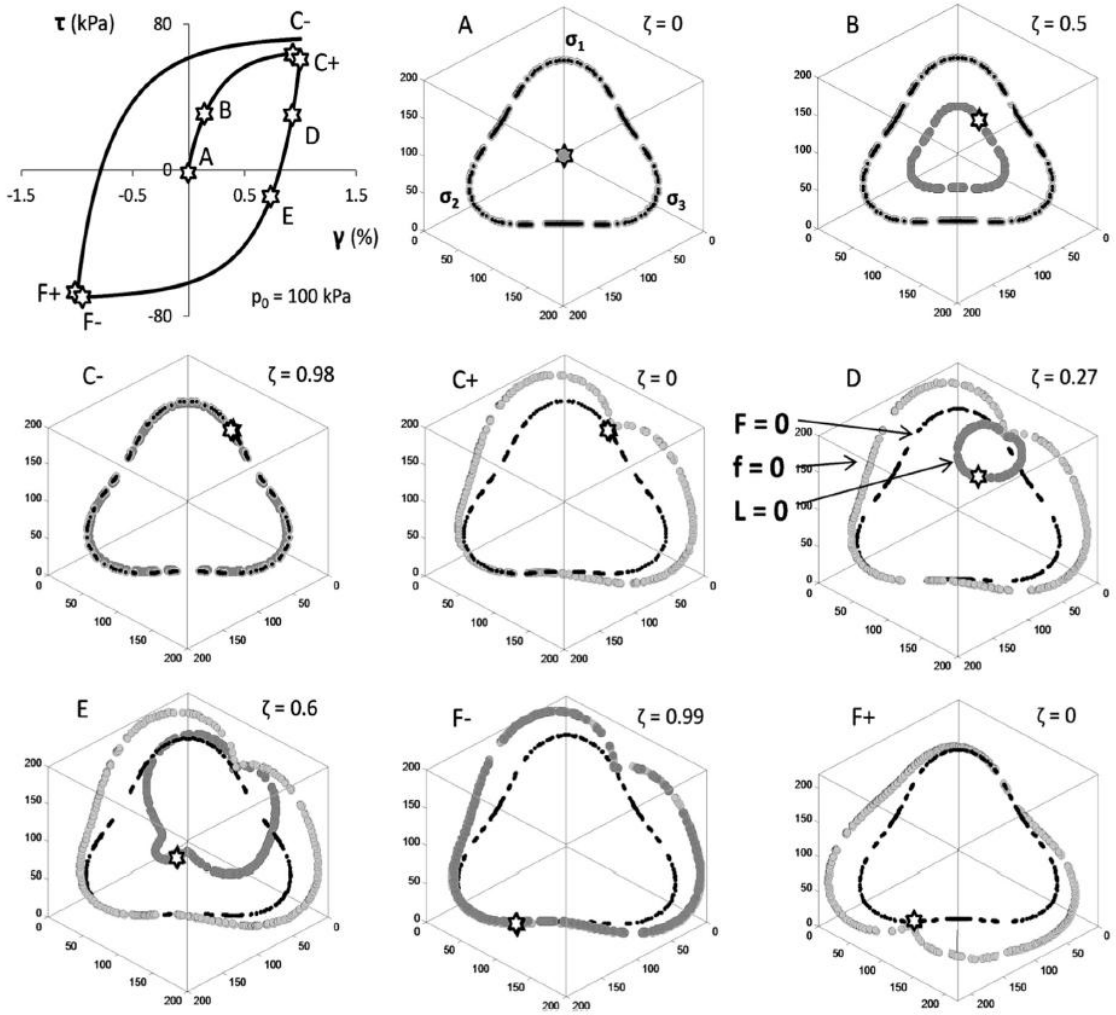

Figure 4.1: Cyclic simple shear constant-p test: evolution of the loading surface ($\mathrm{L} = 0$), bounding surface ($\mathrm{f} = 0$), and target failure surface ($\mathrm{F} = 0$) illustrated in π-plane diagrams. The current stress states are denoted by star symbols (Tasiopoulou and Gerolymos, 2016a).

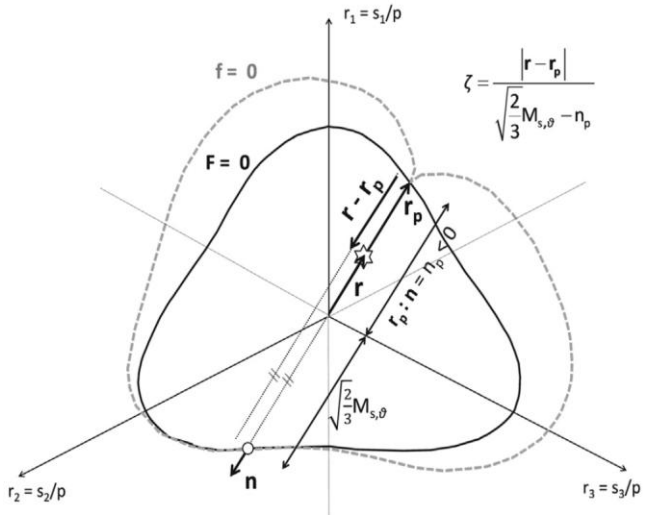

Figure 4.2: Definition of hardening variable ζ at the first loading reversal (point D in Figure 4.1) during a cyclic simple shear constant-p test. The star denotes the current stress state, and the circle marks the corresponding image point on the bounding surface (Tasiopoulou and Gerolymos, 2016a).

4.2.1.3 Flow rule

Ta-Ger adopts a Rowe-inspired stress-dilatancy relation (Rowe, 1962) according to which the scalar dilatancy strain ratio is estimated as:

$$d = R_{\mathrm{d}}\left(\sqrt{\frac{2}{3}}M_{\mathrm{pt}}\chi - \frac{\boldsymbol{s}}{p}:\boldsymbol{n}\right) \tag{4.11}$$

in which M_{pt} signifies the phase transformation line. R_{d} is a variable controlling the amount of densification induced during drained loading conditions and is estimated as:

$$R_{\mathrm{d}} = e^{-\alpha(D_{\mathrm{r}}-D_{\mathrm{r0}})} \tag{4.12}$$

with α being a constant, D_{r} being the current relative density, and D_{r0} being the initial relative density. The role of this stress-dilatancy relationship can be understood from the observation of a simplified version of equation (4.11), excluding R_{d} and χ, in triaxial ($q - p$) space notation:

$$d = \mathrm{d}\varepsilon_p^{\mathrm{p}}/\mathrm{d}\varepsilon_q^{\mathrm{p}} = M_{\mathrm{pt}} - q/p \tag{4.13}$$

where $\mathrm{d}\varepsilon_p^{\mathrm{p}}$ and $\mathrm{d}\varepsilon_q^{\mathrm{p}}$ are the plastic volumetric and deviatoric strain increments, respectively. Equation (4.13) implies that the volumetric behaviour of the material depends on the distance

of the current stress ratio, q/p, from the phase transformation line, M_{pt}, being contractive ($d > 0$) when $q/p < M_{\mathrm{pt}}$ and dilative ($d < 0$) when $q/p > M_{\mathrm{pt}}$. Ta-Ger adopts volumetric non-associativeness, with the gradient to the plastic potential surface, $\boldsymbol{\Phi}_{\mathrm{g}}$, being given by:

$$\boldsymbol{\Phi}_{\mathrm{g}} = \boldsymbol{n} + \boldsymbol{n^2} d \tag{4.14}$$

4.2.1.4 Lode angle dependency

Lode angle effects are accounted for via parameter χ, which as shown in sections 4.2.1.2 and 4.2.1.3, scales the bounding and phase transformation stress ratios. It is defined as:

$$\chi = \frac{M_{\mathrm{s},\theta}}{M_{\mathrm{s,c}}} \tag{4.15}$$

where the stress ratio $M_{\mathrm{s},\theta}$ signifies the ultimate strength of the material when considering the current value of the Lode angle. $M_{\mathrm{s},\theta}$ is calculated as a polynomial interpolation of the ultimate-strength stress ratios in compression, $M_{\mathrm{s,c}}$ ($\theta = 0$), extension, $M_{\mathrm{s,e}}$ ($\theta = 60°$), and simple shear, $M_{\mathrm{s,ss}}$ ($\theta = 30°$):

$$M_{\mathrm{s},\theta} = \left(\frac{M_{\mathrm{s,c}} + M_{\mathrm{s,e}}}{2} - M_{\mathrm{s,ss}}\right)\cos^2(3\theta) + \left(\frac{M_{\mathrm{s,c}} - M_{\mathrm{s,e}}}{2}\right)\cos(3\theta) + M_{\mathrm{s,ss}} \tag{4.16}$$

where $M_{\mathrm{s,c}}$, $M_{\mathrm{s,e}}$ and $M_{\mathrm{s,ss}}$ are calculated as:

$$M_{\mathrm{s,c}} = \frac{6\sin\varphi_{\mathrm{cs}}}{3-\sin\varphi_{\mathrm{cs}}},\ M_{\mathrm{s,e}} = \frac{6\sin\varphi_{\mathrm{cs}}}{3+\sin\varphi_{\mathrm{cs}}},\ M_{\mathrm{s,ss}} = 2\sin\varphi_{\mathrm{cs}} \tag{4.17}$$

where φ_{cs} is the friction angle at critical state. The Lode angle θ is defined as:

$$\cos(3\theta) = \frac{3\sqrt{3}}{2}\frac{J_3}{J_2^{3/2}} \tag{4.18}$$

in which J_2 and J_3 are the second and third invariants, respectively, of the deviatoric stress tensor.

4.2.1.5 Critical-state dependency

Ta-Ger can predict dense and loose sand behaviour, with a single set of material parameters, accounting for both the effects of void ratio and stress level. This is done by incorporating critical state theory (CST) (Roscoe *et al.*, 1958) in conjunction with a sand state parameter (Been and Jefferies, 1985; Bolton, 1986) within its core formulation. Fundamentally, the critical state (CS) concept is that, upon reaching the critical state, there is no alteration in the stress state or the volumetric strain, even as the shear strain continues to increase. Numerically, CS compatibility is achieved via the phase transformation stress ratio, M_{pt}, and the bounding surface stress ratio, M_{s}, gradually converging to the CS stress ratio, M_{cs}, fulfilling the above postulates. As shown in the study by Lashkari (2009), numerous equations have been proposed for this purpose. Tasiopoulou and Gerolymos (2016a) introduced a novel set of equations for the variation of M_{s} and M_{pt}. Additionally, they underscored the adaptability of the Ta-Ger constitutive framework by demonstrating that traditional equations, which describe the evolution of M_{s} and M_{pt} based on the traditional state parameter ψ (Been and Jefferies, 1985), could be utilized as alternatives to their novel equations. For convenience, the formulation employing the new equations (Tasiopoulou and Gerolymos, 2016a; 2016b) is denoted as 'Ta-Ger A', while the one using the traditional ones (Dafalias and Manzari, 2004) as 'Ta-Ger B' respectively. It is important to note that this is the only distinction between Ta-Ger A and B.

Specifically, Ta-Ger B uses the following equations:

$$M_{\mathrm{s}} = M_{\mathrm{cs}} e^{-n_{\mathrm{b}}\psi} \qquad \text{and} \qquad M_{\mathrm{pt}} = M_{\mathrm{cs}} e^{n_{\mathrm{d}}\psi} \tag{4.19}$$

where n_{b} and n_{d} are positive material constants, $\psi = e - e_{\mathrm{c}}$, and e_{c} is the void ratio on the critical state line (CSL) corresponding to the current mean effective stress p (Li and Wang, 1998):

$$e_c = e_0 - \lambda \left(\frac{p}{p_{at}}\right)^{\xi} \tag{4.20}$$

where e_0, λ and ξ are constants.

Ta-Ger A, on the other hand, employs two state parameters for the evolution of the bounding stress ratio, M_s, and phase transformation stress ratio, M_{pt}. The first parameter is the cumulative incremental deviatoric strain, $\Sigma d\varepsilon_q$, which drives the evolution of M_s and M_{pt} towards critical state under both monotonic and cyclic loading (see section 4.3.2.3, where evolution of M_s and M_{pt} to M_{cs} during drained cyclic loading causes unrealistic behaviour). The second parameter is the relative dilatancy index, I_r, originally suggested by Bolton (1986), and is related to the CSL in $D_r - p$ space. Similar to ψ in Ta-Ger B, I_r provides CS compatibility. In Ta-Ger A the bounding surface stress ratio, M_s, is defined as:

$$M_s = M_{cs} + \left[M_{sp} + \left(M_{s0} - M_{sp}\right)e^{-c\Sigma d\varepsilon_q} - M_{cs}\right]e^{-c\Sigma d\varepsilon_q} \tag{4.21}$$

in which M_{s0} signifies the initial value of M_s, M_{sp} is the maximum value of M_s that could potentially be reached depending on the value of constant c (in practice M_{sp} can never be reached and instead a lower value M_{speak} is attained). Tasiopoulou and Gerolymos (2016a) suggest adopting values of c within the range of 3-10. The phase transformation stress ratio, M_{pt}, takes the following form:

$$M_{pt} = M_{cs} + \left(M_{pt0} - M_{cs}\right)e^{-c\Sigma d\varepsilon_q} \tag{4.22}$$

in which M_{pt0} is the initial value of M_{pt}. So far, equations (4.21) and (4.22) seem to be independent of the relative dilatancy index, I_r. The dependence of the stress ratios M_s and M_{pt} on I_r is accomplished indirectly by establishing a relationship that links parameters M_{s0}, M_{sp} and M_{pt0} with I_r. The relative dilatancy index, I_r, is defined as (Bolton, 1986):

$$I_r = D_r(Q - \ln(p)) - R \tag{4.23}$$

where Q and R are constants taking values near 10 and 1, respectively. M_{s0} is given by:

$$M_{s0} = \frac{6\sin(0.8\varphi_{cs} + 3I_{r0})}{3 - \sin(0.8\varphi_{cs} + 3I_{r0})} \tag{4.24}$$

where I_{r0} is the initial value of relative dilatancy index, I_r, implying that M_{s0} remains constant throughout loading. The potential maximum value of M_s, M_{sp}, is evaluated as:

$$M_{sp} = 2M_{speak} - M_{cs} + 0.5\sqrt{\left(2M_{cs} - 4M_{speak}\right)^2 - 16M_{s0}\left(M_{speak} - M_{cs}\right) - 4{M_{cs}}^2} \tag{4.25}^*$$

with the actual maximum value M_{speak} being calculated as:

$$M_{speak} = \frac{6\sin(\varphi_{max})}{3 - \sin(\varphi_{max})} \tag{4.26}$$

with φ_{max} being the maximum friction angle for triaxial compression, approximated $\varphi_{max} - \varphi_{cs} = 3I_r$ (Bolton, 1986). Finally, M_{pt0} is determined as:

$$M_{pt0} = M_{speak}\zeta^n - \frac{3(0.3I_r)}{3 + (0.3I_r)} \tag{4.27}^*$$

Ta-Ger A can be degenerated into a simpler model, independent of I_r, by adopting constant values for M_{s0}, M_{sp} and M_{pt0} (Tasiopoulou and Gerolymos, 2012).

4.2.1.6 Hardening exponent equation

The hardening exponent n is a vital constitutive ingredient for this plasticity scheme, as it regulates the degree of coupling between the elastic and plastic components that comprise a total strain increment. Tasiopoulou and Gerolymos (2016a) suggest adopting a constant value of n within the range of 0.2-0.5 for monotonic drained and undrained conditions. However, for cyclic loading Tasiopoulou and Gerolymos (2016a) recommend expressing n as a function depending on the cumulative incremental deviatoric strain, $\Sigma d\varepsilon_q$:

$$n = n_f + \left[n_{peak} + \left(n_0 - n_{peak}\right)e^{-\beta\Sigma d\varepsilon_q} - n_f\right]e^{-\gamma\left(1-\mathrm{sign}\left(\Sigma|d\varepsilon_p|\right)\right)\Sigma d\varepsilon_q} \tag{4.28}$$

where n_0 is the initial value of n, n_{peak} is the potential peak value of n, and n_{f} is the final desired value (for undrained conditions). The constants β and γ (applying only to undrained conditions) control the evolution of n towards n_{peak} and n_{f}. The function $\left(1 - \text{sign}\left(\Sigma\left|\text{d}\varepsilon_p\right|\right)\right)$ acts as a switch, toggling the activation or deactivation of the rightmost exponential term depending on whether the loading conditions are drained or undrained, respectively. $\Sigma\left|\text{d}\varepsilon_p\right|$ is the accumulation of absolute volumetric strain increments.

4.2.1.7 Load reversal criterion

Cyclic models should incorporate a robust and efficient mechanism for detecting load reversals. Ta-Ger employs a load reversal criterion based on the sign of the incremental first-order work:

$$\text{d}W = \left(\boldsymbol{r} - \boldsymbol{r}_{\text{p}}\right) : \dot{\boldsymbol{\varepsilon}} \tag{4.29}$$

where $\dot{\boldsymbol{\varepsilon}}$ is the strain rate tensor. If $\text{d}W$ changes sign from one increment to the next, a load reversal is detected and the pivot-point stress ratio tensor, $\boldsymbol{r}_{\text{p}}$, is updated, taking the value of the stress ratio tensor, $\boldsymbol{r}$, from the previous increment.

4.2.2 Summary of parameters

This section summarizes the parameters for the Ta-Ger A and Ta-Ger B formulations, including the values used for the simulations of Toyoura sand shown in section 4.2.3. The parameters for both models are taken from Tasiopoulou and Gerolymos (2016a). Table 4.1 outlines the parameters for Ta-Ger A, with 9 parameters for monotonic loading and 13 for cyclic loading, and Ta-Ger B, with 11 parameters for monotonic loading and 15 for cyclic loading. Details regarding the calibration of Ta-Ger A, which goes beyond the scope of this study, can be found in Tasiopoulou and Gerolymos (2016b).

Table 4.1: Model parameters for Toyoura sand (Tasiopoulou and Gerolymos, 2016a).

	Ta-Ger A		**Ta-Ger B**	
Feature	Symbol	Value	Symbol	Value
Elasticity	G_0	130	G_0	130
	v	0.15	v	0.15
	m	0.8	m	0.8
Critical state	M_{cs}	1.25	M_{cs}	1.25
	-	-	e_0	0.934
	-	-	λ	0.019
	-	-	ξ	0.7
Bounding surface	Q	9.1	n_b	0.9
Dilatancy	R	0.75	n_d	0.7
	c	10	-	-
	α	0.3	α	0.3
Hardening	n_0	-	n_0	1
exponent n^*	n_f	-	n_f	0.2
	n_{peak}	-	n_{peak}	4.7
	β	-	β	105
	γ	-	γ	42
	$^*n = 0.35$ for monotonic loading		$^*n = 0.25$ for monotonic loading	

The calibration process for Ta-Ger B is straightforward. This ease of calibration is due to its structural similarities with commonly-used model versions (Dafalias and Manzari, 2004; Taiebat and Dafalias, 2008; Liu *et al.*, 2019) within the SANISAND family, sharing features such as the elasticity, CSL, bounding surface, and phase transformation equations. Specifically, the dimensional shear modulus parameter, G_0, can be determined either from the small-strain region of experimental stress-strain curves, as shown in Taiebat and Dafalias (2008), or obtained through established empirical correlations, such as those proposed by Richart et al. (1970). It is noted that small-strain stiffness inferred from static stress-strain measurements may be lower than values obtained from wave propagation techniques, such as bender elements, due to the pronounced non-linearity of soil stiffness even at very small strains (Atkinson and Sallfors, 1991; Mair, 1993). While wave propagation methods mobilise extremely small shear strains of the order of 10^{-6} to 10^{-5}, conventional monotonic tests typically involve slightly higher strain levels (10^{-4} to 10^{-3}). However, experimental evidence shows that when local strain measurements are employed and strains are restricted

to the very small-strain range, stiffness values derived from monotonic shearing converge to those obtained from bender elements (Jovičić and Coop, 1997). In this sense, calibration of G_0 from the initial portion of carefully measured stress-strain curves provides a practical and meaningful estimate of small-strain stiffness consistent with dynamic measurements.

The elasticity exponent parameter m is often taken as 0.5 (Li and Dafalias, 2000; Taiebat and Dafalias, 2008). Model parameters associated with the critical state (M_{cs}, e_0, λ and ξ), should be derived directly from the CSL measured in laboratory tests. Parameters n_{b} and n_{d} can be specified via the peak strength and the phase transformation state of the sand as demonstrated by Taiebat and Dafalias (2008). The dilatancy parameter α and the hardening exponent n are both parameters specific to the constitutive ingredients of Ta-Ger, and need to be determined by trial and error to obtain best match with the desired experimental curves.

4.2.3 Single-element simulations and numerical implementation recommendations

4.2.3.1 Summary of the stress integration schemes

Ta-Ger A and Ta-Ger B were both numerically implemented in MATLAB. Two different order explicit integration schemes were adopted, including the first-order accurate single-step forward Euler scheme (RK1 or FE) and the third-order accurate Runge-Kutta-Fehlberg substepping scheme (RKF23). RKF23 was implemented using the approach originally suggested by Fellin et al. (2009) which has been widely adopted in other studies such as that of Wang et al. (2018). In addition to the difference in accuracy between the two integration schemes, RK1 and RKF23, their approach to dividing a time increment into substeps (subincrements) is another distinguishing factor. RK1 is a constant substep method, requiring manual division of each increment into several equal substeps for improved accuracy (in this study increments are not further divided into substeps for the RK1 scheme). RKF23 is an adaptive explicit method (Sloan, 1987; Sloan et al., 2001), according to which

an initial number of increments is predefined by the user, but the size of each increment is automatically adjusted according to the local truncation error (Wang *et al.*, 2018). Simply put, if the error estimated for an integration step exceeds the input integration error tolerance, STOL (Sloan, 1987; Sloan et al., 2001), the step is not accepted, and it is repeated with a reduced increment size (Whyte, 2020).

4.2.3.2 Convergence analysis for monotonic loading

A convergence analysis was conducted for both Ta-Ger A and Ta-Ger B, involving variations in the total number of increments used to divide the applied strain. The analysis involved four distinct scenarios: Ta-Ger A with RK1, Ta-Ger A with RKF23, Ta-Ger B with RK1, and Ta-Ger B with RKF23. Two monotonic triaxial compression tests on Toyoura sand (Verdugo and Ishihara, 1996) were chosen for the analysis, one under drained conditions and the other under undrained conditions. The aim of this investigation was to assess the influence of both the number of increments utilized and the integration scheme employed. All the simulations adopting the RKF23 scheme were performed using the same integration error tolerance $\mathrm{STOL} = 10^{-6}$. To complement the visual assessment of the simulated response, a systematic quantitative convergence criterion was implemented. The relative error for a given response variable x was defined as:

$$\mathrm{E}_X = \frac{|x_i - x_{i-1}|}{x_{i-1}} * 100\% \tag{4.30}$$

where x_i and x_{i-1} represent the values obtained from two successive simulations with increasing numbers of increments. The following convergence indicators were selected: (i) the peak deviatoric stress $q^{\max}$ for drained simulations, and (ii) the minimum mean effective stress $p^{\min}$ for undrained simulations. The calculated relative errors are shown alongside the simulation results in the corresponding figures. Convergence was defined as achieving relative errors below 1%.

Figure 4.3 and Figure 4.4 depict drained triaxial test simulations conducted using the Ta-Ger A model with the RK1 and RKF23 numerical implementations, respectively. Figure 4.5 and Figure 4.6 show the corresponding simulations with the Ta-Ger B model employing the RK1 and RKF23 schemes. For the drained tests, the number of increments has a bigger effect on the predictions of the two models when adopting the RK1 integration scheme. In the case of Ta-Ger A with the RK1 scheme, convergence was obtained when the number of increments was increased to 1000, while for Ta-Ger B with the RK1 scheme, convergence was achieved at 500 increments. In contrast, the RKF23 scheme demonstrated superior stability and efficiency for both models, consistently achieving convergence at 30 increments. The predominant impact of varying the number of increments in RKF23 implementations lies in the smoothness achieved in the reproduced curves, without compromising the accuracy in predicting stresses and strains. For undrained conditions, Figure 4.7 and Figure 4.8 present simulations for Ta-Ger A with RK1 and RKF23, while Figure 4.9 and Figure 4.10 depict the corresponding undrained tests for Ta-Ger B with RK1 and RKF23. The undrained simulations exhibit greater numerical sensitivity compared to the drained cases. For the undrained simulations using RK1, convergence for both Ta-Ger A and B was achieved only at 10000 increments. For the RKF23 scheme, convergence was achieved at 1000 increments for Ta-Ger A and at 30 increments for Ta-Ger B.

In summary, the convergence study demonstrated that both explicit integration schemes produce numerically stable results for monotonic single-element simulations, contingent on the selection of an adequate number of increments. Therefore, it is recommended to conduct a convergence analysis with the available integration schemes before performing simulations for a given study. Considering the objectives of the present study, desired accuracy, and practical constraints such as available time and computational resources will help define the most suitable approach. In the present work, particularly for monotonic and low-cycle

loading conditions (such as cyclic tests of a few cycles), where computational time is not a limiting factor, all subsequent simulations were performed using the RKF23 integration scheme with a tolerance $\mathrm{STOL} = 10^{-6}$ and 1000 initial increments.

As far as predictive capability is concerned, it can be observed that both converged simulations of Ta-Ger A and Ta-Ger B provide overall good agreement with the experimental data. In the drained case, both models accurately capture the stress-strain response and the volumetric behaviour, although Ta-Ger A slightly underestimates the initial stiffness of the stress-strain curve. In the undrained case, Ta-Ger A tends to underestimate the peak strength values in the stress-strain response, while both models slightly exaggerate the contractive tendency of the sample as reflected in the stress path simulations.

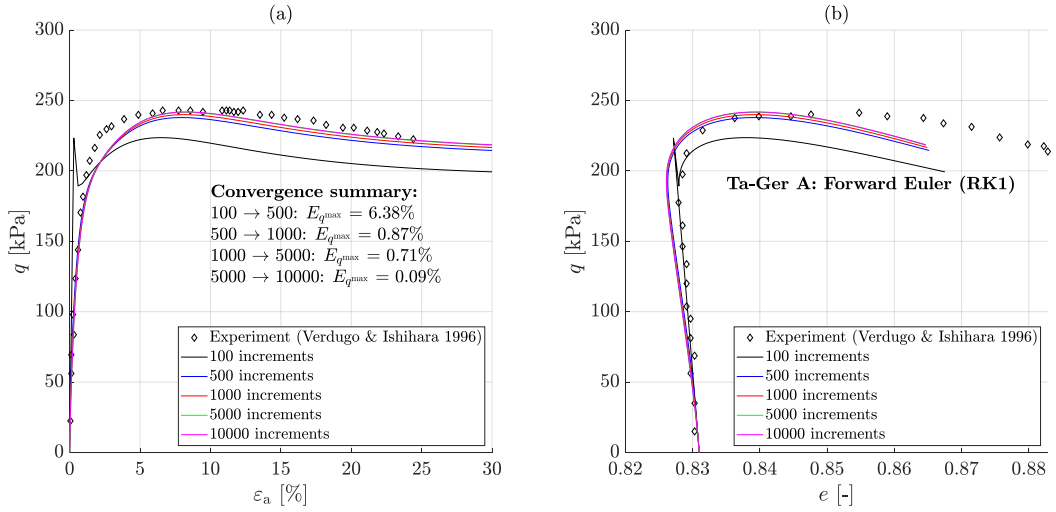

Figure 4.3: Convergence analysis of the Ta-Ger A model (explicit RK1 scheme) for a drained monotonic triaxial compression test on a Toyoura sand sample with an initial void ratio $e_{\mathrm{in}} = 0.831$ and an initial mean effective stress $p_{\mathrm{in}} = 100$ kPa (Verdugo and Ishihara, 1996): (a) stress-strain response; (b) void ratio-stress response.

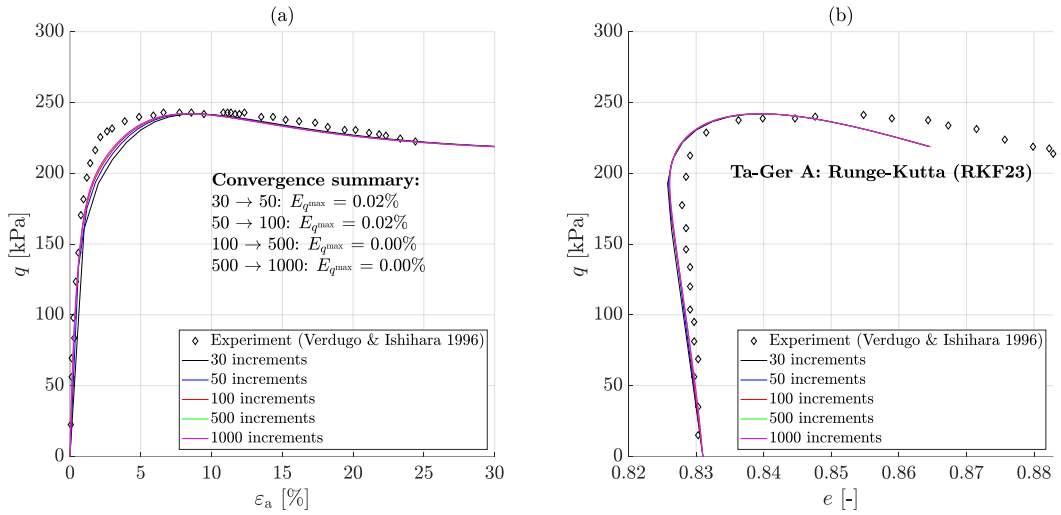

Figure 4.4: Convergence analysis of the Ta-Ger A model (explicit RKF23 scheme) for a drained monotonic triaxial compression test on a Toyoura sand sample with an initial void ratio $e_{in} = 0.831$ and an initial mean effective stress $p_{in} = 100$ kPa (Verdugo and Ishihara, 1996): (a) stress-strain response; (b) void ratio-stress response.

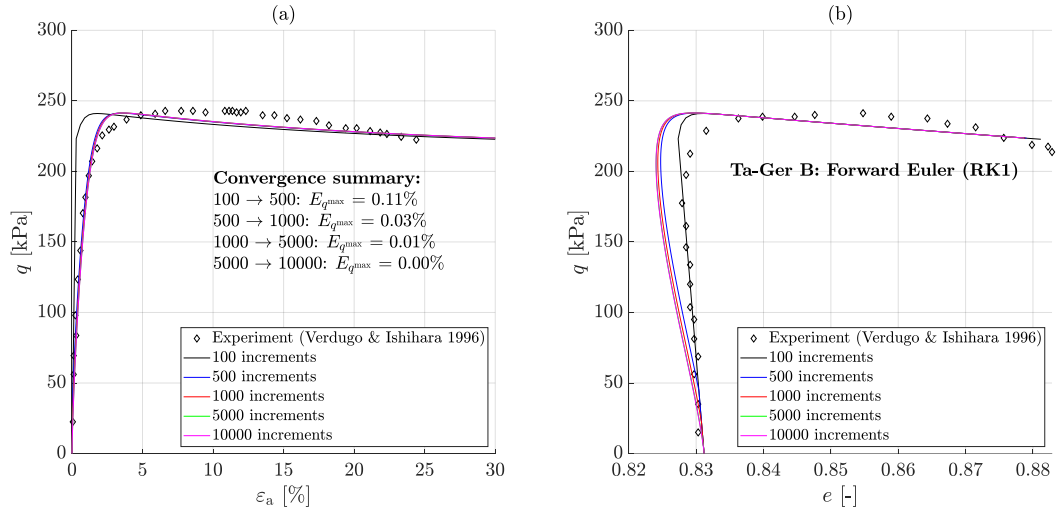

Figure 4.5: Convergence analysis of the Ta-Ger B model (explicit RK1 scheme) for a drained monotonic triaxial compression test on a Toyoura sand sample with an initial void ratio $e_{in} = 0.831$ and an initial mean effective stress $p_{in} = 100$ kPa (Verdugo and Ishihara, 1996): (a) stress-strain response; (b) void ratio-stress response.

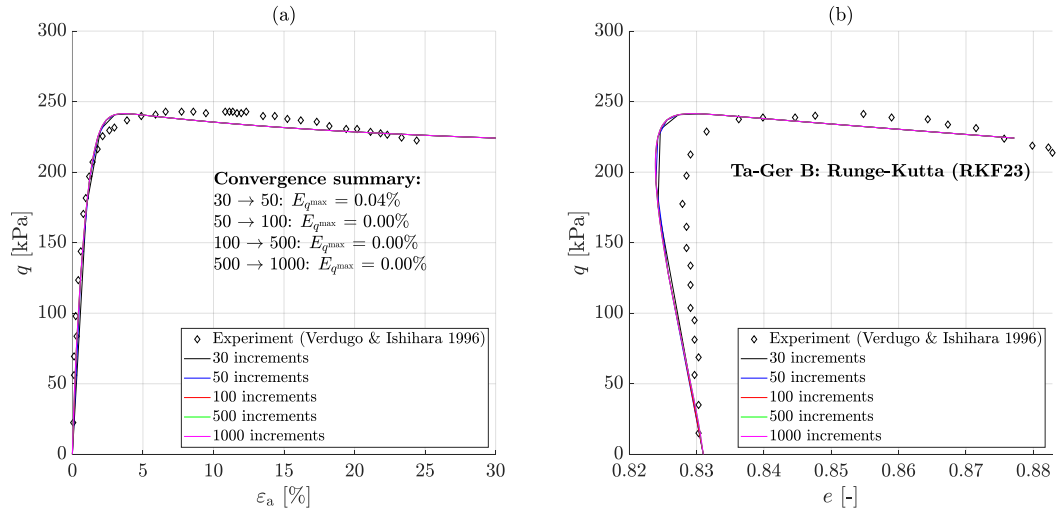

Figure 4.6: Convergence analysis of the Ta-Ger B model (explicit RKF23 scheme) for a drained monotonic triaxial compression test on a Toyoura sand sample with an initial void ratio $e_{in} = 0.831$ and an initial mean effective stress $p_{in} = 100$ kPa (Verdugo and Ishihara, 1996): (a) stress-strain response; (b) void ratio-stress response.

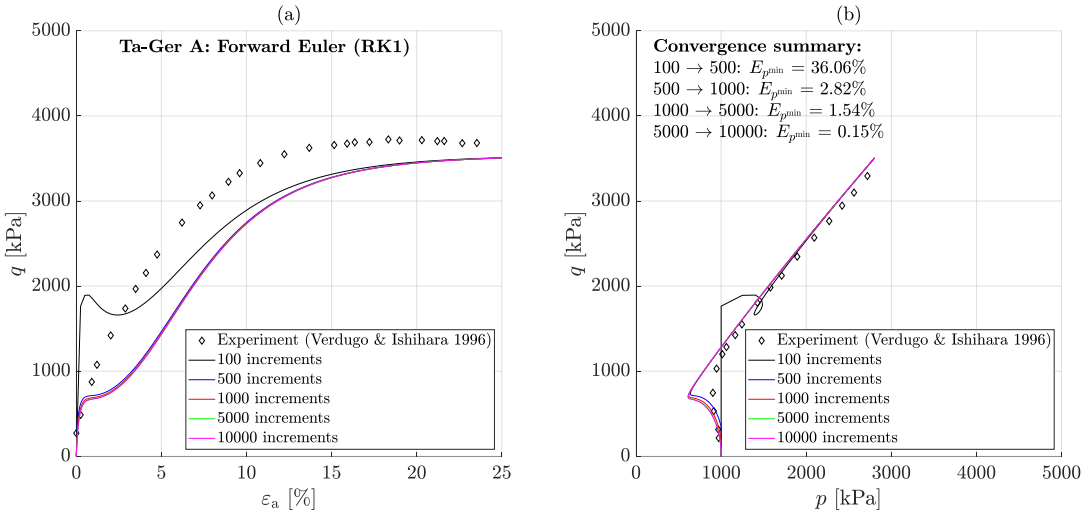

Figure 4.7: Convergence analysis of the Ta-Ger A model (explicit RK1 scheme) for an undrained monotonic triaxial compression test on a Toyoura sand sample with an initial void ratio $e_{\text{in}} = 0.735$ and an initial mean effective stress $p_{\text{in}} = 1000$ kPa (Verdugo and Ishihara, 1996): (a) stress-strain response; (b) stress path.

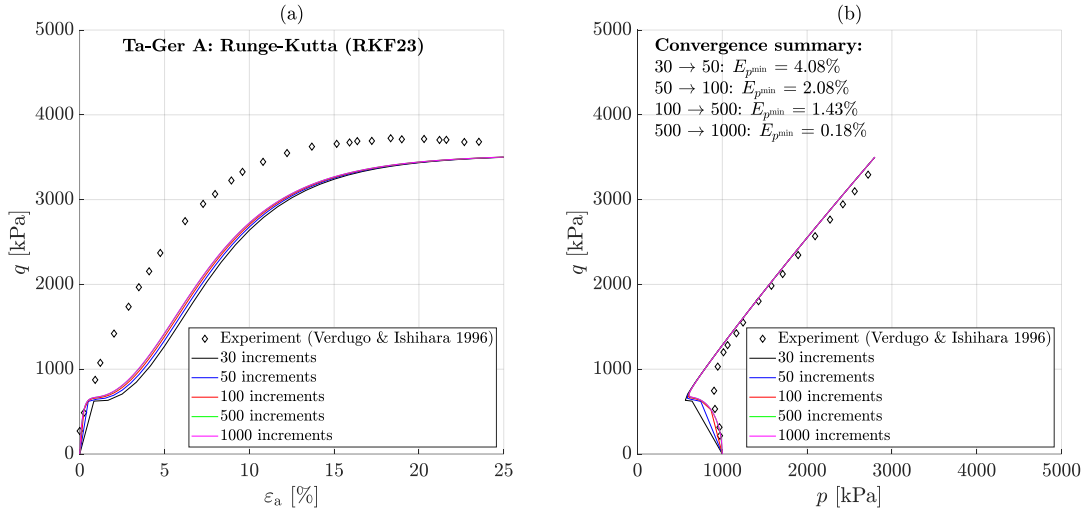

Figure 4.8: Convergence analysis of the Ta-Ger A model (explicit RKF23 scheme) for an undrained monotonic triaxial compression test on a Toyoura sand sample with an initial void ratio $e_{\text{in}} = 0.735$ and an initial mean effective stress $p_{\text{in}} = 1000$ kPa (Verdugo and Ishihara, 1996): (a) stress-strain response; (b) stress path.

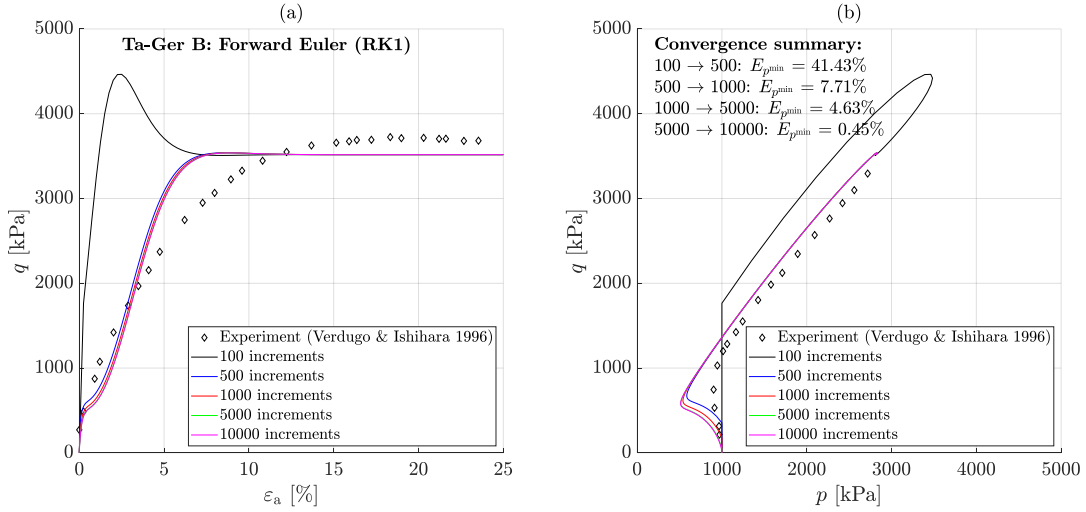

Figure 4.9: Convergence analysis of the Ta-Ger B model (explicit RK1 scheme) for an undrained monotonic triaxial compression test on a Toyoura sand sample with an initial void ratio $e_{\text{in}} = 0.735$ and an initial mean effective stress $p_{\text{in}} = 1000$ kPa (Verdugo and Ishihara, 1996): (a) stress-strain response; (b) stress path.

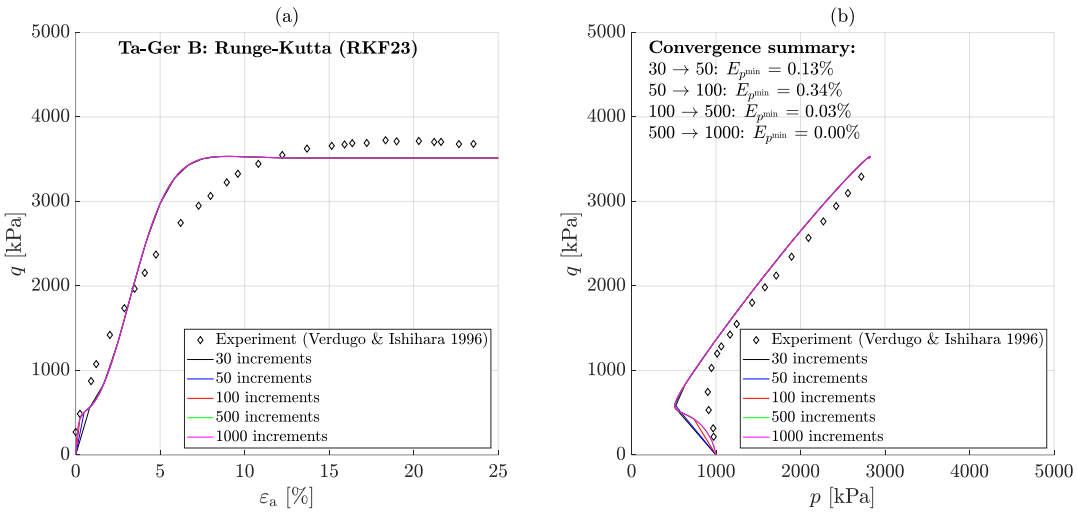

Figure 4.10: Convergence analysis of the Ta-Ger B model (explicit RKF23 scheme) for an undrained monotonic triaxial compression test on a Toyoura sand sample with an initial void ratio $e_{\text{in}} = 0.735$ and an initial mean effective stress $p_{\text{in}} = 1000$ kPa (Verdugo and Ishihara, 1996): (a) stress-strain response; (b) stress path.

4.2.3.3 Guidelines for accurate simulation of softening behaviour

As outlined in section 2.3.3.4, the hardening variable ζ measures the distance between the current stress point and its projection on the bounding surface, mathematically expressed as a ratio. Conceptualizing Ta-Ger as a bounding surface model is helpful in grasping how softening behaviour is captured at a constitutive level. Following Manzari and Dafalias (1997), a numerical approach to simulating softening behaviour involves permitting the current stress state to exist outside the bounding surface. In a 'true' bounding surface model, this is denoted as a negative distance, while in Ta-Ger, it corresponds to a ratio exceeding unity. To better illustrate this concept, consider Figure 4.11, alongside equation (4.8), particularly in the context of a drained monotonic triaxial test, where no stress reversal is detected throughout the loading process ($\boldsymbol{r}_{\text{p}} = \boldsymbol{0}$, $n_{\text{p}} = 0$ and $\chi = 1$). Figure 4.11a shows a simulation where ζ increases freely from its initial value, whereas Figure 4.11b shows a simulation where ζ is strictly bounded between 0 and 1, as prescribed in Tasiopoulou and Gerolymos (2016a). Examination of the two simulations indicates that limiting ζ from surpassing unity effectively inhibits the simulation of softening behaviour. Figure 4.11c shows the evolution of the current stress ratio, $\eta = q/p$, against the bounding stress ratio, M_{s}, for the 'unrestricted' ζ case. The figure is segmented into three zones: (i) hardening

($q/p < M_s$ and $0 \leq \zeta < 1$), (ii) peak strength ($q/p = M_s$ and $\zeta = 1$), and (iii) softening ($q/p > M_s$ and $\zeta > 1$) where the current stress state has crossed the bounding surface, which contracts towards critical state. Preventing ζ from exceeding unity would have suppressed the softening zone. This section does not introduce a new softening approach for Ta-Ger but clarifies that for the model to be generally applicable, ζ should not be strictly bounded between 0 and 1; ζ can exceed unity and gradually reduce to 1 when peak strength 'softens' to its critical value. Since the original authors present successful softening simulations, they likely follow this approach, though their wording may create ambiguity.

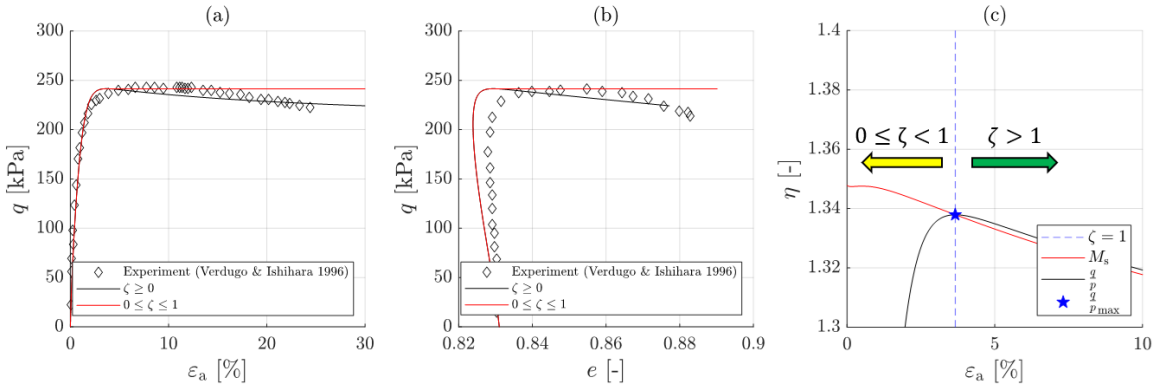

Figure 4.11: Demonstration of softening and non-softening behaviour with a drained monotonic triaxial compression test on a Toyoura sand sample with an initial void ratio $e_{in} = 0.831$ and an initial mean effective stress $p_{in} = 100$ kPa (Verdugo and Ishihara, 1996), using Ta-Ger B model, implemented with the explicit RKF23 integration scheme: (a) stress-strain response; (b) void ratio-stress response ; (c) zoomed-in stress-strain response ($\zeta \geq 0$).

4.3 Key features of the proposed high-cycle formulation

As shown in section 2.4.2, since the original Ta-Ger publications (Tasiopoulou and Gerolymos, 2016a; 2016b), Ta-Ger A, recognized as the flagship formulation, has been further developed, applied, and validated across various practical scenarios. However, these applications primarily focused on short-term cyclic events with a limited number of cycles, overlooking challenges specific to the modelling of high-cycle loading and its effects on sand surrounding OWT monopile foundations. This section presents the key features of a new high-cycle Ta-Ger version, termed Ta-Ger HC. The development of Ta-Ger HC was guided by computational studies evaluating the impact of incorporating new constitutive

elements into the original Ta-Ger framework, following a strategy similar to that employed by Taborda et al. (2014), who enhanced an existing bounding surface plasticity model for undrained monotonic and cyclic loading. Three constitutive components were examined: (i) the elasticity law; (ii) the evolution equations for the bounding surface stress ratio, M_{s}, and the phase transformation stress ratio, M_{pt}; and (iii) the evolution equation for the hardening exponent n. Ta-Ger HC is primarily defined by the first two components (i,ii), which are essential for capturing high-cycle behaviour. The third revised component (iii) is not strictly part of the core formulation but rather highlights the model's flexibility. The importance of each component was evaluated individually, showing the need for these enhancements within the high-cycle context. Furthermore, the significance of adopting a robust integration algorithm for the simulation of sand behaviour under extended cyclic loads is demonstrated via sensitivity analysis and the comparison of two explicit integration schemes. Since Ta-Ger HC is derived from the original Ta-Ger model, all other constitutive components remain unchanged and are not reiterated here. The performance of Ta-Ger HC is assessed using single-element simulations and comparisons with experimental data. Ta-Ger HC offers enhanced accuracy in simulating the long-term cyclic behaviour of sand, without losing its predictive capability for short-term events. Specifically, the new model demonstrates improved proficiency in predicting the transition from ratcheting to shakedown and provides realistic estimations of the accumulated strain magnitude even up to 10000 cycles.

4.3.1 Hyperelasticity

4.3.1.1 Motivation for inclusion of a hyperelastic law in Ta-Ger HC

The small-strain response of the soil is important in geotechnical problems like the design of OWT foundations (Oh *et al.*, 2018). As stated by Lan et al. (2023), small-strain conditions occur in OWT foundations under two circumstances: (i) when the foundations are subjected to high-cycle loading with very small amplitudes inducing only a limited amount of

irreversible cyclic strain; and (ii) during a cyclic loading event, at the two extremities of load within a cycle, since stress reversal takes place causing the soil to behave elastically. While linear elasticity provides a straightforward approach to depicting the mechanical response of soil under small strains within the elastic range, considering the nonlinear and anisotropic aspects of the elasticity are important when predicting sand ratcheting for OWT foundations under serviceability conditions (Lan et al., 2023). Furthermore, it has been demonstrated that adopting an elasticity formulation which violates the first law of thermodynamics can lead to the accumulation of significant residual strain within the soil element, even under purely elastic loading conditions (Einav, 2012). Therefore, employing a non-physically sound elastic relationship could yield a nonconservative response, leading to the spurious accumulation of elastic deformation energy under high-cycle loads (Lan et al., 2023). The original Ta-Ger, like many established constitutive models (see section 2.3, e.g., Dafalias and Manzari (2004)), employs a nonlinear hypoelastic law (Richart et al., 1970) that lacks thermodynamic consistency. Lan et al. (2023) showed that upgrading a bounding surface elastoplasticity model, SANISAND-MS (Liu *et al.*, 2019), by substituting the hypoelastic law with a hyperelastic one, improved its predictive capability in high-cycle simulations. This improvement suggested promising implications for the Ta-Ger model. However, unlike SANISAND-MS, which incorporates a yield locus defining a region of purely elastic behaviour, Ta-Ger lacks such a region (except under isotropic loading and unloading). This key difference further underscores the need to investigate the impact of introducing a hyperelastic formulation into Ta-Ger.

4.3.1.2 Equations of the nonlinear anisotropic hyperelastic law

The nonlinear anisotropic hyperelastic law used in the upgraded Ta-Ger HC model was initially proposed by Houlsby et al. (2019) and was subsequently critically analysed and validated by Amorosi et al. (2020). Houlsby et al. (2019) examined the nonlinearity and

anisotropy independently whereas, Amorosi et al. (2020) introduced a simplified nonlinear anisotropic hyperelastic formulation employing a switch parameter N, to establish the stress datum point at zero strain ($N = 0$). Consistent with Lan et al. (2023), who used the same hyperelastic law for their upgraded SANISAND-MS model, the reference stress point for zero elastic strain along the isotropic axis was assumed to be equivalent to a reference pressure, denoted as P_{r}, set at atmospheric pressure, p_{at}, by assuming $N = 1$. Hence, the adopted hyperelastic law allows for complete coupling of the soil nonlinearity and anisotropy (Lan et al., 2023). The hyperelasticity law under investigation, implies that stress, $\boldsymbol{\sigma}$, can be accurately derived from elastic strain energy, $\mathrm{E}(\boldsymbol{\varepsilon})$, by taking the partial differential of $\mathrm{E}(\boldsymbol{\varepsilon})$ with respect to the strain tensor as $\boldsymbol{\sigma} = \partial \mathrm{E}(\boldsymbol{\varepsilon})/\partial \boldsymbol{\varepsilon}$. Alternatively, the strain tensor $\boldsymbol{\varepsilon}$ can be obtained as a partial differential of complementary energy, $\mathrm{C}(\boldsymbol{\sigma})$, with respect to the stress tensor as $\boldsymbol{\varepsilon} = \partial \mathrm{C}(\boldsymbol{\sigma})/\partial \boldsymbol{\sigma}$. These two expressions are related through a Legendre transform, with the former approach being applied here. The elastic strain energy function proposed by Houlsby et al. (2019) is expressed as:

$$\mathrm{E}(\bar{\boldsymbol{\varepsilon}}, \mathbf{a}) = \frac{P_{\mathrm{r}}}{k(2-\mathrm{n})}\left(\bar{r}_0^{\frac{2-\mathrm{n}}{1-\mathrm{n}}} - N\right) \tag{4.31}$$

in which k is a dimensionless bulk modulus, $0 \leq \mathrm{n} < 1$ is a parameter accounting for the nonlinearity dependence on pressure, $\bar{\boldsymbol{\varepsilon}}$ is the equivalent strain tensor which can be defined as $\bar{\boldsymbol{\varepsilon}} = \mathbf{a}\boldsymbol{\varepsilon}\mathbf{a}$. Here $\mathbf{a}$ is a symmetric fabric tensor quantifying the degree of anisotropy of the soil arising from its internal microstructural characteristics (Lashkari, 2010; Amorosi et al., 2020). Using the normalized approach, where $\det(\mathbf{a}) = 1$, the fabric tensor $\mathbf{a}$ can be defined as follows:

$$\mathbf{a} = \begin{bmatrix} y^{\frac{1}{3}} & 0 & 0 \\ 0 & y^{\frac{1}{3}} & 0 \\ 0 & 0 & y^{-\frac{2}{3}} \end{bmatrix} \tag{4.32}$$

where y^2 corresponds to the shear modulus ratio $G_{\mathrm{hh}}/G_{\mathrm{vh}}$ (with the assumption that the third axis represents the vertical direction). G_{hh} and G_{vh} are the horizontal and vertical shear moduli respectively, which according to Amorosi et al. (2020) can be determined using bender element probing. y can be expressed as:

$$y = a_{11}/a_{33} \tag{4.33}$$

where a_{11} and a_{33} are two diagonal elements of the fabric tensor **a** in its initial form, which served as the basis for deriving equation (4.32) and is expressed as (Houlsby et al., 2019):

$$\mathbf{a} = \begin{bmatrix} a_{11} & 0 & 0 \\ 0 & a_{22} & 0 \\ 0 & 0 & a_{33} \end{bmatrix} \tag{4.34}$$

For the sake of simplicity only transverse anisotropy was considered here, with $a_{11} = a_{22} \neq a_{33}$ (Lan et al., 2023), and the parameter y was incorporated. It is important to highlight that when $y = 1$ is applied to equation (4.32), **a** simplifies to the identity tensor, signifying isotropic elasticity, without sacrificing generality. The variable $\bar{r}_0$ in equation (4.31) corresponds to a positive root as defined by Amorosi et al. (2020):

$$\bar{r}_0^2 = k(1-\mathrm{n})\left\{\left[k(1-\mathrm{n}) - \frac{2}{3}g\right]\mathrm{tr}^2\,(\bar{\boldsymbol{\varepsilon}}) + 2g\mathrm{tr}\,(\bar{\boldsymbol{\varepsilon}}^{\mathrm{sym}})\right\} + N[N - 2k(1-\mathrm{n})\mathrm{tr}\,(\bar{\boldsymbol{\varepsilon}})] \tag{4.35}$$

where $\bar{\boldsymbol{\varepsilon}}^{\mathrm{sym}}$ represents a symmetric equivalent strain tensor and g denotes the dimensionless shear modulus. The dimensionless bulk modulus k is obtained from $\frac{g}{k} = \frac{3(1-2v)}{2(1+v)}$ assuming a constant Poisson's ratio, v. According to the principles of hyperelasticity, the stress tensor can be obtained from differentiating equation (4.31) with respect to the equivalent strain tensor, as $\boldsymbol{\sigma} = \partial \mathrm{E}(\bar{\boldsymbol{\varepsilon}}, \mathbf{a})/\partial\bar{\boldsymbol{\varepsilon}}$. The increment of the stress tensor, $\dot{\boldsymbol{\sigma}}$, can be obtained by further differentiation as:

$$\dot{\boldsymbol{\sigma}} = \frac{\partial \boldsymbol{\sigma}}{\partial \boldsymbol{\varepsilon}} : \dot{\boldsymbol{\varepsilon}} = \left[\frac{\partial \bar{\boldsymbol{\varepsilon}}}{\partial \boldsymbol{\varepsilon}} : \frac{\partial^2 \mathrm{E}(\bar{\boldsymbol{\varepsilon}}, \mathbf{a})}{\partial \bar{\boldsymbol{\varepsilon}} \otimes \partial \bar{\boldsymbol{\varepsilon}}} : \frac{\partial \bar{\boldsymbol{\varepsilon}}}{\partial \boldsymbol{\varepsilon}}\right] : \dot{\boldsymbol{\varepsilon}} \tag{4.36}$$

By performing all the mathematical operations needed, and given that $\frac{\partial \bar{\boldsymbol{\varepsilon}}}{\partial \boldsymbol{\varepsilon}} = \mathbf{a} \bar{\otimes} \mathbf{a}$, the elastic stiffness tensor, $\mathbb{D}$, can be obtained from equation (4.36) as:

$$\mathbb{D} = \mathbf{a} \bar{\otimes} \mathbf{a} : \frac{\partial^2 \mathrm{E}(\bar{\boldsymbol{\varepsilon}}, \mathbf{a})}{\partial \bar{\boldsymbol{\varepsilon}} \otimes \partial \bar{\boldsymbol{\varepsilon}}} : \mathbf{a} \bar{\otimes} \mathbf{a} = \frac{P_{\mathrm{r}}}{k(1-\mathrm{n})} \mathbf{a} \bar{\otimes} \mathbf{a} : \left(\frac{1}{1-\mathrm{n}} \bar{r}_0^{\frac{\mathrm{n}}{1-\mathrm{n}}} \mathbf{A} \otimes \mathbf{A} + \bar{r}_0^{\frac{1}{1-\mathrm{n}}} \mathbb{C} \right) : \mathbf{a} \bar{\otimes} \mathbf{a} \tag{4.37}$$

where:

$$\mathbf{A} = \frac{\partial \bar{r}_0}{\partial \bar{\boldsymbol{\varepsilon}}} = \frac{k(1-n)}{\bar{r}_0} \left\{ \left[k(1-\mathrm{n}) - \frac{2}{3} g \right] \mathrm{tr}\,(\bar{\boldsymbol{\varepsilon}}) \mathbf{I} + 2g \bar{\boldsymbol{\varepsilon}}^{\mathrm{sym}} \right\} - \frac{kN}{\bar{r}_0} (1-\mathrm{n}) \mathbf{I} \tag{4.38}$$

$$\mathbb{C} = \frac{\partial^2 \bar{r}_0}{\partial \bar{\boldsymbol{\varepsilon}} \otimes \partial \bar{\boldsymbol{\varepsilon}}} = \frac{1}{\bar{r}_0} \left\{ k(1-\mathrm{n}) \left[k(1-\mathrm{n}) - \frac{2}{3} g \right] \mathbf{I} \otimes \mathbf{I} + 2gk(1-\mathrm{n}) \mathbf{I} \otimes \mathbf{I} - \frac{\partial \bar{r}_0}{\partial \bar{\boldsymbol{\varepsilon}}} \otimes \frac{\partial \bar{r}_0}{\partial \bar{\boldsymbol{\varepsilon}}} \right\} \tag{4.39}$$

Derivation details of equations (4.36)-(4.39) can be found in Lan et al. (2023). In these expressions, $\otimes$ is the standard outer product of two second-order tensors, defined in subscript notation as $\boldsymbol{a} \otimes \boldsymbol{b} = a_{ij} b_{kl}$, while $\bar{\otimes}$ represents a modified outer product with interchanged indices, defined as $\boldsymbol{a} \bar{\otimes} \boldsymbol{b} = a_{ik} b_{jl}$ (Houlsby et al., 2019).

4.3.1.3 Purely elastic single-element simulations

To delineate the fundamental differences between employing a thermodynamically consistent elastic law and an inadmissible one, single-element simulations were conducted utlilizing both the hypoelastic model (Richart et al., 1970) and the hyperelastic model (Houlsby et al., 2019). Both models were implemented in multiaxial stress space, adopting the RKF23 integration scheme, with the constitutive parameters detailed in Table 4.2.

Table 4.2: Model parameters for the purely elastic single-element simulations.

Hypoelastic model (Richart et al., 1970)		**Hyperelastic model** (Houlsby et al., 2019)	
Symbol	Value	Symbol	Value
m	0.5	n	0.3
v	0.15	v	0.15
G_0	130	k	330
-	-	y	0.9
-	-	N (switch)	1

Figure 4.12 and Figure 4.13 portray closed elastic stress paths simulated with the hypoelastic and the hyperelastic model, respectively. These paths represent a reversible process through sequential stress states a1, a2, a3, a4, before finally returning to the initial stress state a1. Figure 4.12b-Figure 4.12d show the histories of deviatoric stress (q) versus deviatoric strain (ε_q) (b1-b5), volumetric strain (ε_v) versus deviatoric strain (ε_q) (c1-c5), mean effective stress (p) versus volumetric strain (ε_v) (d1-d5), as simulated using the hypoelastic model. Corresponding results from the hyperelastic model are shown in Figure 4.13b-Figure 4.13d. Additionally, Figure 4.12e and Figure 4.13e illustrate the evolution of total strain (ε), defined following Wichtmann (2005) as $\varepsilon = \sqrt{(\varepsilon_\mathrm{v})^2/3 + 1.5(\varepsilon_q)^2}$, where ε_v and ε_q represent volumetric and deviatoric strain, respectively. During cyclic loading, the total strain has two distinct components: an accumulated, residual part ('acc'), $\varepsilon^{\mathrm{acc}}$, and an elastic, resilient part ('ampl'), $\varepsilon^{\mathrm{ampl}}$ (Wichtmann, 2005). Given the reversible nature of the stress path and considering that elastic materials do not retain any deformation upon load removal, both strain components and thus total strain (ε) should be zero at the conclusion of the elastic stress path ($\mathrm{N} = 1$). However, as shown in Figure 4.12e, this condition is not satisfied for the hypoelastic model. Despite complete recovery of volumetric strain, ε_v, the hypoelastic model exhibits accumulated deviatoric strain, ε_q, resulting in a non-zero total strain, ε. In contrast, the hyperelastic model adheres to the energy conservation principles inherent in elasticity theory, giving fully reversible deviatoric strain, ε_q, and volumetric strain, ε_v, thereby yielding a zero ε.

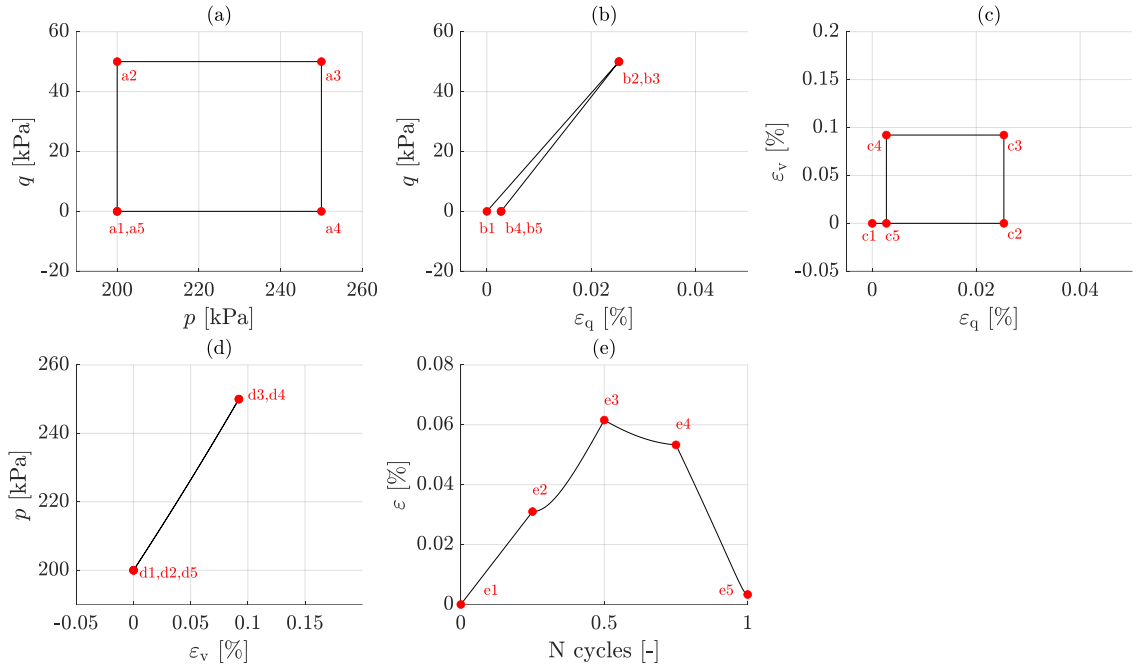

Figure 4.12: Closed elastic stress path simulations (N = 1) for an initial void ratio $e_{in} = 0.580$ and an initial mean effective stress $p_{in} = 200$ kPa, using the hypoelastic model (Richart et al., 1970): (a) $p - q$; (b) $\varepsilon_q - q$; (c) $\varepsilon_q - \varepsilon_v$; (d) $\varepsilon_v - p$; (e) $N - \varepsilon$.

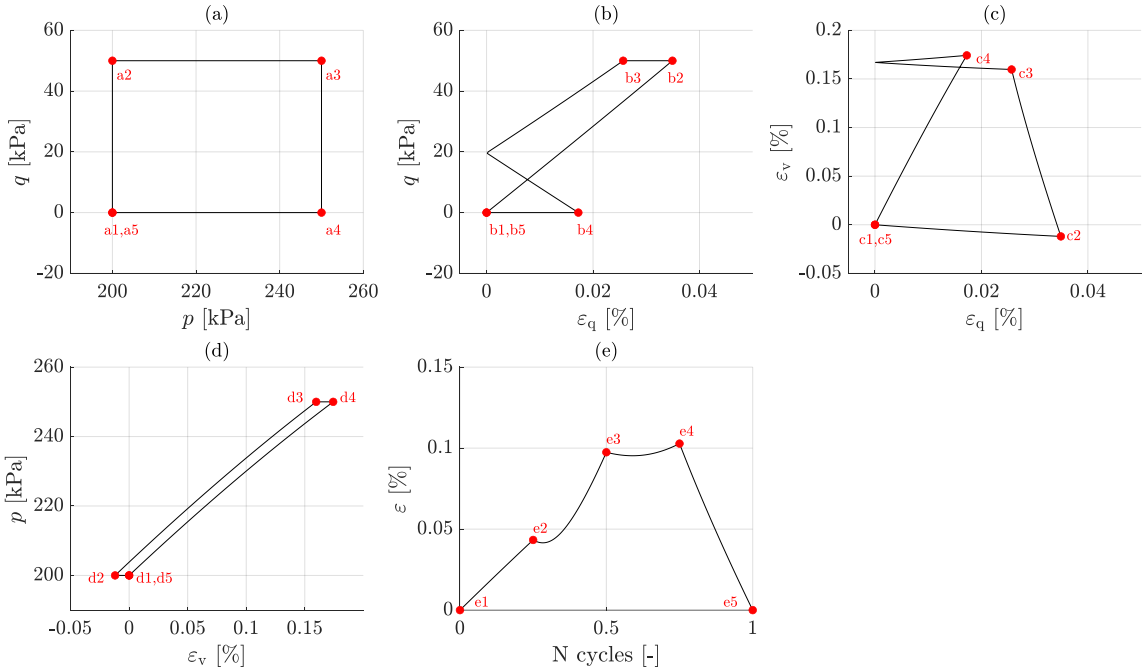

Figure 4.13: Closed elastic stress path simulations (N = 1) for an initial void ratio $e_{in} = 0.580$ and an initial mean effective stress $p_{in} = 200$ kPa, using the hyperelastic model (Houlsby et al., 2019): (a) $p - q$; (b) $\varepsilon_q - q$; (c) $\varepsilon_q - \varepsilon_v$; (d) $\varepsilon_v - p$; (e) $N - \varepsilon$.

Two additional simulations sets were conducted, qualitatively reproducing the closed stress path depicted in Figure 4.13 but with reduced magnitudes: q ranged from 0 to 1.5 kPa, and p varied from 200 to 201 kPa. Figure 4.14 and Figure 4.15 depict the results of repeating these stress paths 10 and 10000 times, respectively, highlighting significant qualitative and

quantitative differences between the two models. Both models demonstrated no accumulation of volumetric strain, ε_v, aligning with earlier observations at higher amplitudes. However, the hypoelastic model displayed considerable accumulation of deviatoric strain, ε_q, reaching approximately 0.02% after $N = 10000$ cycles. Conversely, the hyperelastic model predicted complete strain recovery, consistent with energy conservation principles.

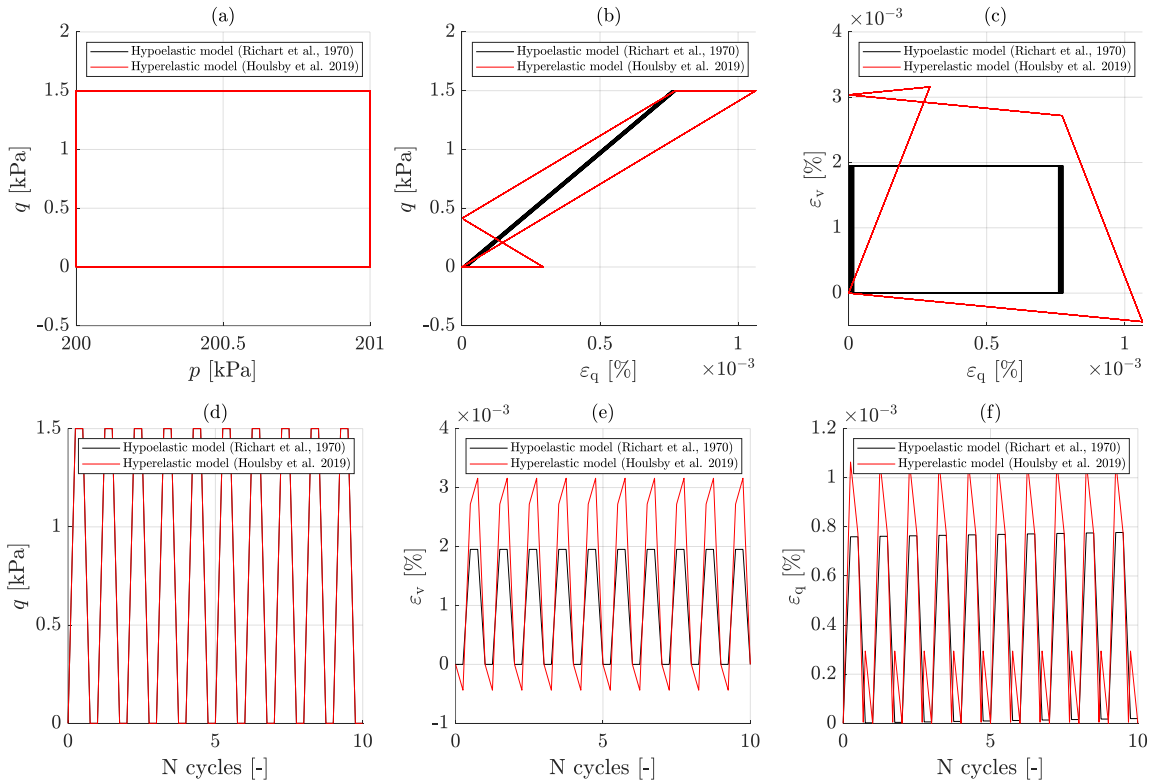

Figure 4.14: Closed elastic stress path simulations ($N = 10$), with the hypoelastic model (Richart et al., 1970) and the hyperelastic model (Houlsby et al., 2019), assuming an initial void ratio $e_{in} = 0.580$ and an initial mean effective stress $p_{in} = 200$ kPa: (a) $p - q$; (b) $\varepsilon_q - q$; (c) $\varepsilon_q - \varepsilon_v$; (d) $N - q$; (e) $N - \varepsilon_v$; (f) $N - \varepsilon_q$.

Similar findings were reported by Duque et al. (2022) for circular closed loop cycles and by Lan et al. (2023) for a stress path resembling that studied here. However, both research teams embedded elasticity laws within elastoplastic models, a methodology not aligned with the present study's objectives at this stage. This investigation specifically employs elasticity laws independently, emphasizing their fundamental behaviour. These analyses underscore the importance of selecting suitable elasticity models to accurately simulate long-term cyclic soil-structure interactions, with obvious implications for robust modelling of OWT

foundations under high-cycle wind or wave loading conditions. It is crucial to select an elasticity model that prevents spurious strain accumulation, thereby avoiding additional strains beyond those genuinely induced by plasticity when the elasticity equations are later integrated into elastoplastic models.

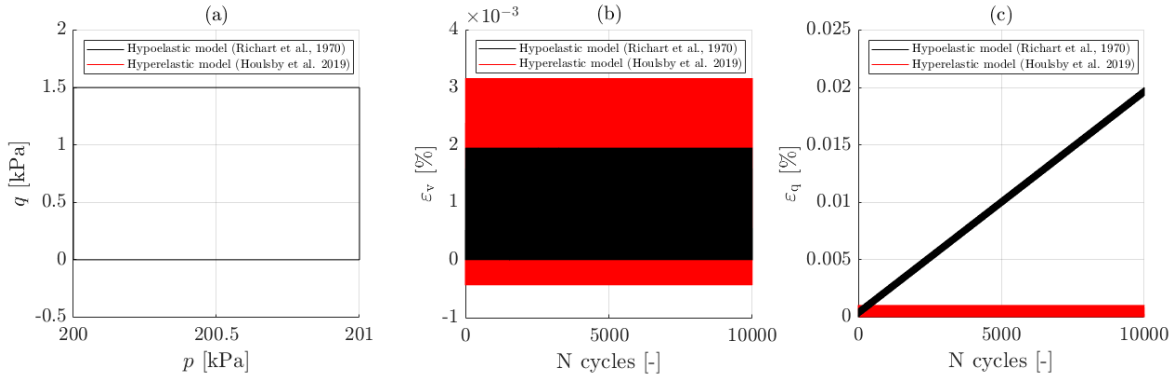

Figure 4.15: Closed elastic stress path simulations (N = 10000), with the hypoelastic model (Richart et al., 1970) and the hyperelastic model (Houlsby et al., 2019), assuming an initial void ratio $e_{\mathrm{in}} = 0.580$ and an initial mean effective stress $p_{\mathrm{in}} = 200$ kPa: (a) $p - q$; (b) $\mathrm{N} - \varepsilon_{\mathrm{v}}$; (c) $\mathrm{N} - \varepsilon_{\mathrm{q}}$.

4.3.1.4 Hyperelastic upgrade of Ta-Ger model

This study assesses the impact of replacing the hypoelastic law (Richart et al., 1970) with a hyperelastic law (Houlsby et al., 2019) in the Ta-Ger A and Ta-Ger B models. The original and upgraded formulations of the models were evaluated using monotonic and cyclic tests by Wichtmann (2005) on quartz sand No. 3 (mean diameter $D_{50} = 0.55$ mm, uniformity coefficient $C_{\mathrm{u}} = 1.8$, maximum and minimum void ratios $e_{\max} = 0.874$, $e_{\min} = 0.577$). Parameters for all four formulations are listed in Table 4.3.

Ta-Ger B incorporates constitutive components similar to those in SANISAND-family models, such as SANISAND-MS (Liu *et al.*, 2019) and its hyperelasticity-enhanced variant (Lan et al., 2023), including elasticity equations, CSL, and bounding surface and phase transformation stress ratios. Common parameters governing these equations remained consistent upon incorporation into Ta-Ger B and were adopted from previous studies (Liu et al., 2019; Lan et al., 2023) that used identical experimental data (Wichtmann, 2005), with

minor modifications for optimal data fit, as discussed below. For the original Ta-Ger B model, CS parameters (M_{cs}, e_0, λ and ξ), along with parameters n_b and n_d governing the evolution of the bounding surface and phase transformation stress ratios, were kept unchanged, as obtained from Liu et al. (2019), slightly modifying only the hypoelasticity parameters, G_0 and v. For the upgraded Ta-Ger B model, hyperelasticity parameters k, v, n, y, N were acquired from Lan, Liu and Zhao (2023). The dilatancy parameter, α, needed for all Ta-Ger formulations, was calibrated by fitting volumetric responses from the drained monotonic triaxial tests shown in Figure 4.16. For monotonic loading, the hardening exponent, n, was set as a constant (Tasiopoulou and Gerolymos, 2016a) and calibrated through fitting the stress-strain responses of Figure 4.16. Original Ta-Ger A monotonic parameters were calibrated following Tasiopoulou and Gerolymos (2016a; 2016b), which again involved fitting the tests of Figure 4.16. Hyperelasticity parameters for upgraded Ta-Ger A matched those of the upgraded Ta-Ger B case. Cyclic parameters n_0, n_{peak}, n_f, β and γ, for all Ta-Ger models were calibrated through trial-and-error fitting to match the cyclic strain accumulation shown in Figure 4.18, particularly for the case of $q^{ampl} = 60$ kPa.

This stage of the study evaluates the impact of substituting two elasticity laws on the elastoplastic performance of Ta-Ger A and Ta-Ger B models, with a particular emphasis on their elastic components. The close agreement between simulated and measured results shown in Figure 4.16, which covers various initial void ratios and mean effective stresses, confirms the reliability of the parameter calibrations. Furthermore, the observed similarity in the initial segments of the stress-strain curves between the original and upgraded versions of both models demonstrates a consistent calibration of the hypoelastic and hyperelastic components. When comparing the original Ta-Ger formulations with their upgraded counterparts, it is evident that changing the elasticity laws leads only to minor alterations in the monotonic responses. This consistency indicates that any differences observed during

high-cycle tests can be attributed to the specific elasticity formulations rather than calibration discrepancies. Accordingly, additional calibration of the elastic parameters was considered unnecessary within the context of this study, as the current parameter sets provided satisfactory agreement with experimental data.

Table 4.3: Model parameters for quartz sand No. 3 tested by Wichtmann (2005) (Lan et al., 2023).

	Ta-Ger A				**Ta-Ger B**			
	Original		**Upgraded**		**Original**		**Upgraded**	
Feature	Symbol	Value	Symbol	Value	Symbol	Value	Symbol	Value
Elasticity	G_0	130	k	330	G_0	130	k	330
	v	0.15	v	0.15	v	0.15	v	0.15
	m	0.8	n	0.3	m	0.5	n	0.3
	-	-	y	0.9	-	-	y	0.9
	-	-	N (switch)	1	-	-	N (switch)	1
Critical state	M_{cs}	1.27	M_{cs}	1.27	M_{cs}	1.27	M_{cs}	1.27
	-	-	-	-	e_0	0.845	e_0	0.845
	-	-	-	-	λ	0.049	λ	0.049
	-	-	-	-	ξ	0.27	ξ	0.27
Bounding surface & Dilatancy	Q	10	Q	10	n_b	2	n_b	2
	R	0.7	R	0.7	n_d	1.17	n_d	1.17
	c	5	c	5	-	-	-	-
	α	0.3	α	0.3	α	0.3	α	0.3
Hardening exponent n^*	n_0	0.8	n_0	0.8	n_0	0.5	n_0	0.5
	n_f	0.3	n_f	0.3	n_f	0.3	n_f	0.3
	n_{peak}	8.5	n_{peak}	8.5	n_{peak}	6.5	n_{peak}	6.5
	β	7	β	7	β	8	β	8
	γ	30	γ	30	γ	30	γ	30
	$^*n = 0.35$ for monotonic loading				$^*n = 0.15$ for monotonic loading			

This decision is also motivated by a fundamental conceptual distinction between the two elasticity laws concerning their treatment of density effects. In the original Ta-Ger formulations, the hypoelastic law depends explicitly on both mean effective stress and void ratio, whereas in the upgraded Ta-Ger formulations the hyperelastic law depends solely on mean effective stress and incorporates intrinsic anisotropy, without explicit void ratio dependence. As a result, density effects in the upgraded formulations are reflected only

through the plastic response, rather than through both elastic and plastic components as in the original Ta-Ger models.

Within the scope of this chapter, no additional density-dependent calibration of the hyperelastic parameters was introduced, since the adopted parameter set reproduces the experimental response adequately over the range of initial void ratios considered. If density effects on elastic stiffness were to be incorporated explicitly, this could be achieved through targeted calibration of the hyperelastic stiffness parameter g, and the associated bulk modulus parameter k, assuming a constant Poisson's ratio v, against small-strain stiffness data obtained at different initial void ratios. While the use of void-ratio-specific elastic parameters would conflict with the unified parameter philosophy inherent to the critical state framework, an alternative approach would involve selecting a representative reference void ratio based on the experimental dataset and calibrating g at that state. In this context, where the parameter G_0 has already been calibrated for the hypoelastic formulation, the tangent shear stiffness inferred from equation (4.2) could be used to establish a consistent correspondence with the hyperelastic response on the isotropic axis. A single effective value of g, and hence k, could then be defined by averaging stiffness across the relevant void ratio range, providing a practical means of accounting for density effects while retaining a single parameter set (see chapter 5). For the present study, it was verified that the adopted values of G_0 in the original Ta-Ger formulations and the corresponding g and k values in the upgraded formulations are compatible with this conceptual approach, ensuring consistency within the intended modelling framework.

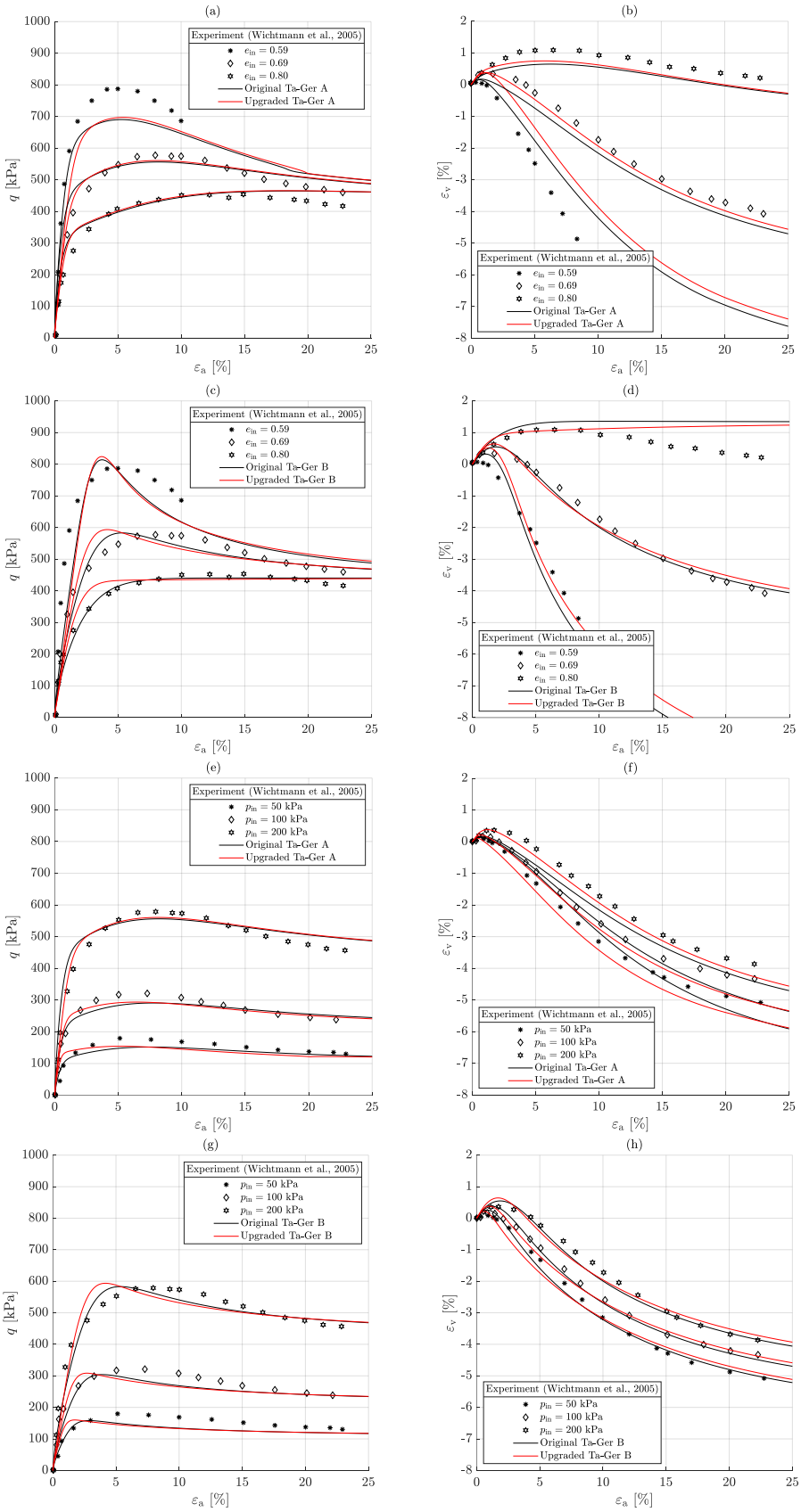

Figure 4.16: Calibration of parameters against drained triaxial tests on quartz sand No. 3 (Wichtmann, 2005). Specifically, for Ta-Ger A: (a) $\varepsilon_a - q$ (constant p_{in}, varying e_{in}); (b) $\varepsilon_a - \varepsilon_v$ (constant p_{in}, varying e_{in}); (e) $\varepsilon_a - q$ (constant e_{in}, varying p_{in}); (f) $\varepsilon_a - \varepsilon_v$ (constant e_{in}, varying p_{in}). For Ta-Ger B: (c) $\varepsilon_a - q$ (constant p_{in}, varying e_{in}); (d) $\varepsilon_a - \varepsilon_v$ (constant p_{in}, varying e_{in}); (g) $\varepsilon_a - q$ (constant e_{in}, varying p_{in}); (h) $\varepsilon_a - \varepsilon_v$ (constant e_{in}, varying p_{in}).

To illustrate the effect of the inclusion of hyperelasticity within the Ta-Ger A and B models, the one-way asymmetric drained cyclic triaxial tests from Wichtmann (2005) were employed (section 2.2.1.2). These tests, summarized in Figure 4.17, involved isotropic consolidation to an initial mean effective stress (p_{in}), followed by shearing along a constant-p path to reach a specified a mean stress ratio ($\eta^{\mathrm{ave}} = q^{\mathrm{ave}}/p_{\mathrm{in}}$). Subsequently, cyclic loading was applied with amplitudes $q = q^{\mathrm{ave}} \pm q^{\mathrm{ampl}}$ under a consistent radial stress ($\sigma_{\mathrm{r}} = p_{\mathrm{in}}$). A convenient metric for evaluating the performance of a constitutive model in high-cycle triaxial tests is the magnitude of the accumulated total strain, $\varepsilon^{\mathrm{acc}}$, defined as (Wichtmann, 2005):

$$\varepsilon^{\mathrm{acc}} = \sqrt{\frac{1}{3}(\varepsilon_{\mathrm{v}}^{\mathrm{acc}})^2 + \frac{3}{2}(\varepsilon_{q}^{\mathrm{acc}})^2} \tag{4.40}$$

in which $\varepsilon_{\mathrm{v}}^{\mathrm{acc}}$ and $\varepsilon_{q}^{\mathrm{acc}}$ are the volumetric and deviatoric accumulated strain correspondingly. As shown in Figure 4.17c, $\varepsilon^{\mathrm{acc}}$ refers to the strain accumulation during regular cycles of a cyclic triaxial test (after the first 'irregular' loading cycle).

Figure 4.18 demonstrates how varying the cyclic amplitude, q^{ampl}, influences the ratcheting behaviour of sand. At a lower amplitude ($q^{\mathrm{ampl}} = 31$ kPa), strain accumulation ceases after approximately $\mathrm{N} = 1000$ loading cycles, a phenomenon termed cyclic shakedown, which both the Ta-Ger A and B models accurately simulate. At this amplitude, incorporating hyperelasticity in place of hypoplasticity has negligible impact. However, for higher cyclic amplitudes ($q^{\mathrm{ampl}} = 60$ kPa and $q^{\mathrm{ampl}} = 80$ kPa), ongoing strain accumulation (ratcheting) occurs, with increased amplitudes yielding greater final accumulated strains ($\varepsilon^{\mathrm{acc}}$). For $q^{\mathrm{ampl}} = 60$ kPa, both the original and upgraded models perform similarly, with Ta-Ger A using hyperelasticity predicting slightly higher strain accumulation throughout the test but predicting identical final $\varepsilon^{\mathrm{acc}}$ values. The upgraded Ta-Ger B shows nearly identical strain accumulation trends to its original version, providing predictions nearer to the experimental

results. For $q^{\mathrm{ampl}} = 80$ kPa, the inclusion of the hyperelastic model significantly reduces strain accumulation after approximately $\mathrm{N} = 2000$ cycles, bringing both Ta-Ger A and Ta-Ger B into better alignment with the experimental curves.

Figure 4.19 depicts the impact of the initial void ratio, e_{in}, on sand ratcheting behaviour. Wichtmann's (2005) experimental findings confirm the expected trend of increased strain accumulation with higher e_{in}. Notably, the denser sand sample with $e_{\mathrm{in}} = 0.580$, exhibits shakedown behaviour beyond $\mathrm{N} = 1000$ cycles, while both the medium-dense ($e_{\mathrm{in}} = 0.674$) and loose ($e_{\mathrm{in}} = 0.803$) sand samples continue to accumulate strain. Consistent with observations in Figure 4.18, incorporating hyperelasticity has a more pronounced effect on samples exhibiting ratcheting behaviour, with the upgraded Ta-Ger B notably improving predictions for medium-dense and loose samples in comparison to experimental results.

Figure 4.20 depicts the effects of the initial mean effective stress, p_{in}, on ratcheting behaviour of sand, with the experiments indicating a minimal influence of the p_{in} on the $\varepsilon^{\mathrm{acc}} - \mathrm{N}$ curves. The effect of the hyperelasticity law inclusion on the simulated curves is also not as pronounced as for the simulations in Figure 4.18 and Figure 4.19.

In summary, Ta-Ger B demonstrates superior performance, particularly when hyperelasticity is incorporated. The upgraded models significantly enhance predictions of tests exhibiting intense ratcheting, without compromising accuracy in tests leading to cyclic shakedown. While the original Ta-Ger B generally outperforms the original Ta-Ger A, both models benefit notably from the inclusion of hyperelasticity. The upgraded Ta-Ger B, in particular, shows substantial promise for simulating high-cycle loading. Thus, incorporating hyperelasticity into the proposed Ta-Ger HC model is considered essential to ensure accurate predictions of sand behaviour under high-cycle loading.

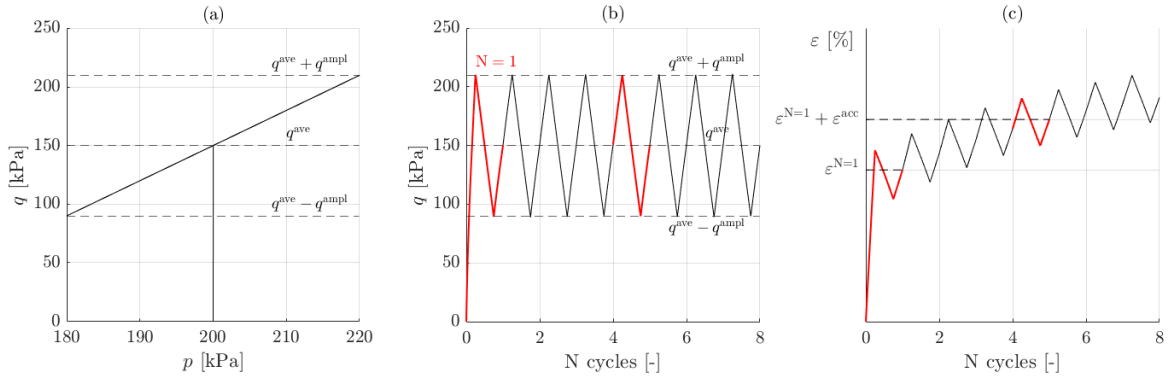

Figure 4.17: Illustration of: (a) stress paths; (b) shear loading sequence; (c) evolution of total strain, in the drained cyclic tests considered for simulation (Wichtmann, 2005).

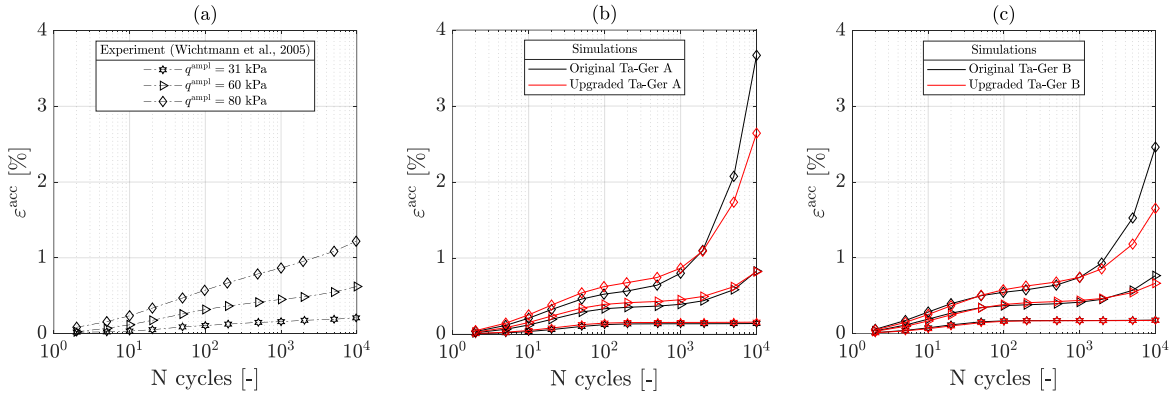

Figure 4.18: Influence of cyclic stress amplitude, q^{ampl}, on cyclic strain accumulation for quartz sand No. 3, with test/simulation settings $p_{in} = 200$ kPa, $\eta^{ave} = 0.75$, $e_{in} = 0.702$: (a) experimental data (Wichtmann, 2005); (b) original versus upgraded Ta-Ger A; (c) original versus upgraded Ta-Ger B.

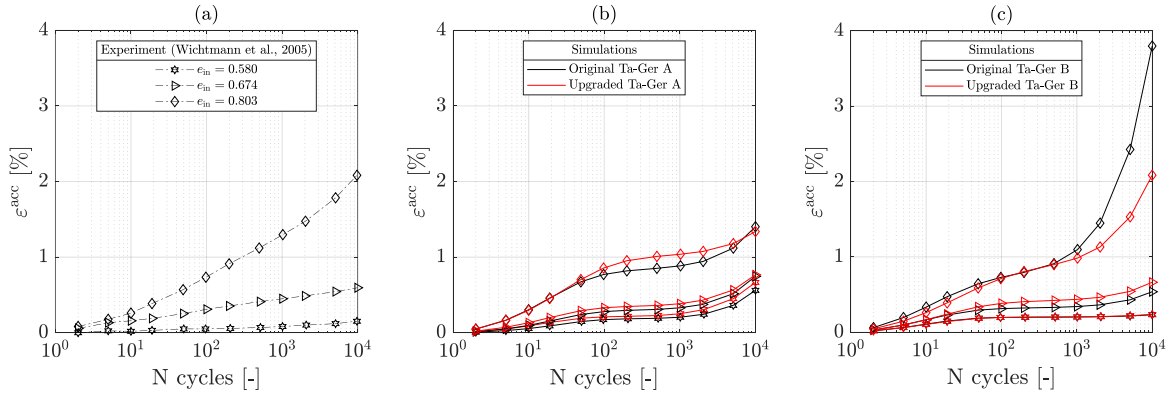

Figure 4.19: Influence of initial void ratio, e_{in}, on cyclic strain accumulation for quartz sand No. 3, with test/simulation settings $p_{in} = 200$ kPa, $\eta^{ave} = 0.75$, $q^{ampl} = 60$ kPa: (a) experimental data (Wichtmann, 2005); (b) original versus upgraded Ta-Ger A; (c) original versus upgraded Ta-Ger B.

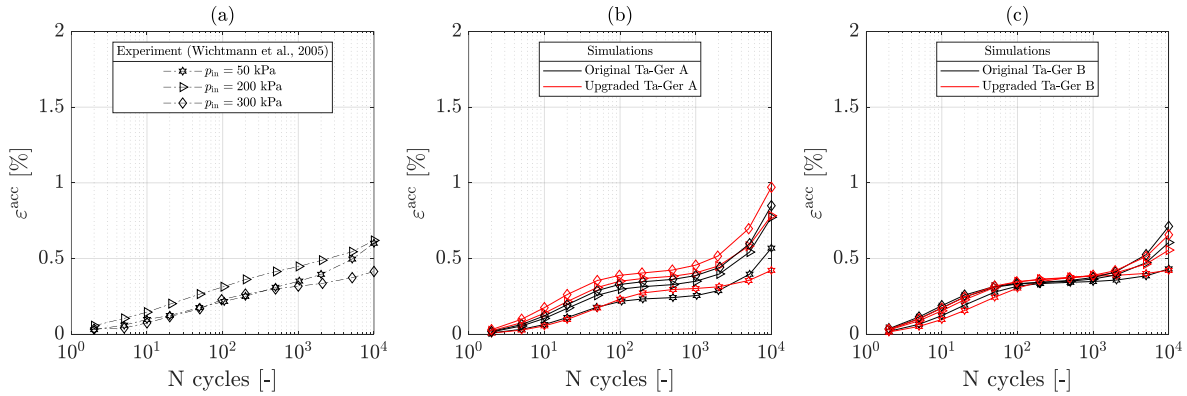

Figure 4.20: Influence of initial mean effective stress, p_{in}, on cyclic strain accumulation for quartz sand No. 3, with test/simulation settings $e_{in} = 0.684$, $\eta^{ave} = 0.75$, stress amplitude ratio $\varsigma^{ampl} = q^{ampl}/p_{in} = 0.3$: (a) experimental data (Wichtmann, 2005); (b) original versus upgraded Ta-Ger A; (c) original versus upgraded Ta-Ger B.

4.3.2 Bounding and phase transformation stress ratio equations

With the decision made to incorporate the hyperelastic law into the new high-cycle constitutive model, the next step is the selection of appropriate equations to ensure compliance with CST principles. This section elucidates the rationale behind the selection, providing insight into the underlying considerations. The final selection is justified based on extensive simulations, presenting only the key insights necessary for clarity.

4.3.2.1 Monotonic critical state compliance

A computational study, akin to Lashkari (2009), was used to evaluate the efficacy of equations for modelling state dependency of granular soils under monotonic loading. The study replicated monotonic triaxial compression tests on Toyoura sand (Verdugo and Ishihara, 1996) using parameters from Tasiopoulou and Gerolymos (2016a) (Table 4.1). Simulations were conducted up to high axial strains ($\varepsilon_a = 100\%$), exceeding experimental limits, to evaluate the models' performance.

Figure 4.21 shows simulations of a drained monotonic triaxial test on Toyoura sand ($e_{in} = 0.810$ and $p_{in} = 500$ kPa) utilizing the Ta-Ger A and Ta-Ger B models. The initial state parameter (ψ_{in}) is estimated as $\psi = e - e_c$, where e_c follows equation (4.20) with CSL parameters from Table 4.1 yielding $\psi_{in} = -0.065$. This indicates a 'denser-than-critical'

response, transitioning from contraction to dilation, with peak shear strength reducing to a residual value at high strains. Comparing the stress-strain curves from both models with experimental data (Figure 4.21a and Figure 4.21d), both adequately capture the observed behaviour. Regarding critical state compliance, Figure 4.21e, shows that in Ta-Ger B, ψ decreases from its initial value and gradually tends toward zero with increasing strain. This trend aligns with theoretical expectations, where ψ should reach zero upon the sample reaching critical state. Following the behaviour of ψ, stress ratios M_{s} and M_{pt}, as dictated by equation (4.19), tend towards the critical value, M_{cs}, with increasing strain values (Figure 4.21f), hence fulfilling the necessary critical state numerical postulate (Tasiopoulou and Gerolymos, 2016a). However, an inconsistent behaviour is observed for Ta-Ger A. Although the stress ratios M_{s} and M_{pt}, dependent on the state parameter, I_{r}, through equations (4.21) and (4.22), accurately converge towards M_{cs}, the state parameter I_{r} itself fails to approach values close to zero.

Similar conclusions apply to the simulations in Figure 4.22, where both models successfully capture the stress-strain response of Toyoura sand ($e_{\mathrm{in}} = 0.886$ and $p_{\mathrm{in}} = 500$ kPa). However, while Ta-Ger B remains consistent with CST, Ta-Ger A does not. Although M_{s} and M_{pt} eventually reach M_{cs}, the state parameter I_{r} crosses the x-axis and maintains a constant distance from zero, never converging to it. This discrepancy arises from two key factors: (i) the indirect dependence of M_{s} and M_{pt} on I_{r}, making critical state compatibility calibration-sensitive and effective only within specific density and stress ranges, and (ii) the inclusion of the cumulative incremental deviatoric strain, $\Sigma \mathrm{d}\varepsilon_q$, as an evolving state variable in the M_{s} and M_{pt} equations, which interferes with their dependency on I_{r}. These inconsistencies with fundamental CS principles raised concerns about incorporating Ta-Ger A's M_{s} and M_{pt} equations in the final model.

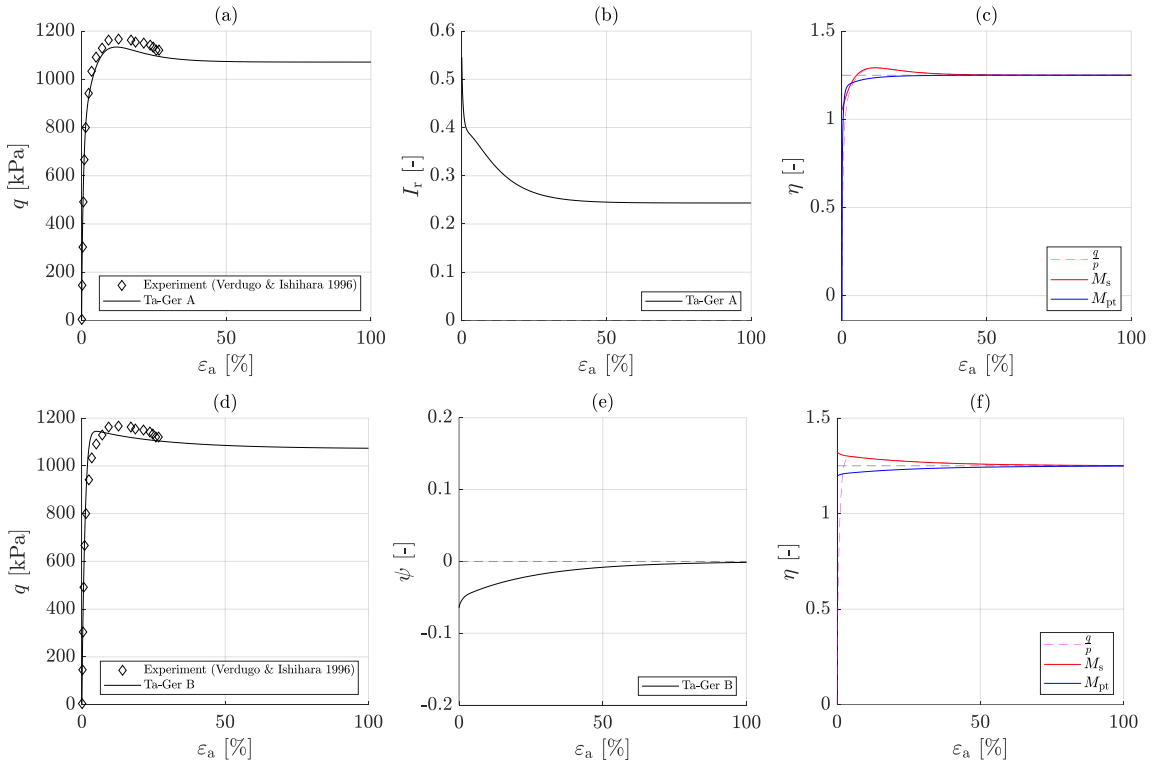

Figure 4.21: Simulations of a drained monotonic triaxial compression test on a Toyoura sand sample with an initial void ratio $e_{in} = 0.810$ and an initial mean effective stress $p_{in} = 500$ kPa (Verdugo and Ishihara, 1996), using: (a)-(c) the Ta-Ger A model; (d)-(f) the Ta-Ger B model.

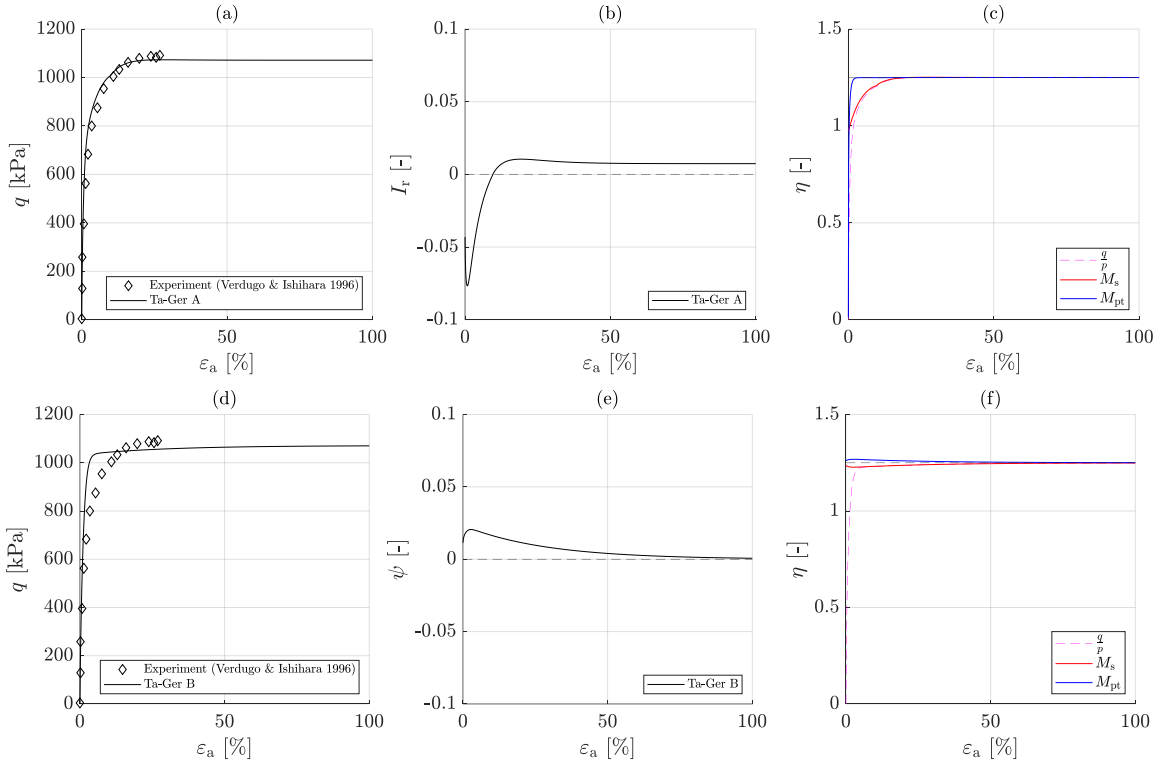

Figure 4.22: Simulations of a drained monotonic triaxial compression test on a Toyoura sand sample with an initial void ratio $e_{in} = 0.886$ and an initial mean effective stress $p_{in} = 500$ kPa (Verdugo and Ishihara, 1996), using: (a)-(c) the Ta-Ger A model; (d)-(f) the Ta-Ger B model.

4.3.2.2 Identified numerical-instability issue in Ta-Ger A

A key issue identified during the implementation and testing of Ta-Ger A pertains to numerical instabilities associated with the bounding stress ratio, M_s and its maximum value, M_{sp}, estimated via equations (4.21) and (4.25). This issue originates from the term appearing under the square root in equation (4.25). This term was derived as the discriminant of equation (4.21), substituting $\Sigma d\varepsilon_q$ at peak deviatoric stress (q) (Tasiopoulou and Gerolymos, 2016a), and hence is denoted here as Δ:

$$\Delta = \left(2M_{cs} - 4M_{speak}\right)^2 - 16M_{s0}\left(M_{speak} - M_{cs}\right) - 4{M_{cs}}^2 \tag{4.41}$$

Single-element simulations revealed instances where Δ became negative, particularly in softening cases, leading to numerical issues such as instability or non-convergence. Figure 4.23 illustrates this in a drained triaxial test on quartz sand No. 3 (Wichtmann, 2005), simulated using parameters from Table 4.1. The test was conducted twice: once using the absolute value of Δ for M_{sp} calculation and once using its non-absolute value. As shown in Figure 4.23a, Δ reaches zero at approximately 18% axial strain and becomes negative as loading progresses. Using the non-absolute Δ values generates complex numbers at these substeps. In MATLAB-based single-element simulations (RKF23 scheme), imaginary parts were disregarded, but in a commercial FE code, this would cause an immediate crash. Additionally, the integration error tolerance (STOL) had to be relaxed from 10^{-6} to 10^{-3} due to non-convergence. As evident in Figure 4.23a and Figure 4.23c, even when the absolute value of Δ is used, the resulting curves exhibit an unrealistic local minimum at $\Delta = 0$, progressively deviating from the curves calculated with the non-absolute Δ values. It can be concluded that this numerical instability renders the original Ta-Ger A formulation unsuitable for application in FE codes without careful mitigation, highlighting the substantial drawbacks of Ta-Ger A compared to Ta-Ger B in terms of robustness and numerical stability.

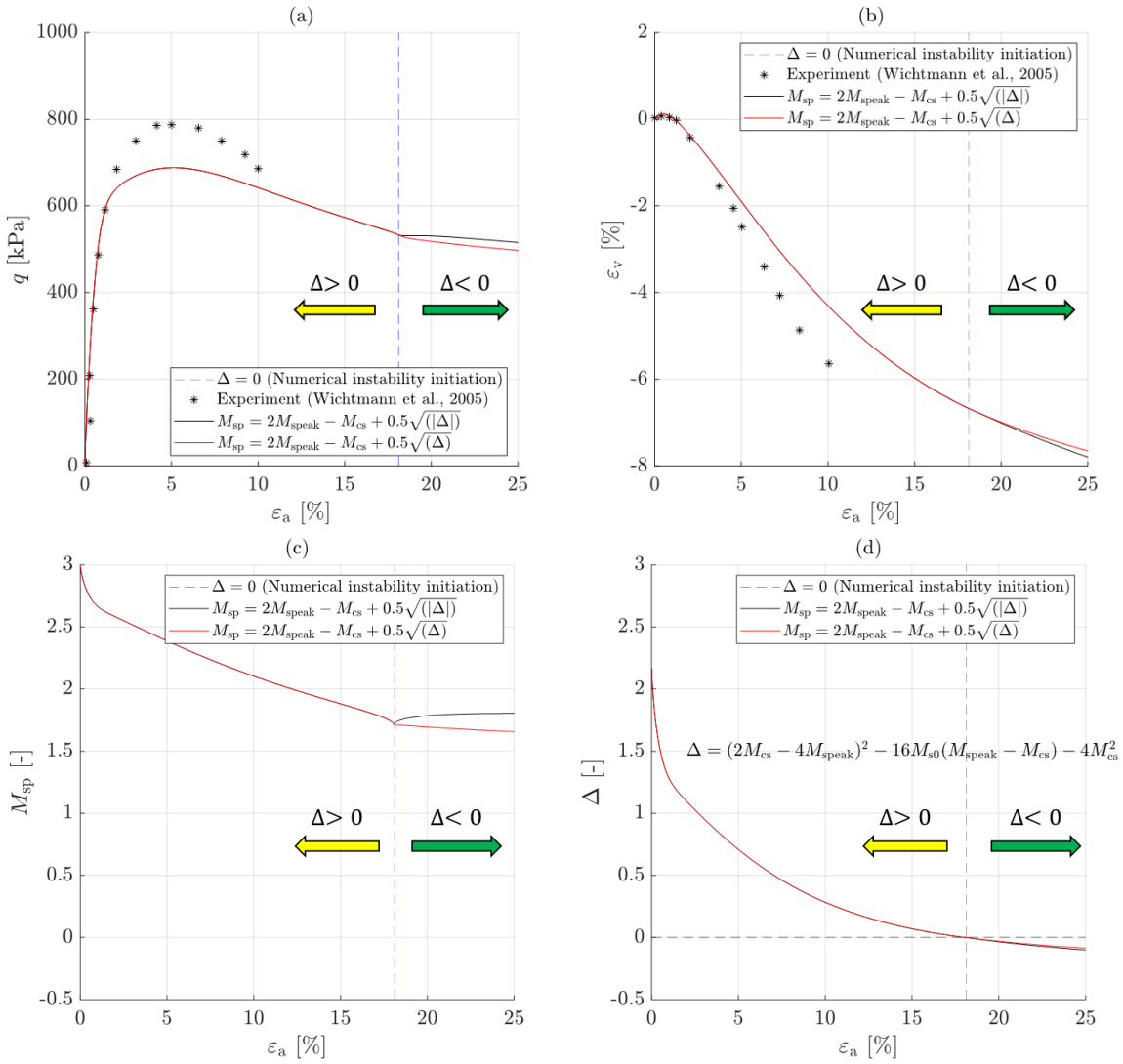

Figure 4.23: Simulations of a drained triaxial test on quartz sand No. 3 (Wichtmann, 2005) with an initial void ratio $e_{in} = 0.590$ and an initial mean effective stress $p_{in} = 200$ kPa, using the Ta-Ger A model. The simulations were conducted both with an absolute Δ term ($|\Delta|$) and a non-absolute Δ term (Δ), within the M_{sp} equation: (a) $\varepsilon_a - q$; (b) $\varepsilon_a - \varepsilon_v$; (c) $\varepsilon_a - M_{sp}$; (d) $\varepsilon_a - M$.

4.3.2.3 High-cycle performance assessment

Section 4.3.2.1 examined the performance of the equations for the stress ratios M_s and M_{pt}, utilized in the Ta-Ger A and Ta-Ger B models, under monotonic loading conditions. Since the proposed Ta-Ger HC model targets high-cycle sand behaviour, this section evaluates these stress ratio formulations under cyclic loading conditions. The aim is to inform the final selection of the equations for M_s and M_{pt}. Figure 4.18-Figure 4.20 compare the performance of the original Ta-Ger A and Ta-Ger B models and their hyperelasticity-upgraded versions in predicting the accumulated strain ε^{acc} after $N = 10000$ cycles. The Ta-Ger B models

consistently show better agreement with experimental data (Wichtmann, 2005). A representative test (Figure 4.18) with settings configured to $q^{\mathrm{ampl}} = 60$ kPa, $p_{\mathrm{in}} = 200$ kPa, $\eta^{\mathrm{ave}} = 0.75$, $e_{\mathrm{in}} = 0.702$, was selected for more detailed analysis. This test was used for the calibration of the models' cyclic parameters, with the $\mathrm{N} - \varepsilon^{\mathrm{acc}}$ curve as a reference point.

Figure 4.24 presents the stress-strain response predicted by the original Ta-Ger A and B models. Both exhibit a transition from ratcheting to shakedown, with reduced plastic strain accumulation and damping, as evidenced by the diminishing area within each stress-strain loop. The corresponding volumetric responses are shown in Figure 4.25. While Ta-Ger B predicts contractive behaviour Ta-Ger A exhibits dilative trends. In addition to comparing the models' ability to predict the accumulated strain $\varepsilon^{\mathrm{acc}}$ (Figure 4.18-Figure 4.20), it is useful to examine the individual accumulation of volumetric $\varepsilon_{\mathrm{v}}^{\mathrm{acc}}$ and deviatoric $\varepsilon_q^{\mathrm{acc}}$ strains (Figure 4.26) against experimental data. The ratio $\omega = \varepsilon_{\mathrm{v}}^{\mathrm{acc}}/\varepsilon_q^{\mathrm{acc}}$, referred to as the direction of strain accumulation, was shown by Wichtmann (2005) to be primarily controlled by the average deviatoric stress ratio (η^{ave}). Figure 4.26 shows that Ta-Ger A fails to capture the experimental volumetric strain accumulation, predicting an unrealistic transition from contraction to dilation and a corresponding shift in the accumulation direction ω. Ta-Ger B offers a significantly improved response, with ω stabilising toward the end, although the predicted slope remains slightly offset from the experimental trend.

Due to the absence of experimental volumetric strain response data, the model predictions are compared with SANISAND-MS (Liu *et al.*, 2019), implemented as a UDSM in PLAXIS (Seequent, 2023). As illustrated in Figure 4.27, SANISAND-MS produces contractive strains across varying values of a key cyclic parameter μ_0 (final calibration shown in red), in agreement with the Ta-Ger B response. While an exact match is not expected, this comparison verifies that the volumetric trend predicted by Ta-Ger B is plausible. Since

SANISAND-MS has been validated on the same database at the element level (section 2.3.4.3) and under similar cyclic conditions at the boundary scale (section 2.4.1), it offers a robust reference supporting the reliability of the Ta-Ger B predictions.

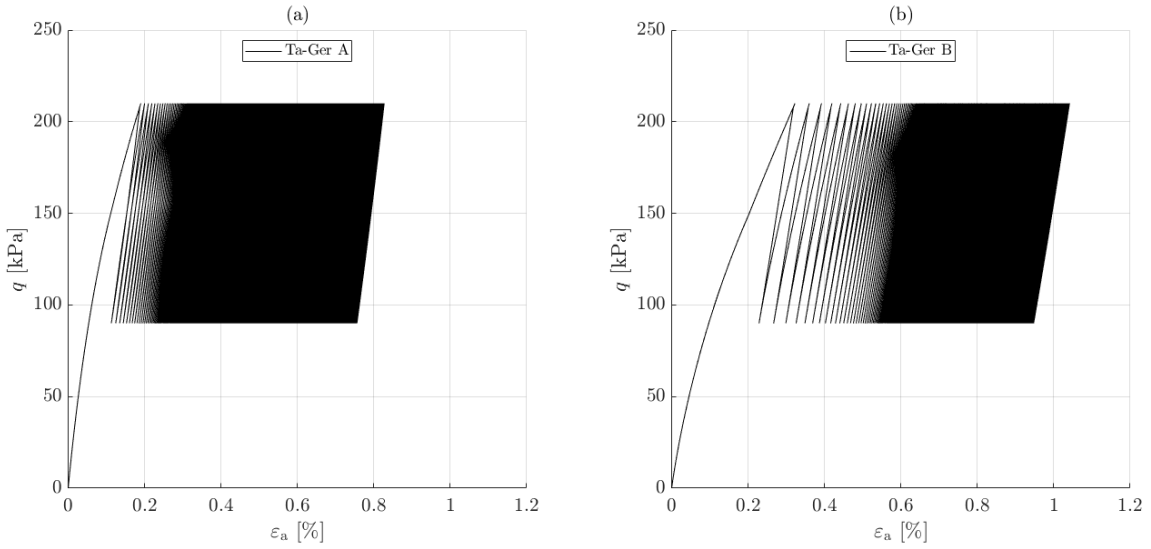

Figure 4.24: Stress-strain response of a drained cyclic triaxial test on quartz sand No. 3 (Wichtmann, 2005) with test settings as $q^{\mathrm{ampl}} = 60$ kPa, $p_{\mathrm{in}} = 200$ kPa, $\eta^{\mathrm{ave}} = 0.75$, $e_{\mathrm{in}} = 0.702$, simulated using: (a) Ta-Ger A; (b) Ta-Ger B.

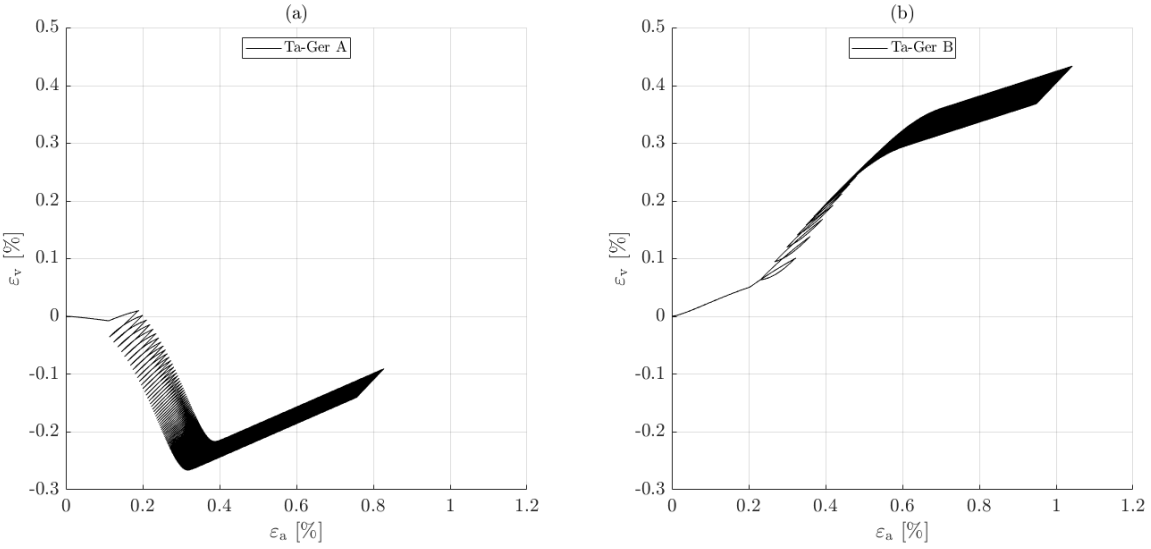

Figure 4.25: Volumetric response of a drained cyclic triaxial test on quartz sand No. 3 (Wichtmann, 2005) with test settings as $q^{\mathrm{ampl}} = 60$ kPa, $p_{\mathrm{in}} = 200$ kPa, $\eta^{\mathrm{ave}} = 0.75$, $e_{\mathrm{in}} = 0.702$, simulated using: (a) Ta-Ger A; (b) Ta-Ger B.

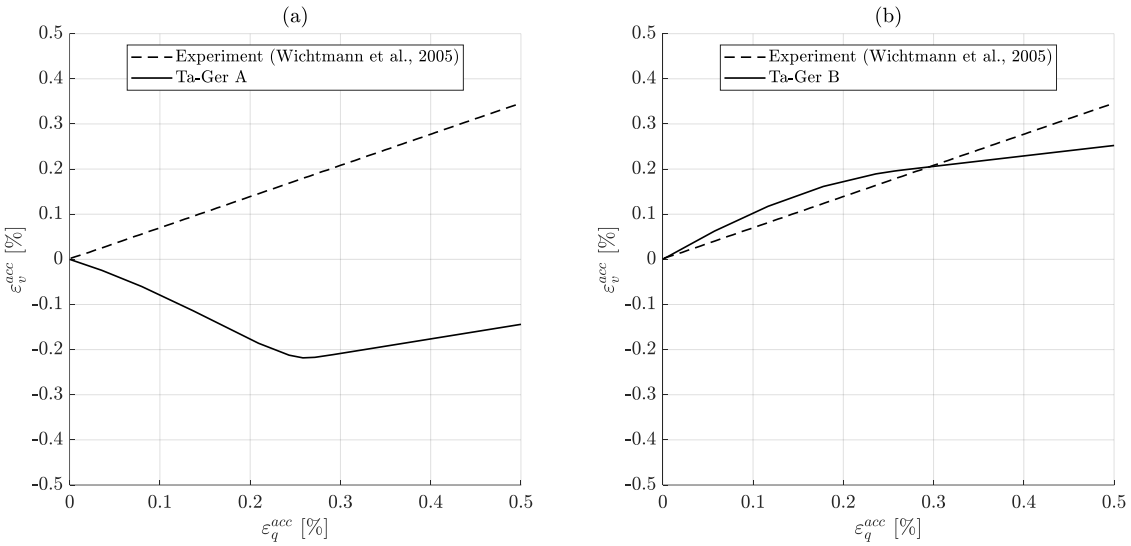

Figure 4.26: High-cycle accumulation of deviatoric and volumetric strain for a drained cyclic triaxial test on quartz sand No. 3 (Wichtmann, 2005) with test settings as $q^{\mathrm{ampl}} = 60$ kPa, $p_{\mathrm{in}} = 200$ kPa, $\eta^{\mathrm{ave}} = 0.75$, $e_{\mathrm{in}} = 0.702$. Simulation results are compared to the experimental data for: (a) Ta-Ger A; (b) Ta-Ger B.

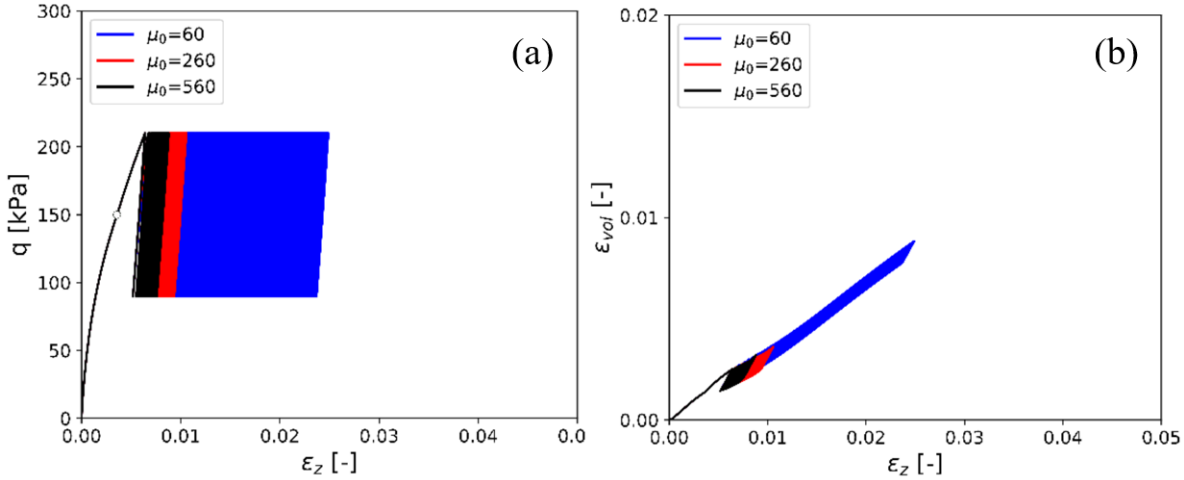

Figure 4.27: Simulation of a drained cyclic triaxial test on quartz sand No. 3 (Wichtmann, 2005), using SANISAND-MS with settings as $q^{\mathrm{ampl}} = 60$ kPa, $p_{\mathrm{in}} = 200$ kPa, $\eta^{\mathrm{ave}} = 0.75$, $e_{\mathrm{in}} = 0.702$: (a) $\varepsilon_z - q$; (b) $\varepsilon_z - \varepsilon_v$ (modified after Seequent (2023)). It is noted that ε_z represents axial strain, and strains should be multiplied by 100% when comparing with Figure 4.24 and Figure 4.25.

Figure 4.28 illustrates the evolution of the parameter ζ^n, which defines the plastic matrix $\mathbf{H}$ via $\mathbf{H} = \zeta^n \mathbf{I}$. This matrix governs the hardening mechanism in the Ta-Ger models and plays a key role under high-cycle loading. For clarity only values up to $\mathrm{N} = 2000$ are presented. Since $\mathbf{H}$ scales the plastic part of the incremental stiffness matrix, $\mathbf{E}^{\mathrm{ep}}$, rather than entering additively in the denominator as in classical plasticity, it is expected to decrease to realistically capture the diminishing rate of strain accumulation observed experimentally. This contrasts with classical plasticity models (Liu *et al.*, 2019), where the hardening

modulus being in the denominator should increase. The reduction in ζ^n and hence **H** depends on the hardening exponent, n, which increases during drained cyclic loading as per equation (4.28). A comparison between Ta-Ger A and B reveals clear differences: Ta-Ger B exhibits the anticipated gradual decrease in ζ^n, whereas Ta-Ger A shows an initial drop followed by a rise, persisting until around $\mathrm{N} = 1000$. This stems from the formulation of the bounding surface stress ratio M_s used in Ta-Ger A (equation (4.21)). As seen in Figure 4.29a, M_s initially peaks leading to a sharp decrease in ζ due to its presence in the denominator of equation (4.8), which is used to calculate ζ. Since M_s continues to evolve, decreasing and gradually converging to the critical state stress ratio, M_{cs}, this leads to an undesired increase in ζ. The convergence of stress ratios M_s and M_{pt} to their critical value, M_{cs}, under cyclic loading, is not typically observed in constitutive models employing traditional definitions for M_s and M_{pt} (Lashkari, 2010), such as the ones used in Ta-Ger B (equations (4.19)). As depicted in Figure 4.29b, the M_s and M_{pt} equations employed in Ta-Ger B demonstrate a tendency for both to slightly increase, corresponding to the normal evolution of ψ becoming more negative, indicating sand densification. This aligns with the desired decrease in ζ and ζ^n, facilitating a more accurate simulation of ratcheting behaviour. The unrealistic volumetric response generated by Ta-Ger A (Figure 4.25a) can be attributed to the M_{pt} equation (4.22). In contrast to Ta-Ger B, where M_{pt} consistently remains higher than the current stress ratio, q/p, Ta-Ger A predicts the occurrence of phase transformation. Specifically, in Ta-Ger A, M_{pt} starts from a very low (negative) initial value (M_{pt0}) while the stress ratio q/p is initially higher. As loading progresses, M_{pt} eventually exceeds the current stress ratio, as illustrated in Figure 4.29a. This crossing point triggers a shift in the material response from dilative to contractive. As this study aims to model sand behaviour intrinsically, capturing accumulated strains alone is not sufficient. The results show that Ta-Ger A approximates final strains at the expense of overall model performance. In contrast,

the equations of Ta-Ger B (equations (4.19)) provide a more robust, adaptable, and CS-consistent formulation, and are thus adopted in the final Ta-Ger HC model.

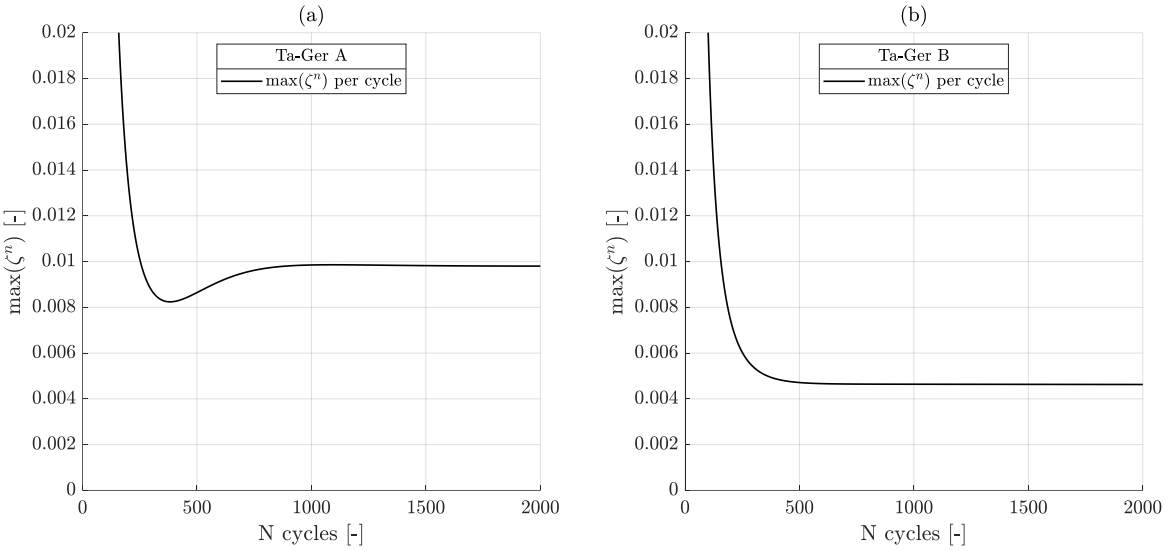

Figure 4.28: Evolution of the maximum ζ^n per cycle during a drained cyclic triaxial test on quartz sand No. 3 (Wichtmann, 2005) with test settings as $q^{\text{ampl}} = 60$ kPa, $p_{\text{in}} = 200$ kPa, $\eta^{\text{ave}} = 0.75$, $e_{\text{in}} = 0.702$, simulated using: (a) Ta-Ger A; (b) Ta-Ger B. For clarity only the values up to $\zeta^n = 0.02$ and for the first N = 2000 cycles are shown, although the simulations progressed until N = 10000.

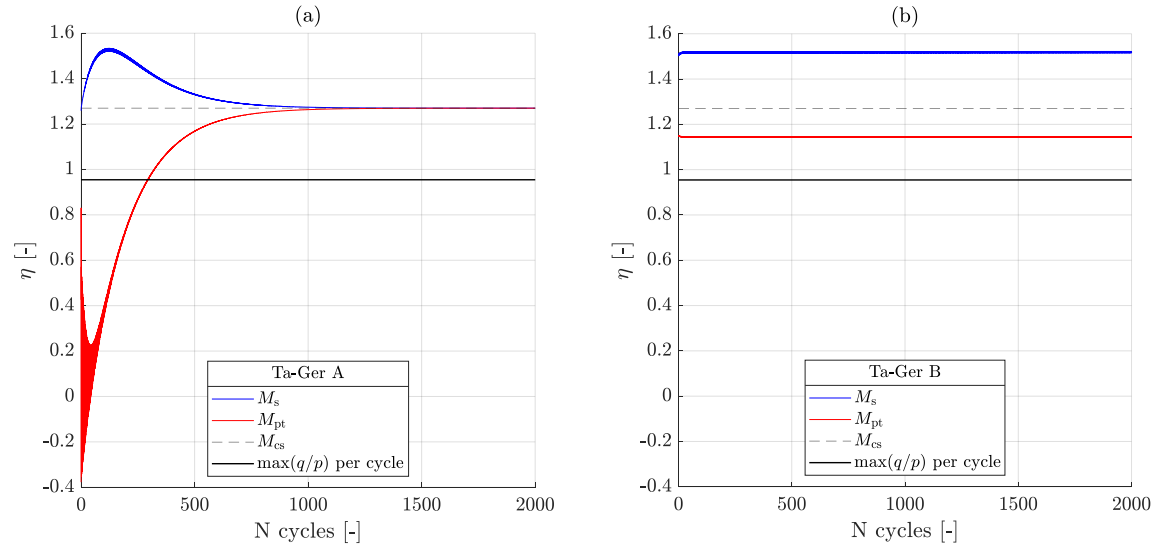

Figure 4.29: Evolution of the phase transformation stress ratio, M_{pt}, the bounding surface stress ratio, M_{s}, and the maximum stress ratio q/p per cycle during a drained cyclic triaxial test on quartz sand No. 3 (Wichtmann, 2005) with test settings as $q^{\text{ampl}} = 60$ kPa, $p_{\text{in}} = 200$ kPa, $\eta^{\text{ave}} = 0.75$, $e_{\text{in}} = 0.702$, simulated using: (a) Ta-Ger A; (b) Ta-Ger B. For clarity, the evolution of the stress ratios is shown for the first N = 2000 cycles, although the simulations progressed until N = 10000.

4.3.3 Hardening exponent equation

This section demonstrates the flexibility of the Ta-Ger framework rather than modifying the core behaviour of the model, focussing on the hardening exponent n, which can be tailored

to specific experimental databases. As outlined in section 4.2.1.6, Tasiopoulou and Gerolymos (2016a) suggest representing n as a function of the cumulative incremental deviatoric strain, $\Sigma \mathrm{d}\varepsilon_q$, (equation (4.28)). Under drained conditions, since the switch $1 - \mathrm{sign}\left(\Sigma\left|\mathrm{d}\varepsilon_p\right|\right) = 0$, thus reduces to:

$$n = n_{\mathrm{peak}} + \left(n_0 - n_{\mathrm{peak}}\right) e^{-\beta \Sigma \mathrm{d}\varepsilon_q} \tag{4.42}$$

This equation forecasts a rising value of n with increasing $\Sigma \mathrm{d}\varepsilon_q$, with the rate regulated by $e^{-\beta \Sigma \mathrm{d}\varepsilon_q}$. While the original form (equation (4.28)) performs well under varied conditions, it was found that a sigmoid function offers better alignment with the specific experimental data for cycles $\mathrm{N} = 1 - 1000$, without compromising performance for higher cycles:

$$n = n_{\mathrm{f}} + \left[n_{\mathrm{peak}} + \left(n_0 - n_{\mathrm{peak}}\right) \frac{A}{B + e^{(\beta \Sigma \mathrm{d}\varepsilon_q)}} - n_{\mathrm{f}} \right] e^{-\gamma \left(1 - \mathrm{sign}\left(\Sigma\left|\mathrm{d}\varepsilon_p\right|\right)\right) \Sigma \mathrm{d}\varepsilon_q} \tag{4.43}$$

where n_0, n_{peak}, n_{f} and β, γ retain their original role as in equation (4.28), and the parameters A and B (default: 1 and 0) can be calibrated to provide more control over the evolution of n. Figure 4.30 presents three representative simulations comparing the original and refined n formulations in Ta-Ger B. These simulations mirror those presented in Figure 4.18 but are limited to $\mathrm{N} = 1 - 1000$, where the improved predictive capacity of the sigmoid function is most apparent. The results support the adoption of equation (4.43) in Ta-Ger HC, reinforcing the model's adaptability without altering its core structure.

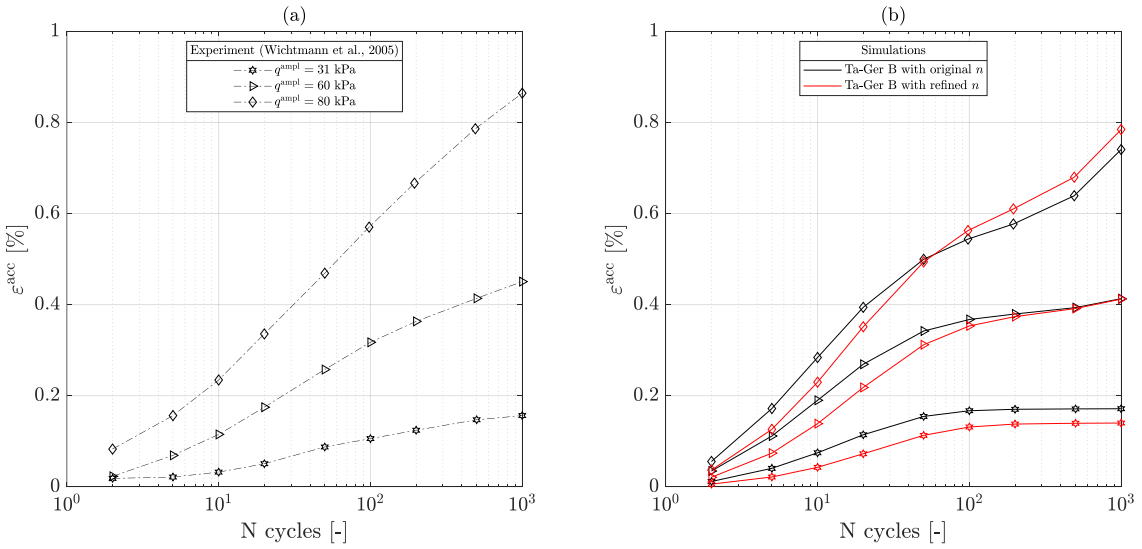

Figure 4.30: Influence of the cyclic stress amplitude, q^{ampl}, on accumulated total strain curves with test/simulation settings as $p_{\mathrm{in}} = 200$ kPa, $\eta^{\mathrm{ave}} = 0.75$, $e_{\mathrm{in}} = 0.702$: (a) experimental data (Wichtmann, 2005); (b) Ta-Ger B with the original n against Ta-Ger B with the refined n.

4.3.4 Significance of the stress integration scheme for high-cycle simulations

Incremental-iterative simulations of offshore foundation response under high-cycle loading (N > 1000 cycles) using intrinsic constitutive models can be computationally demanding (Liu et al., 2022a). More critically, numerical errors may accumulate over thousands of cycles, potentially compromising solution accuracy (Niemunis et al., 2005). It is therefore essential to employ a robust stress integration scheme. This section highlights potential sources of error in high-cycle simulations and evaluates the performance of two explicit integration schemes through a sensitivity analysis, adopting a slightly different approach from that used in section 4.2.3.2 for monotonic loading. It is noted that all high-cycle single-element simulations presented in chapter 4 were conducted in MATLAB. The simulations were performed on a computer equipped with a 13th Gen Intel(R) Core(TM) i9-13900K processor (3.00 GHz), 128 GB of RAM, and running Windows 11 (64-bit).

4.3.4.1 Elastic nonlinearity accumulation

As explained in section 4.3.1.3, when a material is modelled as purely elastic, no deformation should remain at the end of a closed loop loading process. However, analyses performed in this study using the thermodynamically consistent hyperelastic model (Houlsby et al., 2019)

reveal that spurious strains may still accumulate when a lower-order integration scheme is employed, with the effect becoming more pronounced as the number of increments per cycle decreases. Figure 4.31 illustrates the influence of the number of increments per cycle on the simulation of a drained high-cycle triaxial test (Figure 4.17) (Wichtmann, 2005), using either the RK1 or RKF23 explicit integration schemes. The simulations based on the parameters in Table 4.2 with $e_{\mathrm{in}} = 0.580$ and $q^{\mathrm{ampl}} = 60$ kPa, show that the RK1 scheme predicts strain accumulation even with 20000 increments per cycle, whereas the RKF23 scheme predicts no accumulation, even when using the minimum number of increments tested, albeit with significantly higher computational cost. As an indication of this cost, using the computer specified previously, the case of RK1 with 4000 increments per cycle required 19.61 minutes of computation time, whereas RKF23 with 200 increments per cycle took 344.42 minutes. Specifically, Figure 4.31a shows the evolution of total strain (ε) with the number of cycles, while Figure 4.31b presents the accumulated strain ($\varepsilon^{\mathrm{acc}}$) per cycle, generated during the regular cycles. The RK1 curves display a progressive increase in strain, highlighting spurious strain accumulation due to integration error. In contrast, the RKF23 curves remain flat, confirming the absence of numerical artefacts. In practical applications involving elastoplastic models for high-cycle loading, particularly when shakedown is expected, avoiding spurious accumulation of elastic strains is essential. Otherwise, the model may incorrectly predict ratcheting behaviour, compromising the accurate representation of reversible cyclic response. These considerations must be carefully balanced when selecting an appropriate integration scheme.

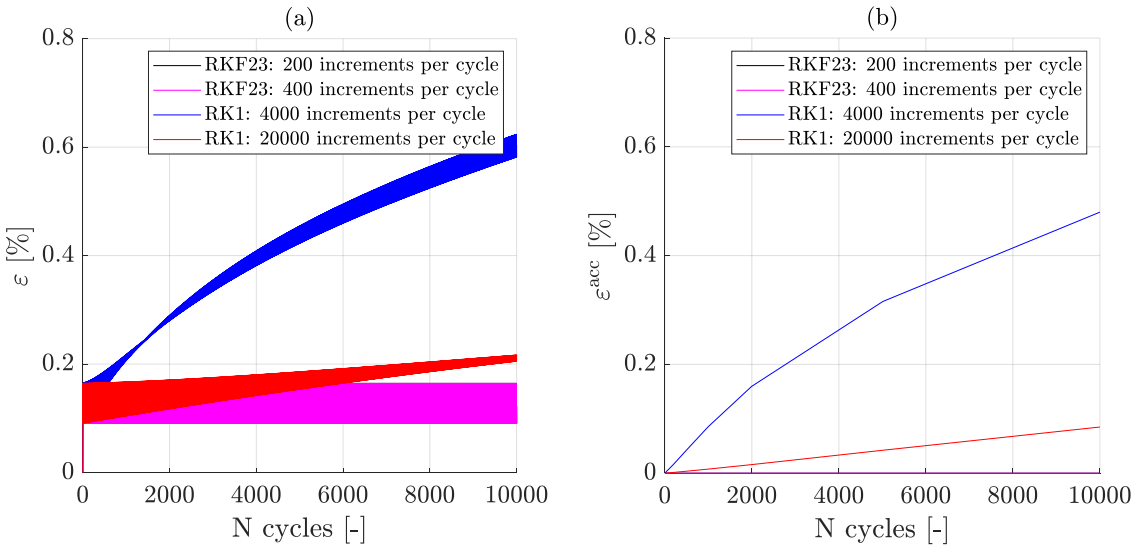

Figure 4.31: Effect of number of increments per cycle on drained cyclic triaxial test (Wichtmann, 2005) simulations, using a hyperelastic model (Houlsby et al., 2019). Simulation settings: $q^{\mathrm{ampl}} = 60$ kPa, $p_{\mathrm{in}} = 200$ kPa, $\eta^{\mathrm{ave}} = 0.75$, $e_{\mathrm{in}} = 0.702$. Simulations were performed with the RK1 integration scheme and the RKF23 integration scheme: (a) $\mathrm{N} - \varepsilon$; (b) $\mathrm{N} - \varepsilon^{\mathrm{acc}}$.

4.3.4.2 Evaluation of two explicit integration schemes for high-cycle loading

A sensitivity analysis using the Ta-Ger B model was conducted to identify the optimal integration scheme and number of increments per cycle for high-cycle simulations. Both the explicit RK1 and RKF23 integration schemes were employed, with RKF23 error tolerance fixed at $\mathrm{STOL} = 10^{-3}$. All simulations employed the parameters listed in Table 4.3 with a minor adjustment to parameter β (set to 10), based on the least accurate case (RK1 with 4000 increments) to ensure fair comparison. It should be noted that the RKF23 simulations perform even better with the value of β unaltered (see Figure 4.18c). The sensitivity analysis simulates a drained high-cycle triaxial test as per Figure 4.17 (Wichtmann, 2005), with settings $q^{\mathrm{ampl}} = 60$ kPa, $p_{\mathrm{in}} = 200$ kPa, $\eta^{\mathrm{ave}} = 0.75$, $e_{\mathrm{in}} = 0.702$. Following Chen et al. (2024), the relative error for response variable x was calculated for each simulation with respect to a benchmark analysis as $\mathrm{E}_X = \left|x_{ref} - x\right| / \left|x_{ref}\right|$, where x_{ref} and x are the benchmark and simulation values, respectively. Two convergence indicators were assessed: (i) accumulated strain $\varepsilon^{\mathrm{acc}}$, and (ii) axial strain ε_{a}. The RKF23 simulation with 400 increments per cycle was used as the benchmark, yielding $\varepsilon^{\mathrm{acc}}_{ref} = 0.803\%$, $\varepsilon^{\mathrm{a}}_{ref} = 1.017\%$,

$t_{ref}^{\mathrm{CPU}} = 2355.04$ minutes. The computed relative errors, together with the corresponding CPU times, are presented in Table 4.4, while the generated simulation curves are presented in Figure 4.32.

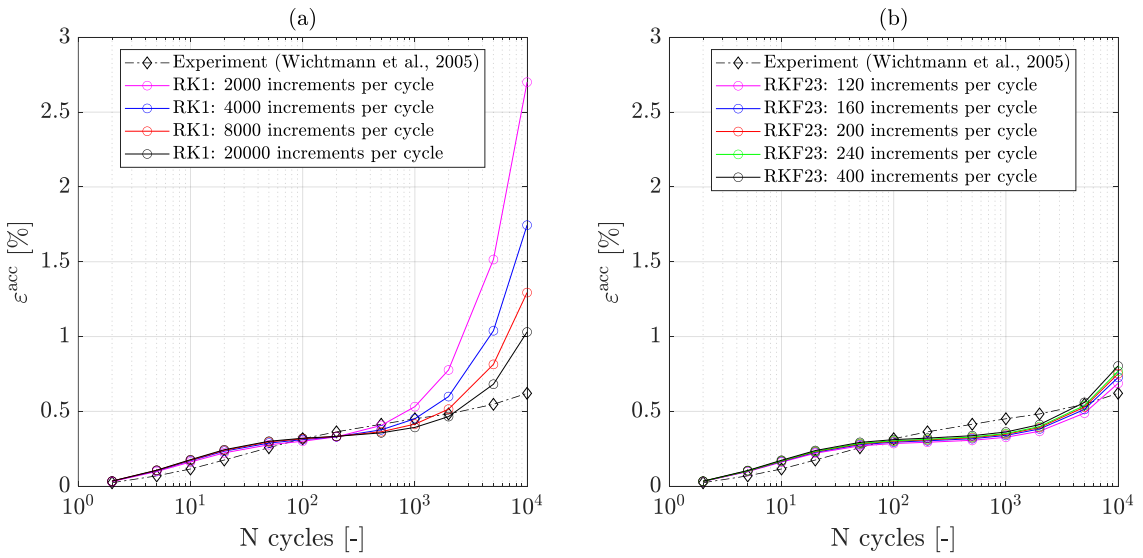

Figure 4.32: Effect of number of increments per cycle on drained cyclic triaxial test (Wichtmann, 2005) simulations, using Ta-Ger B model. Simulation settings: $q^{\mathrm{ampl}} = 60$ kPa, $p_{\mathrm{in}} = 200$ kPa, $\eta^{\mathrm{ave}} = 0.75$, $e_{\mathrm{in}} = 0.702$: (a) RK1 integration scheme; (b) RKF23 integration scheme.

Table 4.4: Effect of the integration scheme and number of increments per cycle on model performance.

Integration scheme	Increments per cycle	Relative error in $\varepsilon^{\mathrm{acc}}$, $\mathrm{E}_{\varepsilon^{\mathrm{acc}}}$	Relative error in ε_{a}, $\mathrm{E}_{\varepsilon_{\mathrm{a}}}$	CPU time, t^{CPU} [minutes]
RK1	2000	2.362	1.853	3.8
RK1	4000	1.171	0.923	7.4
RK1	8000	0.611	0.482	11.5
RK1	20000	0.283	0.221	29
RKF23	120	0.145	0.104	205.4
RKF23	160	0.095	0.064	385.4
RKF23	200	0.064	0.046	581.4
RKF23	240	0.043	0.031	1564.5

As shown in Figure 4.32a, and quantified in Table 4.4, RK1 simulations exhibit significant deviations from the benchmark yielding high errors in both accumulated and axial strain. In contrast, RKF23 simulations (Figure 4.32b) show close agreement with the benchmark across all tested values of increments per cycle, exhibiting significantly smaller errors. However, the improved accuracy of RKF23 comes with a considerable increase in computational cost. Despite the increased computational cost, RKF23 with 200 increments

per cycle was selected for all subsequent high-cycle simulations due to its balance of accuracy and efficiency.

4.3.5 Summary of parameters

The capabilities of the new Ta-Ger HC model are validated using tests on two sands: (i) Hostun sand (Escribano, 2014) (mean diameter $D_{50} = 0.35$ mm, maximum and minimum void ratios $e_{\max} = 1.0$, $e_{\min} = 0.656$), and (ii) quartz sand No. 3 (see section 4.3.1.4) (Wichtmann, 2005). Simulation parameters for both sands are presented in Table 4.5.

For Hostun sand, the monotonic parameters were calibrated to match the stress-strain and volumetric responses of the drained monotonic test on a sample with $e_{\text{in}} = 0.702$ and $p_{\text{in}} = 100$ kPa (Figure 4.33). The cyclic parameters governing the evolution of the hardening exponent n were calibrated through trial and error, targeting the experimental stress-strain curve of a sample with $e_{\text{in}} = 0.742$ and $p_{\text{in}} = 100$ kPa, as shown in Figure 4.36. These two tests were the only ones used for calibration. All other simulations are authentic model predictions. Parameters A and B were kept at their default values (1 and 0, respectively). The initial value n_0 of the exponent n was fitted to the first shearing stage, while n_{peak} and β, which control the transition from ratcheting to shakedown, required iterative tuning. Specifically, n_{peak} determines the maximum level of densification and the minimum plastic dissipation, and β regulates the rate of this transition. Since parameters n_{f} and γ primarily affect undrained or partially drained conditions, they were not explicitly calibrated but were assigned reasonable values. The same approach was followed for quartz sand No. 3.

The adopted monotonic parameters for quartz sand No. 3 remain consistent with those detailed in section 4.3.1.4 (Table 4.3). To ensure consistency following the introduction of Ta-Ger HC's new features, the drained monotonic tests used for calibration were re-simulated. Although keeping n constant is typically recommended for monotonic loading

(Tasiopoulou and Gerolymos, 2016a), simulations were conducted using both constant and evolving n (cyclic configuration) for completeness (Figure 4.34). Despite the generally stiffer response observed when using the cyclic configuration of n, there remains notable agreement between the simulated curves and the experimental data. Calibration of the cyclic parameters focused on matching both the rate of strain accumulation and the final accumulated strain, $\varepsilon^{\mathrm{acc}}$, for the high-cycle test of Figure 4.40 with $q^{\mathrm{ampl}} = 60$ kPa. Parameters A and B were adjusted slightly to improve the fit, though satisfactory results can also be achieved using their default values. The influence of β on the cyclic response is demonstrated in Figure 4.35. In both the original equation (4.28) and the modified equation (4.43) of the hardening exponent n, the parameter β controls the rate at which n approaches n_{peak}. For lower values of β, n evolves more gradually towards n_{peak}, resulting in a prediction of lower elastoplastic stiffness over a greater number of cycles and consequently greater strain accumulation. In contrast, higher values of β lead to a faster approach of n to n_{peak}, resulting in earlier stiffening of the material response and thus reduced strain accumulation.

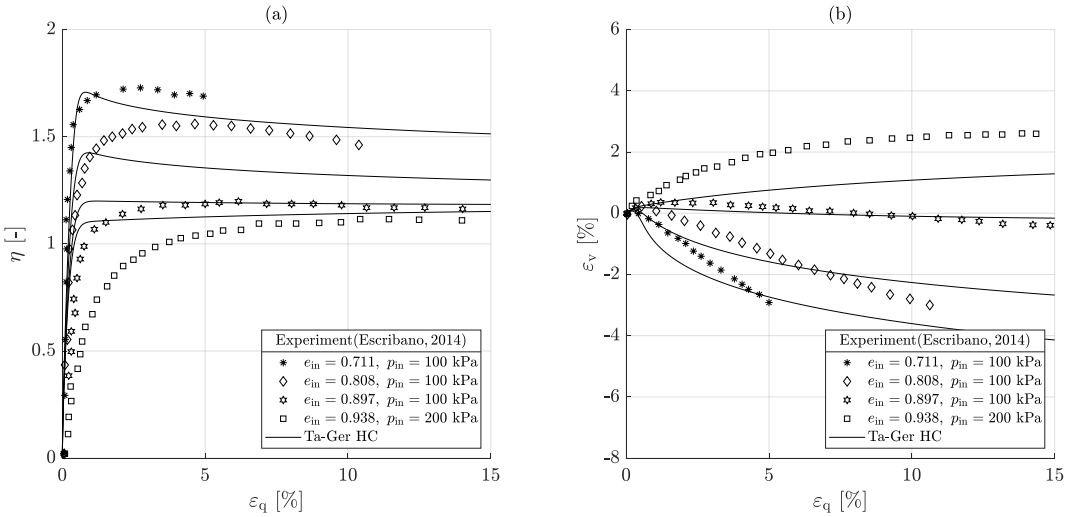

Figure 4.33: Calibration of parameters against drained triaxial tests on Hostun sand (Escribano, 2014): (a) $\varepsilon_q - \eta$; (b) $\varepsilon_q - \varepsilon_{\mathrm{v}}$.

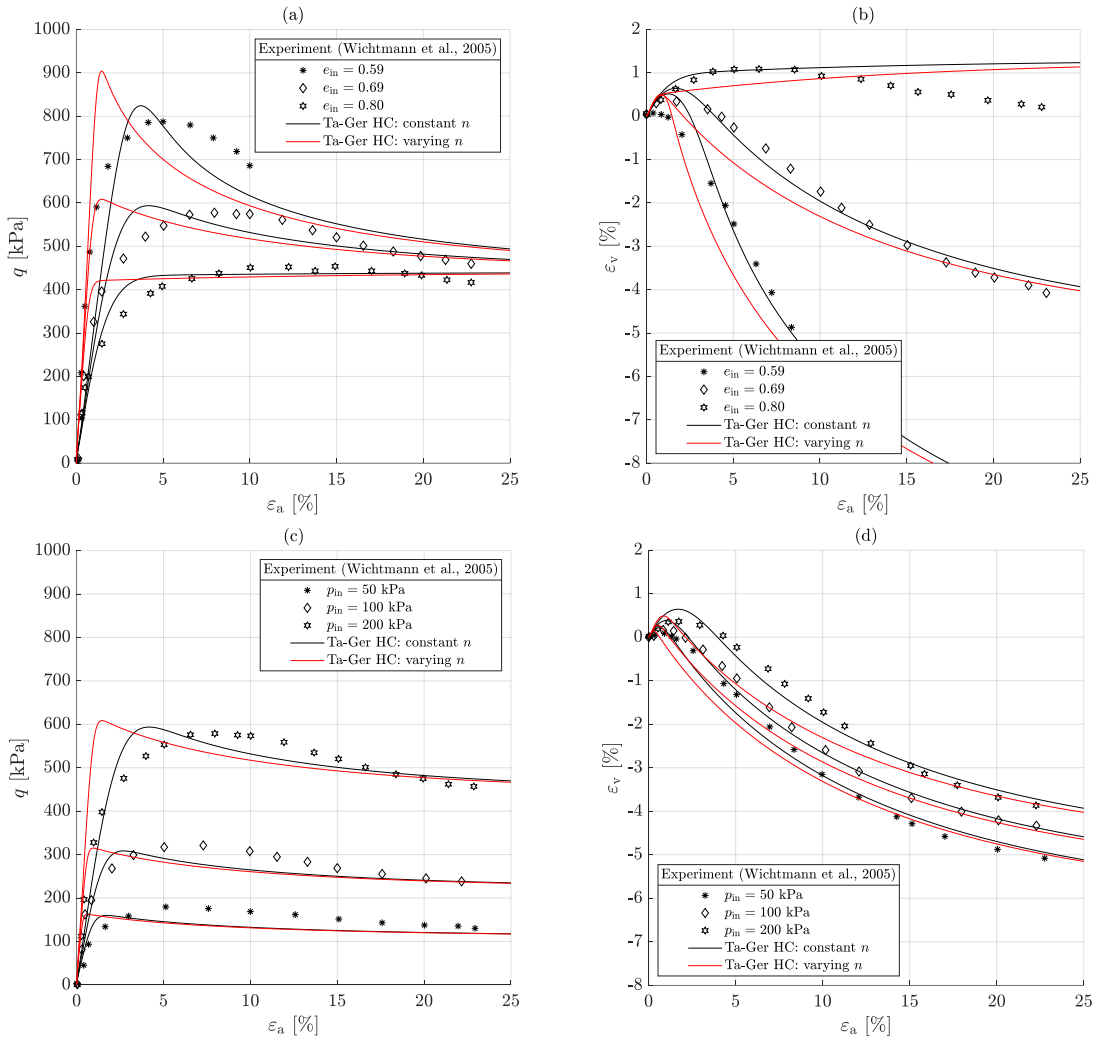

Figure 4.34: Calibration of parameters against drained triaxial tests on quartz sand No. 3 (Wichtmann, 2005): (a) $\varepsilon_a - q$ (constant p_{in}, varying e_{in}); (b) $\varepsilon_a - \varepsilon_v$ (constant p_{in}, varying e_{in}); (c) $\varepsilon_a - q$ (constant e_{in}, varying p_{in}); (d) $\varepsilon_a - \varepsilon_v$ (constant e_{in}, varying p_{in}).

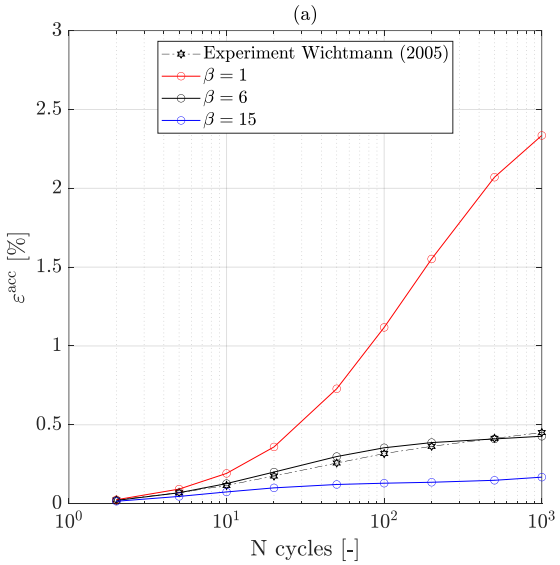

Figure 4.35: Influence of parameter β on the cyclic response ($N - \varepsilon^{acc}$) when simulating a drained cyclic triaxial test (Wichtmann, 2005), ($q^{ampl} = 60$ kPa, $p_{in} = 200$ kPa, $\eta^{ave} = 0.75$, $e_{in} = 0.702$).

Table 4.5: Model parameters for Hostun sand tested by Escribano (2014) and quartz sand No. 3 tested by Wichtmann (2005).

	Ta-Ger HC			
	Hostun sand		**quartz sand No. 3**	
Feature	Parameter	Value	Parameter	Value
Elasticity	k	650	k	330
	v	0.05	v	0.15
	n	0.3	n	0.3
	y	0.9	y	0.9
	N (switch)	1	N (switch)	1
Critical state	M_{cs}	1.18	M_{cs}	1.27
	e_0	1.066	e_0	0.845
	λ	0.142	λ	0.049
	ξ	0.3	ξ	0.27
Bounding surface & Dilatancy	n_b	2.3	n_b	2
	n_d	3.3	n_d	1.17
	-	-	-	-
	α	10	α	0.3
Hardening exponent n^*	n_0	0.1	n_0	0.5
	n_f	0.3	n_f	0.3
	n_{peak}	0.4	n_{peak}	6.5
	A (default)	1	A	0.95
	B (default)	0	B	0.01
	β	400	β	6
	γ	30	γ	30
	$^*n = 0.15$ for monotonic loading		$^*n = 0.15$ for monotonic loading	

4.3.6 Model performance

4.3.6.1 Cyclic tests on Hostun sand

Four drained cyclic tests on Hostun sand, each with 250 loading cycles, conducted by Escribano (2014), were used to evaluate the performance of the Ta-Ger HC model in capturing this sand's cyclic behaviour. Specimens were isotropically consolidated to $p_{in} = 100$ kPa, then sheared along a constant-p path to an average stress ratio η^{ave}, followed by cyclic loading with stress ratios oscillating between $(\eta^{ave} - \frac{1}{2}\Delta\eta)$ and $(\eta^{ave} + \frac{1}{2}\Delta\eta)$ at constant cell pressure. Figure 4.36-Figure 4.39 compare model predictions with experimental data. Except for the case in Figure 4.38, the model reproduces the trend and

final magnitude of strain accumulation with good accuracy. Minor discrepancies in early cycles are likely to be due to variations in experimental loading conditions, as suggested by discontinuities in the measured curves. The divergence in Figure 4.38 aligns with prior findings by Corti et al. (2016) and Li and Liu (2020), whose bounding surface models also struggled with this specific test. Like the present study, their models successfully captured the response for only certain tests. Calibration revealed a high sensitivity of the model to the chosen elastic parameters. Modifying the elastic moduli slightly for different initial void ratios e_{in} could have improved agreement with the experiments. However, such an approach would not align with the objectives of this study, which aim to maintain a consistent and generalizable parameter set across varying conditions. The volumetric response during the first 10 cycles was captured reasonably well, though discrepancies at the 250th cycle may result from calibration limitations and uncertainties in the experimental data.

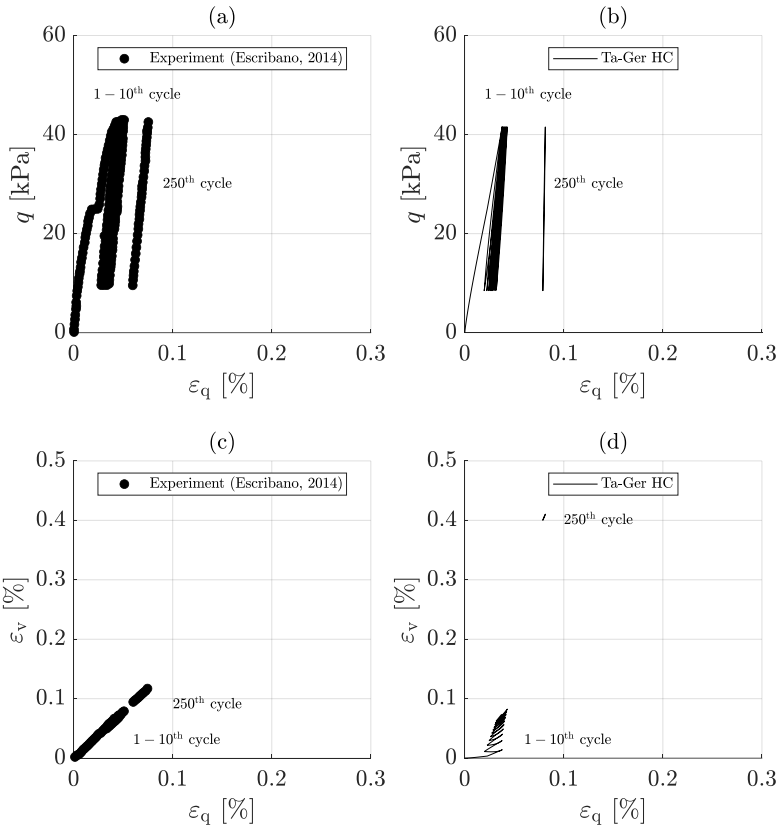

Figure 4.36: Simulation of a drained cyclic triaxial test on Hostun sand (Escribano, 2014) with test/simulation settings as $p_{\mathrm{in}} = 100$ kPa, $\eta^{\mathrm{ave}} = 0.25$, $\Delta\eta = 0.33$, $e_{\mathrm{in}} = 0.742$: (a,c) experimental responses; (b,d) Ta-Ger HC simulations.

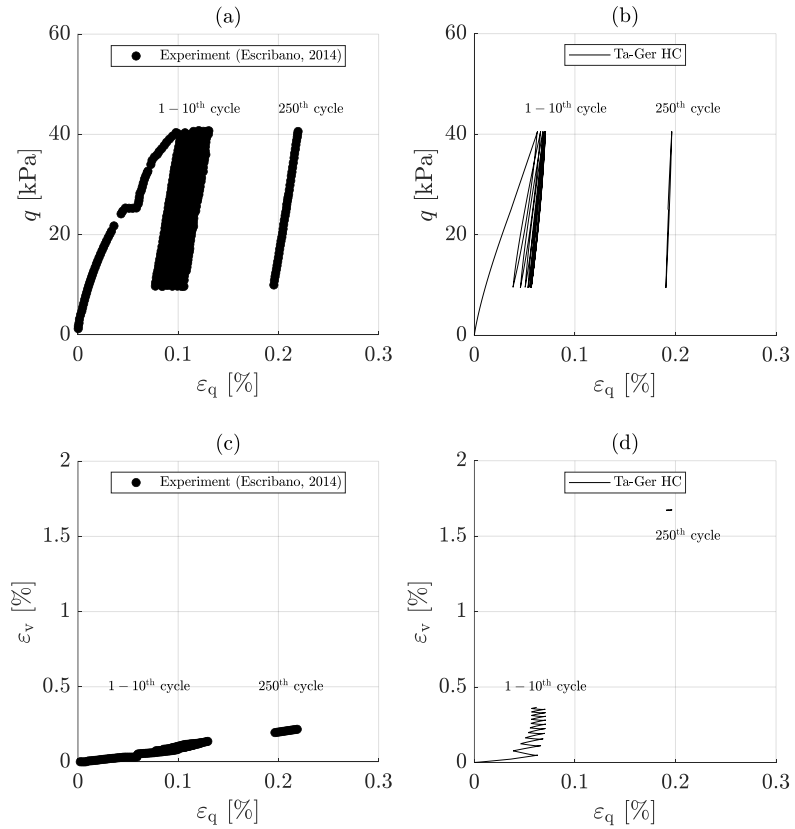

Figure 4.37: Simulation of a drained cyclic triaxial test on a Hostun sand sample (Escribano, 2014) with test/simulation settings as $p_{\text{in}} = 100$ kPa, $\eta^{\text{ave}} = 0.25$, $\Delta\eta = 0.31$, $e_{\text{in}} = 0.977$: (a,c) experimental responses; (b,d) Ta-Ger HC simulations.

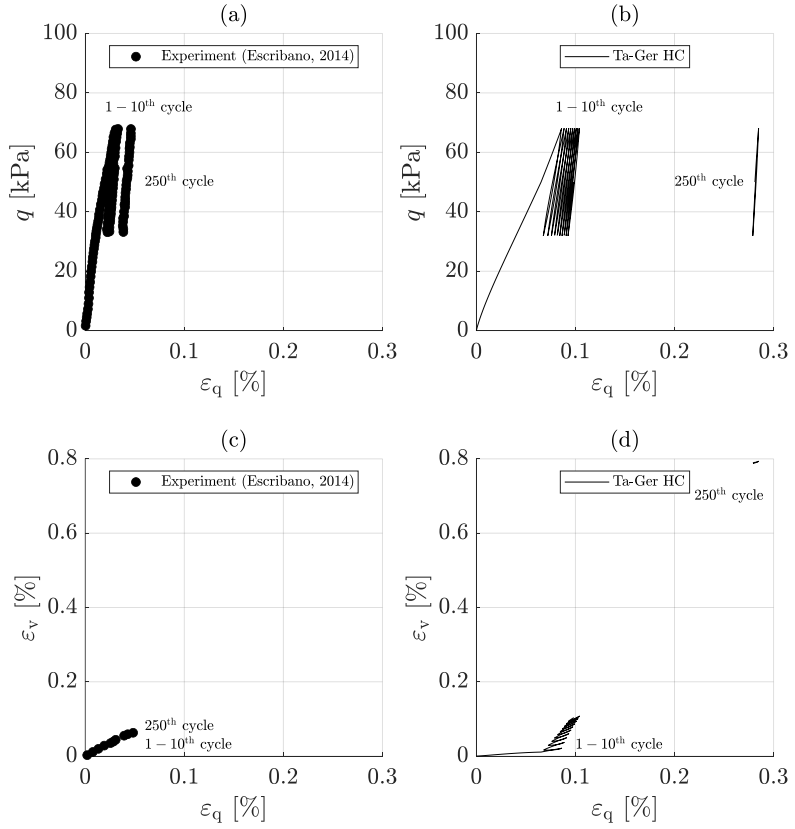

Figure 4.38: Simulation of a drained cyclic triaxial test on a Hostun sand sample (Escribano, 2014) with test/simulation settings as $p_{\text{in}} = 100$ kPa, $\eta^{\text{ave}} = 0.50$, $\Delta\eta = 0.36$, $e_{\text{in}} = 0.718$: (a,c) experimental responses; (b,d) Ta-Ger HC simulations.

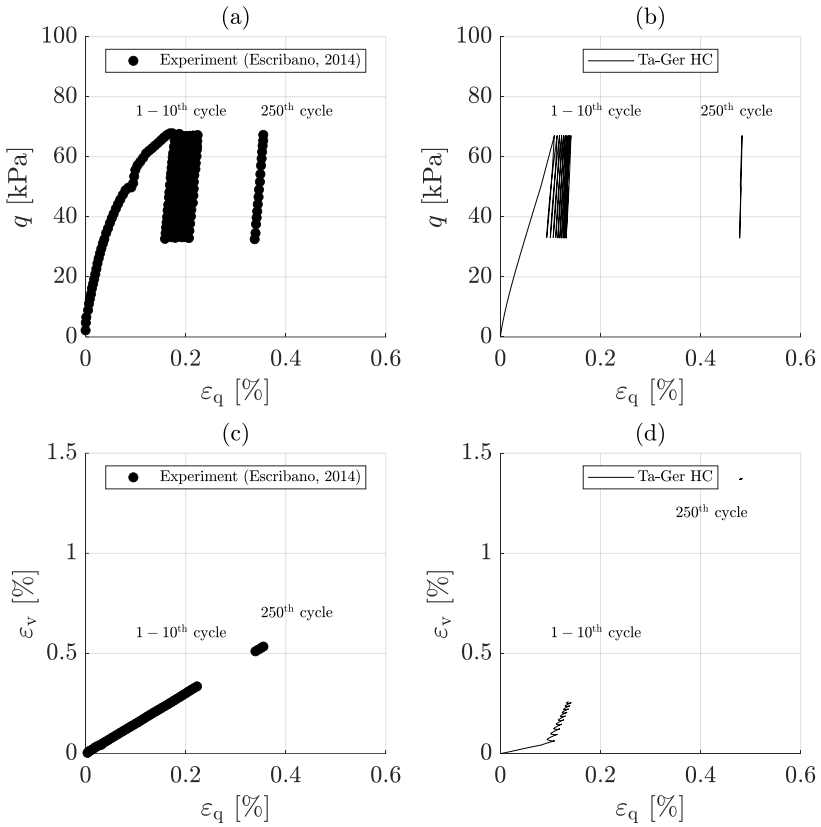

Figure 4.39: Simulation of a drained cyclic triaxial test on a Hostun sand sample (Escribano, 2014) with test/simulation settings as $p_{\mathrm{in}} = 100$ kPa, $\eta^{\mathrm{ave}} = 0.50$, $\Delta\eta = 0.34$, $e_{\mathrm{in}} = 0.937$: (a,c) experimental responses; (b,d) Ta-Ger HC simulations.

4.3.6.2 Cyclic tests on quartz sand No.3

To thoroughly evaluate the Ta-Ger HC model's ability to capture shakedown and ratcheting responses, cyclic triaxial tests with $\mathrm{N} = 10000$ cycles were simulated (Wichtmann, 2005). The testing conditions are detailed in section 4.3.1.4 and Figure 4.17. Previously simulated with Ta-Ger A and B (both the original and hyperelasticity-upgraded versions; Figure 4.18-Figure 4.20), these tests were re-simulated using Ta-Ger HC, with results shown in Figure 4.40-Figure 4.42. Additionally, a new set of simulations was conducted to examine the influence of average stress ratio η^{ave} (Figure 4.43).

In Figure 4.40, Ta-Ger HC accurately captures strain accumulation trends for $q^{\mathrm{ampl}} = 31$ kPa and $q^{\mathrm{ampl}} = 60$ kPa, with slight overestimation of the final accumulated strain for $q^{\mathrm{ampl}} = 80$ kPa. Figure 4.41 shows the effect of initial void ratio e_{in}; while the model slightly overestimates strain accumulation for denser sand ($e_{\mathrm{in}} = 0.580$) and deviates

slightly in predicting the trend for looser and medium-dense specimens ($e_{\mathrm{in}} = 0.803$, 0.674), it generally reproduces the observed behaviour. Figure 4.42 illustrates the impact of initial mean effective stress p_{in}, suggesting minimal effect on the $\varepsilon^{\mathrm{acc}} - \mathrm{N}$ curves for $\mathrm{N} \leq 10^4$ and no discernible trend. While Ta-Ger HC similarly does not predict a clear dependency on p_{in}, it exhibits significant deviations from the experimental results, an issue that could potentially be addressed by incorporating a pressure-dependent factor into its hardening mechanism. Figure 4.43 illustrates the influence of the average stress ratio η^{ave} on strain accumulation. Ta-Ger HC generally captures the experimental trends well across the full range of η^{ave}, with minor discrepancies at lower stress levels, possibly due to the absence of a purely elastic range in the model, as noted by Li and Liu (2020). Another noteworthy observation is that Ta-Ger HC successfully completed the full simulation for $\eta^{\mathrm{ave}} = 1.125$, whereas SANISAND-MS (Liu et al., 2019), reported results only up to 1000 cycles under similar conditions. This underscores the robustness of the Ta-Ger HC formulation and the reliability of its integration scheme.

Finally, across Figure 4.40-Figure 4.43, it is observed that while the experimental data generally exhibit a stable strain accumulation trend up to $\mathrm{N} = 10000$ cycles, the Ta-Ger HC simulations show a tendency for an accelerated rate of accumulated strain as this cycle level is approached. This behaviour indicates a potential limitation of the current model formulation and implementation when approaching very high-cycle counts. Assessment of model performance beyond 10000 cycles, as well as investigation of the mechanisms responsible for this increased accumulation rate, lies beyond the scope of the present study and is identified as a direction for future work.

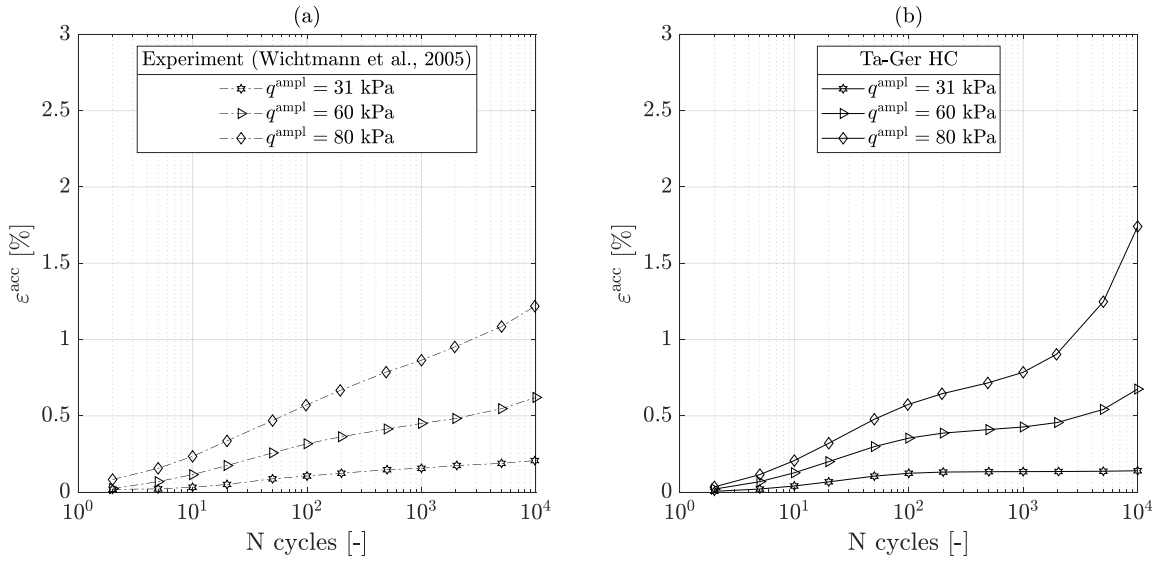

Figure 4.40: Influence of cyclic stress amplitude, q^{ampl}, on cyclic strain accumulation for quartz sand No. 3, with test/simulation settings $p_{\mathrm{in}} = 200$ kPa, $\eta^{\mathrm{ave}} = 0.75$, $e_{\mathrm{in}} = 0.702$: (a) experimental data (Wichtmann, 2005); (b) Ta-Ger HC.

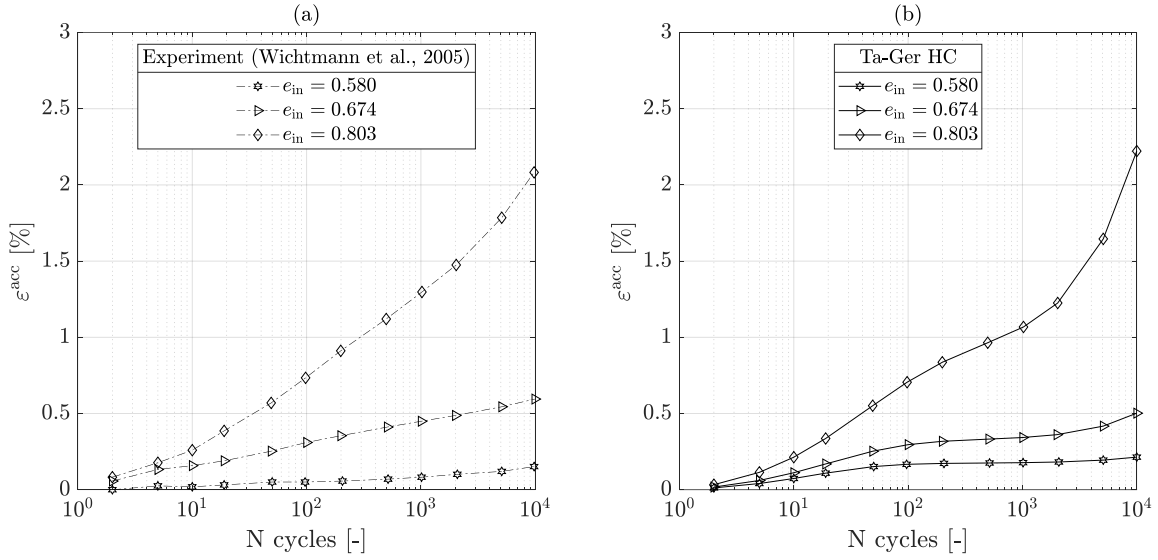

Figure 4.41: Influence of initial void ratio, e_{in}, on cyclic strain accumulation for quartz sand No. 3, with test/simulation settings $p_{\mathrm{in}} = 200$ kPa, $\eta^{\mathrm{ave}} = 0.75$, $q^{\mathrm{ampl}} = 60$ kPa: (a) experimental data (Wichtmann, 2005); (b) Ta-Ger HC.

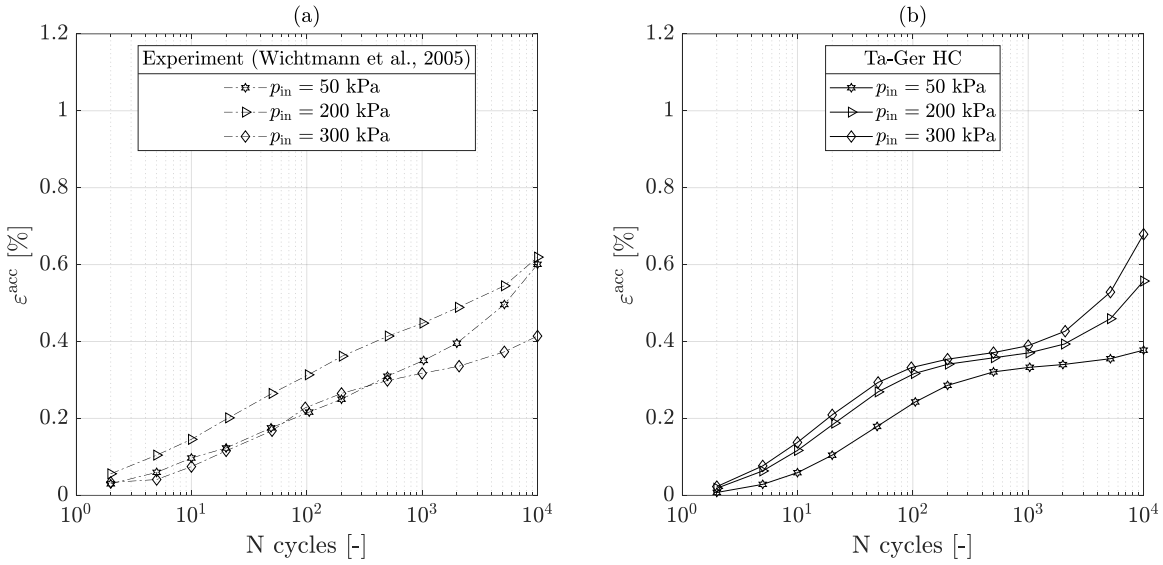

Figure 4.42: Influence of mean effective stress, p_{in}, on cyclic strain accumulation for quartz sand No. 3, with test/simulation settings $e_{in} = 0.684$, $\eta^{ave} = 0.75$, stress amplitude ratio $\varsigma^{ampl} = q^{ampl}/p_{in} = 0.3$: (a) experimental data (Wichtmann, 2005)*;* (b) Ta-Ger HC.

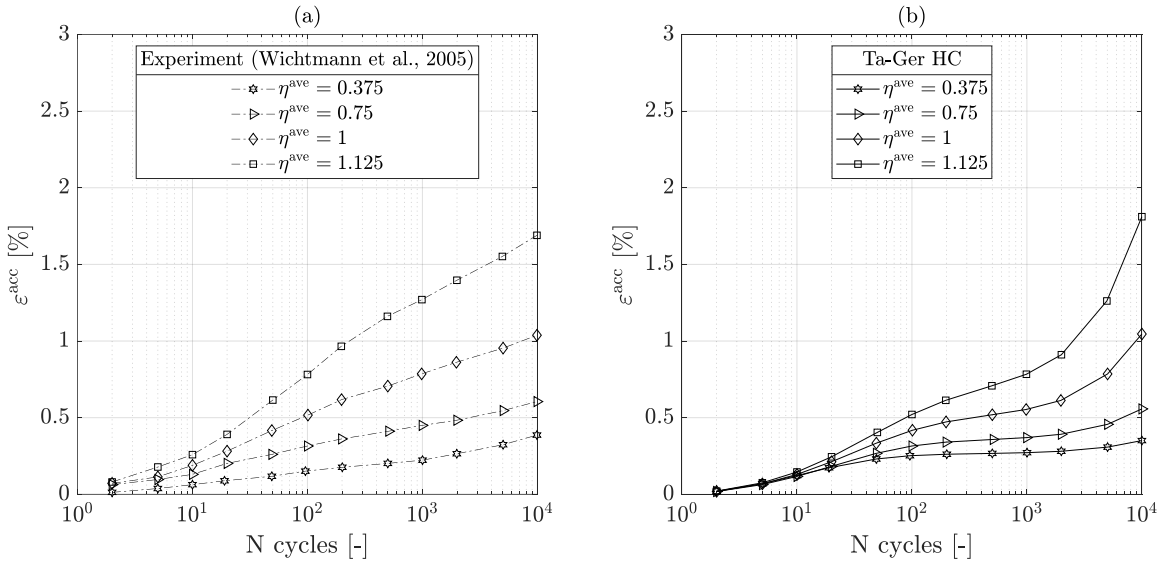

Figure 4.43: Influence of average stress ratio, η^{ave}, on cyclic strain accumulation for quartz sand No. 3, with test/simulation settings $p_{in} = 200$ kPa, $e_{in} = 0.684$, $q^{ampl} = 60$ kPa: (a) experimental data (Wichtmann, 2005)*;* (b) Ta-Ger HC.

4.3.7 Conclusions

This chapter provides systematic documentation of the Ta-Ger family, clarifying the key A and B variants and resolving inconsistencies in the original publications through careful review and selective re-derivation of constitutive equations in multiaxial stress space. Practical guidance for element-level implementation, including conditions for accurate softening simulations, is also established, enhancing transparency and reproducibility. Assessment of the RK1 and RKF23 integration schemes highlights the critical role of robust

stress integration. Convergence analyses of monotonic simulations with Ta-Ger A and B emphasise the need for appropriate increment size. High-cycle simulations with the latter and purely elastic tests, theoretically reversible under the hyperelastic law, revealed that lower-order schemes distort predictions and induce spurious cyclic strain accumulation. The higher-order RKF23 scheme ensures accuracy, albeit at increased computational cost.

In addition, computational investigations identified the need for modifications to key constitutive components to capture high-cycle behaviour, leading to the development and validation of Ta-Ger HC. Incorporating a nonlinear anisotropic hyperelastic law (Houlsby et al., 2019) and appropriate equations for the bounding and phase transformation stress ratios, together with a modified hardening exponent explored as a demonstration of the framework's flexibility, the model reproduces strain accumulation and transitions between ratcheting and shakedown in high-cycle tests up to $N = 10000$ cycles. Compared with more advanced models (Liu et al., 2019; Chen et al., 2024), Ta-Ger HC achieves competitive predictive capability without requiring additional surfaces or parameters, while retaining a simpler formulation, straightforward calibration, and robust numerical implementation.

It is further noted that, although Ta-Ger HC captures the overall trends of cyclic strain accumulation and the transition between shakedown and ratcheting up to $N = 10000$ cycles, the simulations exhibit a tendency for accelerated strain accumulation as this cycle level is approached, whereas the experimental data generally maintain a more stable accumulation rate. This behaviour highlights a potential limitation of the current formulation and numerical implementation when approaching very high-cycle counts. While this observation does not detract from the validity of the model within the cycle range examined in this chapter, it indicates that additional developments may be required for reliable extrapolation beyond 10000 cycles. Investigation of the mechanisms contributing to this response,

including possible influences of the constitutive formulation, bounding surface treatment, and numerical integration strategy, is therefore identified as a direction for future research.

Overall, Ta-Ger HC is established as a reliable high-cycle variant of the Ta-Ger framework, well suited to practical applications involving long-term cyclic loading. For applications involving fewer than 1000 cycles, Ta-Ger B continues to provide robust and accurate predictions and remains a practical and computationally efficient option.

Chapter 5

Adaptations of the Ta-Ger sand model to account for fines content

5.1 Targeting a unified critical state plasticity model for sand with fines

In recent decades, significant progress has been made in the constitutive modelling of clean sands. A major advancement has been the integration of critical state soil mechanics (CSSM) (Roscoe *et al.*, 1958) with the state parameter concept (Been and Jefferies, 1985) into the core formulation of constitutive models for sand. This approach, adopted by several models (e.g., Dafalias and Manzari, 2004; Li and Dafalias, 2012; Taborda et al., 2014; Tasiopoulou and Gerolymos, 2016a), enables unified modelling of dense and loose sand behaviour, capturing the influence of void ratio and stress level through a single parameter set.

However, natural sand deposits commonly contain significant amounts of fines. In particular, the continued development of offshore wind farms (OWFs) in the North Sea has highlighted the frequent occurrence of fines within seabed sands (Schüttenhelm, 1980; Eisma, 1981; Hendriks *et al.*, 2022). The presence of fines has the potential to alter the mechanical behaviour of the soil compared to the ‘clean sand’ case. When modelling sand with fines, one possible approach is to adopt constitutive models originally devised for clean

sand, either by re-calibrating the models to account for the presence of fines or by neglecting their influence. In the context of designing monopile foundations for OWFs where the soil comprises sand with varying fines content, this simplification could lead to: (i) increased workload associated with determining suitable model parameters for each sand-with-fines mixture, and (ii) less reliable predictions resulting from inappropriate or overly simplistic constitutive formulations.

This chapter addresses the challenge by proposing modifications to the state-dependent sand model variants Ta-Ger B and Ta-Ger HC, presented in chapter 4 and forming part of the Ta-Ger model family (Tasiopoulou and Gerolymos, 2016a; 2016b). The goal is to enable accurate predictions of the behaviour of sands with a range of fines contents, f_c, using a single set of parameters. The influence of low-plasticity fines is incorporated through equivalent granular state theory (EGST) (Rahman, 2021), a practical and consistent approach that is equally applicable to non-plastic fines. When applying EGST to a 'clean sand' state-dependent model, the only modification required is the substitution of the void ratio e and state parameter ψ with an equivalent granular void ratio e^* and equivalent granular state parameter ψ^* (Rahman et al., 2014; Rahman and Dafalias, 2022).

5.2 Model adaptation methodology

5.2.1 Equivalent granular void ratio e^* and state parameter ψ^*

This study focuses on sand-fines mixtures classified as 'fines-in-sand', following the framework proposed by Thevanayagam and Martin (2002). To account for the contribution of fines to the load-bearing microstructure and the density of such mixtures, Thevanayagam and Martin (2002) introduced the concept of an equivalent granular void ratio, e^*:

$$e^* = \frac{e + (1-b)f_c}{1 + (1-b)f_c} \tag{5.1}$$

where b represents the fraction of fines that actively contribute to force transmission within the soil skeleton. In this study, the value of b is determined using a semi-empirical expression proposed by Rahman and Lo (2008):

$$b = \left[1 - \exp\left(-0.3 \frac{1}{1-\chi^{-0.25}} \frac{f_c}{f_{thre}}\right)\right] \left(\frac{1}{\chi} \frac{f_c}{f_{thre}}\right)^{1/\chi} \tag{5.2}$$

where χ is the particle size ratio, defined as D_{10}/d_{50} (with D_{10} being the effective size of the host sand and d_{50} the median size of the fines). The threshold fines content, f_{thre}, marks the transition between a 'fines-in-sand' and a 'sand-in-fines' mixture (Thevanayagam and Martin, 2002), and can be identified through empirical correlations (Rahman and Lo, 2008) or experimental methods. Equations (5.1) and (5.2) follow the definitions introduced in chapter 2 and are recalled here for use in the present chapter.

As described by the state parameter framework (Been and Jefferies, 1985), the mechanical behaviour of clean sands is governed by the combined influence of void ratio and mean effective stress, captured through the state parameter $\psi = e - e_c$, where e_c denotes the critical state void ratio corresponding to the current mean effective stress p. In the context of EGST, an equivalent granular state parameter $\psi^* = e^* - e_c^*$ is defined using the equivalent granular void ratio e^*. Since (by the EGST hypothesis) the equivalent granular critical state line (CSL) coincides with the clean sand CSL (i.e., for $f_c = 0$), it follows that $e_c^* = e_c$. These concepts are illustrated in Figure 5.1, which visualises the transformation from e to e^* in the $\ln(p) - e$ or $\ln(p) - e^*$ space, as discussed in Rahman and Dafalias (2022). The solid line represents the CSL for clean sand ($\mathrm{CSL}_{f_c=0}$), which appears identical in either $\ln(p) - e$ or $\ln(p) - e^*$ space ($f_c = 0$, hence $e = e^*$). The CSL for sand with fines content ($f_c > 0$) is shown as a dashed line ($\mathrm{CSL}_{f_c>0}$), and plots lower in the $\ln(p) - e$ space. Transforming from e to e^* shifts any soil state (p, e) and the corresponding critical state (p, e_c) upward by $\Delta e = e^* - e$ and $\Delta e_c = e_c^* - e_c$, respectively. These shifts differ because the

current and critical states do not lie at the same void ratio on $\mathrm{CSL}_{f_c>0}$ ($e \neq e_c$). Importantly, Rahman and Lo (2008) demonstrated experimentally that applying this upward shift Δe_c to all critical states $e = e_c$ on $\mathrm{CSL}_{f_c>0}$ causes the entire line to converge to a unique curve in the $\ln(p) - e^*$ space, which coincides with the clean sand CSL ($\mathrm{CSL}_{f_c=0}$). This unified representation is referred to as the equivalent granular CSL (EG-CSL), and it remains valid for fines contents $f_c < f_{thre}$.

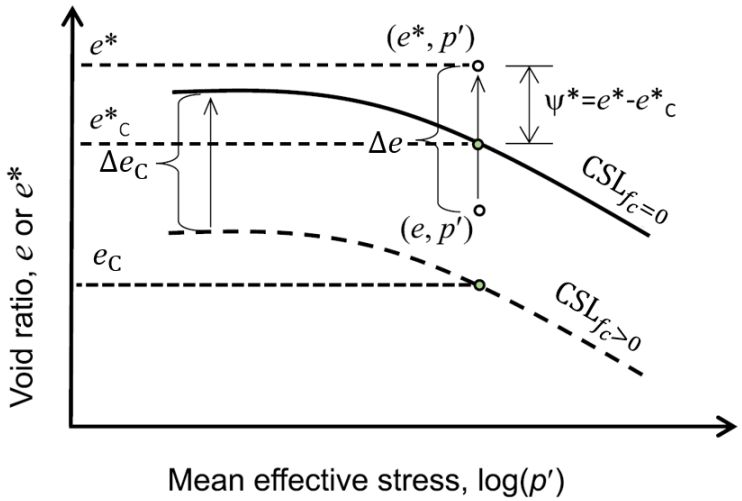

Figure 5.1: Definition of equivalent granular state parameter, ψ^* (modified after Rahman and Dafalias (2022)).

5.2.2 Constitutive equations in multiaxial stress space

Both model variants adapted in this study (Ta-Ger B and Ta-Ger HC) are formulated within the Ta-Ger framework, as detailed in chapters 2, 3 and 4. A key distinction of this framework from conventional plasticity theory lies in the treatment of the plastic modulus, which rather than being introduced as an additive term in the denominator, is used to scale the plastic component of the incremental stiffness matrix (Tasiopoulou and Gerolymos, 2016a):

$$\mathbf{E}^{\mathrm{ep}} = \mathbf{E}^{\mathrm{e}} \left[\mathbf{I} - \frac{\boldsymbol{\Phi}_{\mathrm{g}} \boldsymbol{\Phi}_{\mathrm{f}}{}^{\mathrm{T}} \mathbf{E}^{\mathrm{e}} \mathbf{H}}{\boldsymbol{\Phi}_{\mathrm{f}}{}^{\mathrm{T}} \mathbf{E}^{\mathrm{e}} \boldsymbol{\Phi}_{\mathrm{g}}} \right] \tag{5.3}$$

Here, $\mathbf{E}^{\mathrm{e}}$ is the elastic stiffness matrix, while $\boldsymbol{\Phi}_{\mathrm{f}}$ and $\boldsymbol{\Phi}_{\mathrm{g}}$ are the gradients of the yield surface and plastic potential, respectively. The plastic modulus is defined by $\mathbf{H} = \zeta^n \mathbf{I}$, where ζ controls hardening or softening via a mapping rule, and n is a hardening parameter.

Following the approach of Rahman et al. (2014), all constitutive equations of Ta-Ger B and Ta-Ger HC are retained as described in chapter 4, without further reformulation. The only modifications involve the substitution of e^* and ψ^* for e and ψ, respectively. The model variables affected by this substitution are also denoted with a superscripted star. For brevity, only the modified equations are presented. The only distinction between the two Ta-Ger variants lies in their elasticity formulation: Ta-Ger B adopts a nonlinear hypoelastic law (Richart et al., 1970), whereas Ta-Ger HC employs a nonlinear anisotropic hyperelastic law (Houlsby et al., 2019). In the latter, anisotropic behaviour arising from the microstructural characteristics of the soil is incorporated through a constant, symmetric fabric tensor **a**, which captures fixed inherent anisotropy that does not evolve with strain (Amorosi et al., 2020). Detailed descriptions of the two elasticity formulations are provided in sections 4.2.1.1 and 4.3.1.2, respectively.

For Ta-Ger B the elastic stiffness matrix $\mathbf{E}^{\mathrm{e}}$ is composed of terms that depend on the non-linear shear (G) and bulk (K) moduli, leading to (Richart et al., 1970):

$$G^* = G_0 p_{\mathrm{at}} \frac{(2.97 - e^*)^2}{1 + e^*} \left(\frac{p}{p_{\mathrm{at}}}\right)^m \tag{5.4}$$

Here, G_0 and m are dimensionless parameters, and p_{at} denotes atmospheric pressure. The bulk modulus K^* is computed using the relation $K^* = 2G^*(1 + v)/3(1 - 2v)$, assuming a constant Poisson's ratio, v. Rahman et al. (2012) demonstrated that the influence of fines on the shear modulus G can be adequately captured by substituting e^* for e as shown in equation (5.4). For Ta-Ger HC, the employed hyperelastic law yields the following simple equation for the incremental (tangent) shear stiffness on the isotropic axis (Houlsby et al., 2019):

$$G = g P_{\mathrm{r}} \left(\frac{p}{P_{\mathrm{r}}}\right)^{\mathrm{n}} \tag{5.5}$$

where g is a dimensionless parameter, P_r is a reference pressure, and n is an exponent that captures the nonlinear dependence of shear stiffness on pressure. The dimensionless bulk modulus k is determined from the relation $\frac{g}{k} = \frac{3(1-2v)}{2(1+v)}$, assuming a constant Poisson's ratio, v. The corresponding incremental bulk stiffness on the isotropic axis is estimated by replacing G and g in equation (5.5) with K and k, respectively. A comparison between equations (5.4) and (5.5) highlights a key difference between the hypoelastic and hyperelastic formulations: the former exhibits an explicit dependence on the void ratio e, whereas the latter does not, and will therefore remain unchanged in this study. Instead, as will be shown in section 5.3, the influence of fines on the shear modulus G, for the case of Ta-Ger HC, will be accounted for via calibration.

For both Ta-Ger model variants, critical state (CS) compatibility is ensured through the bounding surface stress ratio M_s and the phase transformation stress ratio M_pt, both of which are modified by substituting the equivalent state parameter ψ^* for ψ:

$$M_\mathrm{s}^* = M_\mathrm{cs} e^{-n_\mathrm{b}\psi^*} \qquad \text{and} \qquad M_\mathrm{pt}^* = M_\mathrm{cs} e^{n_\mathrm{d}\psi^*} \tag{5.6}$$

where M_cs is the critical state stress ratio, and n_b, n_d are positive material constants. As a result, the hardening variable ζ, which depends on M_s, is also modified:

$$\zeta^* = \frac{\left[(\boldsymbol{r}-\boldsymbol{r}_\mathrm{p}):(\boldsymbol{r}-\boldsymbol{r}_\mathrm{p})\right]^{1/2}}{\sqrt{\frac{2}{3}}M_\mathrm{s}^*\chi - n_\mathrm{p}} \tag{5.7}$$

where $\boldsymbol{r} = \boldsymbol{s}/p$ is the current deviatoric stress ratio tensor, $\boldsymbol{r}_\mathrm{p}$ is the deviatoric stress ratio tensor serving as the 'back-stress' ratio in conventional bounding surface models, $n_\mathrm{p} = \boldsymbol{n}:\boldsymbol{r}_\mathrm{p}$ is an inner tensor product, and χ is a model parameter that accounts for Lode angle (θ) effects. Similarly, since the dilatancy d depends on M_pt, it is also modified:

$$d^* = R_{\mathrm{d}}^* \left(\sqrt{\frac{2}{3}} M_{\mathrm{pt}}^* \chi - \frac{\boldsymbol{s}}{p} : \boldsymbol{n} \right) \tag{5.8}$$

where $\boldsymbol{s}$ is the deviatoric stress tensor, and $\boldsymbol{n}$ is a normalised stress ratio tensor with $\mathrm{tr}(\boldsymbol{n}) = 0$ and $\mathrm{tr}(\boldsymbol{n}^2) = 1$. The modified densification variable R_{d}^* is given by:

$$R_{\mathrm{d}}^* = e^{-\alpha(D_{\mathrm{r}}^* - D_{\mathrm{r0}}^*)} \tag{5.9}$$

where α is a constant, D_{r}^* is the current equivalent granular relative density (defined below), and D_{r0}^* is the initial value. At this point, a clarification is necessary regarding the concept and calculation of equivalent relative density. Following the original proposal by Thevanayagam and Mohan (2000), and its conceptual enhancement by Thevanayagam (2003), the equivalent granular relative density D_{r}^* of a fines-in-sand mixture (i.e., when $f_c < f_{thre}$; Thevanayagam and Martin (2002)) is defined as:

$$D_{\mathrm{r}}^* = \frac{e_{\mathrm{max,HS}} - e^*}{e_{\mathrm{max,HS}} - e_{\mathrm{min,HS}}} \tag{5.10}$$

where e^* is the equivalent granular void ratio, and $e_{\mathrm{max,HS}}$, $e_{\mathrm{min,HS}}$ are the maximum and minimum void ratios of the host sand. In contrast, the traditional relative density D_{r} of a fines-in-sand mixture is given by:

$$D_{\mathrm{r}} = \frac{e_{\mathrm{max}} - e}{e_{\mathrm{max}} - e_{\mathrm{min}}} \tag{5.11}$$

where e is the traditional (global) void ratio, and e_{max}, e_{min} are the maximum and minimum void ratios of the soil mixture. As noted by Thevanayagam (2003) the traditional D_{r} 'may, but not always expected to, be the same' as D_{r}^*. Furthermore, Thevanayagam (2003) highlights that accurately determining e_{max} for silty soils is practically challenging, as the result is highly sensitive to small variations in test procedures, particularly the energy input during sample preparation. For this reason, and to ensure consistency with EGST, D_{r}^* was used instead of D_{r} in the estimation of R_{d}^* in equation (5.9).

5.3 Single-element simulations

5.3.1 Simulation strategy and material database selection

The primary objective of the single-element simulation campaign is to verify that the two Ta-Ger model variants, incorporating the modifications presented in section 5.2.2, provide a unified and accurate description of sand-fines mixtures. To evaluate the validity of this approach, simulations were first conducted using experimental data for Sydney sand mixed with Majura silt, as reported by Rahman et al. (2011). This well-characterised dataset serves as a benchmark for model calibration and verification before applying the framework to Karlsruhe fine sand with low-plasticity kaolinite (Tafili *et al.*, 2024).

The importance of using this stepwise strategy, verifying the proposed modelling adaptations on a separate sand-fines mixture before applying them to model Karlsruhe fine sand with kaolinite, lies in several key considerations: (i) benchmarking the approach against the Sydney sand-Majura silt mixture demonstrates that the modelling framework can reliably capture the behaviour of sand-fines mixtures, thereby supporting its application to other materials; (ii) from a theoretical standpoint, once the parameters for clean Karlsruhe fine sand (as established in chapter 3) are known and the CSL of the clean sand is defined, the model is expected to predict the behaviour of sand-fines mixtures based on the fines content and their index properties. This hypothesis is subject to validation in the present study; (iii) the same host material, Karlsruhe fine sand, has previously been tested to form an experimental database for clean sand behaviour (Wichtmann and Triantafyllidis, 2016a; 2016b), which has been widely used in prior studies evaluating constitutive models for clean sand; (iv) the experimental dataset of Tafili et al. (2024) offers loading and drainage conditions that are well aligned with the objectives of the present study, particularly in terms of drained monotonic and high-cycle triaxial tests; (v) this is the first time the dataset of Tafili et al. (2024) has been used for validating constitutive models; (vi) this is also the first

documented application of the proposed modelling approach to high-cycle triaxial tests. Previous studies of the EGST approach have primarily focused on undrained monotonic or short-term cyclic loading (Rahman et al., 2014; Xu et al., 2019; Rahman and Dafalias, 2022).

5.3.2 Sydney sand with Majura silt

5.3.2.1 Parameter calibration

In the first mixture used in this study, Sydney sand, a clean, uniform-size, angular quartz sand (poorly graded sand; effective size $D_{10} = 0.225$ mm, median size $D_{50} = 0.27$ mm; maximum and minimum void ratios $e_{\max,\mathrm{HS}} = 0.855$, $e_{\min,\mathrm{HS}} = 0.565$), serves as the host sand. The fines, on the other hand, consist of a natural silt from the Majura River bank deposits and commercial kaolin (well-graded fines; median size $d_{50} = 0.006$ mm; plasticity index $I_P = 27$).

The simulation parameters adopted for the Ta-Ger B and Ta-Ger HC models to reproduce the behaviour of the Sydney sand-Majura silt mixtures are summarised in Table 5.1 and Table 5.2, respectively. A summary of all simulated triaxial tests and their initial conditions is provided in Table 5.3. The table also indicates which tests were used for calibration, including the corresponding calibration targets, and which tests were treated as independent predictions. The parameters associated with the CSL, the bounding surface, and the phase transformation equations were adopted from Xu et al. (2019), who applied the EGST framework within the SANISAND DM04 model (Dafalias and Manzari, 2004) to simulate the same material. This choice is justified by the fact that Ta-Ger B, Ta-Ger HC and SANISAND DM04 share common formulations for these constitutive components.

For the Ta-Ger B model, the same parameter transfer as Xu et al. (2019) applies to the elastic formulation, as it incorporates the hypoelastic law proposed by Richart et al. (1970), consistent with SANISAND DM04. In contrast, Ta-Ger HC employs a hyperelastic

formulation (Houlsby et al., 2019), which requires separate calibration of the associated elastic parameters (k, v, n, y, N). The switch parameter N, determines the reference stress state for zero elastic strain along the isotropic axis. When $N = 0$, this reference state corresponds to zero stress ($\boldsymbol{\sigma} = \mathbf{0}$). In contrast, setting $N = 1$ shifts the reference to the mean effective stress P_r, such that $\boldsymbol{\sigma} = P_\mathrm{r}\mathbf{I}$ (Amorosi et al., 2020). In this study, N was set to 1, with P_r taken as the atmospheric pressure p_at. The Poisson's ratio v was assigned the same value as in the hypoelastic formulation, namely 0.15. To determine the dimensionless parameter k, which is related to g through v as described in section 5.2.2, the following approach was adopted. Given that G_0 was previously calibrated for the hypoelastic formulation, g (and hence k) was obtained by matching the expressions for shear modulus given in equations (5.4) and (5.5) at the reference pressure $p = p_\mathrm{at} = P_\mathrm{r}$. This yields:

$$g = G_0 \frac{(2.97 - e^*)^2}{1 + e^*} \tag{5.12}$$

As discussed in section 5.2.2, while the hypoelastic formulation accounts for the dependence of the elastic shear modulus on void ratio, the hyperelastic formulation does not. To remain consistent with the EGST framework and the findings of Rahman et al. (2012), who showed that the effect of fines on G can be captured by using e^* in place of e, a practical simplification was made. Instead of recalibrating g (and k) for each test-specific e^*, a single representative value of g was used, calculated by averaging the e^* values of all the Sydney sand-Majura silt samples (Table 5.3). This gave $g = 220$ for $e^* = 0.857$. The parameter n, which controls the nonlinearity of the shear modulus with respect to mean effective stress, was set to 0.3. Higher values produced overly stiff stress-strain responses in the calibration tests, namely the drained tests (A1-A4) and the undrained test S-MII-15-06. The anisotropy parameter $y = \sqrt{G_\mathrm{hh}/G_\mathrm{vh}}$, which appears in the symmetric fabric tensor **a** (see section 4.3.1.2), was calibrated by fitting the simulated stress path to that of test S-MII-15-06.

The remaining two Ta-Ger specific parameters, common to both variants, namely the dilatancy constant a and the hardening exponent n, were estimated so as to achieve good agreement with experiments. Parameter a was fitted against volumetric responses from drained triaxial tests (A1-A4), while n was adjusted to match the stress-strain behaviour observed in the same tests. Finally, the two fines content parameters χ and f_{thre}, which are used in the calculation of the fines influence factor b of equation (5.2), were adopted directly from Rahman et al. (2011).

Table 5.1: Ta-Ger B parameters for Sydney sand with Majura silt mixtures tested by Rahman et al. (2011).

Critical state				**Elasticity**			**Bounding surface**	**Dilatancy**		**Hardening exponent**	**Fines content**	
e_0 [-]	λ [-]	ξ [-]	M_{cs} [-]	G_0 [-]	ν [-]	m [-]	n_b [-]	a [-]	n_d [-]	n [-]	f_{thre} [-]	χ [-]
0.92	0.0375	0.60	1.305	90	0.15	0.5	0.8	0.3	2.5	0.25	0.40	37

Table 5.2: Ta-Ger HC parameters for Sydney sand with Majura silt mixtures tested by Rahman et al. (2011).

Critical state				**Elasticity**					**Bounding surface**	**Dilatancy**		**Hardening exponent**	**Fines content**	
e_0 [-]	λ [-]	ξ [-]	M_{cs} [-]	k [-]	ν [-]	n [-]	y [-]	N [-]	n_b [-]	a [-]	n_d [-]	n [-]	f_{thre} [-]	χ [-]
0.92	0.0375	0.60	1.305	240	0.15	0.3	0.9	1	0.8	0.3	2.5	0.25	0.40	37

Table 5.3: Summary of all simulated triaxial tests on Sydney sand with Majura silt mixtures.

Test name	f_c [%]	p_{in} [kPa]	e_{in} [-]	e^*_{in} [-]	ψ_{in} [-]	ψ^*_{in} [-]	**Source**	**Undrained behaviour***	**Drainage**	**Parameters calibrated**
A1	10	100	0.780	0.955	-0.102	0.073	Bobei (2004)	-	Drained	a, n, n
A2	10	300	0.749	0.921	-0.098	0.075		-	Drained	a, n, n
A3	10	400	0.732	0.903	-0.101	0.070		-	Drained	a, n, n
A4	10	600	0.722	0.892	-0.087	0.083		-	Drained	a, n, n
S-MII-00-06	00	350	0.743	0.743	-0.097	-0.097	Rahman et al. (2011)	NF	Undrained	-
S-MII-05-02	05	600	0.821	0.911	0.012	0.103		F	Undrained	-
S-MII-05-03	05	600	0.770	0.858	-0.039	0.049		LF	Undrained	-
S-MII-05-04	05	850	0.740	0.827	-0.043	0.044		LF	Undrained	-
S-MII-15-06	15	600	0.535	0.759	-0.274	-0.050		NF	Undrained	y, n
S-MII-15-09	15	1100	0.645	0.885	-0.115	0.125		TF	Undrained	-
S-MII-15-10	15	1300	0.569	0.797	-0.174	0.054		LF	Undrained	-
S-MII-20-02	20	600	0.573	0.874	-0.236	0.064		TF	Undrained	-

*F: flow; TF: transitional flow; LF: limited flow; NF: non-flow.

5.3.2.2 Drained monotonic triaxial tests

Figure 5.2 presents drained triaxial tests by Bobei (2004) on Sydney sand with Majura silt, used to calibrate selected model parameters (see Table 5.3), along with corresponding simulations using Ta-Ger B and Ta-Ger HC. The tests involve a fixed fines content (f_c) of 10%, covering a range of initial void ratios (e_{in}) and mean effective stresses (p_{in}). Although used for calibration, the data also provide a basis for assessing model performance. Both Ta-Ger B and Ta-Ger HC reproduce the stress-strain behaviour well, with a slight overprediction of deviator stress at small strains, more evident in Ta-Ger HC. As noted in section 5.3.2.1, this overprediction would increase for larger values of the hyperelastic parameter n, currently set to 0.3. Volumetric responses are also captured accurately by both models, producing nearly identical trends. Overall, under drained monotonic conditions, the different elastic formulations, particularly the absence of void ratio dependence in the hyperelastic Ta-Ger HC compared to the void-ratio-dependent hypoplasticity in Ta-Ger B, had minimal impact on predictive performance, despite the simplified calibration adopted for the former.

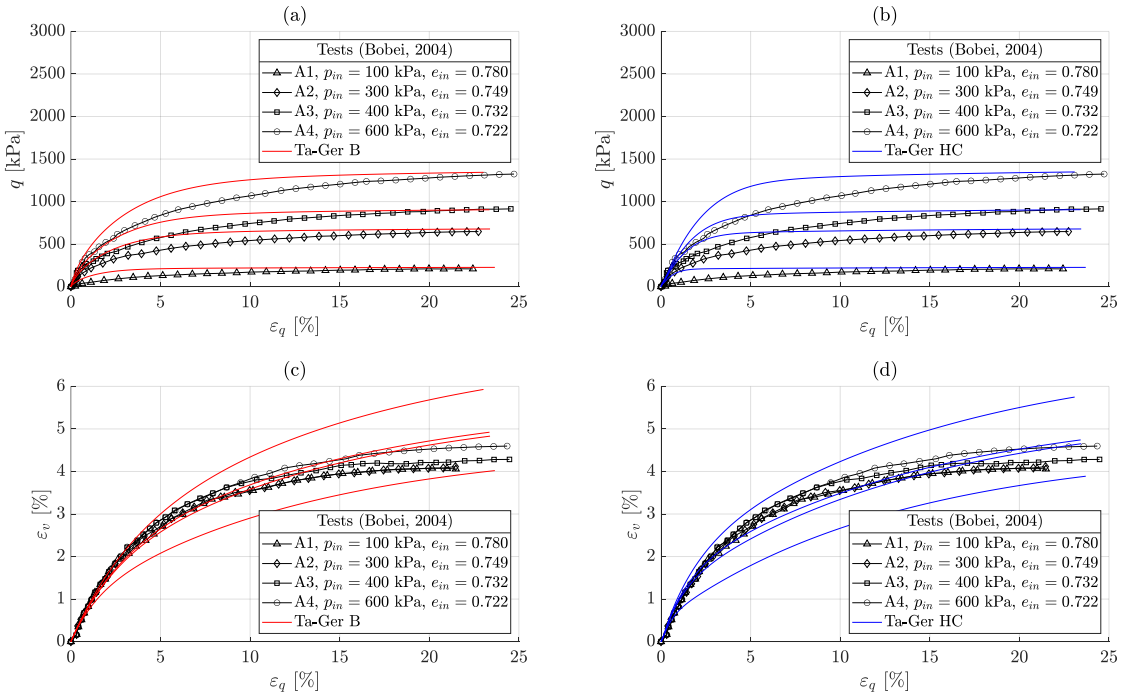

Figure 5.2: Calibration of parameters against drained triaxial tests on Sydney sand with Majura silt (constant $f_c = 10\%$, varying p_{in}, e_{in}) (Bobei, 2004): (a, c) Ta-Ger B; (b, d) Ta-Ger HC.

5.3.2.3 Undrained monotonic triaxial tests

Before evaluating the model predictions, for the tests that were not used for calibration, it is useful to outline the typical undrained responses of sands under triaxial loading, which fall into three primary categories as defined by Rahman et al. (2011) and Rahman and Dafalias (2022): non-flow (NF), limited flow (LF), and flow (F). In non-flow, the specimen strain-hardens continuously towards critical state defined by $\mathrm{d}q = 0$, $\mathrm{d}p = 0$, and $\mathrm{d}u = 0$, where u is the pore water pressure. Limited flow is characterised by an initial stress peak, followed by softening in q to a quasi-steady state (QSS), and a gradual recovery of q towards critical state. In flow, the deviatoric stress q reaches a peak and then softens toward the critical state stress ratio, but without achieving the corresponding critical state void ratio. This results in large strains and a condition that may be described as failure, though the critical state is not fully reached. If both q and p fall to zero, the response culminates in static liquefaction. Rahman et al. (2011) also described a fourth category, transitional flow (TF), which involves partial softening and incomplete recovery, and represents an intermediate response between limited and full flow. Table 5.3 shows the classification of the simulated tests as assigned by Rahman et al. (2011).

Eight undrained monotonic triaxial tests on Sydney sand mixed with Majura silt, conducted by Rahman et al. (2011), were simulated in total. Figure 5.3 presents simulation results against experimental data for samples with varying fines content ($f_c = 0\%$, 15%, 20%), initial void ratio, and initial mean effective stress. Figure 5.4 and Figure 5.5 show similar comparisons for tests with fixed fines contents of $f_c = 5\%$ and $f_c = 15\%$, respectively, but with varying initial void ratios and initial mean effective stresses. In all cases, both of the Ta-Ger models exhibit reasonable agreement with the experimental data.

As shown in Figure 5.3, Ta-Ger B and Ta-Ger HC yield similar stress-strain responses with minor discrepancies and good overall fit. Larger differences appear in the stress paths. For

S-MII-00-06 and S-MII-15-06, where non-flow behaviour is observed, Ta-Ger HC provides a closer match, with smaller deviations. This is consistent with the calibration of the hyperelastic anisotropy parameter y for Ta-Ger HC using S-MII-15-06. The improved match of the stress path with $y = 0.9$ supports the plausibility of sample anisotropy. For S-MII-20-02, which exhibits transitional flow, both models predict nearly identical responses in very good agreement with the experiment.

In Figure 5.4, the differences between the model predictions are more pronounced. For S-MII-05-02, which exhibits flow behaviour, both models produce similar stress-strain responses in good agreement with the experimental data. However, for S-MII-05-03 and S-MII-05-04, which exhibit limited flow behaviour, Ta-Ger B fails to capture the initial peak in q, while Ta-Ger HC accurately reproduces this feature. Nonetheless, Ta-Ger HC underestimates the extent and intensity of the softening phase prior to re-hardening, whereas Ta-Ger B predicts an exaggerated hardening response. Overall, Ta-Ger HC provides a substantially better prediction of the stress-strain response. Regarding the stress paths, Ta-Ger HC better captures the initial contractive tendency ($\mathrm{d}u < 0$), likely due to its ability to account for inherent anisotropy, but it underpredicts the subsequent dilative phase. In contrast, Ta-Ger B provides a more accurate representation of the dilative response.

Figure 5.5 presents results for S-MII-15-09, which exhibits transitional flow, S-MII-15-10, which exhibits limited flow behaviour, and S-MII-15-06, a non-flow case also shown in Figure 5.3. Similar conclusions to those drawn from the two previous figures can be made. Both models provide very good predictions of the stress-strain response for S-MII-15-09, with Ta-Ger HC slightly overestimating the peak stress. For the limited flow sample S-MII-15-10, Ta-Ger HC yields a superior prediction. In terms of stress paths, Ta-Ger HC slightly overpredicts the peak for S-MII-15-09, consistent with its stress-strain response, and better captures the contractive tendency for S-MII-15-10, while underestimating the dilative phase.

Overall, Ta-Ger HC performs better across all test conditions. It provides more accurate stress-strain responses, particularly for non-flow and limited flow cases, and captures contractive behaviour more effectively due to its anisotropic hyperelastic formulation. While Ta-Ger B performs better in the dilative phase, its overall predictive capability is inferior.

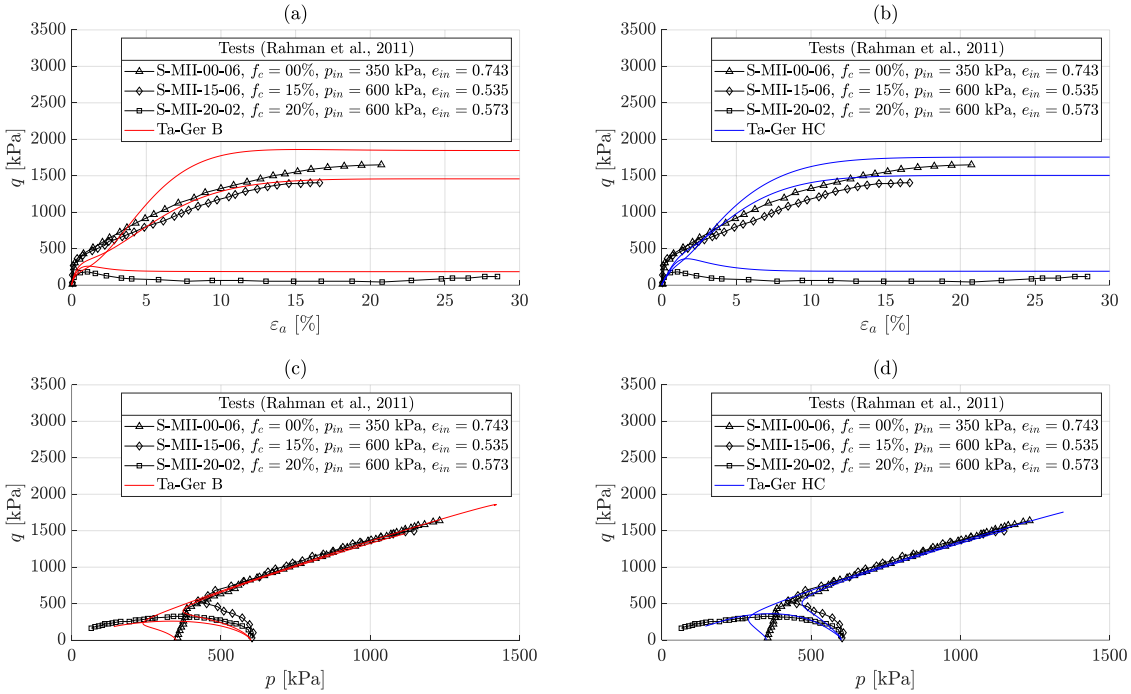

Figure 5.3: Simulations of undrained triaxial tests on Sydney sand with Majura silt (varying f_c, p_{in}, e_{in}) (Rahman, Lo and Baki, 2011): (a, c) Ta-Ger B; (b, d) Ta-Ger HC.

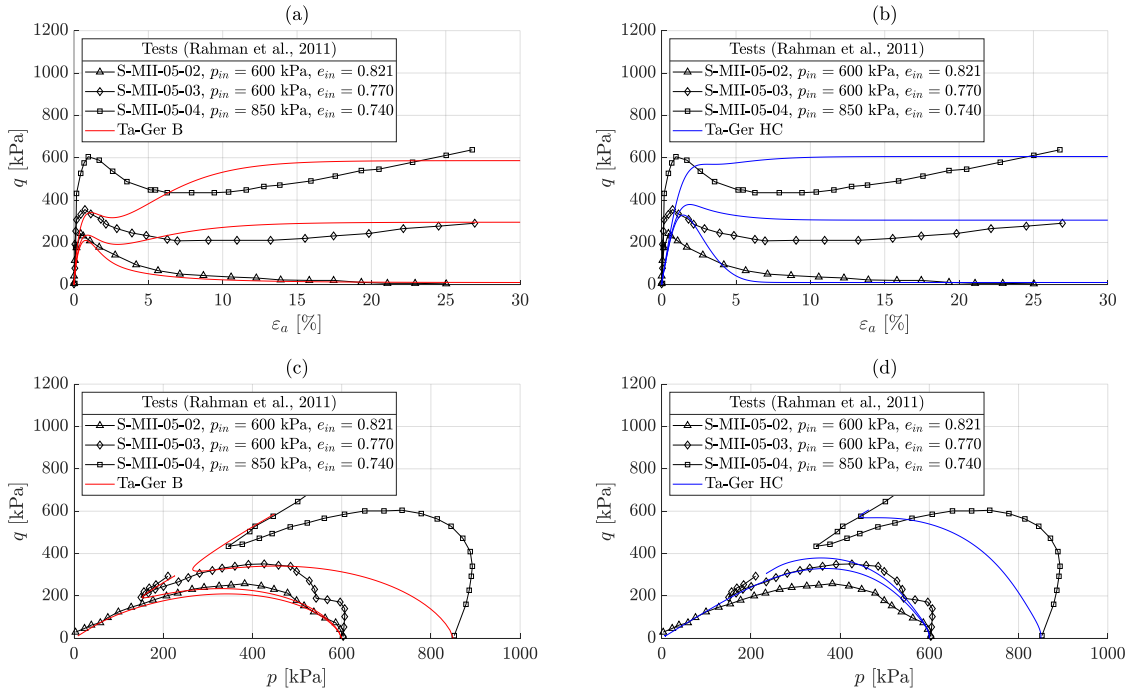

Figure 5.4: Simulations of undrained triaxial tests on Sydney sand with Majura silt (constant $f_c = 5\%$, varying p_{in}, e_{in}) (Rahman, Lo and Baki, 2011): (a, c) Ta-Ger B; (b, d) Ta-Ger HC.

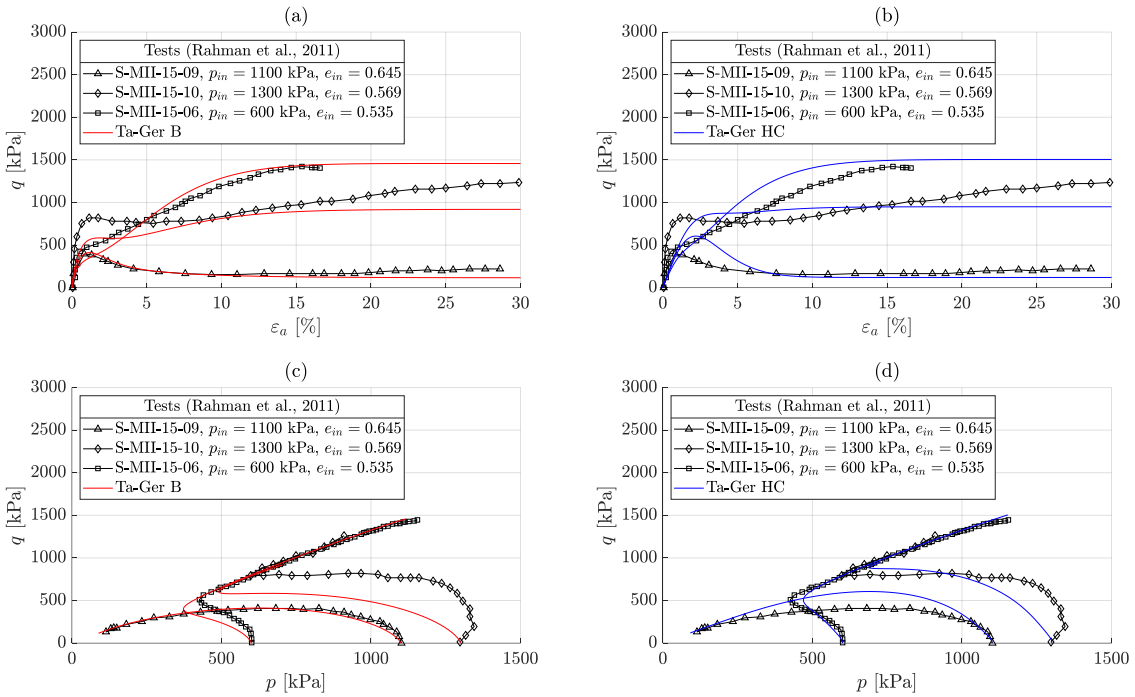

Figure 5.5: Simulations of undrained triaxial tests on Sydney sand with Majura silt (constant $f_c = 15\%$, varying p_{in}, e_{in}) (Rahman, Lo and Baki, 2011): (a, c) Ta-Ger B; (b, d) Ta-Ger HC.

5.3.2.4 Effectiveness of EGST

The effectiveness of incorporating EGST into the two Ta-Ger model variants can be appreciated from Figure 5.6, which compares the experimental stress-strain and stress path curves of specimen S-MII-20-02 against simulations. Results are shown for both the EGST-modified Ta-Ger B model and the original unmodified Ta-Ger B model. In both cases, the same set of parameters from Table 5.1 is used, with the unmodified model assuming $f_c = 0\%$, thus completely disregarding the influence of fines. According to the state parameter framework (Been and Jefferies, 1985), a sample with a negative initial state parameter ψ_{in}, that is, located below the CSL in $\ln(p) - e$ space (denser than critical), is expected to exhibit strong dilative tendencies, typically associated with non-flow behaviour under undrained loading. Conversely, a positive ψ_{in} (looser than critical) implies a contractive tendency, which may correspond to limited flow, transitional flow, or flow. In drained conditions, denser-than-critical samples typically undergo slight initial contraction followed by significant volumetric dilation and a pronounced peak and softening in the stress-strain curve. In contrast, looser-than-critical samples generally exhibit only volumetric contraction

with minimal or no peak in the stress-strain response. The tested sample has $f_c = 20\%$ and an initial void ratio $e_{\text{in}} = 0.573$. Without the incorporation of EGST, focusing solely on the negative initial value of the state parameter ($\psi_{\text{in}} = -0.236$) would misleadingly suggest a dilative response, such as non-flow. However, following the EGST framework, the modified model instead uses the equivalent granular state parameter ψ^* in place of ψ. With an initial equivalent state parameter of $\psi^*_{\text{in}} = 0.064$, the model correctly predicts transitional flow rather than non-flow behaviour, aligning more closely with the experimental response. The difference between the values ψ_{in} and ψ^*_{in} for all simulated Sydney sand with Majura silt samples can be seen in Table 5.3, implying that similarly unrealistic predictions would have been obtained had the simulations completely disregarded the fines content.

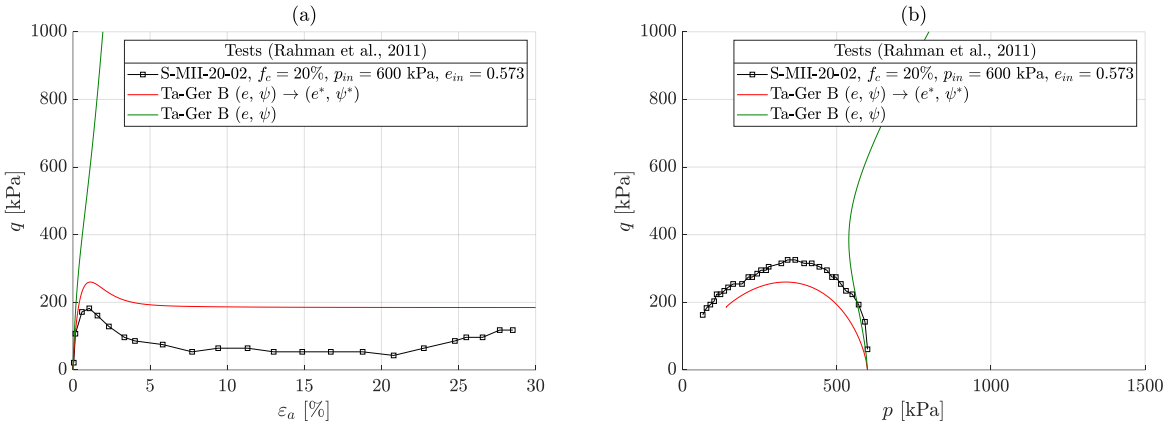

Figure 5.6: Simulations of undrained triaxial test S-MII-20-02 on Sydney sand with Majura silt (Rahman, Lo and Baki, 2011), using Ta-Ger B with EGST modifications (red) and without modifications (green).

5.3.3 Karlsruhe fine sand with low-plasticity kaolinite

5.3.3.1 Parameter calibration

In the second mixture used in this study, Karlsruhe fine sand, a uniform-size, quartz sand (uniformity coefficient $C_{\text{u}} = 1.5$, median size $D_{50} = 0.14$ mm; maximum and minimum void ratios $e_{\text{max,HS}} = 1.054$, $e_{\text{min,HS}} = 0.677$), serves as the host sand. It is noted that this is the same material used in the experimental database developed by Wichtmann and Triantafyllidis (2016a; 2016b). The fines component consists of low-plasticity kaolinite (plasticity index $I_P = 12.2\%$).

Table 5.4 and Table 5.5 present the parameters adopted for the Ta-Ger B and Ta-Ger HC models to simulate the response of Karlsruhe fine sand mixed with low-plasticity kaolinite. The full set of simulated triaxial tests, including drained and undrained monotonic loading and drained high-cycle loading, is summarised in Table 5.6, which also identifies the tests used for parameter calibration and those retained for independent validation. As outlined in section 5.3.1, since the constitutive parameters and CSL for clean Karlsruhe sand (see section 3.3.1.2) are known, and the index properties of the fines, together with parameters χ and f_{thre}, are available from Tafili et al. (2024), it is appropriate to assess whether the two EGST-modified Ta-Ger variants can reproduce the response of Karlsruhe fine sand-kaolinite mixtures without further recalibration.

In particular, since Ta-Ger B shares its hypoelastic law, critical state line, bounding surface, and phase transformation rule with SANISAND DM04, the corresponding parameters are adopted directly from studies that used the latter model for simulating clean Karlsruhe fine sand (Wichtmann, 2016; Wichtmann, et al., 2019). The dilatancy constant a, common to both Ta-Ger B and Ta-Ger HC, was also taken to be the same as assumed for Ta-Ger B for clean Karlsruhe fine sand (see section 3.3.1.2). For Ta-Ger HC, the hyperelastic parameters were selected following the same approach used in section 5.3.3.1 for Sydney sand-Majura silt mixtures. Equation (5.12) was applied using an average equivalent void ratio of $e^* = 0.970$, which gave $g = 205$. The switch parameter N was set to 1, and the Poisson's ratio v was kept equal to that in the hypoelastic formulation, namely 0.05. The nonlinear parameter n was set to 0.3 to avoid overly stiff stress-strain responses in monotonic drained test M01 and undrained test M21. The anisotropy parameter y was calibrated to match the experimental stress path of test M21.

Table 5.4: Ta-Ger B parameters for Karlsruhe fine sand with low-plasticity kaolinite mixtures tested by Tafili et al. (2024).

Critical state				Elasticity			Bounding surface	Dilatancy		Hardening exponent	Fines content	
e_0 [-]	λ [-]	ξ [-]	M_{cs} [-]	G_0 [-]	ν [-]	m [-]	n_b [-]	a [-]	n_d [-]	n^* [-]	f_{thre} [-]	χ [-]
1.103	0.122	0.205	1.34	100	0.05	0.5	1.2	0.3	2.0	0.15	0.395	26.5

*$n = [n_{peak} + (n_0 - n_{peak})e^{-\beta \Sigma d\varepsilon_q}]$ for drained high-cycle loading ($n_0 = 0.5$, $n_{\text{peak}} = 6.5$, and $\beta = 10$).

Table 5.5: Ta-Ger HC parameters for Karlsruhe fine sand with low-plasticity kaolinite mixtures tested by Tafili et al. (2024).

Critical state				Elasticity					Bounding surface	Dilatancy		Hardening exponent	Fines content	
e_0 [-]	λ [-]	ξ [-]	M_{cs} [-]	k [-]	ν [-]	n [-]	y [-]	N [-]	n_b [-]	a [-]	n_d [-]	n^* [-]	f_{thre} [-]	χ [-]
1.103	0.122	0.205	1.34	160	0.05	0.3	0.8	1	1.2	0.3	2.0	0.15	0.395	26.5

*$n = [n_{peak} + (n_0 - n_{peak})e^{-\beta \Sigma d\varepsilon_q}]$ for drained high-cycle loading ($n_0 = 0.5$, $n_{\text{peak}} = 6.5$, and $\beta = 10$).

Table 5.6: Summary of all simulated triaxial tests on Karlsruhe fine sand with low-plasticity kaolinite mixtures (Tafili *et al.*, 2024).

Test name	f_c [%]	p_{in} [kPa]	e_{in} [-]	e^*_{in} [-]	ψ_{in} [-]	ψ^*_{in} [-]	Undrained behaviour*	Loading/ drainage	Parameters calibrated
M01	10	100	0.759	0.932	-0.221	-0.049	-	Monotonic/drained	n
M04	10	100	0.888	1.073	-0.093	0.092	-	Monotonic/drained	-
M07	10	100	0.811	0.989	-0.169	0.008	-	Monotonic/drained	-
M23	10	100	0.707	0.874	-0.274	-0.107	-	Monotonic/drained	-
M08	20	100	0.728	1.055	-0.252	0.074	-	Monotonic/drained	-
M11	20	100	0.626	0.934	-0.354	-0.047	-	Monotonic/drained	-
M20	20	100	0.662	0.976	-0.319	-0.005	-	Monotonic/drained	-
M05	10	100	0.895	1.081	-0.085	0.1	F	Monotonic/undrained	-
M16	10	100	0.683	0.848	-0.298	-0.133	NF	Monotonic/undrained	-
M21	10	100	0.749	0.921	-0.231	-0.06	NF	Monotonic/undrained	y, n
M22	10	100	0.782	0.957	-0.198	-0.024	LF	Monotonic/undrained	-
M13	20	100	0.631	0.939	-0.35	-0.042	LF	Monotonic/undrained	-
M14	20	100	0.742	1.072	-0.238	0.091	TF	Monotonic/undrained	-
M17	20	100	0.577	0.895	-0.387	-0.086	NF	Monotonic/undrained	-
M18	20	100	0.577	0.875	-0.404	-0.106	NF	Monotonic/undrained	-
C01	10	200	0.768	0.942	-0.193	-0.02	-	High-cycle/drained	-
C02	10	200	0.881	1.066	-0.08	0.104	-	High-cycle/drained	-
C03	10	200	0.778	0.952	-0.184	-0.01	-	High-cycle/drained	n_0, n_{peak}, β
C05	20	200	0.744	1.074	-0.218	0.112	-	High-cycle/drained	-
C07	20	200	0.603	0.906	-0.359	-0.056	-	High-cycle/drained	-
C11	20	200	0.758	1.091	-0.203	0.129	-	High-cycle/drained	-

*F: flow; TF: transitional flow; LF: limited flow; NF: non-flow.

Finally, for high-cycle loading, the exponent n was defined in both models as a function of the cumulative incremental deviatoric strain, $\Sigma \mathrm{d}\varepsilon_q$ (see section 4.2.1.6). A simplified form applicable to drained conditions was adopted (Table 5.4, Table 5.5), and parameters n_0, n_{peak}, and β were calibrated to match the strain accumulation observed in test C03.

5.3.3.2 Drained monotonic triaxial tests

Figure 5.7 and Figure 5.8 compare simulation results with experimental data from drained monotonic triaxial tests conducted by Tafili et al. (2024) on Karlsruhe fine sand mixed with kaolinite. Both sets of tests were performed with an initial mean effective stress of 100 kPa and involved samples with varying initial void ratios, for fines contents of $f_c = 10\%$ (Figure 5.7) and $f_c = 20\%$ (Figure 5.8).

In Figure 5.7, both models show overall good agreement with the stress-strain data, with small deviations from the experiments and between each other. Ta-Ger B produces softer responses, aligning more closely with tests M04 and M07, which correspond to looser-than-critical samples, as indicated in Table 5.6 by their positive equivalent granular state parameter ($\psi^*_{\mathrm{in}} > 0$) after incorporating EGST. Conversely, Ta-Ger HC yields stiffer curves, better matching tests M01 and M23, which are denser-than-critical ($\psi^*_{\mathrm{in}} < 0$). The volumetric responses are accurately captured by both models, which produce nearly identical predictions that closely follow the experimental trends.

With the increase in fines content in Figure 5.8, both models again show satisfactory agreement with the experimental stress-strain curves. Ta-Ger B provides slightly better agreement, while Ta-Ger HC tends to overestimate stiffness. The volumetric responses are also well reproduced by both models, with nearly identical predictions. However, the deviation observed for test M11 suggests that the estimated $\psi^*_{\mathrm{in}} = -0.047$ (Table 5.6), computed via EGST, may be too negative or should even be positive. This is supported by

the experimental data, which show purely contractive behaviour, whereas the simulations predict contraction followed by dilation. Both models perform well across all drained tests, with only slight accuracy loss at higher fines contents. This is particularly notable given that both models rely solely on parameters for clean sand, combined with the EGST framework.

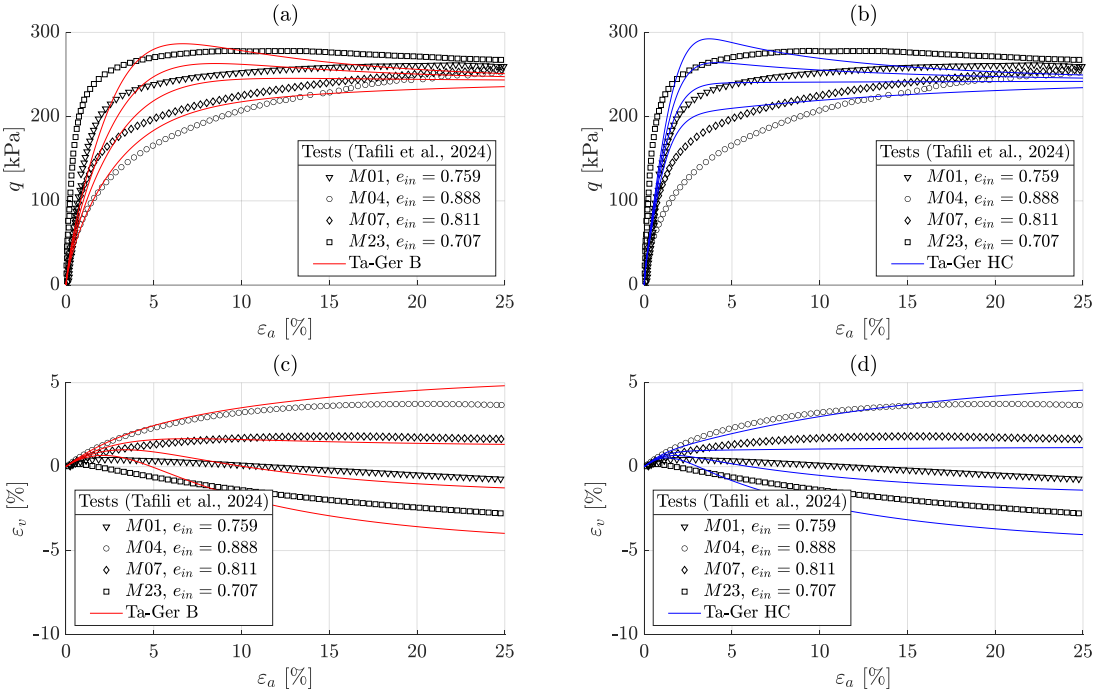

Figure 5.7: Simulations of drained triaxial tests on Karlsruhe fine sand with low-plasticity kaolinite (constant $f_c = 10\%$, $p_{\text{in}} = 100$ kPa, varying e_{in}) (Tafili *et al.*, 2024): (a, c) Ta-Ger B; (b, d) Ta-Ger HC.

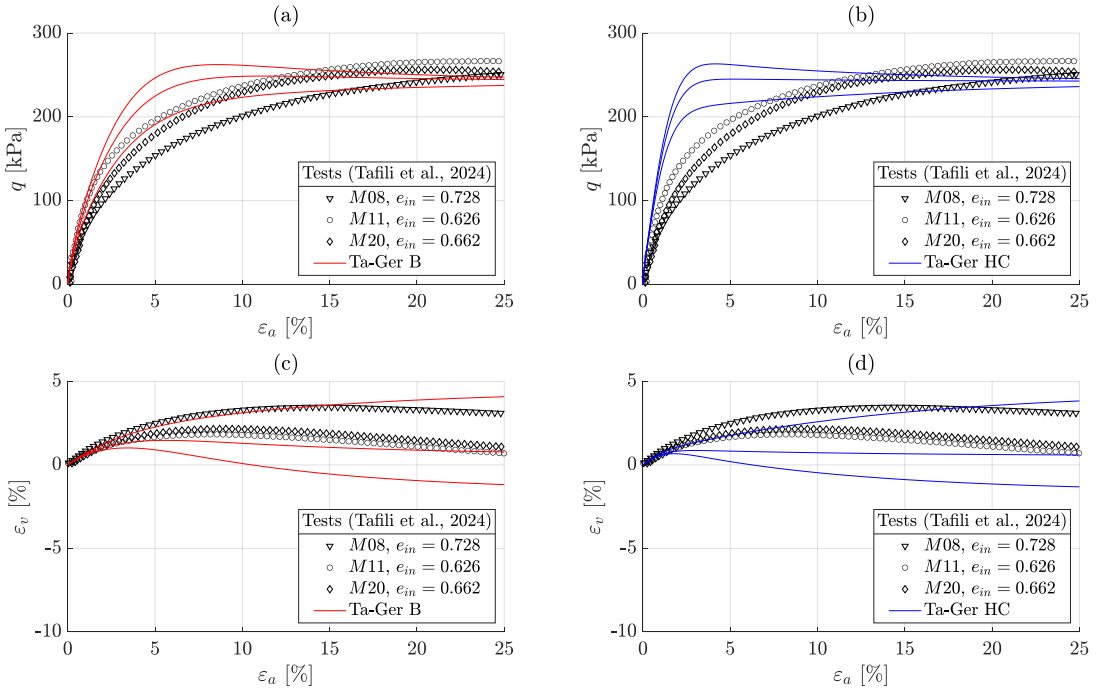

Figure 5.8: Simulations of drained triaxial tests on Karlsruhe fine sand with low-plasticity kaolinite (constant $f_c = 20\%$, $p_{\text{in}} = 100$ kPa, varying e_{in}) (Tafili *et al.*, 2024): (a, c) Ta-Ger B; (b, d) Ta-Ger HC.

5.3.3.3 Undrained monotonic triaxial tests

Figure 5.9 and Figure 5.10 present simulation results alongside undrained monotonic triaxial test data by Tafili et al. (2024) on Karlsruhe fine sand mixed with kaolinite, conducted with an initial mean effective stress of 100 kPa and varying initial void ratios, for fines contents of $f_c = 10\%$ and $f_c = 20\%$, respectively. The behavioural classification of the tests, based on the framework by Rahman et al. (2011) and Rahman and Dafalias (2022) (section 5.3.2.3), is summarized in Table 5.6.

For $f_c = 10\%$ (Figure 5.9), both models provide similarly good agreement with the experimental stress-strain response of test M05, which exhibits flow behaviour. In tests classified as non-flow, Ta-Ger HC better captures the slope of the stress-strain curve in M16, while Ta-Ger B aligns more closely with M21. In contrast, both models show notable deviations from the experimental response in M22, which displays limited flow behaviour. Regarding stress paths, Ta-Ger HC performs better overall, closely reproducing the experimental curves in M16, M21, and M22. This improved accuracy may be attributed to the hyperelastic formulation of Ta-Ger HC, which captures inherent anisotropy, supported by the adopted value of $y = 0.8$, suggesting a degree of anisotropy in the mixture. For M05, both models yield similar stress paths in good agreement with the experimental data.

For $f_c = 20\%$ (Figure 5.10), both models predict stiffer stress-strain responses than observed for M17 and M18 (non-flow) and M13 (limited flow), with Ta-Ger B producing slightly better overall agreement. In test M14, both models predict flow behaviour, deviating from the transitional flow observed experimentally, where the deviatoric stress partially recovered. This misprediction is also evident when comparing the predicted and experimental stress paths. Nonetheless, for M13, M17, and M18, Ta-Ger HC provides a closer match to the experimental stress paths, reaffirming the effectiveness of its anisotropic hyperelastic formulation in reproducing the $p - q$ behaviour of the sand-kaolinite mixtures.

Overall, both models perform well in simulating undrained monotonic tests at both fines contents. Ta-Ger B offers slightly more accurate stress-strain predictions, particularly at higher fines contents, while Ta-Ger HC more effectively captures the stress path evolution due to its anisotropic hyperelastic formulation.

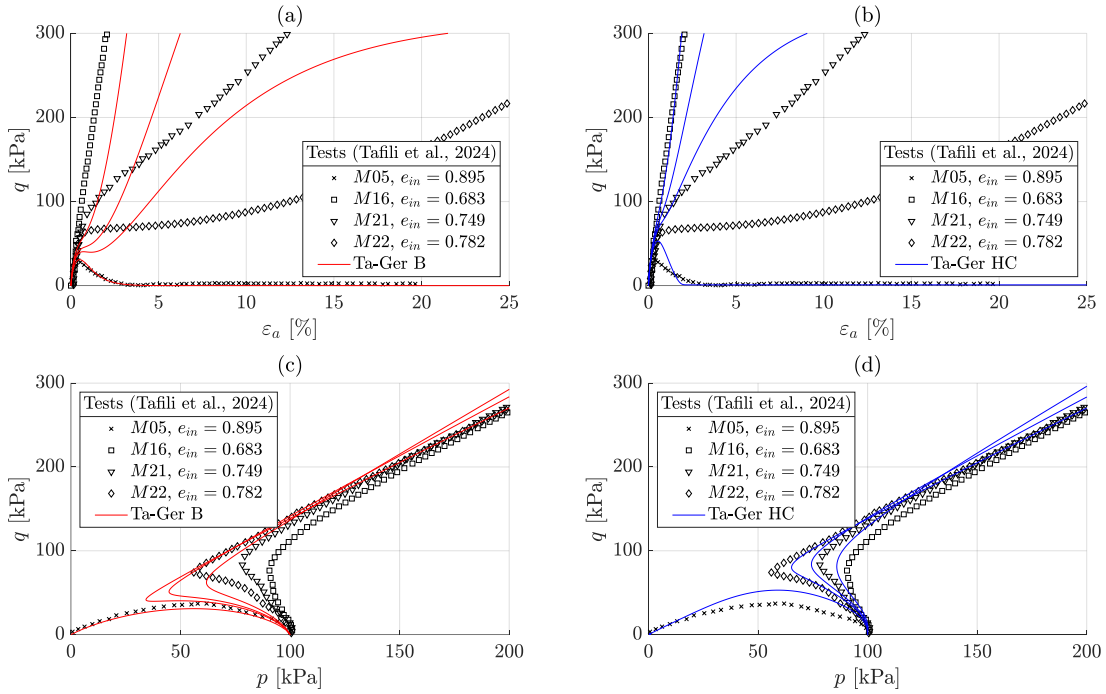

Figure 5.9: Simulations of undrained triaxial tests on Karlsruhe fine sand with low-plasticity kaolinite (constant $f_c = 10\%$, $p_{\text{in}} = 100$ kPa, varying e_{in}) (Tafili *et al.*, 2024): (a, c) Ta-Ger B; (b, d) Ta-Ger HC.

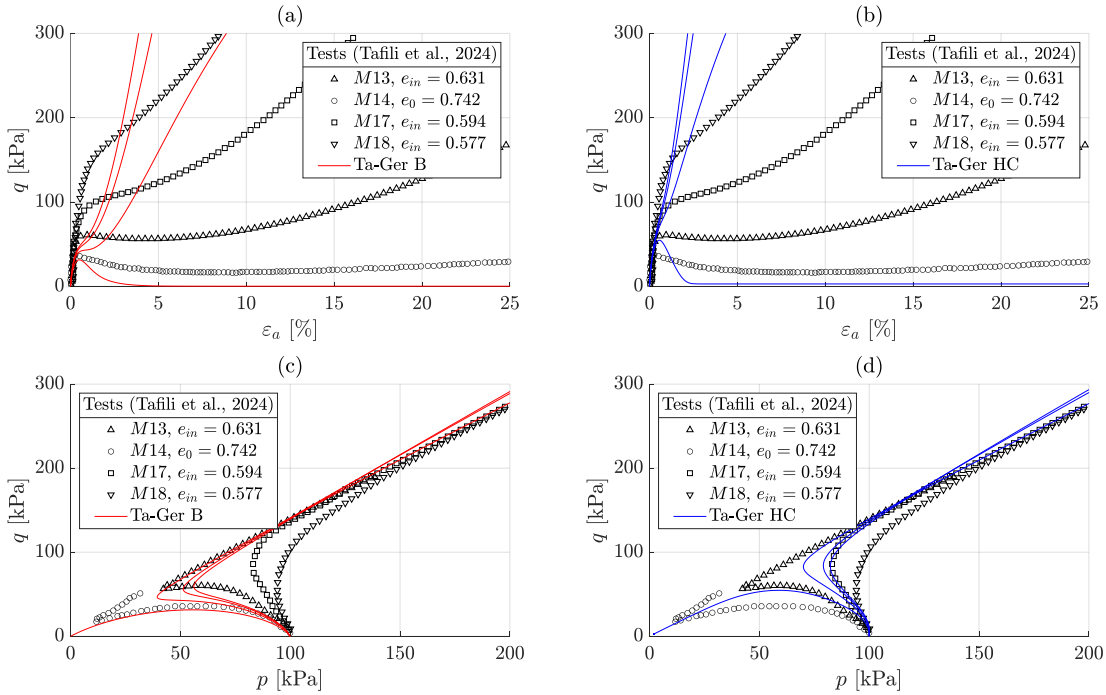

Figure 5.10: Simulations of undrained triaxial tests on Karlsruhe fine sand with low-plasticity kaolinite (constant $f_c = 20\%$, $p_{\text{in}} = 100$ kPa, varying e_{in}) (Tafili *et al.*, 2024): (a, c) Ta-Ger B; (b, d) Ta-Ger HC.

5.3.3.4 Drained high-cycle triaxial tests

Figure 5.11 and Figure 5.12 present simulations of drained high-cycle triaxial tests conducted by Tafili et al. (2024) on Karlsruhe fine sand mixed with kaolinite, showing the number of cycles (N) plotted against the accumulated total strain ($\varepsilon^{\mathrm{acc}}$), which is defined by Wichtmann (2005) as $\varepsilon^{\mathrm{acc}} = \sqrt{(\varepsilon_{\mathrm{v}}^{\mathrm{acc}})^2/3 + 1.5(\varepsilon_q^{\mathrm{acc}})^2}$. The tests were conducted under a prescribed average stress ratio $\eta^{\mathrm{ave}} = q^{\mathrm{ave}}/p_{\mathrm{in}}$, with $\eta^{\mathrm{ave}} = 0$, $q^{\mathrm{ampl}} = 60$ kPa, and $p_{\mathrm{in}} = 200$ kPa, where cyclic loading was applied as $q = q^{\mathrm{ave}} \pm q^{\mathrm{ampl}}$. Samples had varying initial void ratios, with fines contents of $f_c = 10\%$ (Figure 5.11) and $f_c = 20\%$ (Figure 5.12).

Starting with the lower fines content, Figure 5.11 shows that the predictions of both Ta-Ger B and Ta-Ger HC exhibit satisfactory overall agreement with the experimental data. In greater detail, Ta-Ger B appears to better capture the strain accumulation trend up to 100 cycles, whereas Ta-Ger HC offers improved agreement beyond this point. Both models perform better for the looser-than-critical sample C02 ($\psi_{\mathrm{in}}^{*} > 0$), which exhibits greater strain accumulation overall. For the denser-than-critical samples C01 and C03 ($\psi_{\mathrm{in}}^{*} < 0$), both models tend to slightly underpredict the final accumulated strain, though the discrepancies remain within acceptable bounds.

For the increased fines content of $f_c = 20\%$ (Figure 5.12), both Ta-Ger B and Ta-Ger HC produce nearly identical accumulation trends for the denser-than-critical sample C07 ($\psi_{\mathrm{in}}^{*} < 0$), though both models underpredict the strain accumulation throughout the loading phase compared to the experimental trend. For the looser-than-critical samples C05 and C11 ($\psi_{\mathrm{in}}^{*} > 0$), Ta-Ger B provides slightly better agreement up to 100 cycles, while Ta-Ger HC delivers superior performance beyond this point, accurately capturing both the overall accumulation trend and the final accumulated strain $\varepsilon^{\mathrm{acc}}$.

Given the importance of accurately predicting long-term strain accumulation in the design of OWT monopile foundations, Ta-Ger HC is considered the more suitable choice for high-cycle applications. However, a more comprehensive evaluation would require a database featuring a broader range of test conditions beyond initial void ratio, such as variations in mean stress ratio (η^{ave}), cyclic stress amplitude (q^{ampl}), and initial mean effective stress (p_{in}). Such tests are currently not available in the literature for sand-fines mixtures.

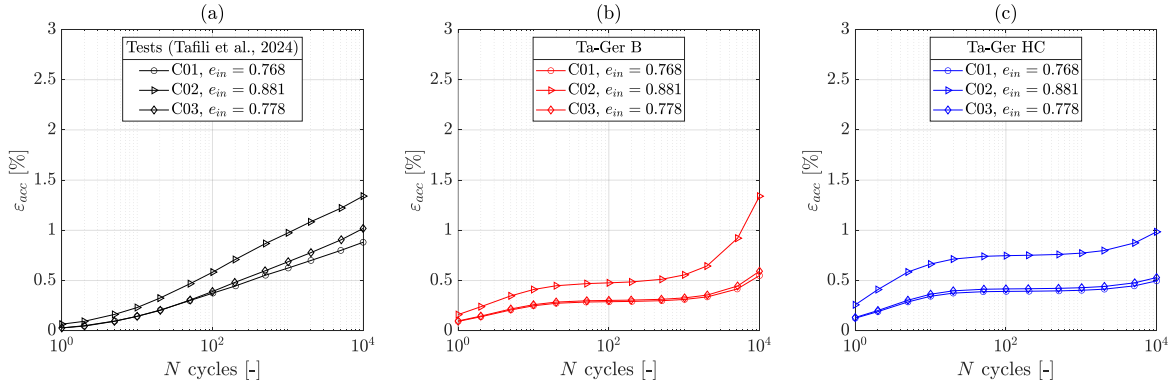

Figure 5.11: Simulations of high-cycle drained triaxial tests on Karlsruhe fine sand with low-plasticity kaolinite (constant $f_c = 10\%$, $p_{\mathrm{in}} = 200$ kPa, varying e_{in}) (Tafili *et al.*, 2024): (a) Experiments; (b) Ta-Ger B; (c) Ta-Ger HC.

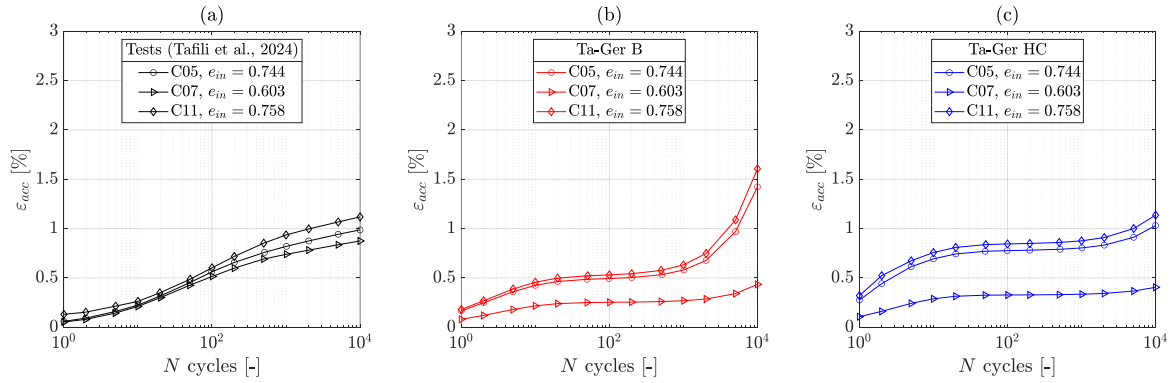

Figure 5.12: Simulations of high-cycle drained triaxial tests on Karlsruhe fine sand with low-plasticity kaolinite (constant $f_c = 20\%$, $p_{\mathrm{in}} = 200$ kPa, varying e_{in}) (Tafili *et al.*, 2024): (a) Experiments; (b) Ta-Ger B; (c) Ta-Ger HC.

5.3.3.5 Effectiveness of EGST for predicting high-cycle strain accumulation

The importance of incorporating EGST in high-cycle simulations without neglecting the presence of fines is illustrated in Figure 5.13, which compares strain accumulation predictions for test C05 using the EGST-modified Ta-Ger B model against the original unmodified formulation. All simulations employ the same parameter set from Table 5.4, but

the unmodified model entirely disregards the influence of fines ($f_c = 0\%$). Test C05 has a fines content of $f_c = 20\%$ and an initial void ratio of $e_{\mathrm{in}} = 0.744$, corresponding to an initial state parameter of $\psi_{\mathrm{in}} = -0.218$. Without EGST, this negative value suggests a denser-than-critical state and leads to an unrealistically low prediction of strain accumulation ($\varepsilon^{\mathrm{acc}}$). In contrast, the EGST-based formulation replaces ψ_{in} with the equivalent granular state parameter $\psi^*_{\mathrm{in}} = 0.112$, accounting for the influence of fines. As a result, it captures both the observed accumulation trend and the final accumulated strain with greater accuracy. This comparison highlights the capability of EGST to produce realistic predictions for drained high-cycle loading of sand-fines mixtures, and strongly supports its use in practical cyclic design. Figure 5.13 shows that neglecting fines may lead to unconservative predictions, potentially compromising design safety.

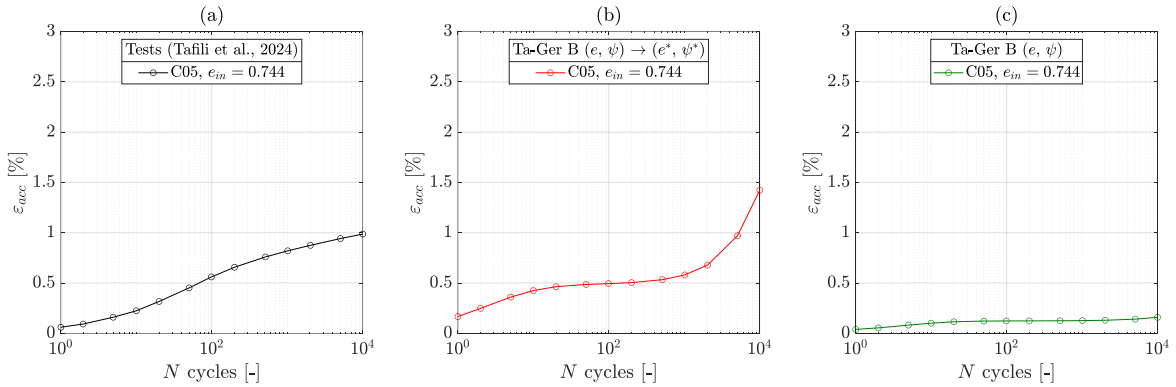

Figure 5.13: Simulations of high-cycle drained triaxial test C05 on Karlsruhe fine sand with low-plasticity kaolinite (Tafili *et al.*, 2024): (a) Experiments; (b) Ta-Ger B with EGST modifications; (c) Ta-Ger B without modifications.

5.3.4 Conclusions

This chapter extends the application of the two Ta-Ger clean-sand model variants introduced in chapter 4, namely Ta-Ger B and Ta-Ger HC, to sand-fines mixtures by integrating EGST (Rahman, 2021), following the approach of Rahman et al. (2014). This extension enables the models to be employed using parameters calibrated for clean sand and a small number of fines index properties. As a result, the need to undertake recalibration across different fines contents is avoided, preserving model consistency and reducing the calibration workload.

Simulations with both Ta-Ger B and Ta-Ger HC demonstrated good agreement with experimental data from two independent sand-with-fines databases, across drained and undrained monotonic tests at fines contents up to $f_c = 20\%$. The incorporation of an anisotropic hyperelastic law (Houlsby et al., 2019) in Ta-Ger HC led to consistently improved prediction of stress paths, particularly in samples exhibiting non-flow behaviour under undrained loading, where Ta-Ger B showed reduced accuracy. This chapter also introduces a simplified calibration procedure to address the absence of void ratio dependency in the hyperelastic law of Ta-Ger HC, while remaining consistent with the EGST approach.

High-cycle drained triaxial simulations up to $N = 10000$ and comparison against experimental data further demonstrated the capability of the EGST-based framework to deliver realistic predictions under conditions relevant to the modelling of OWT foundations in sandy soils, where the seabed typically contains some fraction of fines. This study also marks the first application of a constitutive model to the database developed by Tafili et al. (2024). Owing to its hyperelastic component, Ta-Ger HC outperformed Ta-Ger B, which employs the conventional hypoelastic law (Richart et al., 1970), particularly in high-cycle loading by more accurately predicting the accumulation trend and final strain beyond $N = 100$ cycles, making it the preferred variant for OWT monopile design applications.

It is noted, however, that consistent with the observations for clean sand in chapter 4, both the Ta-Ger B and Ta-Ger HC simulations for sand-fines mixtures exhibit a tendency for accelerated strain accumulation as the number of cycles approaches $N = 10000$, whereas the experimental data generally maintain a more stable accumulation rate, with this tendency being more pronounced for Ta-Ger B. This consistency across clean sand and sand-fines mixtures indicates that the observed behaviour is not primarily driven by fines effects, but is instead associated with more fundamental aspects of the constitutive formulation and numerical implementation under very high-cycle loading conditions. While the EGST-

adapted formulation provides reliable predictions within the cycle range examined, caution is therefore warranted when applying the current formulation and numerical implementation beyond 10000 cycles. As concluded in chapter 4, investigation of the underlying mechanisms and potential mitigation strategies lies beyond the scope of the present study, but represents an important and scientifically relevant direction for future research.

It is also acknowledged that the EGST framework adopted in this chapter relies on the assumption that the critical state line of a sand-fines mixture can be represented using the parameters of the host clean sand, with fines effects incorporated through the equivalent granular void ratio e^* and equivalent granular state parameter ψ^*. This assumption is central to the practical appeal of the approach, as it enables a unified parameter set to be retained without additional recalibration. Nevertheless, at higher fines contents ($f_c \geq 15\%$), it is recognised that the critical state characteristics of the mixture may differ from those of the clean sand, potentially requiring adjustment of parameters such as the critical state slope λ in the $\ln(p) - e$ space. In the present study, this possibility is not pursued in order to retain model consistency and focus on the predictive capability of the unified EGST-based formulation. Additionally, as highlighted by Rahman et al. (2014), EGST concepts are unlikely to extend reliably to high-plasticity fines, and caution is therefore advised when applying the model beyond the fines types examined here. These limitations should be borne in mind in future applications of the framework.

Overall, the results confirm that the EGST-adapted Ta-Ger HC offers a reliable and efficient framework for modelling sand-fines mixtures, in a unified manner in conditions where fines may significantly influence soil response.

Chapter 6

Application of the Ta-Ger model to 3D-FE simulations of monopile foundation

6.1 Introduction

Through a systematic assessment of different constitutive models (chapter 3) and different model variants (chapters 4 and 5) within the Ta-Ger family (Tasiopoulou and Gerolymos, 2016a; 2016b), Ta-Ger B and Ta-Ger HC emerged as the most suitable candidates for application in the final stage of this study, involving boundary value problems (BVPs). The only distinction between these two variants lies in their elasticity formulation: Ta-Ger B adopts a nonlinear hypoelastic law (Richart *et al.*, 1970), while Ta-Ger HC employs a nonlinear anisotropic hyperelastic law (Houlsby *et al.*, 2019). Given that noticeable differences arising from the use of different elastic formulations were shown to occur only beyond 1000 cycles for clean sands at the single-element scale (chapter 4), and since the BVP simulations in the present study involved no more than 400 cycles, their influence was expected to be negligible at the time the model variant was selected. Accordingly, Ta-Ger B was selected for the BVP simulations as a first step, offering a practical baseline for evaluating model performance before advancing to more complex variants.

Given that monopiles are the most commonly used foundations for offshore wind turbines (OWTs) (Byrne *et al.*, 2019), developing reliable design methods to predict their long-term lateral cyclic response remains a critical challenge (Abadie *et al.*, 2023). A cornerstone of such methods is the use of constitutive models capable of representing key features of soil behaviour under cyclic loading. Accordingly, this final stage of the study evaluates the performance of the Ta-Ger B model in BVPs using three-dimensional finite element (3D-FE) simulations, focusing on the cyclic lateral response of monopiles embedded in sand. A modelling methodology similar to Pisanò et al. (2024) was adopted, in which the SANISAND-MS model (Liu *et al.*, 2019) was used to simulate experimental data from the PISA field campaign, specifically the medium-scale cyclic tests conducted at the Dunkirk site, as reported by Byrne et al. (2020b) and Beuckelaers (2017). As in that study, the aim here is to evaluate the model's ability to reproduce the accumulation of permanent lateral deflection (tilt) under cyclic lateral loading, a key aspect in OWT monopile design. Beyond comparing predictions to field data, the study explores the effects of parameter calibration, loading history, and key soil element behaviour near the pile. The latter aims to link global monopile response with local mechanisms. The model's consistency with the empirical power-law relationship proposed by LeBlanc et al. (2010) is also evaluated.

Key contributions of this study include: (i) the numerical implementation of the Ta-Ger B variant in a 3D-FE software; (ii) insights into its robust implementation and application, gained through simulations of monopile foundations in sand under cyclic loading, with relevance to other Ta-Ger variants; (iii) one of the few published fully intrinsic (i.e., step-by-step) 3D-FE simulations of the PISA field dataset (Byrne et al., 2020b), following Pisanò et al. (2024). For reference, Tasiopoulou et al. (2020) previously implemented and applied the Ta-Ger A variant in the finite difference (FD) software FLAC3D to simulate the same field tests, though only under monotonic and cyclic loading at a single amplitude; (iv) an

evaluation of whether the calibration strategy proposed by Pisanò et al. (2024) can be applied to alternative cyclic models beyond SANISAND-MS, together with new insights into the calibration of Ta-Ger B; and (v) a critical reflection on the model's strengths and limitations, offering guidance for future refinements and applications involving a broader range of loading conditions, drainage scenarios, and BVPs.

6.2 Numerical implementation of Ta-Ger B in commercial 3D-FE software

6.2.1 Implementation of a User-Defined Soil Model (UDSM) in PLAXIS 3D

The Ta-Ger B model was implemented as a User-Defined Soil Model (UDSM) within the commercial finite element software PLAXIS 3D (Bentley Systems, 2024a). The implementation was compiled as a dynamic link library (DLL) written in Fortran and was connected to PLAXIS 3D using the UDSM interface. During the simulation process, PLAXIS communicates with the DLL by invoking specific tasks identified by the integer argument IDTask, which can take values between 1 and 6. These tasks are: (i) initialization of state variables (IDTask 1); (ii) evaluation of constitutive stresses (IDTask 2); (iii) computation of the effective material stiffness matrix (IDTask 3); (iv) initialization of the number of state variables (IDTask 4); (v) definition of stiffness matrix attributes (IDTask 5); and (vi) computation of the elastic stiffness matrix (IDTask 6). All tasks are executed at each integration point, but tasks 4, 5, and 1 are performed only once at the beginning of the analysis, whereas tasks 2, 3, and 6 are repeated at every calculation step.

The constitutive equations of the Ta-Ger B model (sections 3.2.2 and 4.2.1) were integrated at individual stress points using both a first-order single-step Forward Euler scheme (RK1 or FE) and a third-order Runge-Kutta-Fehlberg scheme (RKF23) (section 4.2.3.1). The latter is an adaptive explicit method featuring automatic error control and substepping (Sloan, 1987; Sloan et al., 2001). For the BVP simulations, the RKF23 scheme was adopted due to its superior numerical robustness and improved convergence behaviour.

6.2.2 Benchmarking the implementation via triaxial test simulations in PLAXIS 3D

As a first step to validate the Fortran implementation of the Ta-Ger B model, the same drained monotonic triaxial compression test was simulated using three distinct methods: the original MATLAB single integration point implementation used during preliminary development and single-element assessments (chapters 3, 4, and 5), the SoilTest facility in PLAXIS using the compiled DLL of the Ta-Ger B UDSM written in Fortran, and a 3D-FE cube model in PLAXIS 3D also employing the same DLL. While SoilTest offers a fast and accessible way to simulate laboratory experiments at a single integration point, the 3D-FE simulation provides a more representative assessment of the model's integrator performance in a multi-element context. The latter used 86 ten-node tetrahedral elements (Figure 6.1) and exploited three symmetry planes to model one-eighth of the full triaxial specimen. A similar approach was adopted by Simonin (2023) during the initial development stages of the 'HySand' model.

The simulated test corresponds to the experiment by Wichtmann (2005) on quartz sand No. 3 with an initial mean effective stress $p_{\text{in}} = 200$ kPa and an initial void ratio $e_{\text{in}} = 0.69$, using the parameters listed in Table 4.3 (section 4.3.1.4). Results are presented in Figure 6.2 and show that all simulations produce nearly identical stress-strain and volumetric responses.

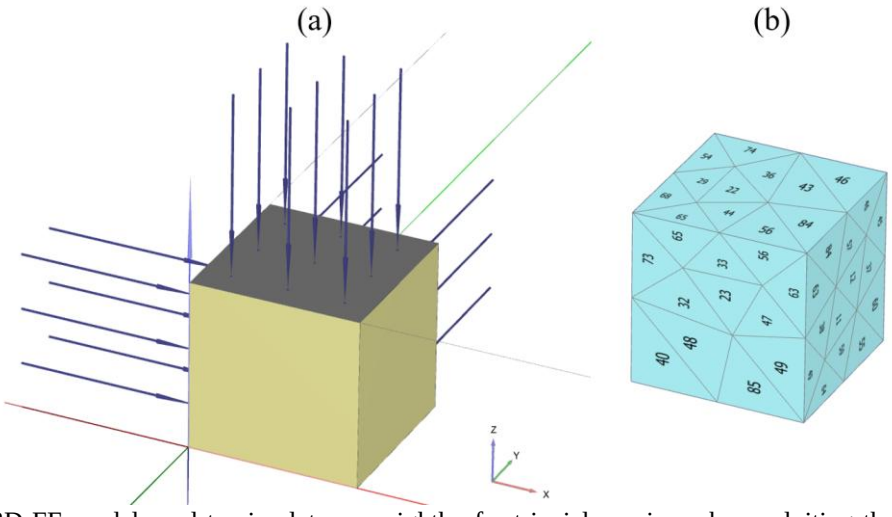

Figure 6.1: 3D-FE model used to simulate one-eighth of a triaxial specimen by exploiting three symmetry planes: (a) applied boundary and loading conditions; (b) mesh comprising 86 ten-node tetrahedral elements.

All simulations (3D-FE cube model, SoilTest PLAXIS facility, and MATLAB) employed the RKF23 scheme for stress integration of the Ta-Ger B constitutive equations. The same comparisons were also carried out using the RK1 scheme during earlier phases of the study. Additionally, similar verification checks were performed for other loading conditions, including cyclic loading, with particular attention to the correct detection of stress reversals (not shown for brevity). The consistent agreement observed across all checks provided a solid basis for proceeding with the subsequent refinements and application to BVPs.

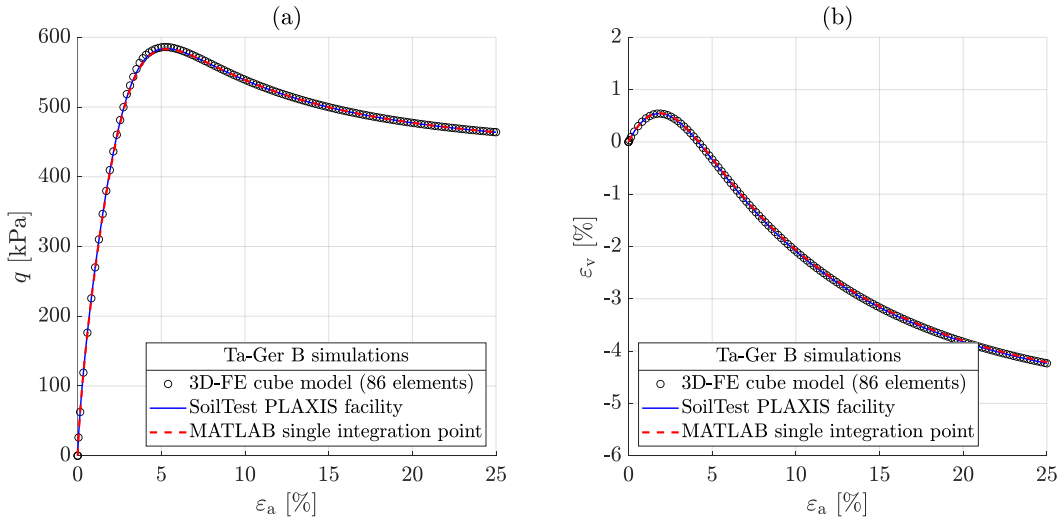

Figure 6.2: Ta-Ger B simulations of a drained triaxial test on quartz sand No. 3 (Wichtmann, 2005) with $p_{in} = 200$ kPa and $e_{in} = 0.69$: (a) $\varepsilon_a - q$; (b) $\varepsilon_a - \varepsilon_v$. Results from 3D-FE cube model (86 elements), PLAXIS SoilTest and MATLAB single integration point implementation are shown.

6.2.3 Implementation considerations for the robust application of Ta-Ger B to BVPs

The use of advanced constitutive models in finite element analysis (FEA) can be challenging due to numerical convergence issues and increased mesh dependency (Brinkgreve, 1994). While simulating simple laboratory tests under well-defined loading paths is typically straightforward, the application of such models to BVPs may require further adjustments to the constitutive equations to ensure numerical robustness and convergence. To address challenges primarily related to non-convergence and potential numerical instabilities, the following considerations were incorporated into the numerical implementation of Ta-Ger B for its subsequent application to 3D-FE monopile simulations:

- The evolution of void ratio was restricted within the bounds defined by the maximum and minimum values, $e_{\max}$ and $e_{\min}$, to prevent the development of unrealistic soil states (Taborda *et al.*, 2020; Pisanò *et al.*, 2024).
- An upper bound equal to ${M_s}^{\max}$ was imposed on the stress ratio that governs the opening angle of the bounding surface, defined by $M_s = M_{cs}e^{-n_b\psi}$ (Taborda *et al.*, 2020; Seequent, 2023; Pisanò *et al.*, 2024). As shown by Taborda et al. (2020), limiting M_s prevents excessive expansion of the bounding surface and potential overestimation of peak strength, particularly when simulating very dense sand states. Since peak strength depends on M_s and varies with Lode angle, this constraint also reduces the risk of overprediction along stress paths not covered during calibration under standard triaxial conditions (Seequent, 2023). Finally, by limiting peak strength, this constraint helps reduce excessive softening, which in turn supports numerical convergence and stability.
- An upper bound equal to $\zeta^{\max}$ was also applied on the hardening variable ζ, which governs the material's hardening-softening behaviour (section 4.2.1.2). Although strictly constraining ζ between 0 and 1, as originally stated by Tasiopoulou and Gerolymos (2016a), would suppress softening from the peak strength, simulations of BVPs indicated that bounding ζ remains necessary to ensure robustness of the implementation. As explained in section 4.2.3.3, values slightly above unity should be permitted to capture the gradual reduction of peak strength towards critical state. Nonetheless, enforcing an upper limit was essential to prevent the development of unrealistically large values of ζ, with bounds in the range of 1.05 to 1.10 proving effective in practice.

These considerations are applicable to any Ta-Ger variant to support stable implementation and its use in BVP simulations using FE software. With these aspects addressed and numerical stability achieved, the model was subsequently applied to simulate BVPs and validate its performance against real field data.

6.3 3D-FE modelling of PISA monopile field tests at Dunkirk

6.3.1 Overview of simulation programme

Section 6.3 presents a sequence of 3D-FE simulations (Table 6.1) undertaken to assess the Ta-Ger B model in monopile BVP applications. The focus is on selected PISA field tests at Dunkirk, specifically piles DM4 and DM2, subjected to monotonic and cyclic lateral loading, respectively, as documented by McAdam et al. (2020) and Byrne et al. (2020b). For the cyclic case (DM2), three configurations are examined. Configurations I and II adopt cyclic parameters fitted to the LS1 field response (set A), with the distinction that load sets are simulated either individually (I) or sequentially (II). Configuration III employs cyclic parameters calibrated from high-cycle drained tests on quartz sand No. 3 (Wichtmann, 2005) (set B), with load sets applied individually to both a wished-in-place monopile and one including installation effects. All Dunkirk simulations share the same ground model (section 6.3.2), with the remaining parameters kept consistent for Dunkirk sand. A complementary qualitative assessment is also undertaken through additional cyclic simulations, using the same 3D-FE model but with simplified ground conditions and parameters for a different sand, quartz sand No. 3, providing further insight into the model's predictive capabilities.

Table 6.1: Summary of the 3D-FE simulation programme and modelling assumptions.

Simulation	Objective	Loading	Sand	Cyclic parameters set (n_0, n_{peak}, β)	Installation	Load history	Cycles
DM4 (§6.3.5)	Dunkirk field test	Monotonic	Dunkirk	N/A	Wished-in-place	N/A	N/A
DM2-configuration I (§6.3.7.1)	Dunkirk field test	Cyclic	Dunkirk	Fit to load set LS1 (set A)	Wished-in-place	Individual sets	100 per set (×4)
DM2-configuration II (§6.3.7.2)	Dunkirk field test	Cyclic	Dunkirk	Fit to load set LS1 (set A)	Wished-in-place	Sequential sets	400 in total
DM2-configuration III (§6.3.7.3)	Dunkirk field test	Cyclic	Dunkirk	High-cycle tests (quartz sand No. 3, Wichtmann 2005) (set B)	Wished-in-place / with installation effects	Individual sets	100 per set (×4)
Simplified configuration (§6.3.8)	Qualitative assessment	Cyclic	Quartz No. 3	High-cycle tests (quartz sand No. 3, Wichtmann 2005) (set B)	Wished-in-place	Individual sets	100 per set (×3)

6.3.2 Ground conditions for Dunkirk simulations

Although the initial goal was to simulate pile DM4 and all three configurations (I, II and III) of pile DM2 (see Table 6.1) under identical Dunkirk soil conditions, as documented by Zdravković et al. (2020), targeted modifications to the ground model were required to ensure numerical stability. These adjustments were implemented carefully so as not to affect the overall soil response, thereby preserving consistency with previous studies, and enabling meaningful comparison with the results reported by Taborda et al. (2020) and Pisanò et al. (2024). Accordingly, the ground model adopted in the present study closely follows that used in both references and was employed for setting up the 3D-FE model and calibrating the Ta-Ger B constitutive parameters. Where available and appropriate, additional comparisons with Tasiopoulou et al. (2020) are also informative, as that study employed the Ta-Ger A variant to simulate similar ground and loading conditions.

The Dunkirk site consists of a dense layer of partially saturated fill overlying a sand deposit that extends from 3 to 30 m below the ground surface, with the groundwater table located at a depth of 5.4 m. In the studies by Taborda et al. (2020) and Pisanò et al. (2024), the fill was assumed to have the same mechanical properties as the underlying sand, albeit with different relative densities: $D_{r0} = 100\%$ (corresponding to an initial void ratio $e_{\text{in}} = 0.54$) for the fill layer and $D_{r0} = 75\%$ ($e_{\text{in}} = 0.628$) for the sand layer. In the present study, a simplified approach was adopted by prescribing a uniform relative density of 75% across both layers. This choice aimed to avoid very dense initial states ($D_{r0} = 100\%$), which were found to induce numerical instability in BVP simulations using the present Ta-Ger B UDSM implementation. A comparable simplification was employed by Tasiopoulou et al. (2020), who adopted relative densities of 90% for the fill and 70% for the sand, instead of the original 100% and 75%, respectively.

The soil unit weights were set to 17.1 kN/m^3 above and 19.9 kN/m^3 below the groundwater table, in line with the values reported by Taborda et al. (2020) and Pisanò et al. (2024). Initial horizontal stresses were computed using an earth pressure coefficient $K_0 = 0.6$, chosen to promote numerical convergence while also compensating for the reduced shear stiffness resulting from the lower density assigned to the fill layer. Preliminary simulations using the present Ta-Ger B UDSM implementation showed that adopting a lower K_0 value, such as 0.4, as used by Taborda et al. (2020) and Pisanò et al. (2024), in combination with the calibrated parameters, led to convergence issues during the later stages of the pushover analysis. It is noted that the study by Tasiopoulou et al. (2020) does not provide information regarding the K_0 value adopted in their simulations, limiting direct comparison.

To shed light on the potential implications of the assumed ground conditions, comparisons are drawn with the corresponding data reported in the aforementioned studies (Taborda *et al.*, 2020; Tasiopoulou *et al.*, 2020; Pisanò *et al.*, 2024). Specifically, Figure 6.3 presents a comparison of the initial depth profiles of pore water pressure (pwp) in subplot (a) and state parameter ψ in subplot (b), both extracted from PLAXIS 3D in the present study and digitised from the publications by Taborda et al. (2020) and Pisanò et al. (2024). Subplot (c) illustrates the initial small-strain shear modulus $G_{\max}$, comparing the present study with Taborda et al. (2020) and Pisanò et al. (2024), along with the digitised profile corresponding to the default calibration of the Ta-Ger A model variant as reported by Tasiopoulou et al. (2020). In addition, it incorporates data from two Seismic Cone Penetration Tests (SCPTs) conducted during the ground characterisation campaign for the PISA project (Zdravković *et al.*, 2020). Starting with the initial pore water pressure profile (Figure 6.3a), small deviations are observed in the unsaturated zone above the water table, likely due to differences in how suction effects were modelled in each study. Below the water table, the pore pressure profiles are essentially identical across all three studies. In the present study, and following the

recommendations of Seequent (2023), the following degrees of saturation (S_r) were prescribed for the three upper unsaturated soil layers: $S_r = 0.43$ between 0 m and 2 m depth, and $S_r = 0.40$ between 2 m and 3 m, and between 3 m and 4 m. Below the water table, from 5.4 m to 12 m depth, the pore water pressure was defined to follow a hydrostatic distribution assuming $\gamma_w = 10$ kN/m^3. For the transition layer between the saturated and unsaturated zones (i.e., between 4 m and 5.4 m depth), pore water pressures were interpolated between the values estimated for the overlying and underlying layers. Regarding the initial profile of the state parameter ψ (Figure 6.3b), the present study diverges from Taborda et al. (2020) and Pisanò et al. (2024) only in the top 3 m, corresponding to the hydraulic fill. This variation stems from the assumption of a uniform relative density across the entire soil column in the present study, whereas the earlier studies assigned a higher density to the fill layer (top 3 m). As far as the small-strain shear modulus $G_{\max}$ profile (Figure 6.3c) is concerned, the present study adopts a stiffness distribution more closely aligned with that reported by Tasiopoulou et al. (2020), with both profiles exhibiting lower stiffness compared to those predicted by Taborda et al. (2020) and Pisanò et al. (2024). The deviations, however, remain within a reasonable range and are not considered critical, as the focus of the present analysis is on the pile response under monotonic (pushover analysis) and long-term cyclic lateral loading, both well beyond the small-strain regime. It is worth noting that the profile by Tasiopoulou et al. (2020) starts from zero stiffness at the surface, unlike the others, due to that study's assumption of fully dry sand throughout the soil profile. As a result, the calibration does not account for the increase in stiffness induced by suction-related gains in mean effective stress within the unsaturated layers, as considered in the other studies shown.

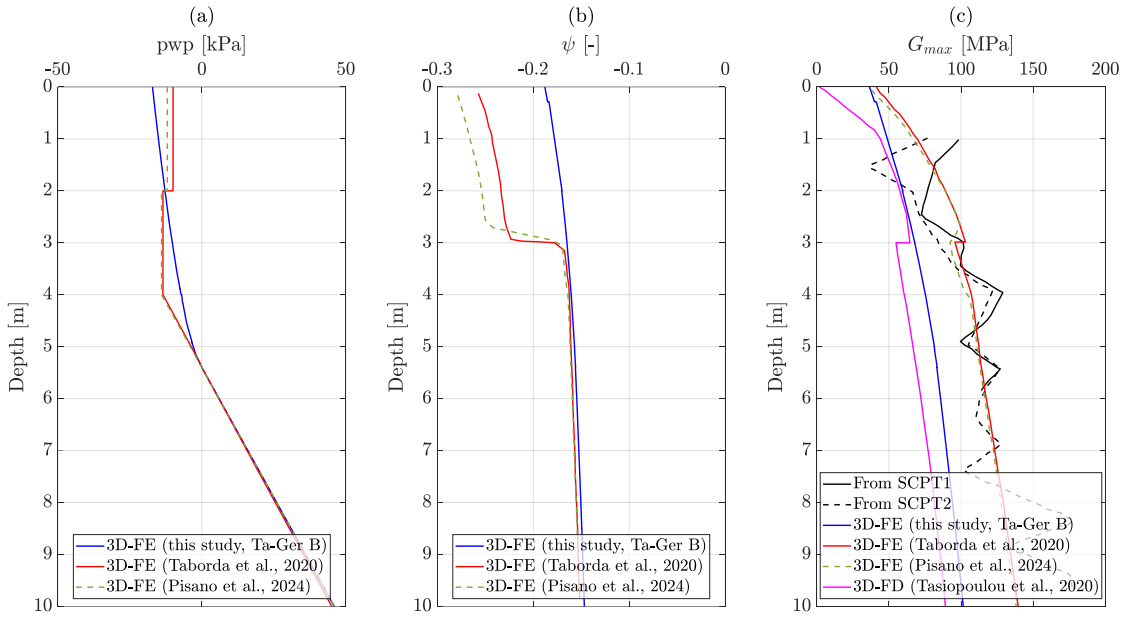

Figure 6.3: Initial ground conditions showing depth profiles of: (a) pore water pressure (pwp), (b) small-strain shear modulus $G_{\max}$; (c) state parameter ψ.

6.3.3 3D-FE model set-up for Dunkirk simulations

Since both the present study and Pisanò et al. (2024) employed PLAXIS 3D to model the same problem with similar objectives, the 3D-FE model adopted here closely follows the setup described in that study. In addition, specific details of the model configuration and simulation phases were based on the recommendations provided by Seequent (2023). This latter study also used the SANISAND-MS model (Liu *et al.*, 2019) to simulate the same tests, reporting results, FE model configuration, ground conditions, and material parameter choices that closely align with those of Pisanò et al. (2024), and thus served as a valuable complementary reference. Figure 6.4 shows the 3D-FE model implemented in the present work. To reduce computational effort, only half of the domain was simulated by exploiting the symmetry of the problem. The soil domain extended 50 m horizontally and 12 m vertically to prevent boundary effects on the monopile response. The mesh consisted of ten-node tetrahedral elements, while boundary conditions included a fixed base and constraints along the vertical sides to prevent displacement normal to the boundary.

The steel pile shown in Figure 6.4, representing DM4 for monotonic loading and DM2 for cyclic loading, was modelled as a zero-thickness cylindrical shell and discretised using plate

elements. A Young's modulus (E) of 211 GPa and a Poisson's ratio (v) of 0.3 were assigned, consistent with Pisanò et al. (2024). The modelled pile has an outer diameter (D) of 0.762 m, a wall thickness (t) of 14 mm, and an embedded length (L) of 4 m, corresponding to a L/D ratio of 5.24. The loading was applied with an eccentricity (h) of 10 m above the ground surface. The unit weight of the pile was set to $\gamma = 0$ kN/m^3, as its influence on lateral response was considered negligible (Seequent, 2023). The interaction between the soil and structural elements of the monopile was modelled using twelve-node zero-thickness interface elements, with strength governed by a Mohr-Coulomb failure criterion defined by the critical state (CS) friction angle of the adjacent soil ($\varphi_{cs} = 32°$) (Taborda *et al.*, 2020; Pisanò *et al.*, 2024). The elastic interface parameters were selected based on the stiffness properties of the surrounding soil, following the approach proposed by Tantivangphaisal et al. (2025), which aims to avoid numerical instabilities due to overly stiff interfaces while ensuring minimal influence on the simulation results. The shear stiffness, varying with the applied effective normal stress (σ_n), was defined as $k_s = 1.320 \times 10^6$ [kPa] $\left(\frac{\sigma_n}{100\ \text{kPa}}\right)$. The corresponding normal stiffness was calculated using $k_n = k_s \frac{2(1-v_{int})}{1-2v_{int}}$, with Poisson's ratio $v_{int} = 0.45$ (Bentley Systems, 2024b).

All FE simulations (Table 6.1), monotonic (DM4) and cyclic (DM2), were performed under drained conditions through combinations of the following phases (Seequent, 2023):

- Initial phase: Establishment of the initial effective geostatic stresses using an earth pressure coefficient of $K_0 = 0.6$ (calculation type: 'K_0-procedure').
- Phase 1: Activation of the structural elements and interfaces (calculation type: 'plastic').
- Phase 2a: Application of a prescribed static lateral displacement at the top of the monopile to achieve a target ground-level displacement $U_x = 0.1D$ (calculation type: 'plastic').

- Phase 2b: Application of a cyclic load history at the top of the monopile to simulate dynamic response (calculation type: 'dynamic').

For the simulation of the monotonic test on pile DM4, the sequence Initial phase → Phase 1 → Phase 2a was applied, whereas for the cyclic tests, Phase 2a was substituted with Phase 2b. To improve convergence at the low effective stresses typical of shallow depths, a uniform 5 kPa surcharge was applied at the ground surface during monotonic simulations and omitted during the cyclic. This is a common practice in similar studies (e.g., Saberi et al., 2025).

In these default simulations, the pile was modelled using the standard 'wished-in-place' assumption, as commonly adopted in the literature (e.g., Taborda et al., 2020). However, as discussed in detail in section 6.3.7.3 (configuration III), the effects of impact piling on the cyclic response of the monopile were also explored through a separate set of simulations. In this alternative setup, following the methodology of Pisanò et al. (2024), an additional 'Extra phase' was introduced between the 'Initial phase' and 'Phase 1'. During this phase, a planar volumetric expansion $\varepsilon_{\mathrm{v}}^{\mathrm{inst}} = 1\%$, characterised by zero vertical strain, was applied to the entire volume of the soil plug (extending up to the soil-pile interface), effectively mimicking the installation-induced disturbance within the plug region.

According to Byrne et al. (2020b), pile DM2 was subjected to a multi-amplitude cyclic loading history consisting of five one-way load sets (LS1 to LS4 and LS11), each applied at a frequency of 0.1 Hz. Table 6.2 summarizes key information for each load set: (i) the maximum applied lateral load ($H_{\max}$); (ii) the dimensionless factor ζ_b, defined by LeBlanc et al. (2010) as $\zeta_b = H_{\max}/H_{\mathrm{ref}}$, where H_{ref} is the load inducing a ground-level displacement of $0.1D$; and (iii) the number of loading cycles N. In terms of modelling, the cyclic load sets were simulated in line with Seequent (2023), adopting a load period of $T = 500$ s ($f = 0.002$ Hz) and a sampling interval of $\mathrm{d}t = 250$ s, as derived through their iterative tuning

to suppress dynamic (inertial) effects. According to Seequent (2023), a sufficiently low frequency should be used when modelling problems of this nature to ensure a quasi-static response and avoid significant localised accelerations. This requirement was verified in the present work by inspecting the acceleration field, which confirmed the absence of significant inertial effects. The dynamic load input for each load set was assigned through a table, oscillating between zero and the specified maximum value ($H_{\max} = H_{\mathrm{ref}} \times \zeta_b$) at each sampling point ($\mathrm{d}t = 250$ s). To simulate load set LS1, the following dynamic settings were used: a time interval of 50000 s (to simulate 100 cycles), a maximum of 5000 steps, and 2 substeps. Load sets LS2, LS3, and LS4 were simulated over five consecutive phases each, with each phase having a time interval of 10000 s (20 cycles per phase), 2000 maximum steps, and 2 substeps. Load set LS11 was not simulated, as its ζ_b value is beyond what is typically experienced by real monopiles (Pisanò *et al.*, 2024) and the runs did not converge.

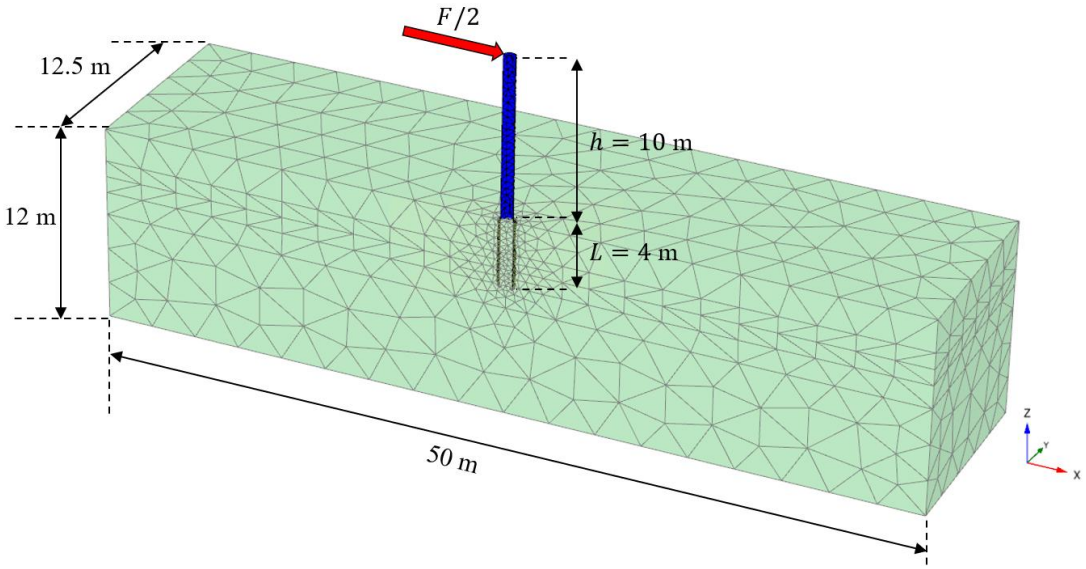

Figure 6.4: 3D-FE model configuration used to simulate the response of piles DM4 and DM2.

Table 6.2: Load sets applied to pile DM2 (Byrne et al., 2020b).

Load set (LS) No.	$H_{\max}$ **[kN]**	ζ_b **[-]**	**Cycles N [-]**
1	10	0.046	5100
2	20	0.093	3300
3	40	0.19	8100
4	80	0.37	11110
11	160	0.74	31

6.3.4 Calibration of Ta-Ger B parameters for Dunkirk sand

The parameters assigned to the Ta-Ger B model for simulating the PISA Dunkirk field tests are summarised in Table 6.3. Figure 6.5 compares the stress-strain and volumetric responses obtained using Ta-Ger B (utilizing the parameters in Table 6.3) against those reported by Taborda et al. (2020), who employed the bounding surface model by Taborda et al. (2014), as well as the original drained monotonic triaxial test data on Dunkirk sand (Zdravković *et al.*, 2020). The model by Taborda et al. (2014) shares similarities with the SANISAND family (i.e., Dafalias and Manzari, 2004), incorporating critical state soil mechanics (CSSM) (Roscoe *et al.*, 1958) and the state parameter concept (Been and Jefferies, 1985). Although Taborda et al. (2020) initially calibrated their model directly against laboratory data, this led to a marked underprediction of the lateral resistance in the field tests. As a result, further parameter tuning was required to ensure agreement with the field-scale monopile response.

In a similar vein, Pisanò et al. (2024) calibrated SANISAND-MS for the same PISA field tests with reference to the 'tuned' parameters reported by Taborda et al. (2020), owing to the similarities between the two constitutive models. Given the further formulation similarities between Ta-Ger B and SANISAND-MS, particularly in components such as elasticity (G_0, v, m), the CSL (e_0, λ, ξ, M_{cs}), the bounding surface (n_b), and the phase transformation surface (n_d), the corresponding parameters were initially taken from Pisanò et al. (2024). Adjustments to G_0 and n_d were then made to resolve convergence issues encountered with the original values. For the monotonic simulations, the Ta-Ger-specific hardening exponent n was assigned a constant value, calibrated by fitting the stress-strain response reported by Taborda et al. (2020) (Figure 6.5a), while the dilatancy parameter α was calibrated against the corresponding volumetric responses (Figure 6.5b).

The preceding discussion focused on the monotonic parameters required to reproduce the lateral response observed in the monotonic test on pile DM4. For cyclic loading conditions,

as demonstrated in chapters 4 and 5 and in line with the original recommendations by Tasiopoulou and Gerolymos (2016a), the hardening exponent n should not be treated as a constant. Instead, under cyclic loading, n is defined as a function of cumulative incremental deviatoric strain, $\Sigma \mathrm{d}\varepsilon_q$ (see section 4.2.1.6):

$$n = n_{\mathrm{f}} + \left[n_{\mathrm{peak}} + \left(n_0 - n_{\mathrm{peak}}\right)e^{-\beta \Sigma \mathrm{d}\varepsilon_q} - n_{\mathrm{f}}\right]e^{-\gamma\left(1-\mathrm{sign}\left(\Sigma|\mathrm{d}\varepsilon_p|\right)\right)\Sigma \mathrm{d}\varepsilon_q} \tag{6.1}$$

Ideally, the calibration of the parameters governing equation (6.1), which controls key aspects of the cyclic response, such as ratcheting, would be based on a dedicated set of high-cycle laboratory test data. However, the calibration approach adopted in this study was guided by three main factors: (i) the lack of high-cycle test data for Dunkirk sand at the time this study was conducted, although relevant data have since become available by Tantivangphaisal et al. (2025); (ii) the availability of a successful calibration methodology previously developed for SANISAND-MS by Pisanò et al. (2024); and (iii) the fact that Pisanò et al.'s methodology relied on prior calibration of the model's cyclic parameters using high-cycle drained tests on quartz sand No. 3 by Wichtmann (2005), which had been carried out during an earlier stage of this study, as detailed in chapter 4.

Specifically, Pisanò et al. (2024), in their simulation of the cyclic field tests on pile DM2, initially adopted the same SANISAND-MS cyclic parameters as those calibrated by Liu et al. (2019) for quartz sand No. 3. These parameters were subsequently refined using the response of pile DM2 to load set LS1. Pisanò et al. (2024) demonstrated that the cyclic parameters for the two sands are very similar, which can be attributed to their comparable index properties and common quartzitic nature. In particular, quartz sand No. 3 has a mean diameter $D_{50} = 0.55$ mm, uniformity coefficient $C_{\mathrm{u}} = 1.8$, and maximum and minimum void ratios $e_{\max} = 0.874$, $e_{\min} = 0.577$, while Dunkirk sand has $D_{50} = 0.28$ mm, $C_{\mathrm{u}} = 1.72$, $e_{\max} = 0.91$, and $e_{\min} = 0.54$. This similarity was further verified by Pisanò et al.

(2024) prior to their simulations, through prediction of very similar parameters for the High-Cycle Accumulation (HCA) model by Niemunis et al. (2005), using micromechanically based empirical correlations proposed by Wichtmann (2016).

Table 6.3: Ta-Ger B model parameters for Dunkirk sand.

Critical state				**Elasticity**			**Bounding surface**	**Dilatancy**		**Hardening exponent**	**Imposed limits (BVPs)**	
e_0 [-]	λ [-]	ξ [-]	M_{cs} [-]	G_0 [-]	ν [-]	m [-]	n_b [-]	a [-]	n_d [-]	n^* [-]	M_s^{max} [-]	ζ^{max} [-]
0.91	0.135	0.179	1.28	300	0.17	0.5	1.9	0.2	0.85	0.15	1.5-1.7	1.1

*Equation (6.1) simplifies to $n = [n_{peak} + (n_0 - n_{peak})e^{-\beta \Sigma d\varepsilon_q}]$ for drained cyclic loading. Two cyclic parameter sets considered: set A ($n_0 = 1.8$, $n_{peak} = 8.25$, $\beta = 10$) and set B ($n_0 = 0.5$, $n_{peak} = 6.5$, $\beta = 8$).

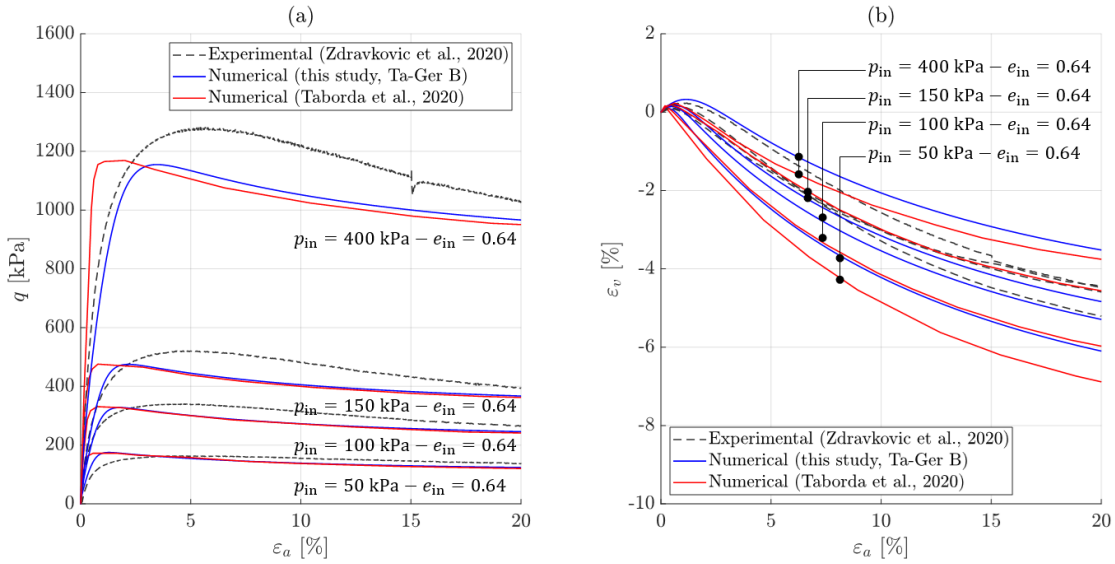

Figure 6.5: Calibration of Ta-Ger B parameters against simulations by Taborda et al. (2020) for drained triaxial tests on Dunkirk sand with constant initial void ratio ($e_{in} = 0.64$) and varying initial mean effective stress (p_{in}): (a) stress-strain response; (b) volumetric response.

In the present study, as outlined in the simulation programme of Table 6.1, two alternative cyclic parameter sets were adopted for the three configurations of the cyclic field tests on pile DM2 and are summarised in Table 6.3. Set A was derived by fitting the predicted response of LS1 to the corresponding field data and was used in configurations I (section 6.3.7.1) and II (section 6.3.7.2). The rationale for this strategy, its limitations, and the implications of refining parameters to match specific field responses, and ultimately why such calibration should be avoided, are discussed in those sections. Set B, following the rationale of Pisanò et al. (2024) as outlined previously, corresponds to the parameters

originally established in section 4.3.1.4 (Table 4.3), calibrated to reproduce strain accumulation observed in high-cycle drained tests on quartz sand No. 3 by Wichtmann (2005). These values, identical to those of quartz sand No. 3, were adopted in configuration III (section 6.3.7.3). It is noted that under drained conditions, equation (6.1) simplifies to $n = [n_{peak} + (n_0 - n_{peak})e^{-\beta \Sigma d\varepsilon_q}]$, so calibration primarily targets the parameters n_0, n_{peak}, and β, which are the only ones differing between the two sets. In this case, n_{f} and γ do not influence the response (see section 4.3.3) and are assigned default values.

Lastly, Table 6.3 includes two parameters defined as imposed limits: ${M_{\mathrm{s}}}^{\max}$ and $\zeta^{\max}$, with their rationale explained in section 6.2.3. A range is provided for ${M_{\mathrm{s}}}^{\max}$, as it was adjusted during simulations to enhance numerical stability. While ${M_{\mathrm{s}}}^{\max} = 1.5$ was used for monotonic loading, values for cyclic cases are reported in the respective results sections.

6.3.5 Monotonic monopile behaviour (DM4)

6.3.5.1 Comparison to field data and other studies

Figure 6.6 compares the measured monotonic response of pile DM4 with 3D-FE simulation results from several studies, including Taborda et al. (2020), Tasiopoulou et al. (2020), and the present study, all adopting the commonly used wished-in-place assumption. Also shown for reference is the simulation by Pisanò et al. (2024), which incorporates an imposed volumetric strain to account for installation effects, resulting in an upward shift due to soil stiffening. The wished-in-place simulation by Pisanò et al. (2024) is omitted, as it produces results in very close agreement with those of Taborda et al. (2020). The comparison is presented in terms of applied lateral load (H) against ground-level pile displacement (U_{x}), with the ultimate lateral capacity conventionally defined at $U_{\mathrm{x}} = 0.1D$.

The results indicate that the present implementation of the Ta-Ger B model captures the monotonic behaviour of pile DM4 well. Compared to Taborda et al. (2020), the calculated

response shows similar trends, with only minor deviations at higher load levels. Both simulations align closely with the field data in terms of ultimate capacity despite a slight underestimation along initial parts of the curve. Differences between predictions are attributed to variations in mesh discretisation, necessary adjustments to the ground model (see section 6.3.2) and the input parameters (section 6.3.4) for enhanced convergence, and fundamental differences in plastic modulus definitions between the bounding surface and Ta-Ger frameworks. The 5 kPa surface surcharge applied in this study, which slightly increases pile capacity, also contributes.

Lastly, comparisons between the Ta-Ger A model by Tasiopoulou et al. (2020) and the Ta-Ger B model used in this study should be treated with caution, as the former does not report its parameter set. Differences are driven by the distinct formulations of the bounding surface and phase transformation surface stress ratios (M_{s} and M_{pt} respectively), which are central to the models' behaviour. Notably, irregularities in the published response of Tasiopoulou et al. (2020), such as fluctuations around $U_{\mathrm{x}} = 0.025$ m, appear to be genuine features of the analysis rather than digitisation artefacts, possibly reflecting stress reversals or numerical instabilities. Without these fluctuations, the response would likely have underpredicted the field data, as the stiffening effect they introduced brought the prediction closer to the measured behaviour.

Figure 6.7 shows the deformed mesh after monotonic loading of pile DM4 at a ground-level displacement of $U_{\mathrm{x}} = 0.08$ m, scaled by a factor of 3.0. The opening of a gap immediately behind the pile is clearly visible. In the analysis, the prescribed initial suction in the unsaturated soil layers above the groundwater table is the mechanism that allows gapping to occur. This outcome is consistent with the findings of Taborda et al. (2020), who also observed similar behaviour and emphasised that this mechanism is irrelevant for offshore conditions, where the seabed is typically fully saturated and such suctions are absent.

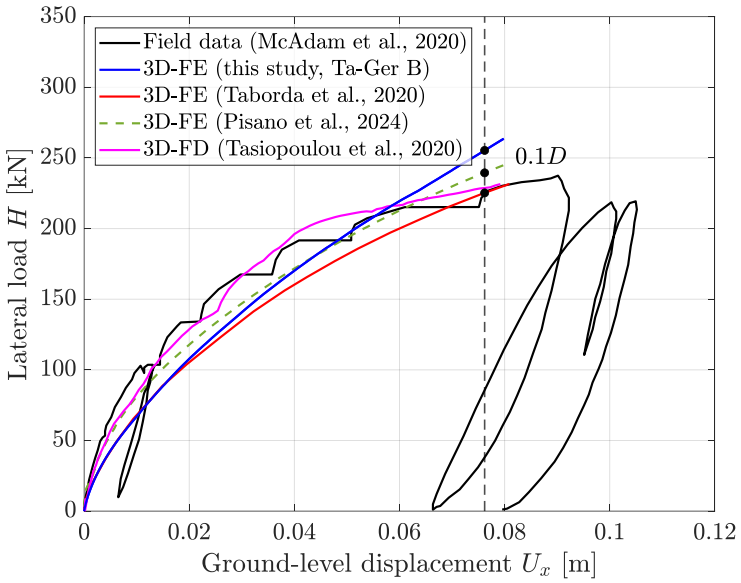

Figure 6.6: Comparison of monotonic lateral responses of pile DM4: (i) PISA field measurements; (ii) 3D-FE from this study (wished-in-place); (iii) 3D-FE from Taborda et al. (2020) (wished-in-place); (iv) 3D-FE from Pisanò et al. (2024) (with imposed installation strain); (v) 3D-FD from Tasiopoulou et al. (2020) (wished-in-place).

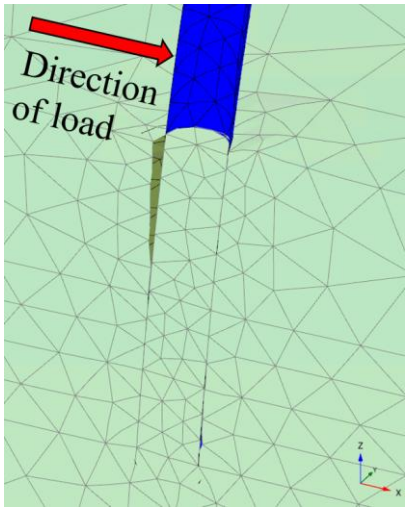

Figure 6.7: Deformed mesh after monotonic loading of pile DM4 at a ground-level displacement of U_x = 0.08 m, scaled by a factor of 3.0.

Figure 6.8 displays contour plots of (a) mean effective stress p, (b) void ratio e, and (c) Lode's angle variable χ, corresponding to the same deformed state, with lateral loading applied from left to right (as in Figure 6.7). In Figure 6.8a, higher positive p values are observed in front of the pile near the top and behind the toe, indicating zones of compression, as shown by lighter contours. In contrast, lower or negative p values appear behind the upper part of the pile and in front of the toe, where unloading causes localised stress relief. These reductions correspond to increased void ratios in Figure 6.8b, reflecting loosening of the sand. This is consistent with the dilative behaviour observed in the single-element calibration tests (Figure 6.5b), where the sand exhibited dilation across all levels of initial mean effective stress. Figure 6.8c shows the Lode angle variable χ (see section 4.2.1.4), defined as the ratio $M_{s,\theta}/M_{s,c}$. Here $M_{s,\theta}$ is obtained via polynomial interpolation of the strength stress ratios under triaxial compression ($\theta = 0$), extension ($\theta = 60°$), and simple shear ($\theta = 30°$), based on the current value of the Lode angle θ. As such, χ expresses the mobilised stress ratio relative to the compressive strength, $M_{s,c}$, and serves as an indicator of the

prevailing stress path. Values of $\chi = 1.0$ are seen in front of the pile, consistent with triaxial compression, while values of $\chi = 0.7$ are observed behind the pile where gapping occurs, indicating triaxial extension. These patterns highlight the complex stress paths and loading conditions mobilised during lateral pile loading.

Overall, the monotonic response of pile DM4 simulated using Ta-Ger B is well benchmarked against results from other numerical studies (Taborda *et al.*, 2020; Tasiopoulou *et al.*, 2020; Pisanò *et al.*, 2024) and the PISA field data (McAdam *et al.*, 2020). This agreement validates the adopted ground conditions, parameter calibration, 3D-FE model configuration, and necessary simplifications. Most importantly, the present Ta-Ger B implementation captures key features of sand behaviour under monotonic loading, providing confidence in its use for evaluating cyclic response and associated mechanisms in the next sections.

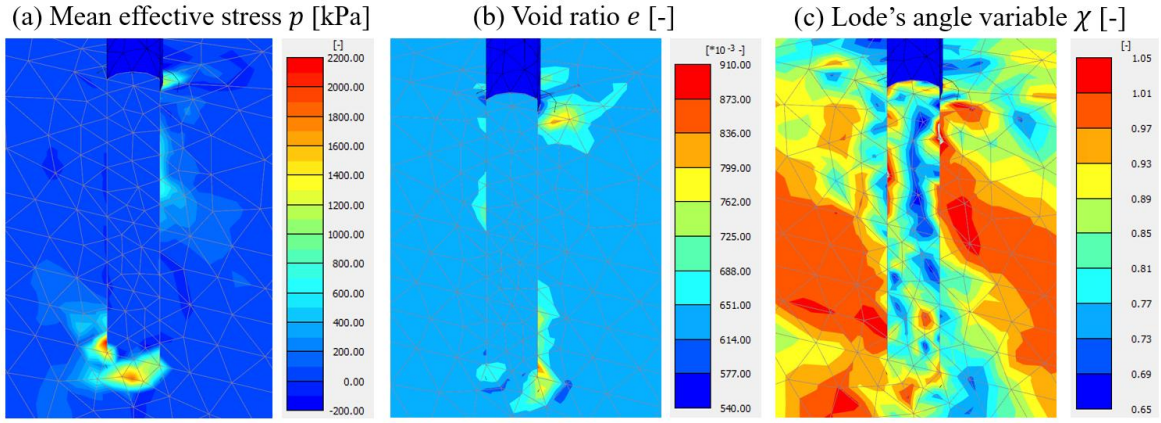

Figure 6.8: Contours of: (a) mean effective stress p; (b) void ratio e; (c) Lode's angle variable χ, where $\chi \cong 1.0$ for triaxial compression, $\chi \cong 0.7$ for triaxial extension, and $\chi \cong 0.80$ for simple shear. Shown for pile DM4 at a ground-level displacement of $U_x = 0.08$ m.

6.3.5.2 Mesh sensitivity

To assess the influence of mesh discretisation on the FE results under monotonic loading, a sensitivity analysis was conducted following an approach similar to Liu et al. (2022a). Given the need for multiple cyclic analyses, minimising computational time without compromising accuracy was essential. Three meshes were used, as shown in Figure 6.9(a-c), comprising 3709, 5367 (adopted mesh, see Figure 6.6), and 12892 elements, respectively. The resulting

load-displacement curves for pile DM4 are compared in Figure 6.10. Results indicate that mesh refinement slightly reduces the predicted ultimate capacity, although the difference between the baseline and finest mesh is minimal. As a convergence trend was observed, the 5367-element mesh was selected as a suitable compromise between accuracy and efficiency and was used for all simulations, including those in Figure 6.6 to Figure 6.8. For reference, a simulation of 100 cycles (section 6.3.7) using this mesh required approximately 7 to 10 hours of runtime on a workstation equipped with a 13th Gen Intel(R) Core(TM) i9-13900K processor (3.00 GHz), 128 GB of RAM, and running Windows 11 (64-bit).

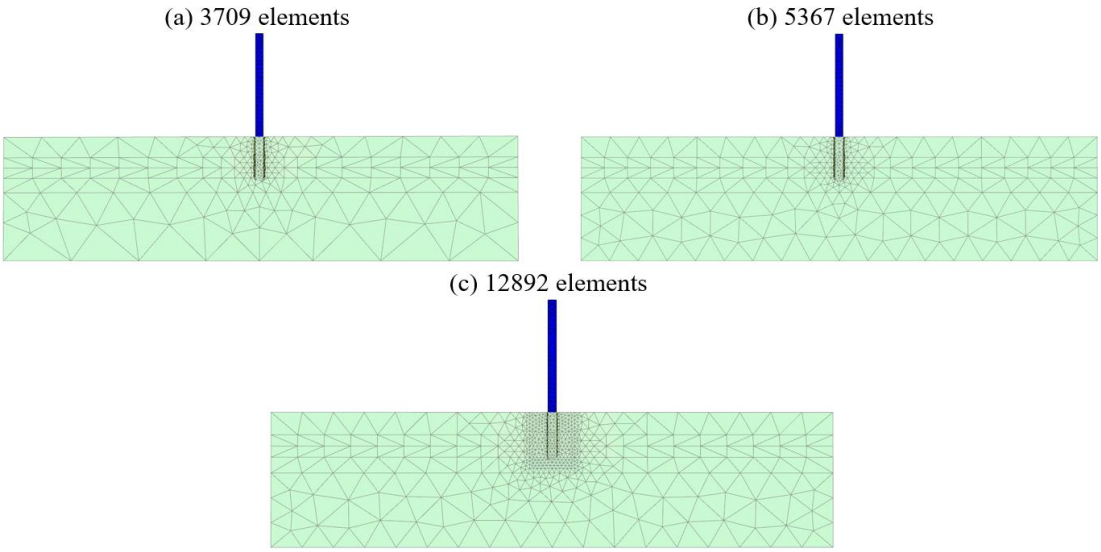

Figure 6.9: 3D-FE models adopted for the mesh sensitivity study: (a) 3709 elements; (b) 5367 elements (mesh used in all main simulations); (c) 12892 elements.

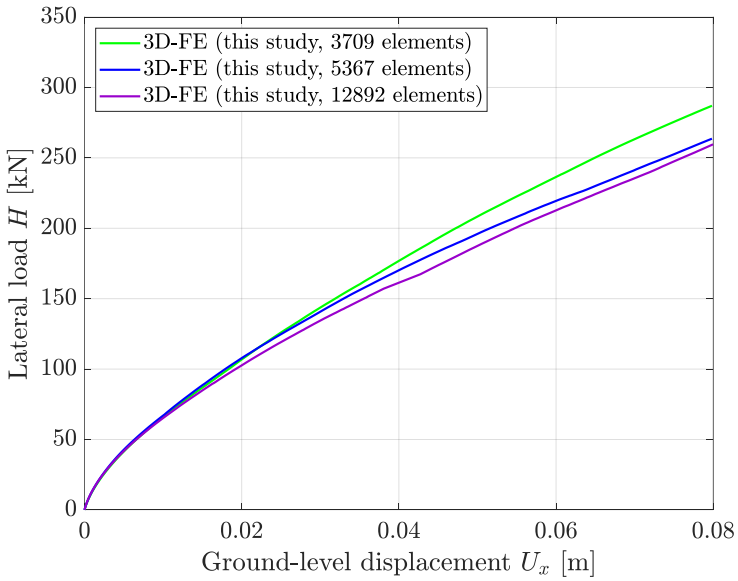

Figure 6.10: Re-simulation of pile DM4 under monotonic lateral loading to evaluate mesh sensitivity effects.

6.3.6 Essential terminology for assessing cyclic monopile response

Before presenting the cyclic monopile responses simulated by Ta-Ger B, this section summarises key terminology, some previously introduced and others new, to provide a consistent reference for interpreting the results. A logical starting point is the description of the applied cyclic loading, which is expressed in terms of the horizontal force H, with the corresponding moment calculated as $M = Hh$, where h is the load eccentricity. To characterise the amplitude and asymmetry of the loading, two dimensionless factors are introduced following LeBlanc et al. (2010), and illustrated in Figure 6.11:

$$\zeta_b = \frac{H_{\max}}{H_{\mathrm{ref}}} = \frac{M_{\max}}{M_{\mathrm{ref}}} \; ; \; \zeta_c = \frac{H_{\min}}{H_{\mathrm{ref}}} = \frac{M_{\min}}{M_{\mathrm{ref}}} \tag{6.2}$$

Here, $H_{\max}$ and $H_{\min}$ (or $M_{\max}$ and $M_{\min}$) denote the maximum and minimum applied lateral loads (or mudline moments), and H_{ref} (or M_{ref}) corresponds to the load inducing a ground-level displacement of $0.1D$. Following Liu et al. (2022a), the term 'pile head' is hereafter used for brevity to refer to measurements taken at the soil surface.

LeBlanc et al. (2010) introduced a convenient approach to assess the evolution of normalised accumulated pile rotation (tilt), using the dimensionless ratio $\Delta\theta/\theta_s$, where $\Delta\theta = \theta_N - \theta_0$ represents the difference between the rotation after N cycles (θ_N) and that at the end of the pre-cycling monotonic phase (θ_0) (Figure 6.12a). The normalising factor θ_s is the rotation in a static test under a load equal to the maximum cyclic load (Figure 6.12b). To capture the evolution of rotation, LeBlanc et al. (2010) proposed the empirical relationship:

$$\frac{\Delta\theta}{\theta_s} = T_b(\zeta_b) \cdot T_c(\zeta_c) \cdot \mathrm{N}^{\alpha} \tag{6.3}$$

where $T_b(\zeta_b)$ and $T_c(\zeta_c)$ are dimensionless functions capturing the influence of load amplitude and asymmetry, respectively, and α is a parameter, taken as 0.31 in LeBlanc et al. (2010). As shown by Liu et al. (2022a), this expression is valuable for evaluating constitutive model performance, even in the absence of field data. In the present work, PISA cyclic field

data from Beuckelaers (2017) are used to evaluate accumulated rotation, also referred to as accumulated relative rotation. For consistency in terminology and assumptions, this study adopts the definition from Beuckelaers (2017), refined by Seequent (2023), expressed as:

$$\bar{\psi}_{\mathrm{acc}} = \frac{\psi^{i}_{\max} - \psi^{1}_{max}}{2°} \tag{6.4}$$

This is equivalent to the definition by LeBlanc et al. (2010), albeit with different notation (ψ instead of θ). Without a pre-cycling monotonic phase, the numerator is the rotation difference between cycle i and the first cycle. The 2° denotes the failure rotation adopted in the PISA project. Calculation of $\psi^{i}_{\max}$ from PLAXIS 3D output is given in Seequent (2023).

Another key metric is the accumulated pile head relative displacement per cycle, denoted U_{R}. For a given load set (LS) j, it is defined as the difference between the maximum horizontal displacement at cycle i, $U^{i}_{j,max}$, and a reference value. The reference is typically the maximum displacement recorded during either the pre-cycling monotonic phase (i.e., 0th cycle, $U^{0}_{j,max}$) or, if absent, as in this study, during the first cycle ($U^{1}_{j,max}$). This gives:

$$U_{\mathrm{R}} = U^{i}_{j,max} - U^{1}_{j,max} \tag{6.5}$$

This is analogous to the accumulated rotation shown in Figure 6.12a. However, it evaluates displacement U rather than rotation θ.

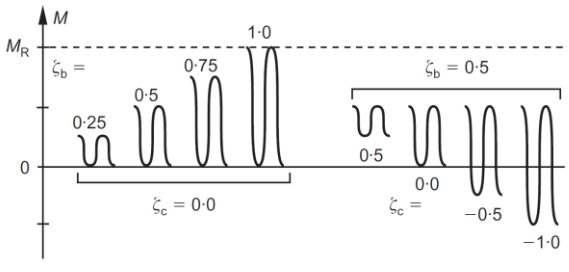

Figure 6.11: Illustration of the key parameters defining uniform-amplitude cyclic loading (LeBlanc et al., 2010).

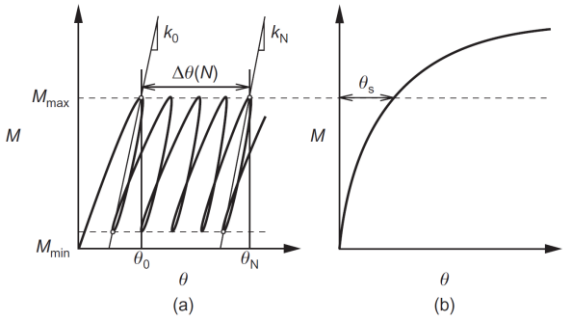

Figure 6.12: Evaluation of stiffness and accumulated rotation from (a) cyclic and (b) monotonic tests (LeBlanc et al., 2010).

6.3.7 Cyclic monopile behaviour (DM2)

As with pile DM4, the cyclic simulations for pile DM2 adopt the Dunkirk ground model of section 6.3.2, keeping Dunkirk sand monotonic parameters fixed and varying only the cyclic parameter set and load history. The simulations are presented in three parts, corresponding to the DM2 configurations in Table 6.1: (i) configuration I: each load set (LS1-LS4) is simulated individually, with cyclic parameter set A (Table 6.3) calibrated by fitting the predicted response of LS1 to the field data for accumulated pile head displacement U_R reported by Byrne et al. (2020b). The implications of this approach are discussed, highlighting its limitations and why it should be considered a last resort; (ii) configuration II: the same cyclic parameter set A is used, but the four load sets are applied sequentially to evaluate whether the Ta-Ger B model performance remains consistent under sequential loading; and (iii) configuration III: cyclic parameter set B (Table 6.3), derived from high-cycle tests on quartz sand No. 3 (Wichtmann, 2005), is used together with Dunkirk sand monotonic parameters, following an approach broadly consistent with Pisanò et al. (2024). Each load set is simulated individually for both a wished-in-place monopile and one including installation effects, with results showing set B to be the most appropriate.

6.3.7.1 Configuration I: parameter fitting to field data

As an initial strategy, the model was calibrated solely to the field response of LS1, which corresponds to the lowest cyclic amplitude (ζ_b). The aim was to assess whether parameters fitted to LS1 could also reproduce the responses of LS2-LS4. Each load set was simulated independently, without influence from the others, and limited to 100 cycles to reduce computational cost. A trial-and-error calibration was performed against the field response of LS1, leading to cyclic parameter set A: $n_0 = 1.8$, $n_{peak} = 8.25$, and $\beta = 10$, with the bounding surface stress ratio capped at ${M_s}^{max} = 1.7$. The procedure began with adjustments to the initial value of the hardening exponent n_0 until the simulated response matched the

measured displacement during the first loading cycle. Once a satisfactory fit was achieved, additional iterations were conducted to refine β, which controls the rate of displacement accumulation (ratcheting), and n_{peak}, which defines the peak value of the hardening exponent. This process proved particularly time-consuming, as each simulation exceeded seven hours, and the full calibration spanned several days, rendering the approach impractical. The value of ${M_{\mathrm{s}}}^{\max}$ was selected based on convergence considerations.

Figure 6.13a compares simulated and field responses of LS1 to LS4 in terms of accumulated pile head displacement U_{R}, while Figure 6.13b shows the corresponding accumulated relative rotation $\bar{\psi}_{acc}$, both plotted against the number of cycles. The plots indicate reasonable agreement but also highlight the limitations of calibrating solely to field response. A reasonable match is obtained for LS1 and LS2, as expected, since the parameters were calibrated to LS1 and LS2 features a similar amplitude, about twice that of LS1 (see Table 6.2). In contrast, LS3 and LS4, with cyclic amplitudes approximately four and eight times higher than LS1, respectively, deviate from the field data. LS3 overpredicts displacement and rotation, while LS4 initially underpredicts the response up to about 30 cycles and overpredicts beyond that. Additionally, both cases show an overprediction in the rate of accumulation of displacement (Figure 6.13a) and rotation (Figure 6.13b). Nevertheless, the lower amplitude of LS3 leads to a predicted reduction in the rate of accumulation beyond 30 cycles, which closely matches the slope observed in the field response.

This preliminary fitting approach bears resemblance to the methodology adopted by Tasiopoulou et al. (2020), who simulated LS4 only but extended the analysis to 230 cycles. Specifically, they first modelled the monotonic lateral response of pile DM4 using a varying hardening exponent n (equation (6.1)), diverging from their earlier recommendation (Tasiopoulou and Gerolymos, 2016a) to adopt a constant value. As a result of the monotonic pushover simulation, n increased due to the corresponding increase in the cumulative

incremental deviatoric strain $\Sigma d\varepsilon_q$, a key state variable in all Ta-Ger model variants. However, this increase in n was insufficient to serve as an initial hardening exponent n_0 for the subsequent cyclic simulation. As a result, they manually increased n by inputting a higher n_0 value to match the LS4 response, effectively overriding the influence of the monotonic behaviour previously simulated. This adjustment was interpreted as a means of accounting for the unmodelled effects of earlier load sets. However, this rationale contrasts with the philosophy underpinning the loading sequence adopted by Byrne et al. (2020b), in which each successive load set, doubling in amplitude, was intended to reset the system's memory. The sequence was deliberately devised so that the response to each load set would reflect the pile behaviour under the new loading conditions, with minimal influence from preceding, lower-amplitude cycles. While one could argue that prior loading history may still affect the response, as suggested by Pisanò et al. (2024), who only modelled the load sets sequentially but not individually, this raises a broader question: how should such effects be realistically accounted for? Simulating only 100 cycles per load set remains a simplification, especially considering that each phase involved more than at least 3300 cycles (see Table 6.2).

All in all, it can be argued that, despite the good agreement achieved with the field data (Figure 6.13), calibrating model parameters directly to field response should be considered a last resort. This approach presents several key limitations: (i) it is extremely time-consuming and laborious; (ii) the resulting parameters are highly sensitive to the specific characteristics of the loading conditions they were calibrated to, in contrast to parameters derived from a database of laboratory tests designed to capture material behaviour across a range of stress levels, densities, and cyclic amplitudes, thus providing more robust and generalizable parameter sets; and (iii) it lacks practical relevance for design, as calibration based on field tests is rarely feasible in real projects, where standard laboratory data typically informs the design process.

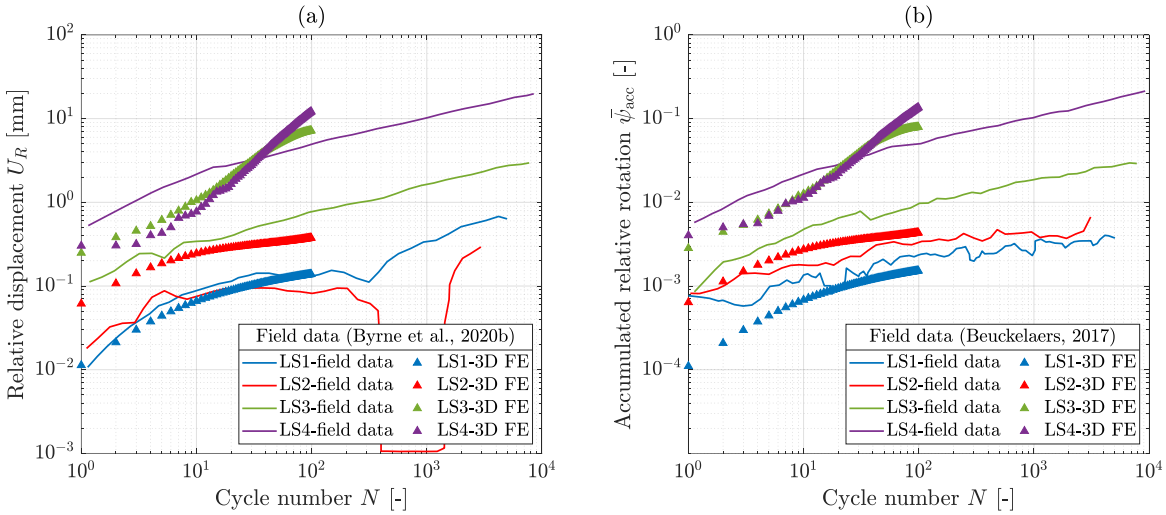

Figure 6.13: 3D-FE simulations using Ta-Ger B for PISA cyclic load sets (LS1 to LS4) on pile DM2 at Dunkirk, simulated individually, with hardening exponent n calibrated to LS1 (configuration I, cyclic parameter set A): (a) relative displacement U_R at ground surface; (b) accumulated relative rotation $\bar{\psi}_{acc}$ at ground surface.

6.3.7.2 Configuration II: load history effects on monopile cyclic response

Building on cyclic parameter set A introduced in section 6.3.7.1, which produced reasonable agreement with field data, the next step was to examine whether applying the load sets sequentially within a single simulation influences the predicted response. Figure 6.14a shows the time history of ground-level displacement U_x, under sequential loading, while Figure 6.14b presents the lateral response of pile DM2 in terms of U_x versus the applied lateral load H. These plots demonstrate that the Ta-Ger B model predicts a progressive accumulation of lateral displacement as the cyclic amplitude increases across successive load sets. To evaluate the influence of load sequencing, Figure 6.15 serves as the counterpart to Figure 6.13 in section 6.3.7.1, contrasting this configuration (II), where load sets are applied sequentially (400 cycles in a single simulation), with configuration I, where they are applied individually (four simulations of 100 cycles each), for accumulated relative displacement U_R (Figure 6.15a) and rotation $\bar{\psi}_{acc}$ (Figure 6.15b).

While the predicted response of Ta-Ger B for LS1 is, as expected, identical to that obtained when simulated individually, the response for LS2 differs significantly from its individual counterpart. This discrepancy arises from the stiffening induced during the preceding

loading phase (LS1), reflected in an increase in the cumulative incremental shear strain $\Sigma d\varepsilon_q$ and hence the hardening exponent n, both of which remain locked-in as state variables within the formulation. In contrast, the responses for LS3 and LS4 are similar to those obtained in the individual simulations and show closer agreement with the field data, both in terms of accumulated displacements and rotations, as well as the rate of accumulation (ratcheting).

While the PISA field tests by Byrne *et al.* (2020b) adopted the assumption that progressively larger load sets erase prior loading history, the physical basis for this remains unproven. Field results suggest that soil response is only weakly influenced by preceding lower-amplitude cycles, lending support to the idealisation. The Ta-Ger B model, however, produces responses strongly influenced by prior loading, improving agreement in some cases (LS3 and LS4) but leading to inaccuracies in others (LS2). In its current form, the Ta-Ger B model treats cumulative incremental shear strain $\Sigma d\varepsilon_q$ as a monotonically increasing state variable, which drives an increase in the hardening exponent n under drained loading and leads to progressive stiffening. A potential refinement would be to introduce additional quantities influencing the hardening exponent n, with the effect of $\Sigma d\varepsilon_q$ modulated by the amplitude of the applied load. This possibility merits further investigation in future developments of the model.

It should be noted that, beyond the limitations discussed, the trial-and-error fitting procedure in section 6.3.7.1 could, in principle, be further refined to identify a parameter set providing closer agreement than cyclic parameter set A with both configuration I (section 6.3.7.1) and configuration II (section 6.3.7.2). However, this process would be highly time-consuming and falls outside the scope of the present study. Configurations I and II are therefore included primarily to contribute to the broader discussion on the calibration of advanced constitutive models such as Ta-Ger, and to illustrate both the strengths and inherent limitations of the formulation.

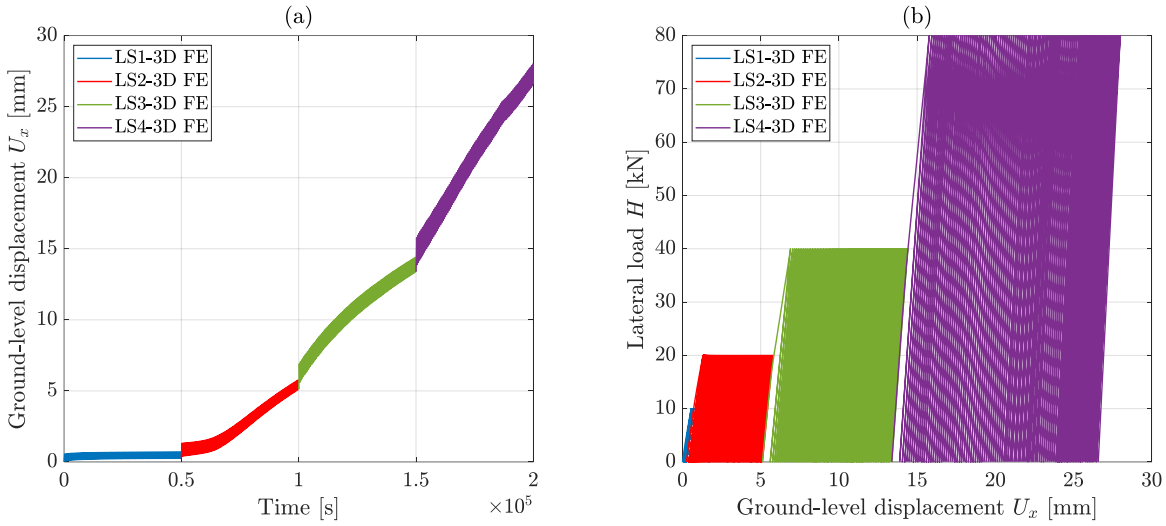

Figure 6.14: 3D-FE simulations using Ta-Ger B for PISA cyclic load sets (LS1 to LS4) on pile DM2 at Dunkirk, applied sequentially, with hardening exponent n calibrated to LS1 (configuration II, cyclic parameter set A): (a) ground-level displacement U_x versus time; (b) cyclic lateral response of pile DM2.

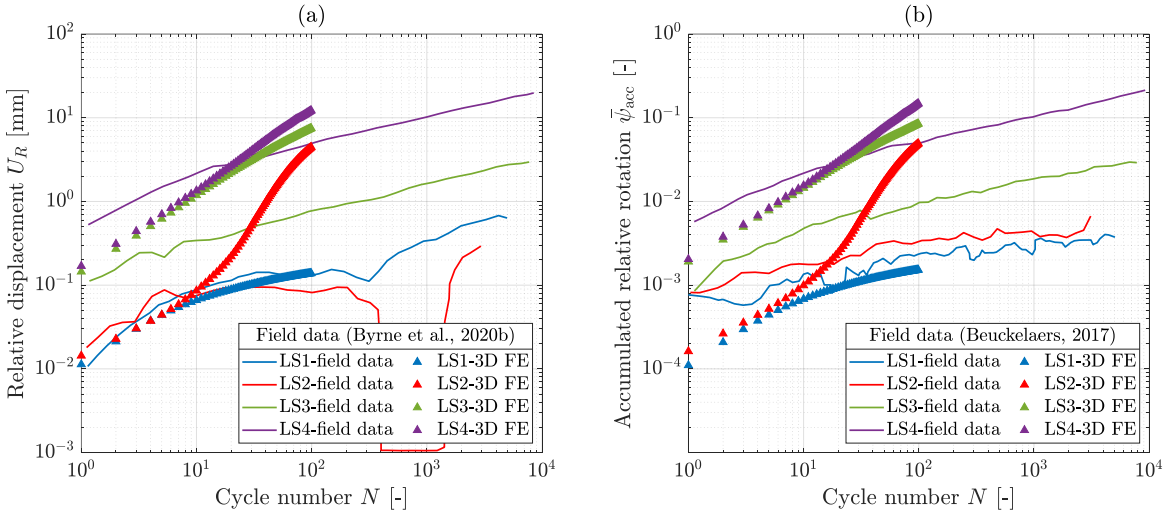

Figure 6.15: 3D-FE simulations using Ta-Ger B for PISA cyclic load sets (LS1 to LS4) on pile DM2 at Dunkirk, applied sequentially, with hardening exponent n calibrated to LS1 (configuration II, cyclic parameter set A): (a) relative displacement U_R at ground surface; (b) accumulated relative rotation $\bar{\psi}_{acc}$ at ground surface.

6.3.7.3 Configuration III: Pisanò et al. (2024) calibration and installation effects

The conclusions from configurations I and II, together with the calibration strategy of Pisanò et al. (2024), motivated the adoption of cyclic parameter set B for configuration III (Table 6.3). While this approach departs slightly from that of Pisanò et al. (2024), it remains broadly consistent with the same underlying principles. As explained in section 6.3.4, these principles are grounded in the absence of dedicated high-cycle test data for Dunkirk sand and the availability of relevant experimental data by Wichtmann (2005) on a sand with similar index properties and quartzitic nature, namely, quartz sand No. 3. Accordingly, set

B ($n_0 = 0.5$, $n_{\mathrm{peak}} = 6.5$, and $\beta = 8$) was adopted in configuration III, with the bounding surface stress ratio limited to ${M_{\mathrm{s}}}^{\max} = 1.6$ for numerical stability. As outlined in Table 6.1, configuration III comprises two sets of individual 100-cycle simulations: one assuming a wished-in-place monopile and the other incorporating installation effects.

Figure 6.16a presents results for accumulated relative displacement U_{R} from load sets LS1, LS2, and LS3 for the wished-in-place case. LS4 was omitted, as the preceding sets were sufficient to support the conclusions. As shown, cyclic parameter set B enabled Ta-Ger B to reproduce a more consistent and accurate rate of displacement accumulation relative to the field data, compared to parameter set A used in configuration I (section 6.3.7.1), where calibration based solely on LS1 compromised predictions at higher amplitudes. However, the simulated U_{R} magnitudes remain slightly overestimated.

A substantially improved agreement with field displacements U_{R} (Figure 6.16b) was achieved by adopting the same installation-effect approach proposed by Pisanò et al. (2024). Using cyclic parameter set B, an additional simulation phase was introduced after initial stress generation, during which a planar volumetric expansion $\varepsilon_{\mathrm{v}}^{\mathrm{inst}} = 1\%$ was imposed on the soil volume representing the internal plug of the tubular monopile. Following the method originally proposed by Broere and van Tol (2006) for displacement piles in sand, this phase does not aim to reproduce the physical deformation of the plug itself, but instead serves as a numerical device to mimic the installation-induced stress state around the pile. The imposed expansion increases the mean effective stress p in the vicinity of the pile, which in turn elevates the small-strain shear modulus $G_{\max}$, thereby reproducing the densification and stiffness enhancement typically associated with impact-driven penetration. Based on this, Pisanò et al. (2024) concluded that $\varepsilon_{\mathrm{v}}^{\mathrm{inst}}$ serves as a calibrated, site-specific installation parameter. The key differences between the strategy adopted in this study and that of Pisanò et al. (2024) lie in the additional parameter fitting applied by Pisanò *et al.* to better capture

the response of LS1, and their use of sequential rather than individual load set simulations. The rationale for not adopting these elements is discussed in sections 6.3.7.1 and 6.3.7.2.

As shown in Figure 6.16b, the installation-induced soil stiffening caused an almost parallel shift of the simulated U_R curves, while preserving the same accumulation trend. This adjustment brought the Ta-Ger B predictions into much closer agreement with the field data, resulting in a very good overall response. Notably, it also introduced a clear distinction between the simulated responses of load sets LS3 and LS4, successfully capturing their significant difference in amplitude, an outcome not achieved with set A (configuration I: section 6.3.7.1). While some deviations from the field data remain, the level of agreement is reasonable, especially considering that no additional parameter fitting was performed.

The good performance of Ta-Ger B is further supported in Figure 6.17, which compares predicted and measured values of the accumulated relative rotation $\bar{\psi}_{acc}$. Subplot (a) shows results for the wished-in-place monopile, while subplot (b) presents simulations with installation effects introduced by imposing an initial volumetric strain $\varepsilon_v^{inst} = 1\%$ to the internal soil plug. Both subplots include field data and power-law fits of the simulated responses based on the empirical relation in equation (6.3), originally proposed by LeBlanc et al. (2010). Although this relation provides a simplified estimate of monopile tilt, it complements the field data effectively serving as a useful benchmark for model evaluation. The fitted trends were obtained through visual fitting, following the approach of Liu et al. (2022a) with SANISAND-MS, here applied to a different monopile scenario. In both cases, the fitted lines approximate the average simulated response, and a value of $\alpha = 0.50$, was adopted in place of the original $\alpha = 0.31$ suggested by LeBlanc et al. (2010), as it provided a better match. Similar conclusions to Figure 6.16 can be drawn when comparing the two cases. Overall trends remain consistent, with minor fluctuations in LS3 accounting for installation case (Figure 6.17b), likely due to numerical artefacts. While the wished-in-place

simulations tend to overpredict rotation, including installation effects lowers the response, improving agreement with the field data across all load sets. Both the wished-in-place and installation-accounted simulations show close agreement with the empirical relationship of LeBlanc et al. (2010) for LS1 and LS2 throughout all 100 cycles. For LS3, the simulations follow the empirical slope during the first 10 cycles before diverging with a steeper trend. LS4, which was only simulated with installation effects, exhibits behaviour similar to LS3.

Overall, this section demonstrates that calibrating the cyclic parameters using relevant experimental data, even from a different but similar sand, leads to a more robust model response that is less sensitive to variations in loading characteristics such as cyclic amplitude. This is evident when comparing results from configuration I (set A) with configuration III (set B). Consistent with Pisanò et al. (2024), the findings further confirm that pile installation effects do not influence the tilt accumulation rate but contribute to more realistic predictions of permanent displacements and rotations under cyclic loading in a coherent, physically informed manner, unlike arbitrary parameter fitting. However, this outcome is based on a single case and may not generalise to other pile configurations.

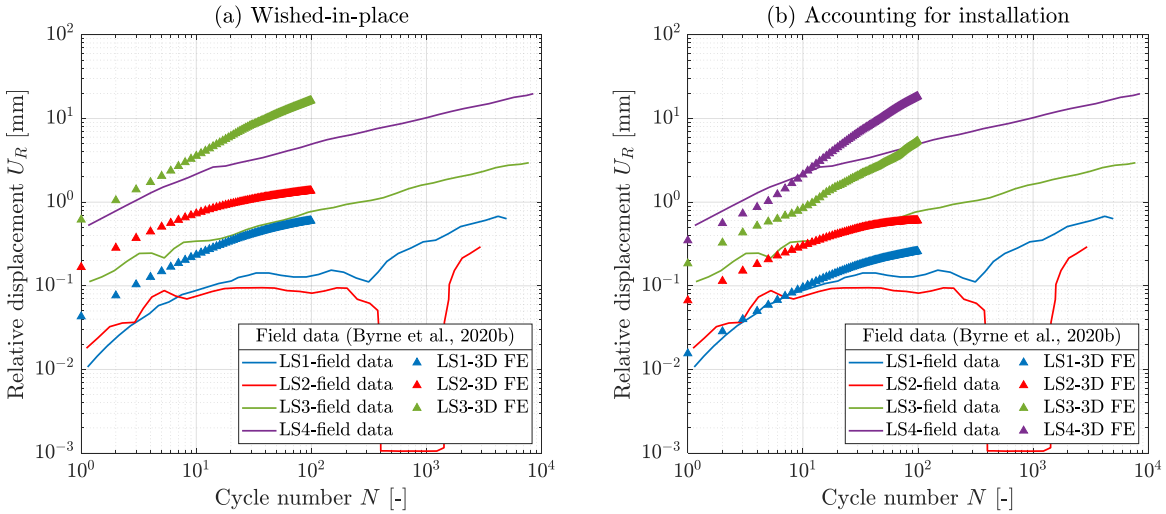

Figure 6.16: 3D-FE simulations using Ta-Ger B for PISA cyclic load sets on pile DM2 at Dunkirk, simulated individually. The hardening exponent n was calibrated from high-cycle drained tests on quartz sand No. 3 by Wichtmann (2005) (configuration III, cyclic parameter set B). Results show relative displacement U_R at ground surface. Simulations include: (a) wished-in-place monopile (LS1 to LS3); (b) installation effects modelled via $\varepsilon_v^{inst} = 1\%$, following Pisanò et al. (2024) (LS1 to LS4).

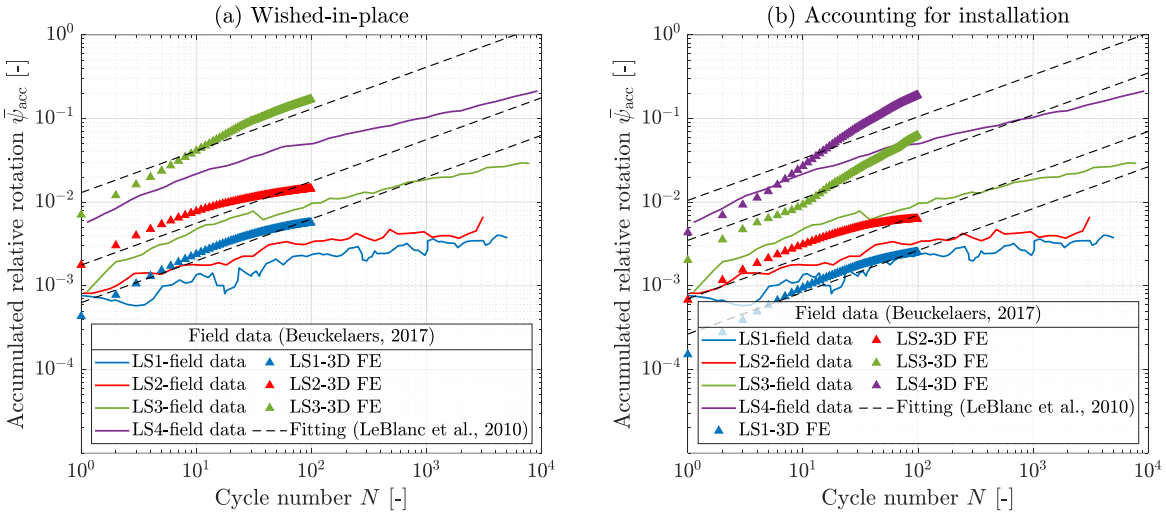

Figure 6.17: 3D-FE simulations using Ta-Ger B for PISA cyclic load sets (LS1 to LS4) on pile DM2 at Dunkirk, simulated individually. The hardening exponent n was calibrated from high-cycle drained tests on quartz sand No. 3 by Wichtmann (2005) (configuration III, cyclic parameter set B). Results show accumulated relative rotation $\bar{\psi}_{acc}$ at ground surface, fitted against the empirical relationship proposed by LeBlanc et al. (2010). Simulations include: (a) wished-in-place monopile (LS1 to LS3); (b) installation effects modelled via $\varepsilon_{\mathrm{v}}^{\mathrm{inst}} = 1\%$, following Pisanò et al. (2024) (LS1 to LS4).

6.3.8 Simplified configuration: qualitative assessment of Ta-Ger B

6.3.8.1 Scope and rationale

As the final step in the simulation programme (Table 6.1), an exploratory study was conducted using a simplified 3D-FE configuration to assess the cyclic performance of the Ta-Ger B model under less complex ground conditions and to gain further insight into its predictive behaviour. The simulations used the same BVP geometry as for the Dunkirk DM4 and DM2 monopiles, but with ground conditions and material parameters representative of quartz sand No. 3. Unlike DM2 configuration III, which combined Dunkirk monotonic parameters with cyclic parameters for quartz sand No. 3 (set B), the simplified study applied both monotonic and cyclic parameters (set B) consistently for quartz sand No. 3.

The simplified configuration provides several advantages: (i) it avoids the complexities of the Dunkirk site, such as suction and very high relative densities in the hydraulic fill layer (section 6.3.2); (ii) it improves numerical stability and reduces the need for parameter adjustments to overcome convergence issues, thereby allowing greater flexibility in conducting simulations; and (iii) it establishes a direct link between the laboratory-scale

evaluation in chapter 4, which was based on high-cycle drained element tests on quartz sand No. 3 (Wichtmann, 2005), and the 3D-FE monopile behaviour, including the response at key soil elements around the pile.

The qualitative assessment focuses on accumulated relative rotation, compared with the empirical power-law relationship of LeBlanc et al. (2010), as well as a separate comparison of the simulated $\zeta_b - T_b$ trends with experimental 1g model results from the same study. In addition, stress and strain paths at selected stress points within key soil elements near the monopile were examined to support interpretation of the model's local response.

6.3.8.2 Ground conditions, 3D-FE model setup, and Ta-Ger B parameters

As this complementary investigation involves only minor adjustments relative to the 3D-FE model previously employed for simulating the monotonic (DM4: section 6.3.5) and cyclic (DM2: section 6.3.7) Dunkirk field tests, this section highlights only the specific modifications. Full details of the ground conditions and 3D-FE model setup, which remain unchanged in this study, are given in sections 6.3.2 and 6.3.3 and are not repeated here.

Regarding ground conditions, the initial horizontal stresses were computed using $K_0 = 1.0$ instead of the previously adopted $K_0 = 0.6$, a choice made to aid numerical convergence. The water table remained at 5.4 m depth, with hydrostatic pore pressure below assumed using $\gamma_w = 10$ kN/m^3. The top three unsaturated layers (0-2 m, 2-3 m, 3-4 m) and the transition layer (4-5.4 m) were modelled as fully dry, in contrast to earlier simulations where suction and interpolation were applied, respectively. A uniform density was assumed across the entire soil profile, corresponding to an initial relative density $D_{r0} = 62\%$ (i.e., $e_{\text{in}} = 0.69$), which falls within the range used for calibrating the parameters of quartz sand No. 3.

The parameters for quartz sand No. 3 used in the simulations are listed in Table 6.4. These were calibrated against drained monotonic triaxial tests for the monotonic parameters and

high-cycle drained tests for the cyclic ones, based on the experimental data of Wichtmann (2005). Minor adjustments were applied to the hardening exponent n (held constant for monotonic loading) and the dilatancy parameter α, primarily to enhance numerical stability throughout the simulations. As in previous simulations, the two additional parameters ${M_s}^{\max}$ and $\zeta^{\max}$ were retained as upper bounds to support numerical stability in BVP analyses. For monotonic loading, ${M_s}^{\max}$ was set to 1.5, consistent with the Dunkirk sand simulations, while a slightly higher value of 1.6 was used for all cyclic cases. Preliminary simulations (not shown) indicated that lower values favour convergence in monotonic analyses, whereas this constraint was found to be less critical during cyclic loading, particularly at low amplitudes. The elastic interface shear stiffness was defined from the surrounding soil properties, following the approach of Tantivangphaisal et al. (2025), with $k_s = 6.816 \times 10^5$ [kPa] $\left(\frac{\sigma_n}{100\ \text{kPa}}\right)$. All other interface settings remained as in the Dunkirk sand simulations.

Figure 6.18 shows the monotonic lateral response of a pile with DM4 geometry, simulated in 3D-FE using Ta-Ger B and the parameters of Table 6.4, under wished-in-place installation and uniform quartz sand No. 3. This analysis was used to determine H_{ref}, defined as the load causing a displacement of $0.1D$, required for evaluating the dimensionless factor $\zeta_b = H_{\max}/H_{\text{ref}}$ (LeBlanc et al., 2010). Figure 6.19 presents the coordinates of four selected stress points located in key soil elements near the monopile, used to extract local stress and strain paths as well as important state variables of the model. These points correspond to the back and front of the pile at shallow depth (A and B, respectively), and near the pile toe (C and D), with the front defined in the direction of loading. This selection facilitates a more detailed evaluation of Ta-Ger B's response at the elemental level within a BVP context, complementing insights gained from single-element laboratory simulations.

Table 6.4: Ta-Ger B model parameters for quartz sand No. 3, taken from Table 4.3 (section 4.3.1.4).

Critical state				Elasticity			Bounding surface	Dilatancy		Hardening exponent	Imposed limits (BVPs)	
e_0 [-]	λ [-]	ξ [-]	M_{cs} [-]	G_0 [-]	ν [-]	m [-]	n_b [-]	a [-]	n_d [-]	n^* [-]	M_s^{max} [-]	ζ^{max} [-]
0.845	0.049	0.27	1.27	130	0.15	0.5	2.0	1.0	1.17	0.5	1.5-1.6	1.1

*Equation (6.1) simplifies to $n = [n_{peak} + (n_0 - n_{peak})e^{-\beta\Sigma d\varepsilon_q}]$ for drained cyclic loading. Only one cyclic parameter set considered (set B, see Table 6.1): $n_0 = 1.8$, $n_{\text{peak}} = 8.25$, $\beta = 10$.

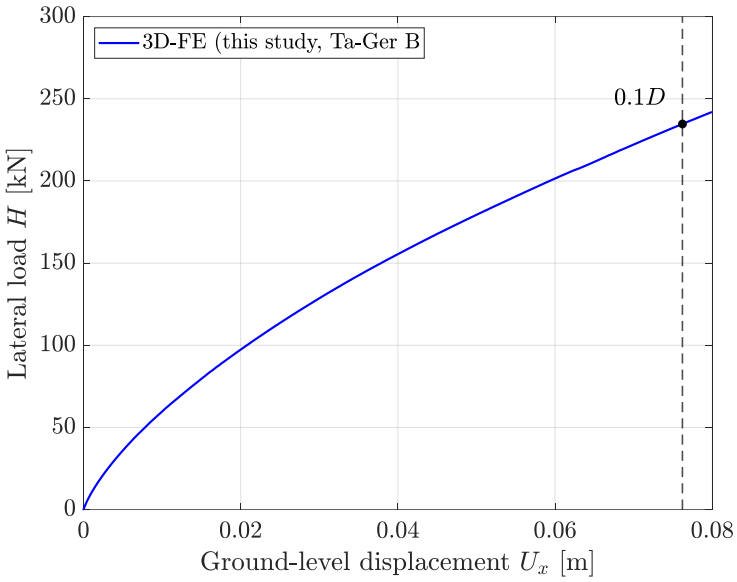

Figure 6.18: Monotonic lateral response of pile DM4 simulated in 3D-FE with Ta-Ger B, assuming wished-in-place installation and a uniform-density profile of quartz sand No. 3.

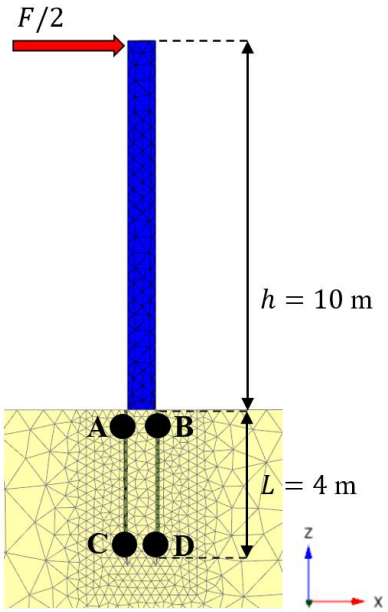

Figure 6.19: Zoomed-in view of the 3D-FE model with coordinates (x, y, z) of key stress points: A (-0.405 m, 0.028 m, -0.432 m), B (0.405 m, 0.030 m, -0.430 m), C (-0.403 m, 0.024 m, -3.807 m), and D (0.405 m, 0.024 m, -3.804 m).

6.3.8.3 Assessment against LeBlanc et al. (2010) empirical power law

Figure 6.20 presents results from 3D-FE simulations using the Ta-Ger B model within the simplified configuration (see Table 6.1) for cyclic load factors ζ_b corresponding to load sets LS1 through LS3 on pile DM2 (Table 6.2). The simulations assumed wished-in-place installation and a uniform-density profile of quartz sand No. 3. Each load set was simulated independently and limited to 100 cycles, similarly to configuration I (section 6.3.7.1) and configuration III (section 6.3.7.3). Figure 6.20a shows the accumulated relative displacement U_R at ground surface, while Figure 6.20b depicts the evolution of accumulated relative rotation $\bar{\psi}_{acc}$, plotted alongside the empirical power-law trend proposed by LeBlanc

et al. (2010), given in equation (6.3). Although Figure 6.20a is included primarily for reference, as no experimental data are available for comparison, it highlights a clear upward shift in the displacement curves with increasing load amplitude. The displacement magnitude approximately doubles when the applied amplitude is doubled, whereas the accumulation rate remains nearly unchanged across the cases. Figure 6.20b is more informative, as it includes both the simulated tilt responses and the empirical LeBlanc model trend. As in the study by Liu et al. (2022a) and section 6.3.7.3, a value of $\alpha = 0.50$ was adopted based on visual fitting. While the model responses do not follow a strictly linear trend in log-log space, they broadly align with the empirical model. Moreover, the simulated responses show a gradual reduction in the rate of tilt accumulation toward 100 cycles, particularly at higher load amplitudes. This contrasts with results from configuration III (section 6.3.7.3), where a steeper slope was observed under Dunkirk conditions. This comparison highlights the role of differing ground conditions in shaping the model response, despite the use of identical cyclic parameters (set B) governing ratcheting.

For the second stage of this assessment, namely the evaluation of the simulated $\zeta_b - T_b$ trends, the required T_b values can be obtained through visual interpretation of Figure 6.20b. These values correspond to the ζ_b factors applied in each simulation and represent their role in the empirical power-law relationship of LeBlanc et al. (2010), expressed in equation (6.3). It is noted that for one-way cyclic loading, as applied in all simulations conducted in this study, the load asymmetry ratio is $\zeta_c = 0$, for which the corresponding dimensionless function is defined as $T_c(\zeta_c = 0) = 1$. To broaden the assessment and serve as a basis for a potential future database, the three simplified-configuration simulations with quartz sand No. 3 were complemented by the corresponding wished-in-place Dunkirk simulations from configuration III (section 6.3.7.3). The latter were selected over those including installation

effects to maintain consistency and enable clearer comparisons. All simulations, along with relevant details and the corresponding estimated T_b values, are summarized in Table 6.5.

Figure 6.21 presents the resulting numerical $\zeta_b - T_b$ trends from these simulations, shown alongside digitized experimental data from 1g model tests by LeBlanc et al. (2010), which were also conducted under one-way cyclic loading ($\zeta_c = 0$). Although a direct comparison is not possible due to differences in the BVP geometry, most notably the higher load eccentricity in the present study ($h = 2.5L$) compared to the experiments ($h = 1.2L$), the experimental trends are included for reference to support interpretation of the numerical results. The PISA BVP geometry with $h = 2.5L$ was retained, rather than adopting the geometry of LeBlanc et al. (2010), to ensure consistency with the simulations of pile DM2 in section 6.3.7. The initial relative densities associated with the experimental tests are reported at both the model scale ($D_{r0}^{m} = 4\%$ and 38%) and prototype scale ($D_{r0}^{p} = 8\%$ and 75%). The model-scale values correspond to the densities prepared in the laboratory, but these do not reflect the frictional behaviour expected at field scale because of the low stress levels in the experiments. To account for this scaling effect, LeBlanc et al. (2010) reported equivalent prototype values, providing a more realistic basis for comparison with full-scale monopile simulations. LeBlanc et al. (2010) observed that the value of T_b increases approximately linearly with ζ_b, with the slope of this relationship being influenced by the sand's relative density. Their data indicate that denser sands exhibit steeper $\zeta_b - T_b$ trends (Figure 6.21). While the ground conditions and sand types differ slightly between the two simulation sets in this study, the use of the same 3D-FE model and BVP geometry allows for meaningful comparison. The two sets, one with quartz sand No. 3 (simplified configuration) and the other with Dunkirk sand (configuration III), each suggest an approximately linear tendency over the limited ζ_b range considered here. Data at higher ζ_b would be required to confirm whether this trend persists; such simulations were not

performed here due to convergence difficulties at high amplitudes and time constraints. Consistent with the experimental findings of LeBlanc et al. (2010) and the numerical observations of Liu et al. (2022a), the simulations involving higher relative density (Dunkirk sand) plot above those for quartz sand No. 3, exhibiting a steeper slope in the $\zeta_b - T_b$ plot.

To conclude, Ta-Ger B captures key aspects of cyclic pile behaviour, with simulated trends broadly aligning with empirical expectations within the range examined. These findings support the model's potential to represent ratcheting under varied soil and loading conditions and motivate further investigation within a more extensive simulation programme.

Table 6.5: Numerical simulations and corresponding T_b, T_c values derived from 3D-FE results using equation (6.3), assuming $\alpha = 0.50$. Configurations are defined in Table 6.1.

Load set	**Sand**	**Configuration**	D_{r0} [%]	ζ_b [-]	ζ_c [-]	T_b [-]	T_c [-]
LS1	Quartz No. 3	Simplified (wished-in-place)	62	0.046	0	0.0007	1
LS2	Quartz No. 3	Simplified (wished-in-place)	62	0.093	0	0.0027	1
LS3	Quartz No. 3	Simplified (wished-in-place)	62	0.19	0	0.0085	1
LS1	Dunkirk	III (wished-in-place)	75	0.046	0	0.00063	1
LS2	Dunkirk	III (wished-in-place)	75	0.093	0	0.00177	1
LS3	Dunkirk	III (wished-in-place)	75	0.19	0	0.013	1

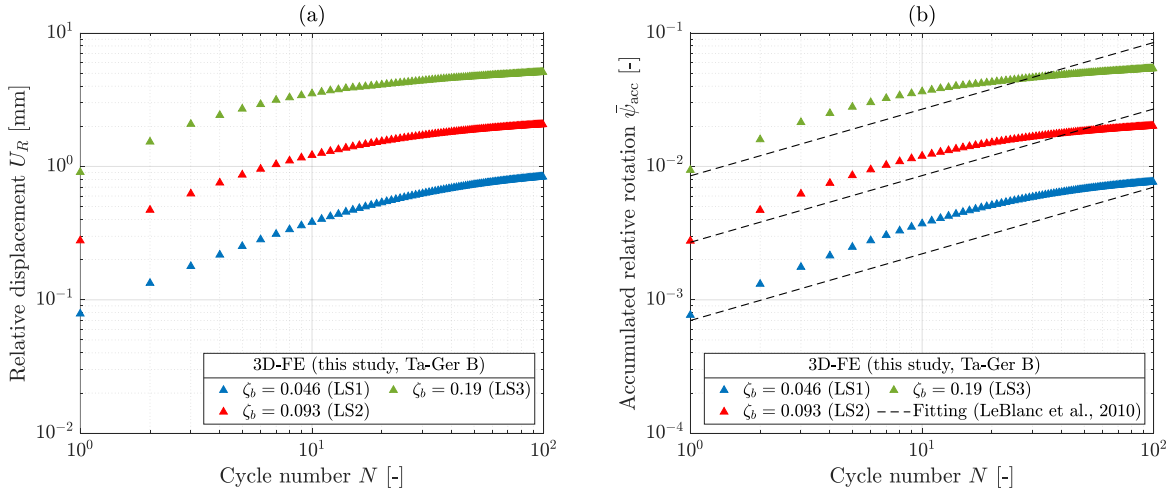

Figure 6.20: 3D-FE simulations using Ta-Ger B for PISA cyclic load sets (LS1 to LS3) on pile DM2, each simulated individually assuming wished-in-place installation and a uniform-density profile of quartz sand No. 3 (simplified configuration): (a) relative displacement U_R at ground surface; (b) accumulated relative rotation $\bar{\psi}_{acc}$ at ground surface, compared against the empirical relationship proposed by LeBlanc et al. (2010).

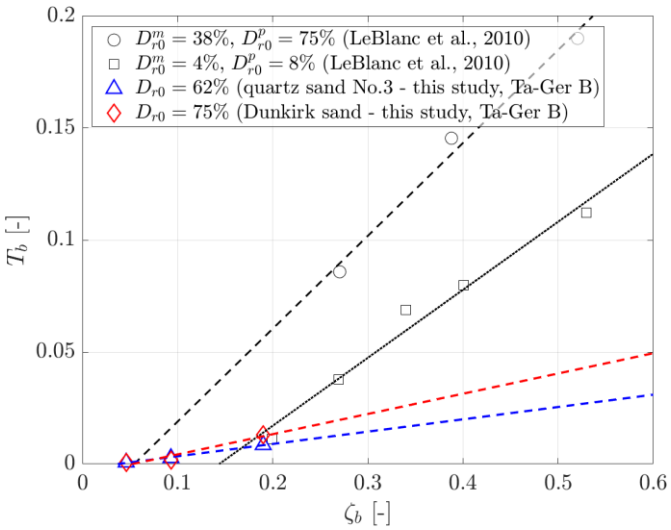

Figure 6.21: Comparison of numerical ζ_b–T_b trends from 3D-FE simulations using Ta-Ger B (simplified configuration with quartz sand No. 3, and configuration III with Dunkirk sand) against experimental results from 1g model tests by LeBlanc et al. (2010), under one-way cyclic loading (ζ_c=0). The initial relative densities from the experimental data are reported for both model (D_{r0}^m) and prototype scales (D_{r0}^p).

6.3.8.4 Insights from key soil element responses around the monopile

As a final step, local soil behaviour was examined at selected stress points within key elements surrounding the monopile (see Figure 6.19 for coordinates), using the simulation with the intermediate load amplitude ($\zeta_b = 0.093$) from the three simplified-configuration cases conducted for quartz sand No. 3 (see Table 6.5). PLAXIS 3D employs ten-node tetrahedral elements, each containing four stress points (Bentley Systems, 2024b). The selected stress points were chosen to be approximately symmetric about the pile axis, with two located on the front side (in the direction of loading) near the pile head (B) and toe (D), and two on the back side at corresponding depths (A and C). This layout was intended to capture the influence of spatial position around the pile on local response under lateral loading and to provide insight into the elemental-scale behaviour predicted by the Ta-Ger B model, linking it to the global cyclic response.

Figure 6.22 presents the cyclic effective stress paths at the four selected stress points. For the shallow points (A and B), the stress paths exhibit similar fluctuations along a slope approximately $\Delta q/\Delta p \approx 3$, characteristic of drained triaxial compression in laboratory conditions. Both start below the critical state stress ratio (M_{cs}) and cycle around it during

loading. In contrast, the deeper points (C and D) show different behaviour, which can be interpreted in line with Liu et al. (2022a), who reported similar stress path features using SANISAND-MS, albeit under different geometry and soil conditions. Their interpretation, supported by the experimental observations of Tsuha et al. (2012), attributed the emergence of 'undrained-like' $p-q$ loops during cyclic loading to kinematic constraints at the pile-soil interface, where the pile's rigidity and roughness restrict vertical and circumferential straining, while radial straining is further limited by the surrounding soil stiffness. This behaviour, leading to an 'inverse radial scale effect', causes the soil respond as if undrained even under drained loading. While such behaviour is not apparent in the shallow elements of the current study, possibly due to reduced constraint, point C shows a reduction in mean effective stress p, indicating contractive tendencies under the assumption of behaviour resembling undrained conditions. In contrast, point D shows an increase in p, suggesting a tendency to dilate. These trends align with the direction of loading (from C to D), which would be expected to induce local densification near C and loosening near D. Figure 6.23 which presents the $e-\ln(p)$ response at the same points, complements these findings. All four stress paths remain clearly separated from the critical state line (CSL). The critical state condition is defined by two simultaneous criteria: (i) the stress ratio satisfies $q/p = M_{\mathrm{cs}}$, and (ii) the void ratio lies on the CSL in $e-\ln(p)$ space, i.e., $e = e_{\mathrm{c}}(p)$ (Dafalias and Manzari, 2004). Accordingly, none of the points has reached the critical state.

Figure 6.24 shows cyclic strain paths in terms of deviatoric and volumetric strain invariants. Results for the shallow points (A and B) are consistent with Liu *et al.* (2022a), who noted that straining intensity and nature depend on the spatial position of each element. Specifically, elements near the ground surface and on the front side of the pile tend to experience greater deformation, with a dominant contractive volumetric response. Similarly, in the present study, point B shows marked contractive strains, whereas point A exhibits

dilation. This contrasting pattern, dilation behind the pile and contraction in front, has also been numerically observed by He and Takahashi (2025). As expected, strain accumulation at the deeper points (C and D) is relatively limited due to their deeper location and the increased confinement, which suppresses volumetric changes.

Figure 6.25 shows the evolution of the Lode angle variable χ, where values near 1.0, 0.7, and 0.8 correspond to triaxial compression, extension, and simple shear, respectively. The stress states fluctuate throughout the loading cycles. Point A (shallow back) oscillates between compression and extension; point D (deep front) varies between extension and simple shear; point B (shallow front) cycles between compression and simple shear; and point C (deep back) remains mostly in compression with minimal fluctuation. While Figure 6.8 represents monotonic loading, the χ ranges observed here are broadly consistent with those for Dunkirk sand, though cyclic loading induces more complex local mechanisms.

Figure 6.26 presents the presents the evolution of the hardening exponent n at the four reference points throughout the cyclic loading. In all cases, n increases monotonically, reflecting the progressive accumulation of shear strain and ongoing mobilisation of the hardening mechanism. The rate of increase is more pronounced at the shallow points (A and B), in line with the higher strain demand and volumetric responses previously observed.

To conclude, the analysis of elemental responses highlights the strong influence of spatial position around the pile on local soil behaviour under cyclic loading, emphasising the complex stress-strain interactions that develop within a BVP compared to the idealised conditions of standard element tests used for calibration. The Ta-Ger B model captures mechanisms consistent with trends reported in experimental and numerical studies, supporting its ability to reproduce key aspects of cyclic monopile behaviour and its suitability for broader application in future simulations.

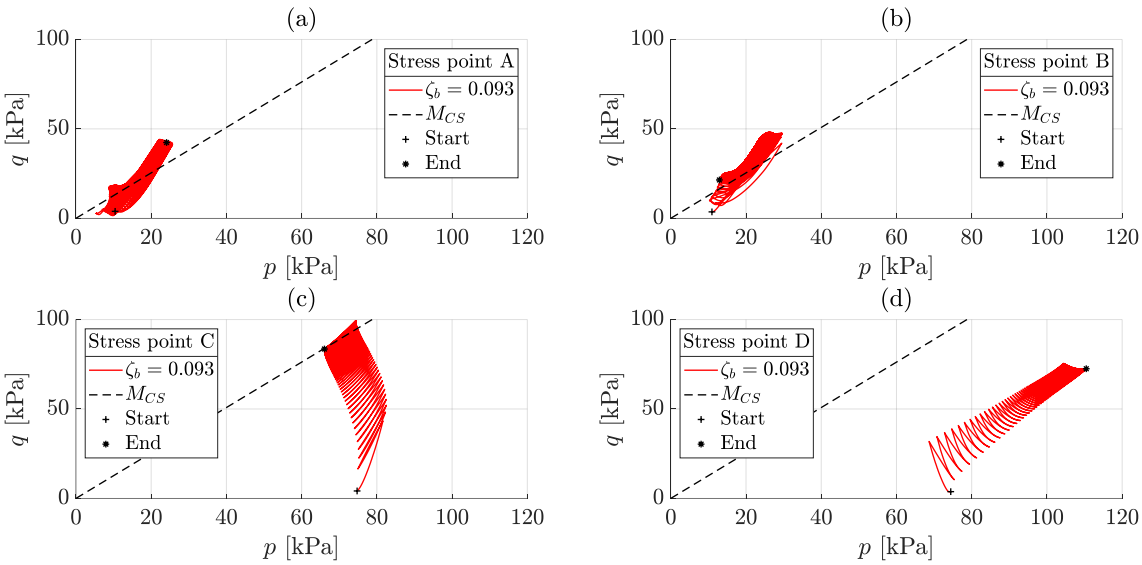

Figure 6.22: Cyclic effective stress paths at reference points: (a, c) rear; (b, d) front (top and bottom).

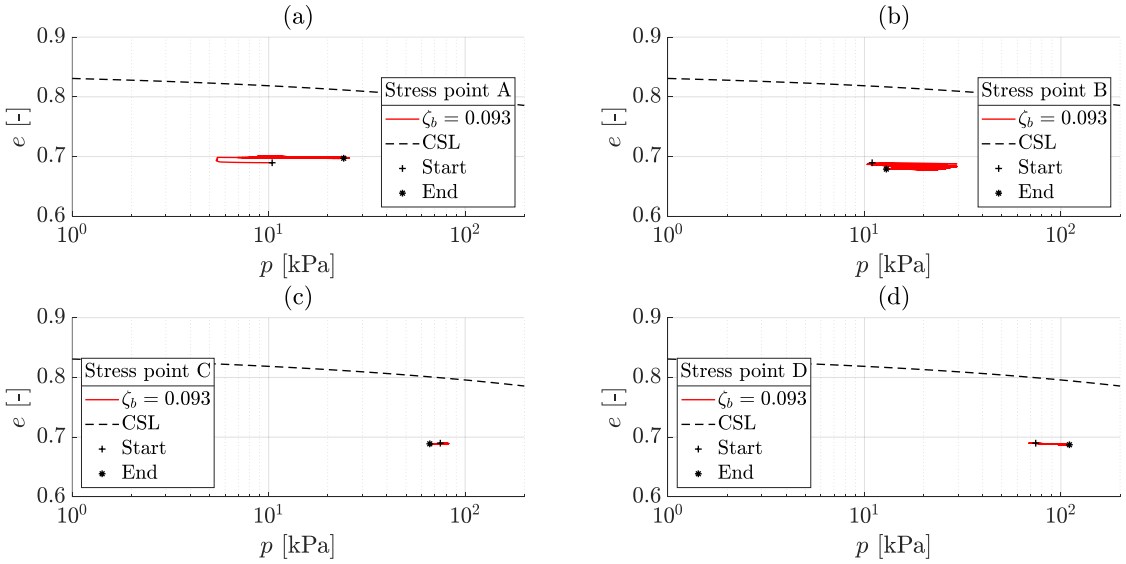

Figure 6.23: Cyclic $e - \ln(p)$ paths at reference points: (a, c) rear; (b, d) front (top and bottom).

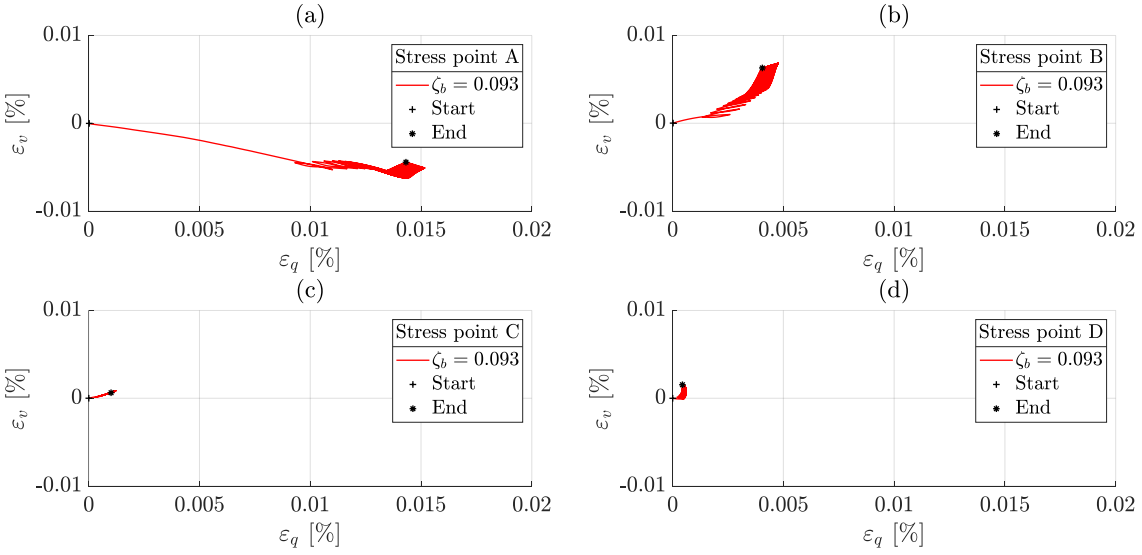

Figure 6.24: Cyclic strain paths at reference points: (a, c) rear; (b, d) front (top and bottom).

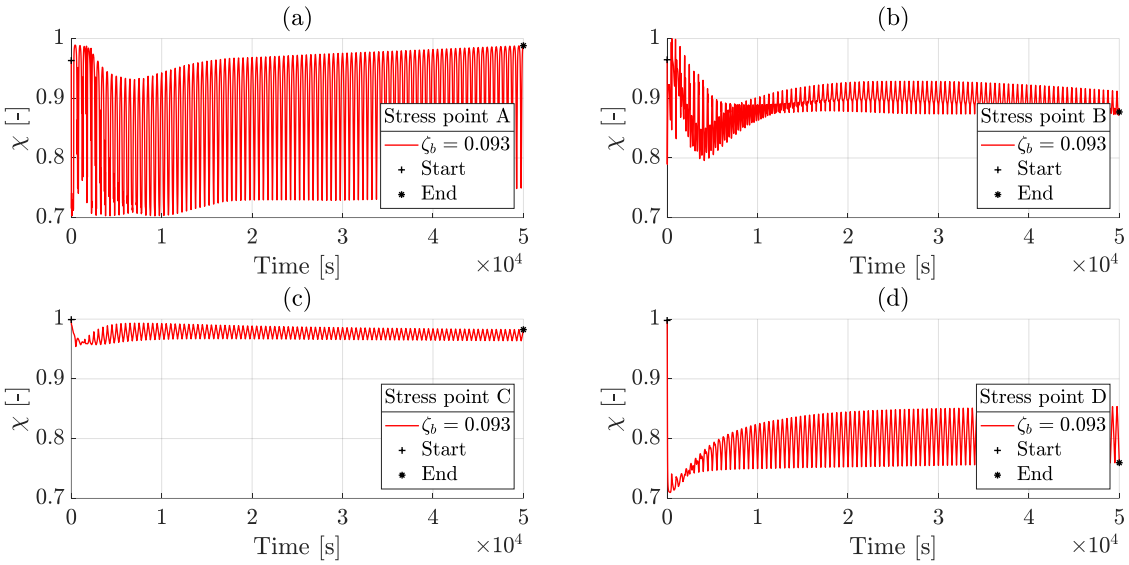

Figure 6.25: Evolution of Lode's angle variable χ at reference points: (a, c) rear; (b, d) front (top and bottom).

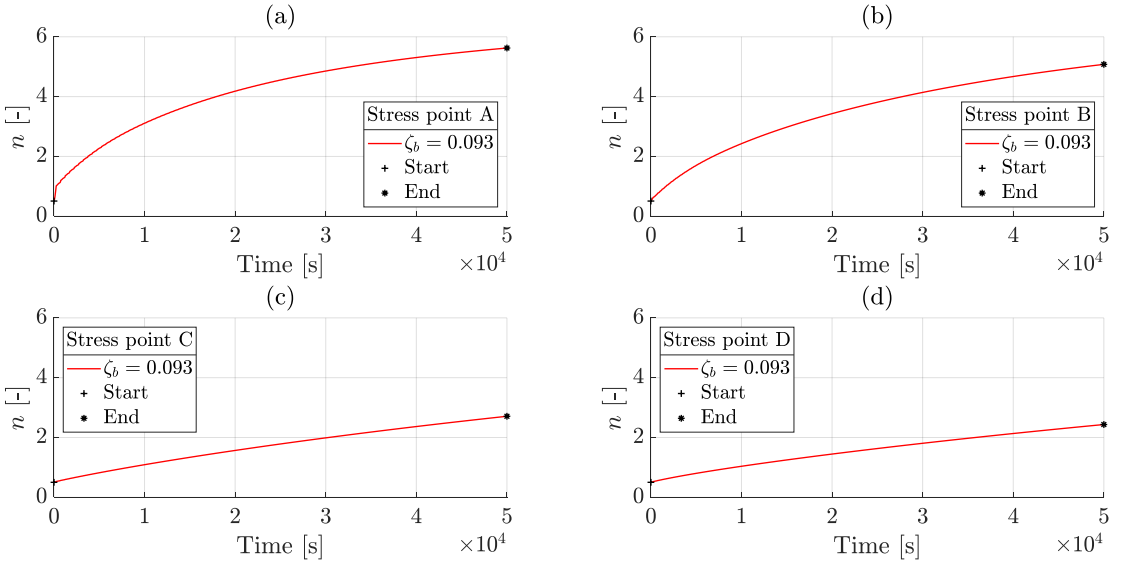

Figure 6.26: Evolution the hardening exponent n at reference points: (a, c) rear; (b, d) front (top and bottom).

6.3.9 Conclusions

This chapter outlines the full numerical implementation of the Ta-Ger B model within a commercial 3D-FE software. Validation was performed against previous studies (Taborda *et al.*, 2020; Tasiopoulou *et al.*, 2020; Pisanò *et al.*, 2024) and PISA field data (Beuckelaers, 2017; Byrne et al., 2020b; McAdam et al., 2020), confirming the model's ability to reproduce key aspects of monopile behaviour under complex loading and ground conditions, including displacement accumulation and tilt, which are critical for OWT monopile design. The study progressed from verifying the Fortran implementation of Ta-Ger B as a PLAXIS 3D UDSM

through benchmark triaxial simulations to full monopile BVP analyses, providing insights to ensure robustness and broader applicability of these numerical considerations across all Ta-Ger variants.

Several important lessons emerged. First, even when the ground model necessarily departed from site conditions, careful calibration and engineering judgement were sufficient to achieve a realistic representation of both monotonic and cyclic monopile response. In particular following the rationale of Pisanò et al. (2024), the use of high-cycle test data from a sand with similar index properties proved more reliable for defining cyclic parameters than fitting directly to field response, which was shown to be highly sensitive to load amplitude. Second, again consistent with Pisanò et al. (2024), applying an initial volumetric strain to the monopile plug was verified as a rational means of representing installation effects, allowing this parameter to be treated in a site-specific manner, though its applicability beyond the PISA DM2 test requires further study. Additionally, comparisons with experimental trends (LeBlanc et al., 2010) confirmed that Ta-Ger B produces results consistent with empirical observations, although broader validation would benefit from a more extensive simulation programme. Finally, the study critically evaluates the model's strengths and limitations, particularly its challenges in capturing sequences of load sets with varying amplitudes. The link between elemental and global monopile response is also explored, extending understanding of model behaviour beyond standard loading paths.

Overall, Ta-Ger B is shown to provide a robust and practical foundation for advanced monopile analyses, supporting future developments involving more complex load histories, variable ground conditions, and extended high-cycle simulations, while remaining suitable for integration into offshore wind design workflows.

Chapter 7
Conclusions

7.1 Introduction

This thesis investigates the constitutive modelling of sand under cyclic loading, with emphasis on applications to offshore wind turbine (OWT) monopile foundations. The main aim was to develop a constitutive model capable of predicting long-term cyclic response without compromising short-term performance, and to apply this model in three-dimensional finite element analyses (3D-FEA) of monopile foundation boundary value problems (BVPs).

Intrinsic (step-by-step) constitutive models based on key plasticity frameworks identified in the literature were examined. A critical evaluation of three established models, together with the newly proposed parallel Iwan model (PIMSS), identified the Ta-Ger framework as the most suitable basis for further development. Model development within this framework was guided by computational studies assessing the role of different constitutive elements. Three variants were considered: (i) Ta-Ger A (Tasiopoulou and Gerolymos, 2016a; 2016b), the original and most recognised formulation, employing relative dilatancy index I_{r} (Bolton, 1986) as the state parameter; (ii) Ta-Ger B (Tasiopoulou and Gerolymos, 2016a), an alternative formulation using the traditional state parameter ψ (Been and Jefferies, 1985) but

not further explored by the original authors; and (iii) Ta-Ger HC, a new variant extending Ta-Ger B by incorporating a nonlinear anisotropic hyperelastic law (Houlsby et al., 2019) in place of the hypoelastic formulation (Richart et al., 1970) and introducing a modified hardening exponent equation. All three variants were benchmarked in element-level simulations against experimental data, including high-cycle tests with up to 10000 cycles.

The scope was extended to account for offshore environments where seabed materials often contain fines. Ta-Ger B and Ta-Ger HC were adapted to represent sands with non-plastic and low-plasticity fines via equivalent granular state theory (EGST) (Rahman, 2021), enabling consistent application without recalibration across fines contents. The extended models were evaluated against laboratory data under monotonic and high-cycle loading.

Implementation in finite element (FE) software formed a central part of the study. Ta-Ger B was coded as a user-defined soil model (UDSM) in PLAXIS 3D and applied to BVP analyses simulating selected PISA Dunkirk field tests (Beuckelaers, 2017; Byrne et al., 2020b; McAdam et al., 2020). Validation against field data and experimental trends demonstrated the model's applicability to monopile BVPs relevant to OWT foundations.

The following sections outline key contributions, design implications, and future research.

7.2 Key contributions

Development of the PIMSS constitutive model (Parallel Iwan Multi-Surface Sand): A complementary but significant contribution of this thesis, presented in chapter 3, is the development of PIMSS, a new effective stress model for sands within the broader class of multi-surface plasticity. PIMSS comprises multiple stationary micro-models arranged in parallel, each incorporating the constitutive ingredients of the Prevost model. By omitting kinematic hardening and associated translation rules, it provides a simplified variant while still reproducing nonlinear hysteretic response. Validation against monotonic and cyclic

triaxial tests on Karlsruhe sand showed performance broadly comparable to Prevost, while also revealing some cyclic limitations linked to the averaging nature of the parallel formulation. Guidance is also provided for multiaxial implementation, applicable to other models within this framework. Designed with practical OWT monopile applications in mind, PIMSS is suited to short-term cyclic sand response, while its modular structure, simplicity, and adaptability provide a flexible platform for future development.

Evaluation of four constitutive models: Another contribution in chapter 3 is the comparative evaluation of four constitutive models for sands under monotonic and cyclic loading: SANISAND DM04, Ta-Ger B, the Prevost model, and PIMSS. SANISAND DM04, already well established, served as the benchmark, with the other three evaluated together for the first time. Drained and undrained triaxial simulations benchmarked against Karlsruhe sand data at varying densities and stress levels highlighted the relative merits of bounding-surface plasticity, series and parallel multi-surface plasticity, and the Ta-Ger framework. Beyond predictive behaviour, the evaluation considered calibration effort, numerical robustness, and ease of implementation, providing a structured basis for model selection, further development and application to BVPs.

Documentation and element-level implementation guidance for the Ta-Ger family: Chapter 4 provides systematic documentation of the Ta-Ger family, clarifying the key A and B variants and addressing inconsistencies in the original publications. Typographical errors and ambiguities were identified, leading to revisions of constitutive equations in multiaxial stress space. Practical guidance for element-level implementation is also provided, including clarification of the conditions necessary for accurate softening simulations. Although not new theoretical developments, these clarifications are valuable, as experience from this study showed how much time and effort can be lost in independent implementation, thereby supporting future applications of the Ta-Ger framework.

Significance of robust stress integration schemes for high-cycle simulations: Also in chapter 4, a systematic assessment of stress integration schemes compared the first-order forward Euler (RK1) and the third-order Runge-Kutta-Fehlberg (RKF23) schemes. Convergence analyses of Ta-Ger A and B under monotonic triaxial loading demonstrated the importance of conducting convergence checks and selecting an adequate number of increments. Purely elastic high-cycle triaxial simulations using the stand-alone hyperelastic model showed that lower-order schemes produce spurious strain accumulation even under theoretically reversible loading. High-cycle simulations with Ta-Ger B further confirmed that integration errors can distort cyclic predictions, for example by incorrectly predicting continuous ratcheting instead of shakedown. RKF23 was shown to deliver robust accuracy, albeit at higher computational cost, highlighting the critical role of integration schemes in reliable long-term cyclic analyses and providing practical guidance for future applications.

Development and of element-level validation of Ta-Ger HC, a new high-cycle variant: One of the core contributions, presented in chapter 4, is the development of Ta-Ger HC, a new intrinsic plasticity model within the Ta-Ger framework tailored for long-term cyclic loading. Its formulation was guided by computational studies on Ta-Ger A and B variants that isolated the role of individual constitutive components, yielding insights in their own right. The final model incorporates: (i) a thermodynamically consistent nonlinear anisotropic hyperelastic law, replacing the original hypoelastic formulation and markedly improving strain accumulation predictions; and (ii) equations for the bounding and phase transformation stress ratios selected to avoid critical state inconsistencies, numerical instabilities, and unrealistic high-cycle responses observed with the equations proposed in the original publications. A modified hardening exponent was also explored, demonstrating the flexibility of the framework. Validation against cyclic tests on Hostun sand (up to 250 cycles), and high-cycle tests on quartz sand No. 3 (up to 10000 cycles), confirmed the

model's ability to capture strain accumulation and transition from ratcheting to shakedown. This establishes Ta-Ger HC as a robust high-cycle variant suitable for practical applications, while Ta-Ger B remains a reliable choice for applications involving fewer than 1000 cycles.

Extension of Ta-Ger B and Ta-Ger HC via EGST to account for fines inclusion: A further contribution, set out in chapter 5, is the extension of the Ta-Ger B and Ta-Ger HC models to sands containing non-plastic and low-plasticity fines through integration of EGST. In this framework, the only modification to the clean-sand formulations is the substitution of the void ratio e and state parameter ψ with their equivalent granular counterparts e^* and ψ^*. This adaptation enables the use of clean-sand parameters together with a few fines index properties, avoiding recalibration across varying fines contents while reducing workload and preserving model consistency. Verification against two experimental databases on Sydney sand with Majura silt and Karlsruhe fine sand with low-plasticity kaolinite showed good agreement in drained and undrained monotonic tests up to 20% fines content. High-cycle simulations up to 10000 cycles on the latter database further confirmed the ability of the extended models to capture strain accumulation, marking the first constitutive application of EGST to high-cycle tests. Between the two variants, Ta-Ger HC overall showed better performance, due to its nonlinear anisotropic hyperelastic law, making it the preferred formulation for OWT foundation applications. A simplified calibration procedure was also introduced to address the absence of void ratio dependency in Ta-Ger HC's hyperelastic law. Overall, these contributions establish the EGST-extended Ta-Ger framework as a reliable and efficient approach for modelling sand-fines mixtures, while underscoring the importance of explicitly accounting for fines to avoid unconservative predictions.

Implementation and validation of Ta-Ger B in 3D-FEA of monopile foundations: A major contribution, presented in chapter 6, is the full implementation of Ta-Ger B as a UDSM in PLAXIS 3D, implemented via Fortran subroutines compiled into a dynamic link

library (DLL) and linked through the PLAXIS UDSM interface, together with its validation in BVP simulations of monopile foundations. The study progressed from addressing numerical considerations and verifying the robustness of the implementation to applying the model in large-scale monopile simulations of PISA field tests. Beyond these field tests, the model's cyclic predictions were also verified against experimental trends. The model successfully reproduced key aspects of monopile behaviour under lateral monotonic and cyclic loading, including load-displacement response and pile tilt accumulation, which are central to OWT monopile design. Importantly, the analyses provide insights into constitutive behaviour at the element level and extend understanding of the model's mechanisms beyond standard laboratory paths. This work establishes Ta-Ger B as a reliable basis for 3D-FE simulations of monopile foundations and provides a foundation for robust implementation across all Ta-Ger variants.

Practical calibration strategies for cyclic monopile BVP applications: Finally, chapter 6 examines practical calibration strategies for monopile applications, grounded in insights from the PISA field tests. The analyses showed that calibration of cyclic parameters is more reliably achieved using high-cycle triaxial tests on sands with similar index properties, in the absence of data for the sand under examination, than by fitting directly to field response, which was shown to be highly sensitive to factors such as load amplitude. Furthermore, the introduction of an initial volumetric strain to the monopile plug was verified as a rational approach to approximate installation effects, allowing this to be treated as a site-specific parameter. These strategies reduce reliance on field-specific fitting and enhance the practical usability of Ta-Ger B and other variants in offshore design contexts. Together, they provide guidance that is directly relevant to future applications of Ta-Ger family models in OWT monopile foundation design.

7.3 Implications for design

Constitutive model suitable for 3D-FEA of monopile foundations with cyclic loading: Serviceability and fatigue limit state design of OWT monopiles requires soil models capable of capturing cyclic loading in 3D-FEA. This thesis provides both a methodological basis for model selection and developments that establish Ta-Ger HC, and to a lesser extent Ta-Ger B, as suitable options with simple and robust formulations.

Importance of accounting for fines in constitutive modelling of seabed sands: The adaptation of Ta-Ger B and Ta-Ger HC to sands with non-plastic and low-plasticity fines through EGST enables a more realistic representation of seabed materials using a unified parameter set applicable across varying fines contents, densities, and stress levels. This reduces calibration effort and mitigates the risk of unconservative predictions, as evidenced by drained high-cycle single-element simulations where neglecting fines led in underestimation of strain accumulation.

Practical calibration strategies: Cyclic parameters for 3D-FE monopile simulations can be reliably derived from high-cycle triaxial tests on sands with comparable index properties when site-specific data are unavailable, provided appropriate caution is applied. Installation effects may be represented by prescribing an initial volumetric strain in the monopile plug, offering a rational site-specific approach and an additional cyclic calibration parameter.

Confidence in usage of more advanced models within 3D-FEA: This work adds a foundation stone to the growing evidence base supporting advanced constitutive models in 3D-FEA of OWT monopile BVPs, reducing reliance on default simpler models in commercial software. Continued studies of this type are essential to demonstrate and consolidate the role of advanced soil models in design practice.

7.4 Research limitations and future work

This section is divided into two parts: the first considers the PIMSS model, and the second the Ta-Ger family of models. Each begins by outlining the main limitations of the present work and then proposes a programme of future studies to address them.

7.4.1 PIMSS research pathway

The PIMSS model has shown promise, but several limitations remain. The current formulation requires recalibration across densities and does not capture softening behaviour. In undrained cyclic simulations, issues of shear locking were observed, and the model has only been evaluated at the single-element level, leaving its relevance for offshore foundations untested. Addressing these limitations suggests two main strands of future work.

Application in 3D-FEA of monopile foundations: An important research direction is the implementation of PIMSS as a UDSM in 3D-FE software and its application to monopile BVPs. This would assess computational efficiency and stability under monotonic and cyclic loading and evaluate performance at foundation scale. Importantly, such application is required before proposing targeted refinements, as it will identify which aspects of the formulation most strongly influence global response and numerical performance.

Refinement of the PIMSS formulation: In addition to the refinements identified through 3D-FEA application, further development based on the single-element findings of this study should incorporate state-dependent mechanisms consistent with critical state soil mechanics (CSSM), enabling a single parameter set across densities and allowing softening to be reproduced. Building on its parallel arrangement of micro-models derived from the Prevost model (Prevost, 1985), a logical extension would be the development of a PIMSS-CS variant employing micro-models from the critical state-enhanced Prevost formulation of Elbadawy et al. (2024). Targeted modifications may also required to improve predictions of cyclic

degradation and to mitigate shear locking observed in undrained simulations, potentially through incorporation of a cyclic overlay method as in Whyte et al. (2020).

7.4.2 Ta-Ger research pathway

The Ta-Ger framework has been further developed (variants B, HC) and applied in this thesis to clean sands and sands with fines. While the extended models have shown encouraging capability, several aspects remain to be explored and strengthened. For clarity, the discussion is organised into three parts: clean sands, sands with fines, and the UDSM implementation.

7.4.2.1 Clean sands

This study has shown that the adapted Ta-Ger models can reproduce key features of cyclic sand behaviour, with 3D-FE studies using PISA field data and comparisons with 1g pile tests. Validation against the latter was limited because: (i) analyses of the $\zeta_b - T_b$ relationship were restricted to a narrow range of ζ_b due to convergence and time constraints; (ii) only one-way cyclic loading ($\zeta_c = 0$) was examined; and (iii) the geometry of the PISA piles was adopted instead of that of the 1g tests, meaning that the comparison could only be qualitative. Future work should therefore begin by extending validation with Ta-Ger B before pursuing refinements and validation of more complex variants such as Ta-Ger HC.

Step 1: 3D-FE validation against 1g cyclic pile tests: Future studies should replicate the geometry and boundary conditions of benchmark 1g experiments, beginning with the data of LeBlanc et al. (2010) and Richards (2019), and extending to other constant-amplitude cyclic tests from the literature. This would enable direct comparison with experimental data, as well as investigations at higher ζ_b values and under a broader set of cyclic loading conditions ($\zeta_c \neq 0$), providing a rigorous assessment of the model's predictive capability.

Step 2: 3D-FE validation under more complex conditions: Once validity against 1g pile tests has been established, Ta-Ger B should be applied in 3D-FE monopile simulations under

complex load sequences with varying amplitudes, to evaluate predictions under realistic cyclic loading. A useful reference is the 600-s load history representing the high phase of a 35-h design storm reported by Chaloulos et al. (2024). Future work should also examine cumulative damage concepts such as Miner's rule (Liu et al., 2022b) and extend validation to a wider range of drainage conditions.

Step 3: 3D-FE extension to partial drainage conditions: While the present BVP simulations were conducted within an effective-stress framework, drainage conditions were idealised by assuming fully drained behaviour during cyclic loading. Partial drainage effects, arising from the interaction between loading rate, soil permeability, drainage path length, and pore pressure dissipation, were therefore not explicitly represented. This assumption is consistent with the focus of the present study on sand constitutive behaviour and long-term cyclic trends, but may not fully capture monopile response under transient or rate-sensitive loading conditions. Incorporating partially drained behaviour within 3D-FE monopile simulations therefore represents a natural and important extension of the present work. Such analyses would require fully coupled hydro-mechanical formulations capable of resolving rate-dependent pore pressure generation and dissipation under realistic cyclic loading histories. While computationally demanding, their integration with advanced effective-stress constitutive models such as Ta-Ger B and Ta-Ger HC is expected to provide valuable insight into the influence of drainage conditions on cyclic monopile response, both at the global foundation scale and at the element level in the vicinity of the monopile.

Step 4: 3D-FE application of Ta-Ger within extrinsic modelling approaches: While the intrinsic Ta-Ger B and Ta-Ger HC formulations provide a detailed constitutive description of cyclic sand behaviour, their step-by-step stress integration makes direct application to loading histories involving very large numbers of cycles computationally demanding. A promising direction for future work is therefore the development of strategies in which Ta-

Ger models are combined with established extrinsic modelling approaches. In such an approach, Ta-Ger B or Ta-Ger HC would be used to simulate the soil response explicitly over a limited number of initial loading cycles, depending on the specific extrinsic framework adopted, while the effects of subsequent cycles would be represented using extrinsic formulations, such as High Cycle Accumulation (HCA) models or stiffness degradation methods (SDM). This strategy would enable efficient simulation of loading histories involving very high-cycle counts and is well suited to practical monopile design applications. Future work could therefore focus on systematically assessing the computational efficiency and predictive accuracy of such modelling strategies, and on comparing the performance of Ta-Ger variants with other intrinsic constitutive models that have been employed in conjunction with extrinsic approaches.

Step 5: Refinements of the Ta-Ger formulations (B and HC): Building on insights from the present study and from validation in steps 1 to 4, a further stage would focus on refining the Ta-Ger framework to move it closer to practical application in OWT foundation design.

7.4.2.2 Sands with fines

The extension of the Ta-Ger B and HC variants to sands with fines through the EGST formulation has produced encouraging results but remains limited in scope. Element-level validation under high-cycle loading was based on small number of tests, and at the boundary-value scale the implications for monopile response remain to be demonstrated.

Element-level validation: Future work should extend the validation of the EGST-extended Ta-Ger models using more comprehensive high-cycle databases, spanning wider range of mean stress ratios (η^{ave}), cyclic amplitudes (q^{ampl}), and initial mean effective stresses (p_{in}).

Effectiveness of EGST in 3D-FE monopile analyses: A natural continuation is the application of the EGST-extended Ta-Ger models in 3D-FEA of monopile foundations

embedded in sands with fines. Such analyses would evaluate how accounting for fines at constitutive level influences system-scale behaviour under monotonic and cyclic loading, clarifying the broader practical significance of fines inclusion for OWT foundation design.

7.4.2.3 Improving the Ta-Ger UDSM implementation

The current Ta-Ger B UDSM has been successfully applied in this study, but its broader use in large-scale FEA would benefit from further strengthening. Additional benchmarking and refinement could enhance convergence behaviour and numerical stability, providing a firm basis for extending the implementation to other variants.

References

Abadie, C.N., Beuckelaers, W.J.A.P., Byrne, B.W., Houlsby, G.T., Burd, H.J. and McAdam, R. (2023) 'Modeling Lifetime Performance of Monopile Foundations for Offshore Wind Applications', *Journal of Geotechnical and Geoenvironmental Engineering*, 149(8), p. 4023051. Available at: https://doi.org/10.1061/JGGEFK.GTENG-9833.

Achmus, M., Kuo, Y.S. and Abdel-Rahman, K. (2009) 'Behavior of monopile foundations under cyclic lateral load', *Computers and Geotechnics*, 36(5), pp. 725–735. Available at: https://doi.org/10.1016/j.compgeo.2008.12.003.

Adamidis, O. and Madabhushi, S.P.G. (2018) 'Experimental investigation of drainage during earthquake-induced liquefaction', *Géotechnique*, 68(8), pp. 655–665. Available at: https://doi.org/10.1680/jgeot.16.P.090.

Amorosi, A., Rollo, F. and Houlsby, G.T. (2020) 'A nonlinear anisotropic hyperelastic formulation for granular materials: comparison with existing models and validation', *Acta Geotechnica*, 15(1), pp. 179–196. Available at: https://doi.org/10.1007/S11440-019-00827-5/FIGURES/11.

Andersen, K. (2009) 'Bearing capacity under cyclic loading - offshore, along the coast, and on land. The 21st Bjerrum Lecture presented in Oslo, 23 November 2007', *Canadian Geotechnical Journal*, 46, pp. 513–535. Available at: https://doi.org/10.1139/T09-003.

Andersen, K. (2015) *Cyclic soil parameters for offshore foundation design. The 3rd McClelland Lecture*.

API (2011) 'Geotechnical and Foundation Design Considerations ANSI/API RP 2GEO'. API (American Petroleum Institute).

Arany, L., Bhattacharya, S., Macdonald, J. and Hogan, S.J. (2017) 'Design of monopiles for offshore wind turbines in 10 steps', *Soil Dynamics and Earthquake Engineering*, 92, pp. 126–152. Available at: https://doi.org/10.1016/J.SOILDYN.2016.09.024.

Arulmoli, K., Muraleetharan, K., Hossain, M. and Fruth, L. (1992) *VELACS (Verification of Liquefaction Analyses by Centrifuge Studies) Laboratory Testing Program: Soil Data Report*. Available at: https://doi.org/10.13140/2.1.3740.8320.

Atkinson, J.H. and Sallfors, G. (1991) 'Experimental determination of soil properties', in *Proc. 10th Eur. Conf. Soil Mech. and Fnd Engng (ECSMFE)*. Florence, pp. 915–956.

Been, K. and Jefferies, M.G. (1985) 'A state parameter for sands', *Géotechnique*, 35, pp. 99–112. Available at: https://doi.org/10.1680/geot.1985.35.2.99.

Bentley Systems (2024a) 'PLAXIS 3D'. Available at: https://www.seequent.com/products-solutions/plaxis-3d/ (Accessed: 26 June 2025).

Bentley Systems (2024b) 'PLAXIS 3D 2024.1: 2 – Reference Manual'.

Beuckelaers, W. (2017) *Numerical Modelling of Laterally Loaded Piles for Offshore Wind Turbines*.

Bhattacharya, S. (2019) *Design of Foundations for Offshore Wind Turbines*. Available at: https://doi.org/10.1002/9781119128137.

Bobei, D. (2004) *Static liquefaction of sand with a small amount of fines*. Doctoral Dissertation. UNSW Sydney.

Bolton, M.D. (1986) 'The strength and dilatancy of sands', *Géotechnique*, 36(1), pp. 65–78. Available at: https://doi.org/10.1680/geot.1986.36.1.65.

Bouc, R. (1967) 'Forced Vibration of Mechanical Systems with Hysteresis'.

Bouckovaklas, G., Whitman, R., ASCE, F., Marr, W.A. and ASCE, M. (1985) 'Permanent displacement of sand with cyclic loading', *International Journal of Rock Mechanics*

and Mining Sciences & Geomechanics Abstracts, 22, p. A73. Available at: https://doi.org/10.1016/0148-9062(85)93277-2.

Bouckovalas, G., Whitman, R. V. and Marr, W.A. (1984) 'Permanent Displacement of Sand With Cyclic Loading', *Journal of Geotechnical Engineering*, 110(11), pp. 1606–1623. Available at: https://doi.org/10.1061/(ASCE)0733-9410(1984)110:11(1606).

Brinkgreve, R. (1994) *Geomaterial models and numerical analysis of softening*. PhD Thesis. Delft University.

Broere, W. and van Tol, A.F. (2006) 'Modelling the bearing capacity of displacement piles in sand', *Proceedings of the Institution of Civil Engineers - Geotechnical Engineering*, 159(3), pp. 195–206. Available at: https://doi.org/10.1680/geng.2006.159.3.195.

Burd, H.J., Taborda, D.M.G., Zdravković, L., Abadie, C.N., Byrne, B.W., Houlsby, G.T., Gavin, K.G., Igoe, D.J.P., Jardine, R.J., Martin, C.M., McAdam, R.A., Pedro, A.M.G. and Potts, D.M. (2020) 'PISA design model for monopiles for offshore wind turbines: application to a marine sand', *Géotechnique*, 70, pp. 1048–1066. Available at: https://doi.org/10.1680/jgeot.18.p.277.

Byrne, B. (2011) 'Foundation Design for Offshore Wind Turbines', *Géotechnique Lecture 2011* [Preprint]. London, UK: British Geotechnical Association, Institution of Civil Engineers.

Byrne, B., Mcadam, R., Burd, H., Houlsby, G., Martin, C., Beuckelaers, W., Zdravkovic, L., Taborda, D.M.G., Potts, D., Jardine, R., Ushev, E., Liu, T., Abadias, D., Gavin, K., Igoe, D., Doherty, P., Gretlund, J., Pacheco Andrade, M., Wood, A. and Plummer, M. (2017) *PISA: New Design Methods for Offshore Wind Turbine Monopiles*.

Byrne, B.W. (2020) 'Editorial: geotechnical design for offshore wind turbine monopiles', *Géotechnique*, 70(11), pp. 943–944. Available at: https://doi.org/10.1680/jgeot.2020.70.11.943.

Byrne, B.W., Burd, H.J., Zdravkovic, L., Abadie, C.N., Houlsby, G.T., Jardine, R.J., Martin, C.M., McAdam, R.A., Pacheco Andrade, M., Pedro, A.M.G., Potts, D.M. and Taborda, D.M.G. (2019) 'PISA Design Methods for Offshore Wind Turbine Monopiles', in. OTC. Available at: https://doi.org/10.4043/29373-ms.

Byrne, B.W., Houlsby, G.T., Burd, H.J., Gavin, K.G., Igoe, D.J.P., Jardine, R.J., Martin, C.M., McAdam, R.A., Potts, D.M., Taborda, D.M.G. and Zdravković, L. (2020) 'PISA design model for monopiles for offshore wind turbines: application to a stiff glacial clay till', *Géotechnique*, 70, pp. 1030–1047. Available at: https://doi.org/10.1680/jgeot.18.p.255.

Byrne, B.W., McAdam, R.A., Beuckelaers, W.J.A.P., Burd, H.J., Gavin, K., Houlsby, G.T., Igoe, D.J.P., Jardine, R. and Martin, C.M. (2020) 'Cyclic laterally loaded medium scale field pile testing for the PISA project', in *4th International Symposium on Frontiers in Offshore Geotechnics (postponed)*, pp. 1323–1332.

Cerfontaine, B. (2014) *The cyclic behaviour of sand, from the Prevost model to offshore geotechnics*.

Chaloulos, Y.K., Tasiopoulou, P., Giannakou, A., Chacko, J., Aghakouchak, A. and Stergiou, T. (2024) 'Fully-Coupled cyclic time-history analyses of monopile foundations in sand', *Ocean Engineering*, 298, p. 116691. Available at: https://doi.org/https://doi.org/10.1016/j.oceaneng.2024.116691.

Chang, C.S. and Whitman, R. V. (1988) 'Drained Permanent Deformation of Sand Due to Cyclic Loading', *Journal of Geotechnical Engineering*, 114(10), pp. 1164–1180. Available at: https://doi.org/10.1061/(ASCE)0733-9410(1988)114:10(1164).

Charalampakis, A. and Koumousis, V. (2010) *Parameters of Bouc–Wen model revisited*.

Chen, L., Ghorbani, J. and Kodikara, J. (2024) 'Modelling of shakedown, ratcheting and liquefaction of saturated granular soils using kinematic hardening with memory

surface', *Computers and Geotechnics*, 165, p. 105830. Available at: https://doi.org/10.1016/J.COMPGEO.2023.105830.

Cheng, Z. and Detournay, C. (2021) 'Formulation, validation and application of a practice-oriented two-surface plasticity sand model', *Computers and Geotechnics*, 132, p. 103984. Available at: https://doi.org/https://doi.org/10.1016/j.compgeo.2020.103984.

Chiang, D.Y. and Beck, J.L. (1994) 'A new class of distributed-element models for cyclic plasticity—I. Theory and application', *International Journal of Solids and Structures*, 31, pp. 469–484. Available at: https://doi.org/10.1016/0020-7683(94)90087-6.

Chong, S.-H. and Pasten, C. (2017) 'Numerical study on long-term monopile foundation response', *Marine Georesources & Geotechnology*, 36, pp. 190–196. Available at: https://doi.org/10.1080/1064119x.2017.1293200.

Collins, I.F. and Boulbibane, M. (2000) 'Geomechanical Analysis of Unbound Pavements Based on Shakedown Theory', *Journal of Geotechnical and Geoenvironmental Engineering*, 126, pp. 50–59. Available at: https://doi.org/10.1061/(asce)1090-0241(2000)126:1(50).

Corti, R., Diambra, A., Wood, D.M., Escribano, Daniella E and Nash, D.F.T. (2016) 'Memory Surface Hardening Model for Granular Soils under Repeated Loading Conditions', *Journal of Engineering Mechanics*, 142, p. 4016102. Available at: https://doi.org/10.1061/(asce)em.1943-7889.0001174.

Cuéllar, P., Mira, P., Pastor, M., Fernandez-Merodo, J.A., Baeßler, M. and Rücker, W. (2014) 'A numerical model for the transient analysis of offshore foundations under cyclic loading', *Computers and Geotechnics*, 59, pp. 75–86. Available at: https://doi.org/10.1016/j.compgeo.2014.02.005.

Dafalias, Y.F. (1986) 'Bounding Surface Plasticity. I: Mathematical Foundation and Hypoplasticity', *Journal of Engineering Mechanics*, 112, pp. 966–987. Available at: https://doi.org/10.1061/(asce)0733-9399(1986)112:9(966).

Dafalias, Y.F. and Manzari, M.T. (2004) 'Simple Plasticity Sand Model Accounting for Fabric Change Effects', *Journal of Engineering Mechanics*, 130(6), pp. 622–634. Available at: https://doi.org/10.1061/(asce)0733-9399(2004)130:6(622).

Dafalias, Y.F. and Popov, E.P. (1975) 'A model of nonlinearly hardening materials for complex loading', *Acta Mechanica*, 21, pp. 173–192. Available at: https://doi.org/10.1007/bf01181053.

Dawson, E., Roth, W. and Su, B. (2013) '3-D masing behavior of a parallel iwan model', in, pp. 549–556. Available at: https://doi.org/10.1061/9780784413128.065.

Dawson, E.M. (2013) 'A Parallel Iwan Model for 3D Cyclic Loading of Frictional Materials', in. Itasca International.

Dawson, E.M. and Roth, W. (2018) 'Stress-rotation response of a parallel iwan model for sand', in, pp. 149–161. Available at: https://doi.org/10.1061/9780784482049.015.

DNV GL (2016) 'DNVGL-ST-0126: Support Structures for Wind Turbines'. DNV GL.

Dobry, R., Pierce, W.G., Dyvik, R., Thomas, G.E. and Ladd, R.S. (1985) 'Pore pressure model for cyclic straining of sand', *Rensselaer Polytechnic Institute, Troy, New York*, pp. 1985–1986.

Duque, J., Yang, M., Fuentes, W., Mašín, D. and Taiebat, M. (2022) 'Characteristic limitations of advanced plasticity and hypoplasticity models for cyclic loading of sands', *Acta Geotechnica*, 17(6), pp. 2235–2257. Available at: https://doi.org/10.1007/S11440-021-01418-Z.

Einav, I. (2012) 'The unification of hypo-plastic and elasto-plastic theories', *International Journal of Solids and Structures*, 49(11–12), pp. 1305–1315. Available at: https://doi.org/10.1016/J.IJSOLSTR.2012.02.003.

Eisma, D. (1981) ‘Supply and Deposition of Suspended Matter in the North Sea’, in *Holocene Marine Sedimentation in the North Sea Basin*. John Wiley & Sons, Ltd, pp. 415–428. Available at: https://doi.org/https://doi.org/10.1002/9781444303759.ch29.

E-Kan, M. and Taiebat, H.A. (2014) ‘On implementation of bounding surface plasticity models with no overshooting effect in solving boundary value problems’, *Computers and Geotechnics*, 55, pp. 103–116. Available at: https://doi.org/10.1016/j.compgeo.2013.08.006.

Elbadawy, M.A., Zhou, Y.-G. and Chen, Y.-M. (2024) ‘An improved pressure dependent multi-yield surface model: calibration and validation’, *Computers and Geotechnics*, 172, p. 106445. Available at: https://doi.org/https://doi.org/10.1016/j.compgeo.2024.106445.

Elgamal, A., Yang, Z., Parra, E. and Ragheb, A. (2003) ‘Modeling of cyclic mobility in saturated cohesionless soils’, *International Journal of Plasticity*, 19(6), pp. 883–905. Available at: https://doi.org/https://doi.org/10.1016/S0749-6419(02)00010-4.

Escribano, D. (2014) *Evolution of stiffness and deformation of Hostun sand under drained cyclic loading*. PhD. University of Bristol.

European Commission (2020) *Boosting Offshore Renewable Energy for a Climate Neutral Europe*. Available at: https://ec.europa.eu/commission/presscorner/detail/en/ip_20_2096 (Accessed: 17 February 2025).

Fellin, W., Mittendorfer, M. and Ostermann, A. (2009) ‘Adaptive integration of constitutive rate equations’, *Computers and Geotechnics*, 36(5), pp. 698–708. Available at: https://doi.org/10.1016/J.COMPGEO.2008.11.006.

François, S., Karg, C., Haegeman, W. and Degrande, G. (2009) ‘A numerical model for foundation settlements due to deformation accumulation in granular soils under repeated small amplitude dynamic loading’, *International Journal for Numerical and Analytical Methods in Geomechanics*, pp. 273–296. Available at: https://doi.org/10.1002/nag.807.

Fuentes, W. and Triantafyllidis, Th. (2015a) ‘ISA: A constitutive model for deposited sand’, in. (Aktuelle Forschung in der Bodenmechanik), pp. 169–187.

Fuentes, W. and Triantafyllidis, Th. (2015b) ‘ISA model: A constitutive model for soils with yield surface in the intergranular strain space’, *International Journal for Numerical and Analytical Methods in Geomechanics*, 39(11), pp. 1235–1254. Available at: https://doi.org/https://doi.org/10.1002/nag.2370.

Gajo, A. and Muir Wood, D. (1999) ‘A kinematic hardening constitutive model for sands: the multiaxial formulation’, *International journal for numerical and analytical methods in geomechanics*, 23(9), pp. 925–965.

Gao, Z., Yan, L. and Whyte, S. (2023) ‘B-SDM: A bounding surface stiffness degradation method for modelling the long-term ratcheting response of offshore wind turbine foundations’, *Computers and Geotechnics*, 154, p. 105157. Available at: https://doi.org/10.1016/J.COMPGEO.2022.105157.

Gao, Z. and Zhao, J. (2015) ‘Constitutive Modeling of Anisotropic Sand Behavior in Monotonic and Cyclic Loading’, *Journal of Engineering Mechanics*, 141(8), p. 04015017. Available at: https://doi.org/10.1061/(ASCE)EM.1943-7889.0000907.

Gavin, K. and Doherty, P. (2012) ‘Laterally loaded monopile design for offshore wind farms’, *Proceedings of the ICE - Energy*, 165, pp. 7–17. Available at: https://doi.org/10.1680/ener.11.00003.

Gourvenec, S. and Randolph, M. (2011) *Offshore Geotechnical Engineering*, *Offshore Geotechnical Engineering*. Available at: https://doi.org/10.1201/9781315272474.

Grammatikopoulou, A., Schroeder, F.C., Brosse, A.M., Andersen, K.W. and Potts, D.M. (2017) 'On the Use of Constitutive Models in Numerical Analyses of Offshore Structures', *Offshore Site Investigation Geotechnics 8th International Conference Proceeding*, pp. 423–430. Available at: https://doi.org/10.3723/OSIG17.423.

Grimstad, G.J., Rønningen, A. and Nøst, H.A. (2014) 'Use of IWAN Models for Modelling Anisotropic and Cyclic Behavior of Clays', *Numerical Methods in Geotechnical Engineering*, pp. 49–54.

He, W. and Takahashi, A. (2025) 'Dynamic response analysis of monopile-supported offshore wind turbine on sandy ground under seismic and environmental loads', *Soil Dynamics and Earthquake Engineering*, 189, p. 109105. Available at: https://doi.org/https://doi.org/10.1016/j.soildyn.2024.109105.

Hendriks, E., van Prooijen, B.C., Cheng, C.H., Aarninkhof, S.G.J., Winterwerp, J.C. and Soetaert, K.E. (2022) 'An explanatory model for the burial of fines in the sandy seabed of the southern North Sea', *Marine Geology*, 454, p. 106953. Available at: https://doi.org/https://doi.org/10.1016/j.margeo.2022.106953.

HEREMA (2022) *Offshore Wind - Regulatory Framework*. Available at: https://herema.gr/offshore-wind/regulatory-framework/ (Accessed: 21 February 2025).

Houlsby, G. (1981) *A Study of Plasticity Theories and Their Applicability to Soils*. Doctoral thesis. University of Cambridge. Available at: https://doi.org/https://doi.org/10.17863/CAM.14121.

Houlsby, G. and Mortara, G. (2004) 'A continuous hyperplasticity model for sands under cyclic loading', in, pp. 21–26. Available at: https://doi.org/10.1201/9781439833452.ch3.

Houlsby, G.T., Abadie, C.N., Beuckelaers, W.J.A.P. and Byrne, B.W. (2017) 'A model for nonlinear hysteretic and ratcheting behaviour', *International Journal of Solids and Structures*, 120, pp. 67–80. Available at: https://doi.org/10.1016/j.ijsolstr.2017.04.031.

Houlsby, G.T., Amorosi, A. and Rollo, F. (2019) 'Non-linear anisotropic hyperelasticity for granular materials', *Computers and Geotechnics*, 115, p. 103167. Available at: https://doi.org/10.1016/J.COMPGEO.2019.103167.

Houlsby, G.T., Byrne, B.W., Burd, H.J. and Balaam, T.D. (2020) 'Methods of numerical analysis of monopiles under pseudo-random lateral loading', in. ISFOG.

Houlsby, G.T. and Puzrin, A.M. (2006) *Principles of Hyperplasticity An Approach to Plasticity Theory Based on Thermodynamic Principles*. Limited. Springer London.

Iai, S., Matsunaga, Y. and Kameoka, T. (1992) 'Strain Space Plasticity Model for Cyclic Mobility', *Soils and Foundations*, 32(2), pp. 1–15. Available at: https://doi.org/https://doi.org/10.3208/sandf1972.32.2_1.

Ishihara, K. (1996) *Soil Behaviour in Earthquake Geotechnics*. Oxford University Press. Available at: https://doi.org/10.1093/oso/9780198562245.001.0001.

Ishihara, K., Tatsuoka, F. and Yasuda, S. (1975) 'Undrained Deformation and Liquefaction of Sand Under Cyclic Stresses', *Soils and Foundations*, 15(1), pp. 29–44. Available at: https://doi.org/https://doi.org/10.3208/sandf1972.15.29.

Iwan, W.D. (1966) 'A Distributed-Element Model for Hysteresis and Its Steady-State Dynamic Response', *Journal of Applied Mechanics*, 33, pp. 893–900. Available at: https://doi.org/10.1115/1.3625199.

Iwan, W.D. (1967) 'On a Class of Models for the Yielding Behavior of Continuous and Composite Systems', *Journal of Applied Mechanics*, 34, pp. 612–617. Available at: https://doi.org/10.1115/1.3607751.

Jefferies, M., Shuttle, D. and Been, K. (2015) 'Principal stress rotation as cause of cyclic mobility', *Geotechnical Research*, 2, pp. 66–96. Available at: https://doi.org/10.1680/gr.15.00002.

Jefferies, M.G. (1993) ‘Nor-Sand: a simple critical state model for sand’, *Géotechnique*, 43, pp. 91–103. Available at: https://doi.org/10.1680/geot.1993.43.1.91.

Jostad, H., Grimstad, G., Andersen, K. and Sivasithamparam, N. (2015) ‘A FE procedure for calculation of cyclic behaviour of offshore foundations under partly drained conditions’, in V. Meyer (ed.). Taylor & Francis Group, pp. 153–172.

Jovičić, V. and Coop, M.R. (1997) ‘Stiffness of coarse-grained soils at small strains’, *Géotechnique*, 47(3), pp. 545–561. Available at: https://doi.org/10.1680/geot.1997.47.3.545.

Kaklamanos, J., Dorfmann, L. and Baise, L. (2015) ‘A Simple Approach to Site-Response Modeling: The Overlay Concept’, *Seismological Research Letters*, 86, pp. 413–423. Available at: https://doi.org/10.1785/0220140100.

Kallehave, D., Byrne, B., Thilsted, C. and Mikkelsen, K. (2015) ‘Optimization of monopiles for offshore wind turbines’, *Philosophical transactions. Series A, Mathematical, physical, and engineering sciences*, 373. Available at: https://doi.org/10.1098/rsta.2014.0100.

Kaltekis, K., Whyte, S., Vahdatirad, M. and Hilton, J. (2023) *A Review of Constitutive Models for an FEA-based Monopile Design*.

Kolymbas, D. (2000) *Constitutive modelling of granular materials*. Springer-Verlag.

Krieg, R.D. (1975) ‘A Practical Two Surface Plasticity Theory’, *Journal of Applied Mechanics*, 42(3), pp. 641–646. Available at: https://doi.org/10.1115/1.3423656.

Lan, H., Liu, H. and Zhao, H. (2023) ‘Impact of hyper-elasticity on cyclic sand modelling: A numerical study based on SANISAND-MS’, *Computers and Geotechnics*, 159, p. 105428. Available at: https://doi.org/10.1016/j.compgeo.2023.105428.

Lashkari, A. (2009) ‘On the modeling of the state dependency of granular soils’, *Computers and Geotechnics*, 36(7), pp. 1237–1245. Available at: https://doi.org/10.1016/J.COMPGEO.2009.06.003.

Lashkari, A. (2010) ‘A SANISAND model with anisotropic elasticity’, *Soil Dynamics and Earthquake Engineering*, 30(12), pp. 1462–1477. Available at: https://doi.org/10.1016/J.SOILDYN.2010.06.015.

Lashkari, A. (2014) ‘Recommendations for extension and re-calibration of an existing sand constitutive model taking into account varying non-plastic fines content’, *Soil Dynamics and Earthquake Engineering*, 61–62, pp. 212–238. Available at: https://doi.org/10.1016/j.soildyn.2014.02.012.

LeBlanc, C., Houlsby, G.T. and Byrne, B.W. (2010) ‘Response of stiff piles in sand to long-term cyclic lateral loading’, *Géotechnique*, 60(2), pp. 79–90. Available at: https://doi.org/10.1680/geot.7.00196.

Lee, J.-S., Choo, Y.-W. and Kim, D.-S. (2009) ‘A modified parallel IWAN model for cyclic hardening behavior of sand’, *Soil Dynamics and Earthquake Engineering*, 29(4), pp. 630–640. Available at: https://doi.org/https://doi.org/10.1016/j.soildyn.2008.06.008.

Lekarp, F. and Dawson, A. (1998) ‘Modelling permanent deformation behaviour of unbound granular materials’, *Construction and Building Materials*, 12(1), pp. 9–18. Available at: https://doi.org/https://doi.org/10.1016/S0950-0618(97)00078-0.

Lentz, R.W. and Baladi, G.Y. (1981) ‘Constitutive equation for permanent strain of sand subjected to cyclic loading’, *Transportation research record*, 810, pp. 50–54.

Li, S., Zhang, Y. and Jostad, H.P. (2019) ‘Drainage conditions around monopiles in sand’, *Applied Ocean Research*, 86, pp. 111–116. Available at: https://doi.org/https://doi.org/10.1016/j.apor.2019.01.024.

Li, X.S. and Dafalias, Y.F. (2000) ‘Dilatancy for cohesionless soils’, *Géotechnique*, 50(4), pp. 449–460. Available at: https://doi.org/10.1680/geot.2000.50.4.449.

Li, X.S. and Dafalias, Y.F. (2012) ‘Anisotropic Critical State Theory: Role of Fabric’, *Journal of Engineering Mechanics*, 138, pp. 263–275. Available at: https://doi.org/10.1061/(asce)em.1943-7889.0000324.

Li, X.S. and Wang, Y. (1998) ‘Linear Representation of Steady-State Line for Sand’, *Journal of Geotechnical and Geoenvironmental Engineering*, 124(12), pp. 1215–1217. Available at: https://doi.org/10.1061/(ASCE)1090-0241(1998)124:12(1215).

Li, Z. and Liu, H. (2020) ‘An isotropic-kinematic hardening model for cyclic shakedown and ratcheting of sand’, *Soil Dynamics and Earthquake Engineering*, 138, p. 106329. Available at: https://doi.org/https://doi.org/10.1016/j.soildyn.2020.106329.

Liu, H. (2020) *Constitutive Modelling of Cyclic Sand Behaviour for Offshore Foundations*. Doctoral thesis. Delft University of Technology.

Liu, H., Abell, J.A., Diambra, A. and Pisanò, F. (2019) ‘Modelling the cyclic ratcheting of sands through memory-enhanced bounding surface plasticity’, *Géotechnique*, 69, pp. 783–800. Available at: https://doi.org/10.1680/jgeot.17.p.307.

Liu, H., Diambra, A., Abell, J.A. and Pisanò, F. (2020) ‘Memory-Enhanced Plasticity Modeling of Sand Behavior under Undrained Cyclic Loading’, *Journal of Geotechnical and Geoenvironmental Engineering*, 146, p. 4020122. Available at: https://doi.org/10.1061/(asce)gt.1943-5606.0002362.

Liu, H. and Kaynia, A.M. (2022) ‘Monopile responses to monotonic and cyclic loading in undrained sand using 3D FE with SANISAND-MSu’, *Water Science and Engineering*, 15(1), pp. 69–77. Available at: https://doi.org/https://doi.org/10.1016/j.wse.2021.12.001.

Liu, H., Kementzetzidis, E., Abell, J.A. and Pisanò, F. (2022) ‘From cyclic sand ratcheting to tilt accumulation of offshore monopiles: 3D FE modelling using SANISAND-MS’, *Geotechnique*, 72(9), pp. 753–768. Available at: https://doi.org/10.1680/jgeot.20.P.029.

Liu, H., Pisanò, F., Jostad, H.P. and Sivasithamparam, N. (2022) ‘Impact of cyclic strain accumulation on the tilting behaviour of monopiles in sand: An assessment of the Miner’s rule based on SANISAND-MS 3D FE modelling’, *Ocean Engineering*, 250, p. 110579. Available at: https://doi.org/https://doi.org/10.1016/j.oceaneng.2022.110579.

Loukidis, D. and Salgado, R. (2009) ‘Modeling sand response using two-surface plasticity’, *Computers and Geotechnics*, 36(1), pp. 166–186. Available at: https://doi.org/https://doi.org/10.1016/j.compgeo.2008.02.009.

Mair, R.J. (1993) ‘Developments in geotechnical engineering research: application to tunnels and deep excavations’, in *Proc. Instn. Civ. Engrs. Civ. Engng.*, pp. 27–41.

Manzari, M.T. and Dafalias, Y.F. (1997) ‘A critical state two-surface plasticity model for sands’, *Géotechnique*, 47(2), pp. 255–272. Available at: https://doi.org/10.1680/geot.1997.47.2.255.

Masing, G. (1926) ‘Eigenspannungen und verfestigung beim messing (Self stretching and hardening for brass)’, in, pp. 332–335.

McAdam, R.A., Byrne, B.W., Houlsby, G.T., Beuckelaers, W.J.A.P., Burd, H.J., Gavin, K.G., Igoe, D.J.P., Jardine, R.J., Martin, C.M., Muir Wood, A., Potts, D.M., Skov Gretlund, J., Taborda, D.M.G. and Zdravković, L. (2020) ‘Monotonic laterally loaded pile testing in a dense marine sand at Dunkirk’, *Géotechnique*, 70(11), pp. 986–998. Available at: https://doi.org/10.1680/jgeot.18.PISA.004.

Mroz, Z. (1967) ‘On the description of anisotropic workhardening’, *Journal of the Mechanics and Physics of Solids*, 15(3), pp. 163–175.

Mroz, Z. (1969) ‘An attempt to describe the behavior of metals under cyclic loads using a more general workhardening model’, *Acta mechanica*, 7(2), pp. 199–212.

Mroz, Z. and Pietruszczak, S. (1983) ‘A constitutive model for sand with anisotropic hardening rule’, *International Journal for Numerical and Analytical Methods in Geomechanics*, 7(3), pp. 305–320.

Narsilio, G. and Santamarina, J. (2008) ‘Terminal Densities’, *Géotechnique*, 58, pp. 669–674. Available at: https://doi.org/10.1680/geot.2008.58.8.669.

Niemunis, A. and Herle, I. (1997) ‘Hypoplastic model for cohesionless soils with elastic strain range’, *Mechanics of Cohesive-frictional Materials*, 2(4), pp. 279–299. Available at: https://doi.org/https://doi.org/10.1002/(SICI)1099-1484(199710)2:4<279::AID-CFM29>3.0.CO;2-8.

Niemunis, A., Wichtmann, T. and Triantafyllidis, Th. (2005) ‘A high-cycle accumulation model for sand’, *Computers and Geotechnics*, 32(4), pp. 245–263. Available at: https://doi.org/10.1016/j.compgeo.2005.03.002.

Numanoglu, O.A. (2019) *Numerical modeling and simulation of seismic settlements on dense sands*.

Numanoglu, O.A., Hashash, Y.M.A., Olson, S.M., Cerna-Diaz, A., Rutherford, C.J., Bhaumik, L., Centella R, D.M. and Weaver, T. (2023) ‘A simplified three-dimensional constitutive model for seismic modeling of dense sands’, *Soil Dynamics and Earthquake Engineering*, 167, p. 107794. Available at: https://doi.org/https://doi.org/10.1016/j.soildyn.2023.107794.

Oh, K.Y., Nam, W., Ryu, M.S., Kim, J.Y. and Epureanu, B.I. (2018) ‘A review of foundations of offshore wind energy convertors: Current status and future perspectives’, *Renewable and Sustainable Energy Reviews*, 88, pp. 16–36. Available at: https://doi.org/10.1016/J.RSER.2018.02.005.

Page, A., Næss, V., Vaal, J., Eiksund, G. and Nygaard, T. (2019) ‘Impact of foundation modelling in offshore wind turbines: Comparison between simulations and field data’, *Marine Structures*, 64, pp. 379–400. Available at: https://doi.org/10.1016/j.marstruc.2018.11.010.

Page, A.M., Klinkvort, R.T., Bayton, S., Zhang, Y. and Jostad, H.P. (2021) ‘A procedure for predicting the permanent rotation of monopiles in sand supporting offshore wind turbines’, *Marine Structures*, 75, p. 102813. Available at: https://doi.org/10.1016/j.marstruc.2020.102813.

Papadimitriou, A., Bouckovalas, G. and Dafalias, Y.F. (2001) ‘Plasticity model for sand under small and large cyclic strains’, *Journal of Geotechnical and Geoenvironmental Engineering*, 127, pp. 973–983. Available at: https://doi.org/10.1061/(ASCE)1090-0241(2001)127:11(973).

Park, J. and Santamarina, J. (2020) ‘Soil Response to Repetitive Changes in Pore-Water Pressure under Deviatoric Loading’, *Journal of Geotechnical and Geoenvironmental Engineering*, 146, p. 04020023. Available at: https://doi.org/10.1061/(ASCE)GT.1943-5606.0002229.

Parra, E. (1996) ‘Numerical modeling of liquefaction and lateral ground deformation including cyclic mobility and dilation response in soil systems’, *Rensselaer Polytechnic Institute, Troy, NY, USA* [Preprint].

Pasten, C., Shin, H. and Santamarina, J.C. (2014) ‘Long-Term Foundation Response to Repetitive Loading’, *Journal of Geotechnical and Geoenvironmental Engineering*, 140, p. 4013036. Available at: https://doi.org/10.1061/(asce)gt.1943-5606.0001052.

Pastor, M., Zienkiewicz, O.C. and Leung, K.H. (1985) ‘Simple model for transient soil loading in earthquake analysis. II. Non-associative models for sands’, *International Journal for Numerical and Analytical Methods in Geomechanics*, 9(5), pp. 477–498. Available at: https://doi.org/https://doi.org/10.1002/nag.1610090506.

Peralta, P., Ballard, J.C., Rattley, M. and Erbrich, C.E. (2017) 'Dynamic and Cyclic Pile-Soil Response Curves for Monopile Design', in *Offshore Site Investigation and Geotechnics: Proceedings of the 8th International Conference*. Society for Underwater Technology (SUT), pp. 1054–1061. Available at: https://doi.org/10.3723/OSIG17.1054.

Pestana, J.M. and Whittle, A.J. (1999) 'Formulation of a unified constitutive model for clays and sands', *International Journal for Numerical and Analytical Methods in Geomechanics*, 23(12), pp. 1215–1243. Available at: https://doi.org/https://doi.org/10.1002/(SICI)1096-9853(199910)23:12<1215::AID-NAG29>3.0.CO;2-F.

Petalas, A., Dafalias, Y. and Papadimitriou, A. (2019) 'SANISAND-FN: An evolving fabric-based sand model accounting for stress principal axes rotation', *International Journal for Numerical and Analytical Methods in Geomechanics*, 43, pp. 97–123. Available at: https://doi.org/10.1002/nag.2855.

Petalas, A.L., Dafalias, Y.F. and Papadimitriou, A.G. (2020) 'SANISAND-F: Sand constitutive model with evolving fabric anisotropy', *International Journal of Solids and Structures*, 188–189, pp. 12–31. Available at: https://doi.org/https://doi.org/10.1016/j.ijsolstr.2019.09.005.

Pisanò, F., Del Brocco, I., Ho, H.M. and Brasile, S. (2024) '3D FE simulation of PISA monopile field tests at Dunkirk using SANISAND-MS', *Geotechnique Letters*, 14(2), pp. 35–45. Available at: https://doi.org/https://doi.org/10.1680/jgele.23.00073.

Pisanò, F. and Gavin, K. (2017) 'General Report for TC209 Offshore Geotechnics', in *19th International Conference on Soil Mechanics and Geotechnical Engineering*. Seoul.

Prevost, J.-H. (1977) 'Mathematical modelling of monotonic and cyclic undrained clay behaviour', *International Journal for Numerical and Analytical Methods in Geomechanics*, 1(2), pp. 195–216.

Prevost, J.H. (1978) 'Plasticity theory for soil stress-strain behavior', *Journal of the Engineering Mechanics Division*, 104(5), pp. 1177–1194.

Prevost, J.H. (1982) 'Two-surface versus multi-surface plasticity theories: A critical assessment', *International Journal for Numerical and Analytical Methods in Geomechanics*, 6, pp. 323–338. Available at: https://doi.org/10.1002/nag.1610060305.

Prevost, J.H. (1985) 'A simple plasticity theory for frictional cohesionless soils', *International Journal of Soil Dynamics and Earthquake Engineering*, 4, pp. 9–17. Available at: https://doi.org/10.1016/0261-7277(85)90030-0.

di Prisco, C. and Wood, D.M. (2012) *Mechanical Behaviour of Soils Under Environmentally Induced Cyclic Loads*. Springer.

Puech, A. and Garnier, J. (2017) *Design of piles under cyclic loading : SOLCYP recommendations [electronic resource]*.

Rahman, M.M. (2021) 'The State of Art on Equivalent State Theory for Silty Sands', in R. and K.S. Sitharam T.G. and Jakka (ed.) *Latest Developments in Geotechnical Earthquake Engineering and Soil Dynamics*. Singapore: Springer Singapore, pp. 225–246. Available at: https://doi.org/10.1007/978-981-16-1468-2_11.

Rahman, M.M., Cubrinovski, M. and Lo, S.R. (2012) 'Initial shear modulus of sandy soils and equivalent granular void ratio', *Geomechanics and Geoengineering*, 7(3), pp. 219–226. Available at: https://doi.org/10.1080/17486025.2011.616935.

Rahman, M.M. and Dafalias, Y.F. (2022) 'Modelling undrained behaviour of sand with fines and fabric anisotropy', *Acta Geotechnica*, 17(6), pp. 2305–2324. Available at: https://doi.org/10.1007/s11440-021-01410-7.

Rahman, M.M. and Lo, S.-C. (2007) 'Equivalent granular void ratio and state parameters for loose clean sand with small amount of fines'.

Rahman, M.M., Lo, S.-C. and Gnanendran, C. (2008) ‘On equivalent granular void ratio and steady state behaviour of loose sand with fines’, *Canadian Geotechnical Journal*, 45, pp. 1439–1456. Available at: https://doi.org/10.1139/T08-064.

Rahman, M.M., Lo, S.C.R. and Dafalias, Y.F. (2014) ‘Modelling the static liquefaction of sand with low-plasticity fines’, *Geotechnique*, 64(11), pp. 881–894. Available at: https://doi.org/10.1680/geot.14.P.079.

Rahman, M.M. and Lo, S.R. (2008) ‘The prediction of equivalent granular steady state line of loose sand with fines’, *Geomechanics and Geoengineering*, 3(3), pp. 179–190. Available at: https://doi.org/10.1080/17486020802206867.

Rahman, M.M., Lo, S.R. and Baki, M.A.L. (2011) ‘Equivalent granular state parameter and undrained behaviour of sand-fines mixtures’, *Acta Geotechnica*, 6(4), pp. 183–194. Available at: https://doi.org/10.1007/s11440-011-0145-4.

Richards, I. (2019) *Monopile foundations under complex cyclic lateral loading*. University of Oxford.

Richart, F.E., Hall, J.R. and Woods, R.D. (1970) ‘Vibrations of soils and foundations’, in. Available at: https://api.semanticscholar.org/CorpusID:106629913.

Roscoe, K.H., Schofield, An., Wroth and P, C. (1958) ‘On the yielding of soils’, *Geotechnique*, 8(1), pp. 22–53.

Rowe, P. (1962) ‘The Stress-Dilatancy Relation for Static Equilibrium of an Assembly of Particles in Contact’, *Proceedings of The Royal Society A: Mathematical, Physical and Engineering Sciences*, 269, pp. 500–527. Available at: https://doi.org/10.1098/rspa.1962.0193.

Roy, A., Liu, H., Bienen, B., Chow, S.H. and Diambra, A. (2024) ‘Suction bucket performance in sand under vertical cyclic loading: Numerical modelling using SANISAND-MS’, *Computers and Geotechnics*, 173, p. 106497. Available at: https://doi.org/https://doi.org/10.1016/j.compgeo.2024.106497.

Saberi, M., Simonin, L., Houlsby, G. and Byrne, B. (2025) ‘Three dimensional finite element simulation of monopiles for offshore wind turbines using the HySand constitutive model’, in *5th International Symposium on Frontiers in Offshore Geotechnics (ISFOG2025)*. Nantes, France, pp. 1692–1698.

Sawicki, A. and Swidzinski, W. (1989) ‘Mechanics of a sandy subsoil subjected to cyclic loadings’, *International Journal for Numerical and Analytical Methods in Geomechanics*, 13(5), pp. 511–529.

Schüttenhelm, R.T.E. (1980) ‘The superficial geology of the Dutch sector of the North Sea’, *Marine Geology*, 34(1), pp. M27–M37. Available at: https://doi.org/https://doi.org/10.1016/0025-3227(80)90134-6.

Seequent (2023) *SANISAND-MS User Defined Soil Model Manual for PLAXIS 3D 2023.2*.

Simonin, L. (2023) *Development of an effective stress model for sand under cyclic loading in the hyperplastic framework*. Doctoral thesis. University of Oxford.

Simonin, L., Houlsby, G. and Byrne, B. (2023) ‘HySand: A New Constitutive Model for Sand Under Cyclic Loading’, in, pp. 142–149. Available at: https://doi.org/10.1007/978-3-031-12851-6_18.

Sloan, S.W. (1987) ‘Substepping schemes for the numerical integration of elastoplastic stress–strain relations’, *International Journal for Numerical Methods in Engineering*, 24(5), pp. 893–911. Available at: https://doi.org/10.1002/NME.1620240505.

Sloan, S.W., Abbo, A.J. and Sheng, D. (2001) ‘Refined explicit integration of elastoplastic models with automatic error control’, *Engineering Computations*, 18(1–2), pp. 121–154. Available at: https://doi.org/10.1108/02644400110365842.

Soga, K. and Mitchell, J. (2005) *Fundamentals of Soil Behavior, 3rd Edition*.

Staubach, P. and Wichtmann, T. (2020) ‘Long-term deformations of monopile foundations for offshore wind turbines studied with a high-cycle accumulation model’, *Computers and Geotechnics*, 124, p. 103553. Available at: https://doi.org/10.1016/j.compgeo.2020.103553.

Stehly, T., Duffy, P. and Hernando, D.M. (2024) ‘Cost of Wind Energy Review: 2024 Edition’, in. Available at: https://api.semanticscholar.org/CorpusID:126702527.

Suiker, A.S.J. and de Borst, R. (2003) ‘A numerical model for the cyclic deterioration of railway tracks’, *International Journal for Numerical Methods in Engineering*, 57, pp. 441–470. Available at: https://doi.org/10.1002/nme.683.

Sweere, G.T.H. (1990) *Unbound Granular Bases for Roads.*

Taborda, D.M.G., Zdravković, L., Kontoe, S. and Potts, D.M. (2014) ‘Computational study on the modification of a bounding surface plasticity model for sands’, *Computers and Geotechnics*, 59, pp. 145–160. Available at: https://doi.org/https://doi.org/10.1016/j.compgeo.2014.03.005.

Taborda, D.M.G., Zdravković, L., Potts, D.M., Burd, H.J., Byrne, B.W., Gavin, K.G., Houlsby, G.T., Jardine, R.J., Liu, T., Martin, C.M. and McAdam, R.A. (2020) ‘Finite-element modelling of laterally loaded piles in a dense marine sand at Dunkirk’, *Géotechnique*, 70(11), pp. 1014–1029. Available at: https://doi.org/10.1680/jgeot.18.PISA.006.

Tafili, M., Knittel, L., Gauger, V., Wichtmann, T. and Stutz, H.H. (2024) ‘Experimental study on monotonic to high-cyclic behaviour of sand-silt mixtures’, *Acta Geotechnica*, 19(7), pp. 4227–4240. Available at: https://doi.org/10.1007/s11440-023-02126-6.

Taiebat, M. and Dafalias, Y.F. (2008) ‘SANISAND: Simple anisotropic sand plasticity model’, *International Journal for Numerical and Analytical Methods in Geomechanics*, 32, pp. 915–948. Available at: https://doi.org/10.1002/nag.651.

Takahashi, A., Omura, N., Kobayashi, T., Kamata, Y. and Inagaki, S. (2022) ‘Centrifuge model tests on large-diameter monopiles in dense sand subjected to two-way lateral cyclic loading in short-term’, *Soils and Foundations*, 62(3), p. 101148. Available at: https://doi.org/https://doi.org/10.1016/j.sandf.2022.101148.

Tantivangphaisal, P., Taborda, D.M.G. and Kontoe, S. (2025) ‘Implementation of a practical sand constitutive model coupled with the High Cycle Accumulation framework in PLAXIS.’, *MethodsX*, p. 103183. Available at: https://doi.org/https://doi.org/10.1016/j.mex.2025.103183.

Tantivangphaisal, P., Taborda, D.M.G., Kontoe, S., Liu, T. and Jardine, R.J. (2025) ‘Numerical modelling of the long-term cyclic response of laterally loaded piles driven in sands using the high-cycle accumulation framework’, *Géotechnique [Published online ahead of print]*, 0(0), pp. 1–17. Available at: https://doi.org/10.1680/jgeot.24.01404.

Tasiopoulou, P., Chacko, J., Chaloulos, Y., Giannakou, A. and Gerolymos, N. (2020) ‘INSIGHT INTO THE CYCLIC RESPONSE OF OWT PILE FOUNDATIONS IN SAND: NUMERICAL SIMULATION OF PISA FIELD TESTS’, in *International Symposium on Frontiers in Offshore Geotechnics*.

Tasiopoulou, P., Chaloulos, Y., Gerolymos, N., Giannakou, A. and Chacko, J. (2019) *3D and 2D simulations of liquefaction-induced settlements of shallow foundations using Ta-Ger model*.

Tasiopoulou, P., Chaloulos, Y., Gerolymos, N., Giannakou, A. and Chacko, J. (2021) ‘Cyclic lateral response of OWT bucket foundations in sand: 3D coupled effective stress analysis with Ta-Ger model’, *Soils and Foundations*, 61(2), pp. 371–385. Available at: https://doi.org/https://doi.org/10.1016/j.sandf.2020.12.002.

Tasiopoulou, P. and Gerolymos, N. (2012) ‘Development of a modified elastoplasticity model for sand’, in *Second International Conference on Performance–Based Design in Earthquake Geotechnical Engineering*. Taormina, Italy.

Tasiopoulou, P. and Gerolymos, N. (2016a) ‘Constitutive modeling of sand: Formulation of a new plasticity approach’, *Soil Dynamics and Earthquake Engineering*, 82, pp. 205–221. Available at: https://doi.org/10.1016/j.soildyn.2015.12.014.

Tasiopoulou, P. and Gerolymos, N. (2016b) ‘Constitutive modelling of sand: a progressive calibration procedure accounting for intrinsic and stress-induced anisotropy’, *https://doi.org/10.1680/jgeot.15.P.284*, 66(9), pp. 754–770. Available at: https://doi.org/10.1680/JGEOT.15.P.284.

Thevanayagam, S. (2003) *Role of Intergranular Contacts on Mechanisms Causing Liquefaction & Slope Failures in Silty Sands: Final Report*. New York: University at Buffalo, State University of New York, Department of Civil, Structural, and Environmental Engineering. Available at: https://books.google.co.uk/books?id=h1lcGwAACAAJ.

Thevanayagam, S. and Martin, G.R. (2002) ‘Liquefaction in silty soils—screening and remediation issues’, *Soil Dynamics and Earthquake Engineering*, 22(9), pp. 1035–1042. Available at: https://doi.org/https://doi.org/10.1016/S0267-7261(02)00128-8.

Thevanayagam, S. and Mohan, S. (2000) ‘Intergranular state variables and stress–strain behaviour of silty sands’, *Géotechnique*, 50(1), pp. 1–23. Available at: https://doi.org/10.1680/geot.2000.50.1.1.

Truesdell, C. (1955) ‘Hypo-elasticity’, *Journal of Rational Mechanics and Analysis*, 4, pp. 83–1020.

Truong, P., Lehane, B.M., Zania, V. and Klinkvort, R.T. (2018) ‘Empirical approach based on centrifuge testing for cyclic deformations of laterally loaded piles in sand’, *Geotechnique*, 69(2), pp. 133–145. Available at: https://doi.org/https://doi.org/10.1680/jgeot.17.P.203.

Tsuha, C.H.C., Foray, P.Y., Jardine, R.J., Yang, Z.X., Silva, M. and Rimoy, S. (2012) ‘Behaviour of displacement piles in sand under cyclic axial loading’, *Soils and Foundations*, 52(3), pp. 393–410. Available at: https://doi.org/https://doi.org/10.1016/j.sandf.2012.05.002.

United Kingdom government (2022) *British energy security strategy*. Available at: https://www.gov.uk/government/publications/british-energy-security-strategy/british-energy-security-strategy (Accessed: 17 February 2025).

Vaid, Y.P. and Chern, J.C. (1985) ‘Cyclic and monotonic undrained response of saturated sands’, in. Available at: https://api.semanticscholar.org/CorpusID:274935457.

Verdugo, R. and Ishihara, K. (1996) ‘The Steady State of Sandy Soils’, *Soils and Foundations*, 36(2), pp. 81–91. Available at: https://doi.org/10.3208/SANDF.36.2_81.

Versteijlen, W.G., Metrikine, A., Hoving, J., Smidt, E. and de Vries, W. (2011) ‘Estimation of the vibration decrement of an offshore wind turbine support structure caused by its interaction with soil’, *Knowledge, Technology & Policy* [Preprint].

Wang, S. and Larsen, T.J. (2019) ‘Permanent accumulated rotation of an offshore monopile wind turbine in sand during a storm’, *Ocean Engineering*, 188, p. 106340. Available at: https://doi.org/https://doi.org/10.1016/j.oceaneng.2019.106340.

Wang, S., Wu, W., Peng, C., He, X. and Cui, D. (2018) ‘Numerical integration and FE implementation of a hypoplastic constitutive model’, *Acta Geotechnica*, 13(6), pp. 1265–1281. Available at: https://doi.org/10.1007/s11440-018-0684-z.

Wang, Z., Dafalias, Y.F. and Shen, C. (1990) ‘Bounding Surface Hypoplasticity Model for Sand’, *Journal of Engineering Mechanics*, 116(5), pp. 983–1001. Available at: https://doi.org/10.1061/(ASCE)0733-9399(1990)116:5(983).

Wei, X., Chen, Y. and Yang, J. (2020) 'A unified critical state constitutive model for cyclic behavior of silty sands', *Computers and Geotechnics*, 127, p. 103760. Available at: https://doi.org/https://doi.org/10.1016/j.compgeo.2020.103760.

Wei, X. and Yang, J. (2019) 'A critical state constitutive model for clean and silty sand', *Acta Geotechnica*, 14(2), pp. 329–345. Available at: https://doi.org/10.1007/s11440-018-0675-0.

Wen, Y.-K. (1976) 'Method for Random Vibration of Hysteretic System', *ASCE J Eng Mech Div*, 102. Available at: https://doi.org/10.1061/JMCEA3.0002106.

Whyte, S. (2020) *Development, Implementation, Calibration and Use of Practical Constitutive Models in Finite Element Analysis of Offshore Foundations*.

Whyte, S.A., Burd, H.J., Martin, C.M. and Rattley, M.J. (2020) 'Formulation and implementation of a practical multi-surface soil plasticity model', *Computers and Geotechnics*, 117. Available at: https://doi.org/10.1016/j.compgeo.2019.05.007.

Wichtmann, T. (2005) *Explicit Accumulation Model for Non-cohesive Soils under Cyclic Loading*.

Wichtmann, T. (2016) *Soil behaviour under cyclic loading - experimental observations, constitutive description and applications*.

Wichtmann, T., Fuentes, W. and Triantafyllidis, T. (2019) 'Inspection of three sophisticated constitutive models based on monotonic and cyclic tests on fine sand: Hypoplasticity vs. Sanisand vs. ISA', *Soil Dynamics and Earthquake Engineering*, 124, pp. 172–183. Available at: https://doi.org/10.1016/j.soildyn.2019.05.001.

Wichtmann, T., Niemunis, A. and Triantafyllidis, T. (2010) 'Towards the FE prediction of permanent deformations of offshore wind power plant foundations using a high-cycle accumulation model', in, pp. 635–640.

Wichtmann, T. and Triantafyllidis, T. (2016a) 'An experimental database for the development, calibration and verification of constitutive models for sand with focus to cyclic loading: part II—tests with strain cycles and combined loading', *Acta Geotechnica*, 11(4), pp. 763–774. Available at: https://doi.org/10.1007/s11440-015-0412-x.

Wichtmann, T. and Triantafyllidis, T. (2016b) 'An experimental database for the development, calibration and verification of constitutive models for sand with focus to cyclic loading: part I—tests with monotonic loading and stress cycles', *Acta Geotechnica*, 11(4), pp. 739–761. Available at: https://doi.org/10.1007/s11440-015-0402-z.

Wichtmann, T. and Triantafyllidis, T. (2017) 'Strain accumulation due to packages of cycles with varying amplitude and/or average stress – On the bundling of cycles and the loss of the cyclic preloading memory', *Soil Dynamics and Earthquake Engineering*, 101, pp. 250–263. Available at: https://doi.org/https://doi.org/10.1016/j.soildyn.2017.07.012.

Wind Europe (2024) *Wind energy in Europe: 2023 Statistics and the outlook for 2024-2030*. Available at: https://windeurope.org/intelligence-platform/product/wind-energy-in-europe-2023-statistics-and-the-outlook-for-2024-2030/#overview (Accessed: 17 February 2025).

Xu, L.-Y., Zhang, J.-Z., Cai, F., Chen, W.-Y. and Xue, Y.-Y. (2019) 'Constitutive modeling the undrained behaviors of sands with non-plastic fines under monotonic and cyclic loading', *Soil Dynamics and Earthquake Engineering*, 123, pp. 413–424. Available at: https://doi.org/https://doi.org/10.1016/j.soildyn.2019.05.021.

Yang, J. and Sze, H.Y. (2011) 'Cyclic behaviour and resistance of saturated sand under non-symmetrical loading conditions', *Géotechnique*, 61(1), pp. 59–73. Available at: https://doi.org/10.1680/geot.9.P.019.

Yang, M., Taiebat, M. and Dafalias, Y. (2022) 'SANISAND-MSf: a sand plasticity model with memory surface and semifluidised state', *Géotechnique*, 72, pp. 227–246. Available at: https://doi.org/10.1680/jgeot.19.P.363.

Yang, Z. and Elgamal, A. (2008) 'Multi-surface Cyclic Plasticity Sand Model with Lode Angle Effect', *Geotechnical and Geological Engineering*, 26(3), pp. 335–348. Available at: https://doi.org/10.1007/s10706-007-9170-3.

Yang, Z., Elgamal, A. and Parra, E. (2003) 'Computational Model for Cyclic Mobility and Associated Shear Deformation', *Journal of Geotechnical and Geoenvironmental Engineering*, 129, pp. 1119–1127. Available at: https://doi.org/10.1061/(asce)1090-0241(2003)129:12(1119).

Youd, T.L., Idriss, I.M., D, A.R., Ignacio, A., Gonzalo, C., T, C.J., Richardo, D., Liam, F.W.D., F, H.L., Ellen, H.M., Kenji, I., P, K.J., C, L.S.S., F, M.W., R, M.G., K, M.J., Yoshiharu, M., S, P.M., K, R.P., B, S.R. and H, S.K. (2001) 'Liquefaction Resistance of Soils: Summary Report from the 1996 NCEER and 1998 NCEER/NSF Workshops on Evaluation of Liquefaction Resistance of Soils', *Journal of Geotechnical and Geoenvironmental Engineering*, 127(10), pp. 817–833. Available at: https://doi.org/10.1061/(ASCE)1090-0241(2001)127:10(817).

Yu, H.-S. (2006) *Plasticity and geotechnics*. Springer.

Zdravković, L., Jardine, R.J., Taborda, D.M.G., Abadias, D., Burd, H.J., Byrne, B.W., Gavin, K.G., Houlsby, G.T., Igoe, D.J.P., Liu, T., Martin, C.M., McAdam, R.A., Muir Wood, A., Potts, D.M., Skov Gretlund, J. and Ushev, E. (2020) 'Ground characterisation for PISA pile testing and analysis', *Géotechnique*, 70(11), pp. 945–960. Available at: https://doi.org/10.1680/jgeot.18.PISA.001.

Zerfa, F.Z. and Loret, B. (2003) 'Coupled dynamic elastic–plastic analysis of earth structures', *Soil Dynamics and Earthquake Engineering*, 23, pp. 435–454. Available at: https://doi.org/10.1016/s0267-7261(03)00060-5.

Zhang, Y., Andersen, K., Klinkvort, R.T., Jostad, H., Sivasithamparam, N., Boylan, N. and Langford, T. (2016) *Monotonic and Cyclic p-y Curves for Clay Based on Soil Performance Observed in Laboratory Element Tests*. Available at: https://doi.org/10.4043/26942-MS.

Ziegler, H. (1976) *An Introduction to Thermomechanics*. (2nd Edition, 1983). Amsterdam: North-Holland Publishing Company (North-Holland series in applied mathematics and mechanics).

Ziotopoulou, K. and Boulanger, R.W. (2013) 'Calibration and implementation of a sand plasticity plane-strain model for earthquake engineering applications', *Soil Dynamics and Earthquake Engineering*, 53, pp. 268–280. Available at: https://doi.org/https://doi.org/10.1016/j.soildyn.2013.07.009.